Université de Strasbourg

UNIVERSITÉ DE STRASBOURG

EDSC École Doctorale des Sciences Chimiques

ÉCOLE DOCTORALE DES SCIENCE CHIMIQUE

UMR 7006 – Institut de Science et d'Ingénierie Supramoléculaire

THÈSE

présentée par :

Haixin QIU

soutenue le : **27 Mai 2021**

pour obtenir le grade de : **Docteur de l'université de Strasbourg**

Discipline/ Spécialité: Chimie-Physique

Interfaçage des molécules réactives avec des semi-conducteurs 2D: fabrication de dispositifs multifonctionnels

THÈSE dirigée par :

M. SAMORì Paolo	Professeur, Institut de Science et d'Ingénierie Supramoléculaires, Université de Strabourg, France

RAPPORTEURS :

M. BELJONNE David	Directeur de recherche du FNRS, Chimie des Matériaux Nouveaux & Centre d'Innovation et de Recherche en Matériaux Polymères, Université de Mons, Belgique
M. VUILLAUME Dominique	Directeur de recherche du CNRS, Institut d'électronique, de microélectronique et de nanotechnologie, Université de Lille, France

AUTRES MEMBRES DU JURY :

M. BIANCO Alberto	Directeur de recherche du CNRS, Immunologie, immunopathologie et chimie thérapeutique, Université de Strabourg, France

Direction de la **recherche**
et de la **valorisation**
Collège **doctoral**
Université de Strasbourg

Déclaration sur l'honneur
Declaration of Honour

J'affirme être informé que le plagiat est une faute grave susceptible de mener à des sanctions administratives et disciplinaires pouvant aller jusqu'au renvoi de l'Université de Strasbourg et passible de poursuites devant les tribunaux de la République Française.

Je suis conscient(e) que l'absence de citation claire et transparente d'une source empruntée à un tiers (texte, idée, raisonnement ou autre création) est constitutive de plagiat.

Au vu de ce qui précède, **j'atteste sur l'honneur que le travail décrit dans mon manuscrit de thèse est un travail original et que je n'ai pas eu recours au plagiat ou à toute autre forme de fraude.**

I affirm that I am aware that plagiarism is a serious misconduct that may lead to administrative and disciplinary sanctions up to dismissal from the University of Strasbourg and liable to prosecution in the courts of the French Republic.

I am aware that the absence of a clear and transparent citation of a source borrowed from a third party (text, idea, reasoning or other creation) is constitutive of plagiarism.

In view of the foregoing, ***I hereby certify that the work described in my thesis manuscript is original work and that I have not resorted to plagiarism or any other form of fraud.***

Nom : Qiu

Prénom : Haixin

Ecole doctorale : ED222

Laboratoire : Nanochemistry

Date : 18/06/2021

Signature :

Résumé

Le travail mené dans le cadre de cette thèse s'est axé sur la fabrication de dispositifs multifonctionnels basés sur des semi-conducteurs bidimensionnels (2DS) décorés par de molécules. Les 2DS ont attiré une attention considérable tant dans la science fondamentale que dans la technologie, du fait de leurs propriétés exceptionnelles. Dans l'ère post-silicium, leurs épaisseurs à l'échelle atomique ont validé ces matériaux comme les candidats prometteurs dans l'industrie électronique avancée, et ils ont été utilisés dans un large éventail d'applications comme les photodétecteurs,[1] les mémoires non volatiles à haute densité[2] et les capteurs biocompatibles.[3] Bien que des avancées impressionnantes aient été réalisées, des défis se posent encore en matière de commercialisation. L'un des véritables verrous est le contrôle du type de porteur de charge et du niveau de dopage dans les 2DS, qui est la condition essentielle pour la production de dispositifs et de circuits à logique complémentaire.[4] Notre projet de recherche consiste à fournir une solution prometteuse et polyvalente pour résoudre ce défi, c'est-à-dire intégrer des molécules sensibles aux stimuli dans des dispositifs à base de 2DS, non seulement pour réaliser le contrôle du transport des porteurs de charge, mais également pour ajouter de nouvelles fonctions au circuits numériques, enrichissant la diversification des technologies «More than Moore».[5]

Les molécules sensibles aux stimuli sont particulièrement intéressantes en raison de leur capacité à être interconverties entre deux ou plusieurs états, ayant des propriétés nettement distinctes, lorsqu'elles sont soumises à des stimuli externes tels que des champs électromagnétiques, électriques ou magnétiques ou des changements dans l'environnement (pH, température, etc).[6] En incorporant de telles molécules dans des transistors à effet de champ (FET) classiques, une nouvelle capacité de réponse aux stimuli peut être conférée au dispositif, permettant ainsi de contrôler leurs propriétés électriques par diverses entrées externes. De plus, ayant un rapport surface: volume élevé, les 2DSs en monocouches et en quelques couches ont une surface extrêmement sensible au moindre changement environnemental avoisinant, ce qui ouvre la possibilité de modifier leurs propriétés intrinsèques.[7] Des études récentes innovantes sur l'utilisation de molécules répondants aux stimuli pour décorer la surface des 2DSs ont montré que cette stratégie est prometteuse pour moduler la densité des porteurs de charge de manière non destructive, en déplaçant l'interrupteur déclenché par les stimuli au niveau moléculaire par la modification des propriétés des 2DS sans introduire de défaut.[8]

Parmi les stimuli externes possibles, la lumière et le champ électrique sont apparus comme des stimuli externes attrayants, tous deux non invasifs, contrôlables à distance et numériquement avec une résolution spatiale et temporelle élevée. En tant que stimulus doux et bien appliqué, la température représente également l'une des voies les plus largement explorées dans la conception de plates-formes sensibles aux stimuli.

Les molécules photochromiques sont des systèmes optiquement réactifs, capables de subir une photoisomérisation réversible lorsqu'ils sont irradiés avec de la lumière à des longueurs d'onde spécifiques.[9] Les molécules photochromiques les plus populaires rapportées à ce jour sont les azobenzènes, les spiropyranes (SPs) et les diaryléthènes (DAEs). Les deux premières molécules mentionnées ont d'abord été combinées avec des 2DSs pour conduire à un dopage réversible optiquement contrôlé par la variation de leurs moments dipolaires moléculaires entre leurs deux photoisomères.[10] Par contre, notre recherche utilise le mécanisme de transfert de charge pour réaliser des FET à base de 2DS optiquement sensible en les combinant avec des molécules DAE appropriées. Cette molécule possède des avantages significatifs pour les applications électroniques numériques car elle combine une photoisomérisation efficace à l'état solide avec une résistance à la fatigue élevée, une bistabilité thermique et des niveaux énergétiques phototunables strictement définis.[11] D'autre part, des matériaux ferroélectriques ont également été utilisés pour contrôler précisément le niveau de dopage des 2DS.[12] Selon la direction du champ électrique externe, leur polarisation bistable intrinsèque peut être réorientée, conduisant à une accumulation ou un épuisement des porteurs de charge dans le matériau semi-conducteur interfacé.[13] Fait intéressant, ces transistors à effet de champ ferroélectriques (FeFET) tirent parti des états de polarisation restants binaires du ferroélectrique pour stocker des informations et ont donc été utilisés avec succès dans des mémoires non volatiles.[14]

Dans le premier projet, des FETs optiquement commutables ont été réalisés en décorant la surface des 2DSs, du WSe_2 de type n et du phosphore noir (BP) de type p, avec des molécules DAE conçues de manière à moduler leur transport d'électrons et de trous, respectivement.[15] Les molécules DAE subissent une isomérisation photochimique entre leur isomère en cycle ouvert et en cycle fermé par la lumière UV et visible, accompagnée d'un changement de leur orbitale moléculaire occupée la plus élevée (HOMO) et de leur orbitale moléculaire inoccupée la plus basse (LUMO), offrant la possibilité d'affecter différemment le processus de transport de charge lorsqu'ils sont combinés avec des 2DSs. Par conséquent, la nécessité de réaliser une telle photomodulation repose sur l'adaptation des niveaux d'énergie entre les 2DSs hôtes et les molécules DAE, pour former l'état de piégeage. Une illustration schématique de l'alignement du niveau d'énergie entre 2DS/DAE est représentée sur la **Figure 1**. Pour WSe_2 intrinsèquement dopé de type n avec des électrons agissant comme les porteurs de charge principaux, l'énergie de sa bande de conduction minimale (CBM) doit se situer entre les niveaux LUMO de DAE_1$_O$ et DAE_1$_C$. C'est-à-dire que la LUMO de DAE_1$_O$ présente une valeur d'énergie plus élevée que le CBM de WSe_2, empêchant ainsi le transfert d'électrons de WSe_2 à DAE_1$_O$. D'autre part, DAE_1$_C$ avec un niveau d'énergie inférieur se comporte comme un site de piégeage pour les électrons de WSe_2, ce qui entraîne une diminution de la densité électronique. Dans le dispositif FET correspondant, la conversion de DAE_1o en DAE_1c par irradiation UV induit un dopage de type p avec une modulation de courant de 61%. De même, pour BP avec un transport dominant de type p, son maximum de bande de valance (VBM) doit se trouver énergiquement entre les niveaux HOMO de

DAE_2$_{O}$ et DAE_2$_{C}$. La force motrice pour le piégeage des trous n'existe donc que dans DAE_2$_{O}$, conduisant à une densité de trous réduite. Dans le dispositif FET, l'irradiation UV révèle une diminution du courant de sortie d'une modulation de 42%. Pour révéler davantage le rôle des niveaux d'énergie des DAE par rapport à la modification du transport de charge dans 2DS, nous avons également étendu notre étude à BP/DAE_3. La HOMO de DAE_3$_{C}$ étant isoénergétique par rapport au VBM de BP, le piégeage de trou photodéclenché est annulé dans cette paire, donc aucun comportement de modulation n'est observé dans le dispositif FET par irradiation UV/vis. Il convient de noter que les dispositifs FET basés sur un tel système 2DS/DAE affichent une excellente capacité de rétention des données et une lecture de haute précision avec plusieurs niveaux de courant distincts, ouvrant des perspectives vers son utilisation comme mémoire non volatile à plusieurs niveaux.

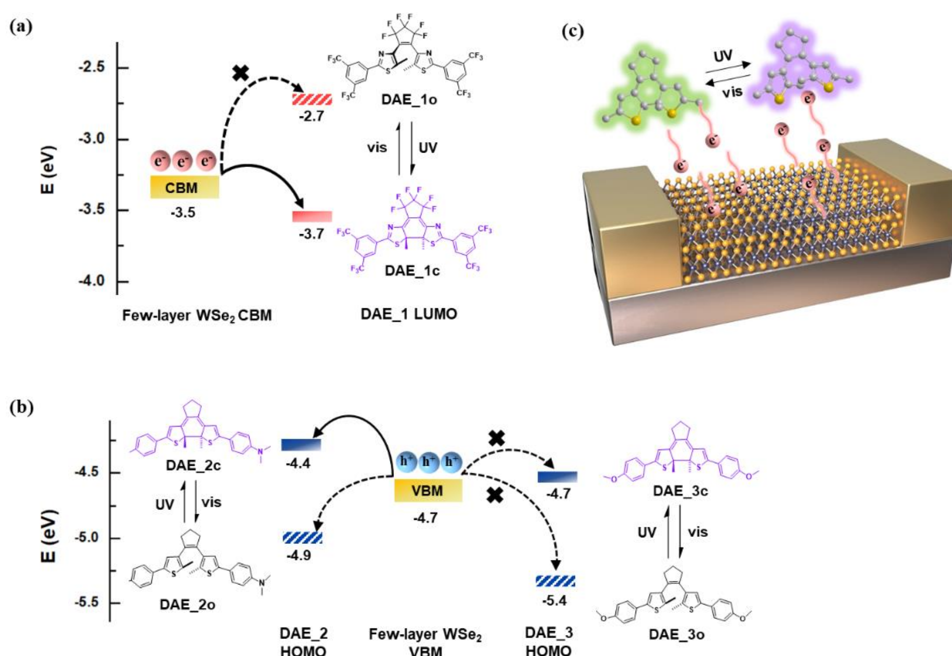

Figure 1. Molécules, niveaux d'énergie et structure de l'appareil. (a, b) Diagramme du niveau d'énergie du transport d'électrons entre WSe_2/DAE_1 (a) et du transport de trous entre BP/DAE_2 et BP/DAE_3 (b). Les structures chimiques des molécules DAE sont également illustrées. Les valeurs de niveau d'énergie pour les DAE sont déterminées par voltamétrie cyclique; pour WSe_2 et BP, ils sont calculés dans la fonction d'échange filtrée. (c) Représentation schématique du FET basé sur 2DS/DAE.

Après avoir démontré l'applicabilité générale et l'efficacité de cette approche 2DS/DAE pour la modulation de transport d'électrons et de trous en fonction de la nature de la cible 2DS, dans le deuxième projet, nous abordons la commutation ambipolaire complète du transport de charge dans le 2DS.[16] Inspiré par le phénomène selon lequel le porteur principal de charge dans WSe_2 évolue avec son épaisseur, allant du type p, ambipolaire au type n, nous visons des multicouche de WSe_2 à quelques couches avec un comportement ambipolaire plus équilibré, avec ses courants d'électrons et de trous à la même échelle (10^{-6} A). Nous proposons ici un FET multiniveaux optiquement commutable en interfaçant WSe_2 avec un mélange DAE à deux constituants composés de deux molécules avec des

niveaux d'énergie spécifiques, qui sont conçues pour être capables de piéger les électrons ou les trous de WSe_2 par des stimuli lumineux à distance (**Figure 2**). Il est intéressant de noter que la modulation du courant de sortie pour les trous atteint 97%, tandis que pour les électrons, la modulation atteint 52%. Une telle photomodulation s'est avérée efficace et réversible avec une fatigue de commutation négligeable après plus de 20 cycles d'éclairage. De plus, le rapport de modulation peut être facilement réglé en contrôlant la dose de lumière, ce qui signifie qu'en ajustant la durée d'irradiation, le dispositif FET peut atteindre une multitude d'états courants. En particulier, la caractéristique ambipolaire équilibrée de WSe_2 permet à notre appareil d'atteindre 64 niveaux de courant distincts pour les trous et les électrons, soulignant son potentiel à être davantage développé en mémoires à plusieurs niveaux avec une capacité de stockage de données de 7 bits. De plus, en tirant parti de la bistabilité thermique des molécules de DAE dans les deux états photoisomères, il est démontré que le dispositif possède un temps de rétention prolongé dépassant 20 jours dans l'obscurité. Il est à noter que, tirant pleinement parti des exellentes propriétés mécaniques du 2D WSe_2 ultramince, notre dispositif est également capable de fonctionner sur un substrat en poly(téréphtalate d'éthylène) (PET) flexible et transparent, sans perdre sa capacité de commutation optique, ce qui est attrayant pour la nouvelle génération d'électronique portable multifonctionnelle.

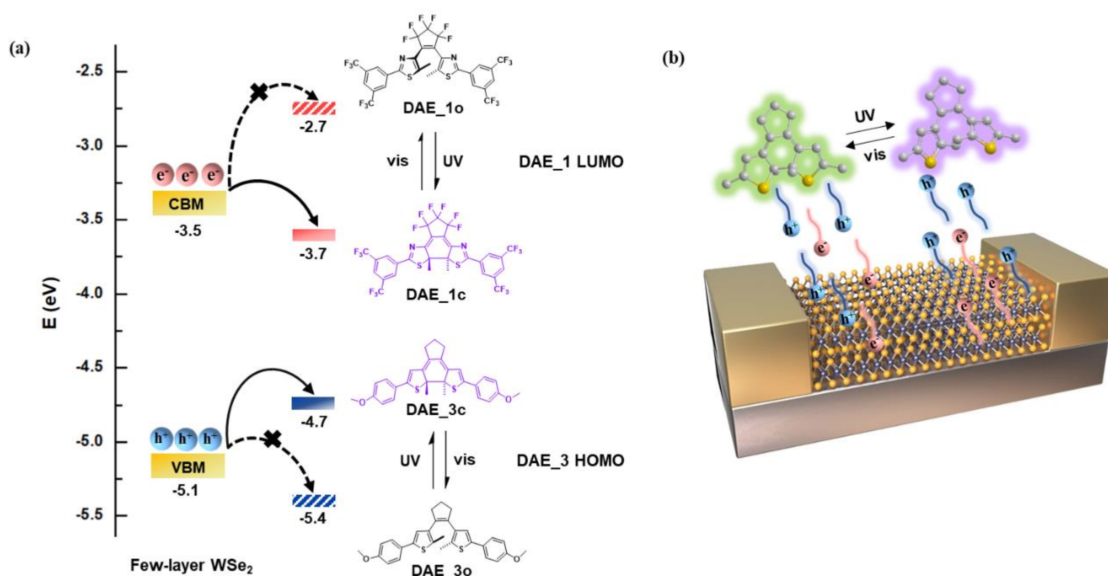

Figure 2. Diagramme de niveau d'énergie, structure moléculaire et du dispositif. (a) Structures chimiques de DAE_1 et DAE_3, en tant qu'isomères ouverts et fermés. Diagramme de niveau d'énergie du transport d'électrons entre WSe_2/DAE_1 et transport de trous entre WSe_2/DAE_3. (b) Illustration schématique de l'architecture du dispositif FET basée sur WSe_2/DAE sur substrat Si/SiO_2.

Dans les deux projets ci-dessus, des FETs optiquement commutables ont été réalisés en déposant directement des molécules DAE au-dessus de la surface supérieure du canal. La structure inversée du dispositif pourrait également être obtenue en déposant d'abord les molécules sur un substrat approprié, puis en transférant les 2DSs. Dans tous les FETs 2D-mono-stimuli-réactifs fonctionnalisés par des

molécules rapportés, une seule face du 2DS est interfacée aux molécules, n'exploitant ainsi pas une asymétrie potentielle déterminée par les deux surfaces qui pourraient être rendues inégales par exposition à deux environnements différents. Un tel scénario peut être réalisé par la fonctionnalisation indépendante de chaque surface avec une molécule fonctionnelle différente,[17] offrant des perspectives intéressantes vers la réalisation de FET multi-stimuli-réactifs. Pour résoudre ce problème, dans le troisième projet, nous rapportons une approche sans précédent basée sur la décoration de feuillets WSe_2 à quelques couches avec deux (macro)molécules différentes réactives aux stimuli générant ainsi un matériau Janus 2D. En particulier, sur la surface inférieure reposait une couche de DAE_1 sensible à la lumière et la surface supérieure était revêtue d'une couche de copolymère poly(fluorure de vinylidène-trifluoroéthylène) (P(VDF-TrFE)) réactif à l'électricité (**Figure 3a**). De cette manière, un FET sensible à plusieurs stimuli a été fabriqué dans lequel le courant de sortie peut être modulé de manière réversible et précise au moyen soit d'une irradiation lumineuse soit d'un champ électrique. Par rapport aux FET conventionnels mono-stimuli sensibles, cette nouvelle architecture de dispositif ternaire combine à la fois une complexité fonctionnelle améliorée avec une simplicité de fabrication. Nous fournissons des preuves sans équivoque de la compatibilité de la réponse du dispositif aux stimuli optiques et électriques, offrant ainsi une prise en main orthogonale sur le fonctionnement de l'appareil, ce qui est également favorable pour les applications de mémoire. En tirant parti de l'effet synergique entre les deux commutateurs (macro)moléculaires, le dispositif a atteint une modulation améliorée du courant de sortie, avec un rendement pouvant atteindre 87%. De plus, comme chaque stimulus manifeste un grand nombre de sorties différentes sans interférences mutuelles (9 niveaux induits par l'électricité et 84 niveaux induits par la lumière), le dispositif produit un nombre total de 756 états distincts, surpassant le transistor mono-stimuli sensibles, en fournissant ainsi un pas en avant décisif pour répondre à la demande de mémoires de stockage à haute densité. La fiabilité de chaque état est en outre reflétée par les tests d'endurance et de rétention pour 5 états arbitraires, présentant une endurance notable pendant plus de 10 cycles et une excellente rétention des données dépassant 1000 heures. De plus, comparée à la synthèse complexe de molécules uniques incorporant différents groupes fonctionnels pour réaliser les éléments multi-adressables, cette structure ternaire modifiée Janus repose sur un processus de fabrication simple et elle semble être une stratégie plus universelle qui peut être étendue à d'autres 2DS et molécules fonctionnelles, offrant une plate-forme polyvalente pour la construction de dispositifs multi-stimuli-sensibles.

Dans le projet ci-dessus, la couche de DAE physiosorbée offre une voie prometteuse vers la fonctionnalisation non destructive du matériau du canal. Cependant, l'interaction faible de van der Waals entre les molécules et le substrat Si/SiO_2 permet d'enlever facilement les molécules au cours d'une simple procédure de rinçage. En conséquence, le processus de photolithographie conventionnel n'est pas faisable dans une telle architecture de dispositif, et le choix du second élément sensible à des stimuli est également limité. Pour surmonter ce problème, dans le quatrième projet, nous avons

synthétisé un dérivé de SP à terminaison silane, qui peut densément s'assembler sur un substrat Si/SiO_2 grâce à une silylation covalente forte. Une telle chimisorption non volatile de celui-ci facilite la fabrication du dispositif et offre une meilleure compatibilité lors de l'intégration d'un troisième élément dans le système. De plus, la réaction photochromique du SP à la mérocyanine (MC) peut être déclenchée par un éclairage à la lumière UV, et l'isomérisation inverse de MC à SP peut être accomplie par illumination de la lumière visible ainsi que par chauffage, ce qui ajoute une nouvelle capacité de réponse thermique aux dispositifs FET correspondants par rapport au système composant DAE. Suivant la structure modifiée Janus similaire, la molécule photochromique SP à terminaison silane et le polymère ferroélectrique P(VDF-TrFE) ont été incorporés dans des dispositifs FET à base de WSe_2 (**Figure 3b**). Avec cette combinaison, nous avons obtenu un FET sensible aux stimuli quaternaires capable de percevoir les stimuli comme la chaleur, la lumière et de champ électrique, et de moduler le courant de sortie en conséquence. Une telle architecture permet un contrôle indépendant du courant de sortie sous de multiples stimuli distincts. Profitant de l'effet synergique entre les stimuli, avec une efficacité de modulation de courant d'électrons significative de 84% de SP, et de 99% de P (VDF-TrFE), les électrons dans le canal peuvent être totalement épuisés en combinant les deux commutateurs et le dispositif peut être modulé du type n au type p. De plus, en regroupant collectivement plusieurs stimuli en tant qu'entrées, la dépendance excessive à un seul stimulus a été réduite, ce qui augmente en outre la sensibilité et la conformité de la plate-forme de réponse aux stimuli moléculaires.

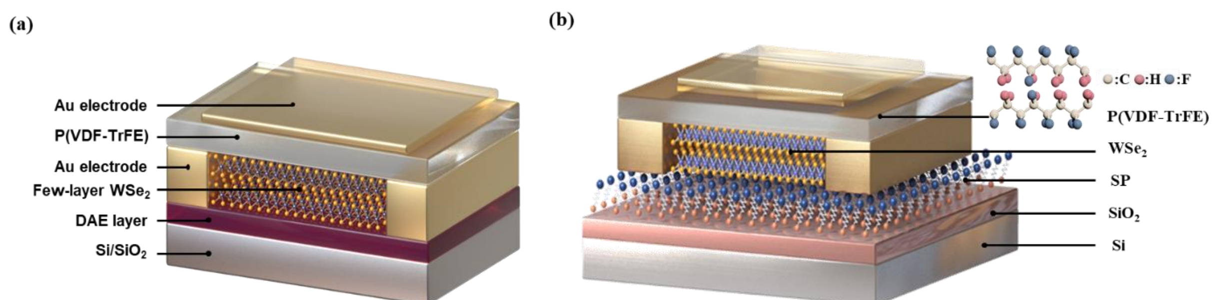

Figure 3. (a) Schéma de principe du dispositif DAE_1/WSe_2/FeFET avec décoration double face: la face inférieure avec film DAE_1 et la face supérieure avec couche P(VDF-TrFE). (b) Schéma de principe du dispositif SP/WSe_2/FeFET avec décoration double face: la face inférieure avec film SP et la face supérieure avec couche P(VDF-TrFE).

En conclusion, nous avons exploité l'approche moléculaire sensible aux stimuli pour fabriquer des FET multifonctionnels dont le courant de sortie peut être contrôlé de manière réversible non seulement par son champ électrique interne, mais également par divers stimuli externes, comme la lumière, la chaleur et le champ électrique. En particulier, des FET à réponse binaire ont été fabriqués en intégrant des 2DS avec des molécules photochromiques DAE. Des FET à réponse ternaire ont ensuite été réalisés en ajoutant un troisième composant, le polymère ferroélectrique P(VDF-TrFE). En tirant pleinement parti de la bistabilité des éléments sensibles aux stimuli, les dispositifs ont démontré leur application en tant

que mémoires non volatiles à haute densité. Enfin, en remplaçant DAE par SP, des FET à réponse quaternaire aux stimuli ont été fabriqués. Notre architecture de dispositif est généralement applicable à d'autres 2DS et molécules réactives aux stimuli, ouvrant de nouvelles opportunités pour l'électronique multi-stimuli-sensible de nouvelle génération et favorisant le développement de technologies «More than Moore» en enrichissant la diversification.

References

[1] a) S. H. Yu, Y. Lee, S. K. Jang, J. Kang, J. Jeon, C. Lee, J. Y. Lee, H. Kim, E. Hwang, S. Lee, *ACS Nano* **2014**, *8*, 8285; b) F. H. L. Koppens, T. Mueller, P. Avouris, A. C. Ferrari, M. S. Vitiello, M. Polini, *Nat. Nanotechnol.* **2014**, *9*, 780.

[2] a) D. Lee, E. Hwang, Y. Lee, Y. Choi, J. S. Kim, S. Lee, J. H. Cho, *Adv. Mater.* **2016**, *28*, 9196; b) D. Xiang, T. Liu, J. Xu, J. Y. Tan, Z. Hu, B. Lei, Y. Zheng, J. Wu, A. H. C. Neto, L. Liu, W. Chen, *Nat. Commun.* **2018**, *9*, 2966.

[3] a) B. Zong, Q. Li, X. Chen, C. Liu, L. Li, J. Ruan, S. Mao, *ACS Appl. Mater. Interfaces* **2020**, *12*, 50610; b) D. Sarkar, W. Liu, X. Xie, A. C. Anselmo, S. Mitragotri, K. Banerjee, *ACS Nano* **2014**, *8*, 3992.

[4] a) N. Onofrio, D. Guzman, A. Strachan, *J. Appl. Phys.* **2017**, *122*, 185102; b) V. P. Pham, G. Y. Yeom, *Adv. Mater.* **2016**, *28*, 9024.

[5] M. M. Waldrop, *Nature* **2016**, *530*, 144.

[6] a) C. Simão, M. Mas-Torrent, N. Crivillers, V. Lloveras, J. M. Artés, P. Gorostiza, J. Veciana, C. Rovira, *Nat. Chem.* **2011**, *3*, 359; b) M. E. Itkis, X. Chi, A. W. Cordes, R. C. Haddon, *Science* **2002**, *296*, 1443.

[7] a) L. Yang, K. Majumdar, H. Liu, Y. Du, H. Wu, M. Hatzistergos, P. Hung, R. Tieckelmann, W. Tsai, C. Hobbs, *Nano Lett.* **2014**, *14*, 6275; b) D. M. Sim, M. Kim, S. Yim, M.-J. Choi, J. Choi, S. Yoo, Y. S. Jung, *ACS Nano* **2015**, *9*, 12115; c) S. Bertolazzi, S. Bonacchi, G. Nan, A. Pershin, D. Beljonne, P. Samorì, *Adv. Mater.* **2017**, *29*, 1606760.

[8] a) Y. Zhao, S. Bertolazzi, M. S. Maglione, C. Rovira, M. Mas-Torrent, P. Samorì, *Adv. Mater.* **2020**, *32*, 2000740; b) S. Wang, L. Tan, P. Liang, T. Liu, J. Wang, C. Fu, J. Yu, J. Dou, H. Li, X. Meng, *J. Mater. Chem. B* **2016**, *4*, 2133; c) L. Chen, X. Zhou, W. Nie, W. Feng, Q. Zhang, W. Wang, Y. Zhang, Z. Chen, P. Huang, C. He, *ACS Appl. Mater. Interfaces* **2017**, *9*, 17786.

[9] L. Wang, Q. Li, *Chem. Soc. Rev.* **2018**, *47*, 1044.

[10] a) Y. Zhao, S. Bertolazzi, P. Samorì, *ACS Nano* **2019**, *13*, 4814; b) M. Gobbi, S. Bonacchi, J. X. Lian, A. Vercouter, S. Bertolazzi, B. Zyska, M. Timpel, R. Tatti, Y. Olivier, S. Hecht, M. V. Nardi, D. Beljonne, E. Orgiu, P. Samorì, *Nat. Commun.* **2018**, *9*, 2661.

[11] M. Irie, *Chem. Rev.* **2000**, *100*, 1685.

[12] a) C. Zhou, Y. Chai, *Adv. Electron. Mater.* **2017**, *3*, 1600400; b) X. Chen, X. Han, Q.-D. Shen, *Adv. Electron. Mater.* **2017**, *3*, 1600460.

[13] a) Y. T. Lee, D. K. Hwang, S. Im, *J. Korean Phys. Soc.* **2015**, *67*, 1499; b) X. Wang, P. Wang, J. Wang, W. Hu, X. Zhou, N. Guo, H. Huang, S. Sun, H. Shen, T. Lin, M. Tang, L. Liao, A. Jiang, J. Sun, X. Meng, X. Chen, W. Lu, J. Chu, *Adv. Mater.* **2015**, *27*, 6575; c) D. Li, X. Wang, Y. Chen, S. Zhu, F. Gong, G. Wu, C. Meng, L. Liu, L. Wang, T. Lin, S. Sun, H. Shen, X. Wang, W. Hu, J. Wang, J. Sun, X. Meng, J. Chu, *Nanotechnology* **2018**, *29*, 105202.

[14] R. C. G. Naber, K. Asadi, P. W. M. Blom, D. M. de Leeuw, B. de Boer, *Adv. Mater.* **2010**, *22*, 933.

[15] H. Qiu, Y. Zhao, Z. Liu, M. Herder, S. Hecht, P. Samorì, *Adv. Mater.* **2019**, *31*, 1903402.

[16] H. Qiu, Z. Liu, Y. Yao, M. Herder, S. Hecht, P. Samorì, *Adv. Mater.* **2020**, *32*, 1907903.

[17] M.-A. Stoeckel, M. Gobbi, T. Leydecker, Y. Wang, M. Eredia, S. Bonacchi, R. Verucchi, M. Timpel, M. V. Nardi, E. Orgiu, P. Samorì, *ACS Nano* **2019**, *13*, 11613.

Abstract

The work carried out within this thesis is centered on the fabrication of multifunctional devices based on molecular tailored two-dimensional semiconductors (2DSs). 2DSs have attracted tremendous attention in both fundamental science and technology due to their outstating properties. In the post-silicon era, the atomic-scale thicknesses have endorsed these materials as the promising candidates in the advanced electronic industry, and they have been used in a wide range of applications spanning from photodetectors,[1] high density nonvolatile memories[2] to biocompatible sensors.[3] Although impressive advances have been put forward, challenges are still being faced when it comes to commercialization. One of the veritable bottlenecks is the control of the charge-carrier type and the doping level in 2DSs, which is the crucial requirement for the production of practical complementary-logic devices and circuits.[4] Our research project is to provide a promising and versatile solution to solve this challenge, that is, integrating stimuli-responsive molecules into 2DS-based devices, not only to realize the control over the charge-carrier transport, but also add novel functions to the digital circuits, enriching the diversification in “More than Moore” technologies.[5]

Stimuli-responsive molecules are of particularly interest because of their capacity to be interconverted between two or more states, having markedly distinct properties, when subjected to external stimuli such as electromagnetic, electric or magnetic fields or changes in the environment (pH, temperature, etc.).[6] By incorporating such molecules in conventional field-effect transistors (FETs), novel stimuli-responsive capacity can be imparted to the device thereby enabling to manipulate their electrical output by means of various external inputs. Moreover, due to their high surface-to-volume ratio, monolayer and few-layer 2DSs have an exquisite surface sensitivity to any subtle surrounding environmental change, which opens up the opportunity to modify their intrinsic properties.[7] Recent ground-breaking studies on the exploitation of stimuli-responsive molecules to decorate the surface of 2DSs has been demonstrated being a promising strategy to non-destructively modulate the charge carrier density of the latter, via translating the stimuli-triggered switch at the molecular level into the modification of 2DS’s properties without introducing any defect.[8]

Light and electric field have been emerged as attractive external stimuli, both of which are noninvasive, remotely and digitally controllable with high spatial and temporal resolution. As a mild and conveniently applied stimuli, temperature also represents one of the most widely explored inputs in the design of stimuli-responsive platforms.

Photochromic molecules are optically responsive systems able to undergo reversible photoisomerization when irradiated with light at specific wavelengths.[9] The most popular photochromic molecules reported so far are azobenzenes, spiropyrans (SPs), and diarylethenes (DAEs).

The former two molecules were firstly combined with 2DSs to lead a light-controlled reversible doping by the variation of their molecular dipole moments between their perspective two photoisomers.[10] Our research unprecedentedly uses the charge transfer mechanism to realize light responsive 2DS-based FETs by combining with suitable DAE molecules, which possess significant advantages for applications in (digital) electronics as they combine efficient photoisomerization in the solid state with high fatigue resistance, thermal bistability, and strictly defined phototunable energetic levels.[11] On the other hand, ferroelectric materials have also been employed to precisely control the doping level of 2DSs.[12] According to the direction of the external electric field, their intrinsic bistable polarization can be reoriented, leading to an accumulation or depletion of the charge carriers in the interfaced semiconducting material.[13] Interestingly, these ferroelectric field-effect transistors (FeFETs) take advantage of the binary remnant polarization states of the ferroelectric to store information and therefore have successfully been utilized in practical non-volatile memories.[14]

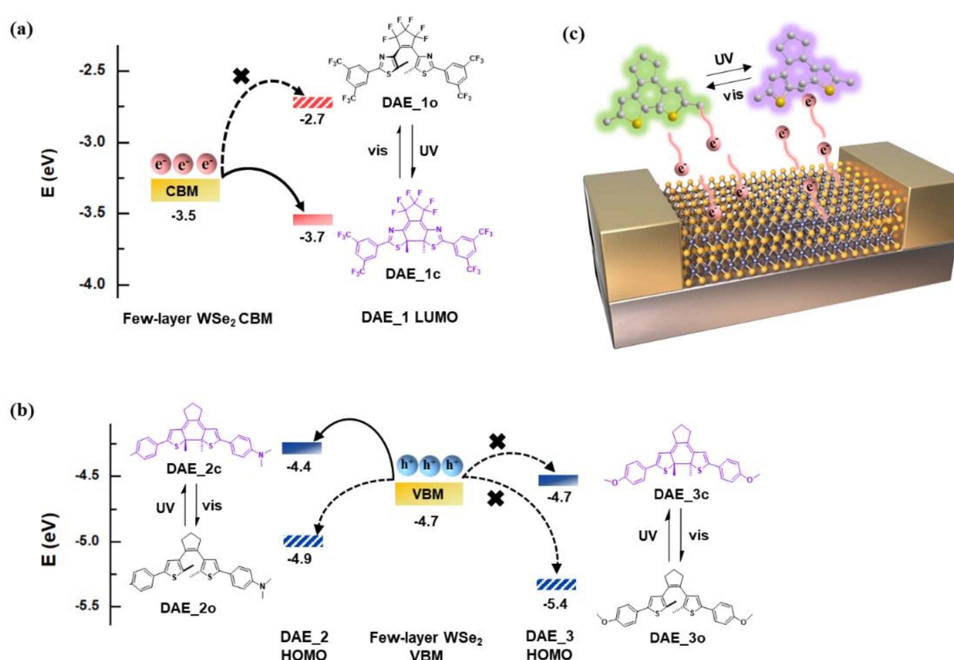

Figure 1. Molecules, energy levels, and device structure. (a,b) Energy-level diagram of electron transport between WSe_2/DAE_1 (a), and hole transport between BP/DAE_2 and BP/DAE_3 (b). Chemical structures of DAE molecules are also illustrated. Energy-level values for DAEs are determined by cyclic voltammetry; for WSe_2 and BP are calculated in the screened-exchange functional. (c) Schematic representation of the 2DS/DAE-based FET.

In the first project, optically switchable FETs have been realized by decorating the surface of the semiconducting 2DSs, n-type dominant WSe_2 and p-type dominant black phosphorus (BP) with suitably designed DAE molecules, to modulate their electron and hole transport, respectively.[15] DAE molecules undergo a photochemical isomerization between its ring-open and ring-closed isomer by UV and vis light, accompanied with a switch of their corresponding highest occupied molecular orbital (HOMO) and lowest unoccupied molecular orbital (LUMO) energy levels, providing the possibility to affect

differently the charge transport process when they are combined with 2DSs. Therefore, the requirement to achieve such photomodulation relies on the matching of the energy levels between the host 2DSs and DAE molecules, to enable the appearance of trapping states. A schematic illustration of the energy-level alignment between 2DS/DAE is depicted in Figure 1. For intrinsically n-type doped WSe_2 with electrons act as the main charge carrier, the energy of its conduction band minimum (CBM) should locate between the LUMO levels of DAE_1_O and DAE_1_C. That is, the LUMO of DAE_1_O features a higher energy value compared to the CBM of WSe_2, thereby impeding the electron transfer from WSe_2 to DAE_1_O. Conversely, DAE_1_C with lower energy value behaves as trapping site for WSe_2 electrons, resulting in a decrease of electron density. In the corresponding FET device, the conversion from DAE_1o to DAE_1c by UV irradiation induced a p-type doping with a current modulation of 61%. Similarly, for BP with p-type dominant transport, its valance band maximum (VBM) should lie energetically between the HOMO levels of DAE_2_O and DAE_2_C. The driving force for hole trapping therefore exists only in DAE_2_O, leading to a reduced hole density. In the corresponding FET device, UV irradiation enduces a decrease of output current by a modulation of 42%. To further reveal the role of energy levels of DAEs with respect to the tuning of the charge transport in 2DS, we also extended our study to BP/DAE_3. With the HOMO of DAE_3_C being isoenergetic to the VBM of BP, the phototriggered hole trapping is nullified in this pair, therefore no modulation behavior is observed in the FET device by UV/vis irradiation. Noteworthy, the FET devices based on such a 2DS/DAE system display excellent data-retention capacity and a high-accuracy readout with several distinguishable current levels, opening perspectives toward its use as multilevel nonvolatile memory.

After demonstrating the general applicability and effectiveness of this 2DS/DAE approach for both electron and hole transport modulation depending on the nature of target 2DS, in the second project, we tackle full ambipolar switching of charge transport in the 2DS.[16] Inspired by the phenomenon that the main type of charge carrier in WSe_2 evolves with its thickness, ranging from p-type, ambipolar to n-type, we target on few-layer WSe_2 flakes with a more balanced ambipolar behavior, with its electron and hole current on the same scale (10^{-6} A). Here we propose an optically switchable multilevel FET by interfacing WSe_2 with a bicomponent DAE blend consisting of two molecules with specific energy levels, which are engineered in order to be capable of trapping either the electrons or the holes of WSe_2 by remote light stimuli (Figure 2). Noteworthy, the output current modulation for holes is as high as 97%, while for electrons the modulation amounts to 52%. Such photomodulation is demonstrated to be efficient and reversible with negligible switching fatigue after over 20 illumination cycles. Moreover, the modulation ratio can be readily tuned by controlling the light dose, which means by adjusting the irradiation duration the FET device can reach a multitude of current states. In particular, the balanced ambipolar characteristic of WSe_2 enables our device to attain 64 distinct current levels for both holes and electrons, highlighting its potential to be further developed into multilevel memories with data storage capacity of 7 bit. Additionally, by taking advantage of the thermal bistability of DAE molecules

in both photoisomeric states, the device is shown to possess a prolonged retention time exceeding 20 days in the dark. Remarkably, taking full advantage of the superior mechanical properties of ultrathin 2D WSe_2, our device is also able to be operated on a flexible and transparent poly(ethylene terephthalate) (PET) substrate, without losing its optical switching capability, which is attractive for future generation of multifunctional wearable electronics.

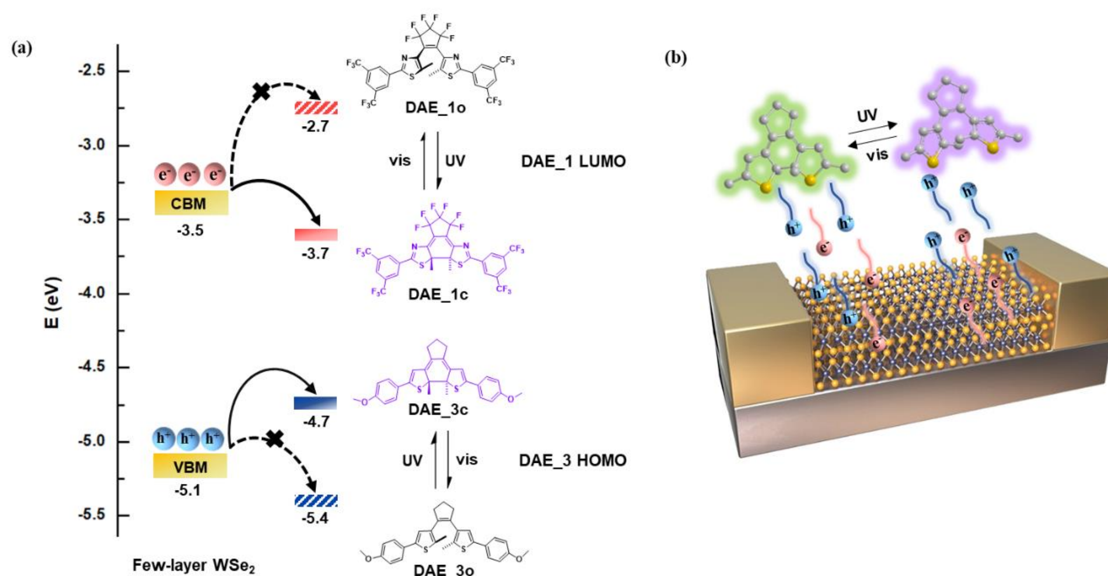

Figure 2. Energy level diagram, molecular and device structure. (a) Chemical structures of DAE_1 and DAE_3, as both open and closed isomers. Energy level diagram of electron transport between WSe_2/DAE_1 and hole transport between WSe_2/DAE_3. (b) Schematic illustration of the FET device architecture based on WSe_2/DAE on Si/SiO_2 substrate.

In the above two projects, optically switchable FETs have been demonstrated, by directly depositing DAE molecules on top of the upper channel surface. The inversed device structure could also be obtained by first depositing the molecules on a suitable substrate, followed by transfer of the 2DSs. In all the reported molecular functionalized 2D-mono-stimuli-responsive FETs only one face of the 2DS is interfaced to the molecules, thereby not exploiting a potential asymmetry determined by the two surfaces that could be rendered unequal by exposure to two different local environments. Such a scenario can be achieved by the independent functionalization of each surface with a different functional molecule,[17] providing intriguing perspectives towards the realization of multi-stimuli-responsive FETs. To address this issue, in the third project, we report an unprecedented approach based on the decoration of few-layer WSe_2 flakes with two different stimuli-responsive (macro)molecules thereby generating a Janus 2D material (Figure 3a). In particular, the bottom surface was sitting on a light-responsive DAE_1 layer and the top surface was coated with an electric-responsive copolymer poly(vinylidene fluoride-trifluoroethylene) (P(VDF-TrFE)) layer. In this way a multi-stimuli-responsive FET has been fabricated in which the output current could be reversibly and precisely modulated by means of either light irradiation or electric field. Compared with conventional mono-stimuli-responsive FETs, this novel

ternary device architecture combines enhanced functional complexity with fabrication simplicity. We provide unambiguous evidence for the compatibility of the device response to both optical and electrical stimuli, thereby offering an orthogonal handle over the device operation, which is also beneficial for memory applications. By taking advantage of the synergic effect between the two (macro)molecular switches, the device has attained an enhanced modulation of the output current, with an efficiency reaching up to 87%. Furthermore, with each stimuli manifesting a large number of different outputs without mutual interferences (9 electric-induced levels and 84 light-induced levels), the device yields a total number of 756 distinct states, outperforming the current state-to-art mono 2D stimuli-responsive transistors thereby providing a decisive step forward to address the demand for high density storage memories. The reliability of each state is further reflected by the endurance and retention tests for 5 arbitrary states, exhibiting a notable endurance for over 10 cycles and an excellent data retention exceeding 1000 hours. Moreover, compared with cumbersome synthesis of single molecules incorporating different functional groups to realize the multi-addressable elements, this Janus modified ternary structure relies on a simple fabrication process and it appears to be a more universal strategy that can be extended to other 2DSs and functional molecules, offering a versatile platform for the construction of multi-stimuli-responsive devices.

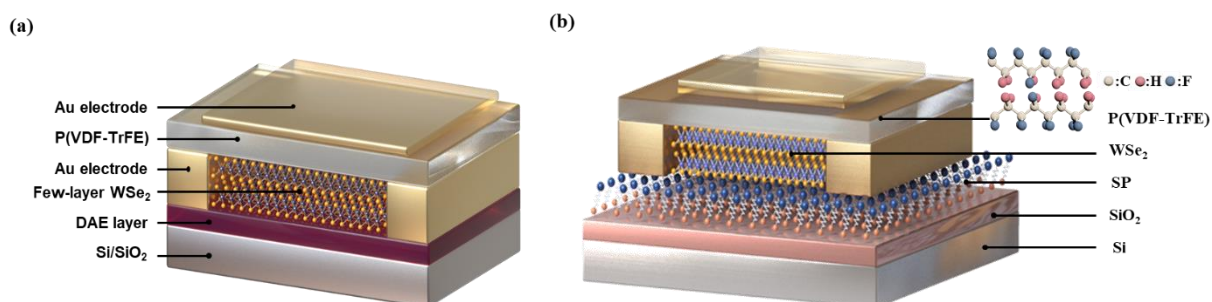

Figure 3. (a) Schematic diagram of the DAE_1/WSe_2/FeFET device with double-sided decoration: the bottom surface with DAE_1 film and the top surface with P(VDF-TrFE) layer. (b) Schematic diagram of the SP/WSe_2/FeFET device by replacing the physisorbed DAE_1 layer in (a) with chemisorbed SP layer.

In the above project, the physiosorbed DAE layer provides a promising way towards non-destructive functionalization of the channel material, however, the weak van der Waals interaction between the molecules and the Si/SiO_2 substrate results in easily removable of the molecules during a simple rinsing procedure. As a consequence, conventional photolithography process is not feasible in such device architecture, and the choice of the second stimuli-responsive element is also limited. To overcome this issue, in the fourth project, we synthesized a silane-terminated SP derivative, which can densely pack on Si/SiO_2 substrate through a strong covalent silylation. Such nonvolatile chemisorption thereof facilitates the device fabrication and provides a better compatibility when integration a third element into the system. Moreover, the photochromic reaction from SP to merocyanine (MC) can be triggered

by UV light illumination, and the reverse isomerization from MC to SP can be accomplished by vis light illumination as well as heating, adding a further thermal-responsive capacity to the corresponding FET device compared with DAE system. Following the similar Janus modified structure, silane-terminated SP photochromic molecule and ferroelectric polymer P(VDF-TrFE) have been incorporated into WSe_2-based FET devices (Figure 3b). With this combination, we obtained quaternary-stimuli-responsive FET capable of perceiving heat, light and electric field stimuli inputs and modulate output current accordingly. Such hierarchical architecture enables an independently control of the output current under distinct multiple stimuli. Taking advantage of the synergic effect between the stimuli, with a significant electron current modulation efficiency of 84% from SP, and 99% from P(VDF-TrFE), the electrons in the channel can be totally exhausted when combining the two switches and the device thereof can be modulated from n-type to p-type. Moreover, by collectively pool multiple stimuli as inputs, the overreliance in a single stimulus has been reduced, which moreover increases the sensitivity and compliance of the molecular-tailored stimuli-responsive platform.

In conclusion, we have exploited the stimuli-responsive molecular approach to fabricate multifunctional FETs whose output current can be remotely and reversibly controlled not only by its internal electric field, but also by various external stimuli including light, heat and electric field. In particular, binary-responsive FETs have been fabricated by integrating 2DSs with photochromic DAE molecules. Ternary-responsive FETs have later been realized by adding a third component, the ferroelectric P(VDF-TrFE) polymer. By taking full advantage of the bistability of the stimuli-responsive elements, the devices have been demonstrated the application as high-density nonvolatile memories. Finally, by replacing DAE with SP, quaternary-stimuli-responsive FET have been fabricated. Our molecular-tailored strategy is generally applicable to other 2DS and stimuli-responsive molecules, opening new opportunities for next-generation multi-stimuli-responsive electronics and promoting the development of “More than Moore” technologies by enriching diversification.

References

[1] a) S. H. Yu, Y. Lee, S. K. Jang, J. Kang, J. Jeon, C. Lee, J. Y. Lee, H. Kim, E. Hwang, S. Lee, *ACS Nano* **2014**, *8*, 8285; b) F. H. L. Koppens, T. Mueller, P. Avouris, A. C. Ferrari, M. S. Vitiello, M. Polini, *Nat. Nanotechnol.* **2014**, *9*, 780.

[2] a) D. Lee, E. Hwang, Y. Lee, Y. Choi, J. S. Kim, S. Lee, J. H. Cho, *Adv. Mater.* **2016**, *28*, 9196; b) D. Xiang, T. Liu, J. Xu, J. Y. Tan, Z. Hu, B. Lei, Y. Zheng, J. Wu, A. H. C. Neto, L. Liu, W. Chen, *Nat. Commun.* **2018**, *9*, 2966.

[3] a) B. Zong, Q. Li, X. Chen, C. Liu, L. Li, J. Ruan, S. Mao, *ACS Appl. Mater. Interfaces* **2020**, *12*, 50610; b) D. Sarkar, W. Liu, X. Xie, A. C. Anselmo, S. Mitragotri, K. Banerjee, *ACS Nano* **2014**, *8*, 3992.

[4] a) N. Onofrio, D. Guzman, A. Strachan, *J. Appl. Phys.* **2017**, *122*, 185102; b) V. P. Pham, G. Y. Yeom, *Adv. Mater.* **2016**, *28*, 9024.

[5] M. M. Waldrop, *Nature* **2016**, *530*, 144.

[6] a) C. Simão, M. Mas-Torrent, N. Crivillers, V. Lloveras, J. M. Artés, P. Gorostiza, J. Veciana, C. Rovira, *Nat. Chem.* **2011**, *3*, 359; b) M. E. Itkis, X. Chi, A. W. Cordes, R. C. Haddon, *Science* **2002**, *296*, 1443.

[7] a) L. Yang, K. Majumdar, H. Liu, Y. Du, H. Wu, M. Hatzistergos, P. Hung, R. Tieckelmann, W. Tsai, C. Hobbs, *Nano Lett.* **2014**, *14*, 6275; b) D. M. Sim, M. Kim, S. Yim, M.-J. Choi, J. Choi, S. Yoo, Y. S. Jung, *ACS Nano* **2015**, *9*, 12115; c) S. Bertolazzi, S. Bonacchi, G. Nan, A. Pershin, D. Beljonne, P. Samorì, *Adv. Mater.* **2017**, *29*, 1606760.

[8] a) Y. Zhao, S. Bertolazzi, M. S. Maglione, C. Rovira, M. Mas-Torrent, P. Samorì, *Adv. Mater.* **2020**, *32*, 2000740; b) S. Wang, L. Tan, P. Liang, T. Liu, J. Wang, C. Fu, J. Yu, J. Dou, H. Li, X. Meng, *J. Mater. Chem. B* **2016**, *4*, 2133; c) L. Chen, X. Zhou, W. Nie, W. Feng, Q. Zhang, W. Wang, Y. Zhang, Z. Chen, P. Huang, C. He, *ACS Appl. Mater. Interfaces* **2017**, *9*, 17786.

[9] L. Wang, Q. Li, *Chem. Soc. Rev.* **2018**, *47*, 1044.

[10] a) Y. Zhao, S. Bertolazzi, P. Samorì, *ACS Nano* **2019**, *13*, 4814; b) M. Gobbi, S. Bonacchi, J. X. Lian, A. Vercouter, S. Bertolazzi, B. Zyska, M. Timpel, R. Tatti, Y. Olivier, S. Hecht, M. V. Nardi, D. Beljonne, E. Orgiu, P. Samorì, *Nat. Commun.* **2018**, *9*, 2661.

[11] M. Irie, *Chem. Rev.* **2000**, *100*, 1685.

[12] a) C. Zhou, Y. Chai, *Adv. Electron. Mater.* **2017**, *3*, 1600400; b) X. Chen, X. Han, Q.-D. Shen, *Adv. Electron. Mater.* **2017**, *3*, 1600460.

[13] a) Y. T. Lee, D. K. Hwang, S. Im, *J. Korean Phys. Soc.* **2015**, *67*, 1499; b) X. Wang, P. Wang, J. Wang, W. Hu, X. Zhou, N. Guo, H. Huang, S. Sun, H. Shen, T. Lin, M. Tang, L. Liao, A. Jiang, J. Sun, X. Meng, X. Chen, W. Lu, J. Chu, *Adv. Mater.* **2015**, *27*, 6575; c) D. Li, X. Wang, Y. Chen, S. Zhu, F. Gong, G. Wu, C. Meng, L. Liu, L. Wang, T. Lin, S. Sun, H. Shen, X. Wang, W. Hu, J. Wang, J. Sun, X. Meng, J. Chu, *Nanotechnology* **2018**, *29*, 105202.

[14] R. C. G. Naber, K. Asadi, P. W. M. Blom, D. M. de Leeuw, B. de Boer, *Adv. Mater.* **2010**, *22*, 933.

[15] H. Qiu, Y. Zhao, Z. Liu, M. Herder, S. Hecht, P. Samorì, *Adv. Mater.* **2019**, *31*, 1903402.

[16] H. Qiu, Z. Liu, Y. Yao, M. Herder, S. Hecht, P. Samorì, *Adv. Mater.* **2020**, *32*, 1907903.

[17] M.-A. Stoeckel, M. Gobbi, T. Leydecker, Y. Wang, M. Eredia, S. Bonacchi, R. Verucchi, M. Timpel, M. V. Nardi, E. Orgiu, P. Samorì, *ACS Nano* **2019**, *13*, 11613.

Table of contents

Résumé I

Abstract VIII

Symbols and abbreviations XIV

Chapter 1 Introduction 1

Chapter 2 Theoretical background 4

2.1. Basic concept of semiconductor physics 4

2.1.1. Band theory 4

2.1.2. Types of semiconductors 5

2.2. Semiconductor applications 8

2.2.1. Diode 9

2.2.2. Transistor 11

2.3. Tuning properties of two-dimensional materials 12

2.3.1. Conventional doping techniques 13

2.3.2. Doping techniques for 2DMs 14

2.3.2.1. Alloying 14

2.3.2.2. Transition metal substitution/incorporation 15

2.3.2.3. Plasma-assisted doping 16

2.3.3. Molecular chemistry approach 17

2.3.3.1. Covalent interaction between molecules and 2DSs 17

2.3.3.2. Non-covalent interaction between molecules and 2DSs 20

2.4. References 25

Chapter 3 Materials and molecules 27

3.1. Two-dimensional materials 27

3.1.1. Graphene 28

3.1.2. Transition metal dichalcogenides (TMDs) 34

3.1.2.1. Molybdenum disulfide MoS_2 34

3.1.2.2. Tungsten diselenide WSe_2 37

3.1.3. Black phosphorous BP 38

3.2. Stimuli-responsive molecules 41

3.2.1. Photochromic molecules ... 41
3.2.1.1. Azobenzenes ... 41
3.2.1.2. Spiropyrans ... 44
3.2.1.3. Diarylethenes ... 47
3.2.1.4. Dihydroazulenes ... 52
3.2.2. Ferroelectric materials ... 53
3.3. References ... 62

Chapter 4 Experimental techniques ... 67

4.1. Device fabrication ... 67
4.1.1. Substrate preparation ... 67
4.1.1.1. Si/SiO_2 substrates ... 67
4.1.1.2. Polyethylene terephtalate substrates ... 68
4.1.2. Mechanical exfoliation ... 68
4.1.3. Laser writer photolithography ... 69
4.1.4. Metal evaporation ... 70
4.2. Molecular deposition by spin-coating ... 72
4.3. Wet transfer method ... 73
4.3.1. Polymer-assisted FET device transfer process ... 73
4.3.2. Polymer-assisted CVD 2D material transfer process ... 74
4.4. Synthesis of the DAE derivatives used in the thesis ... 75
4.5. Characterization techniques ... 77
4.5.1. Surface characterization: Atomic Force Microscopy ... 77
4.5.2. Raman and photoluminescence spectroscopy ... 79
4.5.3. UV-vis absorption spectroscopy ... 81
4.5.4. Water contact angle ... 83
4.5.5. Energy level determination ... 85
4.5.6. Electrical characterization ... 85
4.5.6.1. Field-effect transistors ... 85
4.5.6.2. Extraction of electrical parameters ... 87
4.5.6.3. Electrical setup ... 92
4.6. References ... 93

Chapter 5 Modulating the charge transport in n-type WSe_2/p-type BP via energy level phototuning ... 94

5.1. Introduction ... 94

5.2. Experimental methods ... 96
5.2.1. Match of energy levels between DAE and 2DM ... 96
5.2.2. Device preparation ... 98
5.2.3. Sample preparation for UV-vis absorption spectroscopy ... 98
5.2.4. Characterization methods ... 99
5.3. Results and discussion ... 100
5.3.1. Optical characterization ... 100
5.3.2. Characterization of 2DSs ... 102
5.3.3. Electrical characterization ... 104
5.3.3.1. Electrical characterization for WSe_2/DAE_1 ... 104
5.3.3.2. Electrical characterization for BP/DAE_2 and BP/DAE_3 ... 112
5.4. Conclusion ... 114
5.5. References ... 115

Chapter 6 Simultaneous optical tuning of hole and electron transport in ambipolar WSe_2 interfaced with a bicomponent photochromic layer ... 117

6.1. Introduction ... 117
6.2. Experimental methods ... 119
6.2.1. Match of energy level between ambipolar WSe_2 and DAEs ... 119
6.2.2. Device fabrication ... 121
6.2.2.1. WSe_2 FET on Si substrate ... 121
6.2.2.2. WSe_2 FET on PET substrate ... 122
6.2.3. Sample preparation for UV-vis absorption spectroscopy ... 122
6.2.4. Characterization methods ... 123
6.3. Results and discussion ... 123
6.3.1. Optical characterization ... 123
6.3.2. WSe_2 characterization ... 125
6.3.3. Electrical characterization ... 127
6.3.3.1. Optical switching capacity test ... 127
6.3.3.2. Multilevel test ... 134
6.3.3.3. Retention capacity test ... 137
6.3.3.4. Adaptability on flexible substrate ... 138
6.4. Conclusions ... 139
6.5. References ... 141

Chapter 7: Ternary-Responsive Field-Effect Transistors Based on Asymmetrically Functionalized Janus Few-Layer WSe_2 143

7.1. Introduction 143
7.2. Experimental methods 146
7.2.1. Match of energy level between WSe_2 and DAEs 146
7.2.2. Device fabrication 147
7.2.2.1. P(VDF-TrFE) capacitor 147
7.2.2.2. DAE/WSe_2/FeFET 147
7.2.3. Characterization methods 149
7.3. Results and discussion 150
7.3.1. Characterization of DAE molecules, WSe_2 flake and P(VDF-TrFE) film 150
7.3.2. Optical switching capacity of the DAE/WSe_2 FET 152
7.3.3. Electrical characterization of P(VDF-TrFE) capacitor 152
7.3.4. Electrical characterization of DAE/WSe_2/FeFET 153
7.3.4.1. In top gate configuration 153
7.3.4.2. The electrical and optical switching capacity of DAE/WSe_2/FeFET 154
7.3.4.3. Multilevel test 159
7.3.4.4. Retention and endurance test 165
7.4 Conclusion 166
7.5 References 166

Chapter 8: Quaternary-Responsive Field-Effect Transistors Based on Asymmetrically Functionalized Janus Few-Layer WSe_2 169

8.1. Introduction 169
8.2. Experimental method 171
8.2.1. SP film functionalization 171
8.2.2. Fabrication of SP/WSe_2/FeFET 172
8.2.3. Characterization methods 173
8.3. Results and discussion 174
8.3.1. Characterization of SP film 174
8.3.1.1. UV-vis absorption spectra 175
8.3.1.2. Water contact angle 176
8.3.1.3. AFM 177
8.3.1.4. PL mapping 178
8.3.2. Electrical characterization 181

8.3.2.1. SP/WSe_2 FET ... 181
8.3.2.2. SP/WSe_2/FeFET ... 181
a. SP/WSe_2/FeFET in top-gate configuration ... 181
b. Optical/thermal/electrical switching capacity of SP/WSe_2/FeFET in back-gate configuration ... 182
8.4. Conclusion ... 190
8.5. References ... 191

Chapter 9: Conclusion and perspectives ... 193

Statement of work ... 198

List of publications ... 199

List of communications ... 200

Acknowledgements ... 201

Symbols and abbreviations

0D	Zero-dimensional
0DM	Zero-dimensional material
1D	One-dimensional
1DM	One-dimensional material
2D	Two-dimensional
2DM	Two-dimensional material
2DS	Two-demensional semiconductor
3D	Three-dimensional
AFM	Atomic force microscopy
BP	Black phosphorous
CB	Conduction band
CBM	Conduction band minimum
CVD	Chemical vapor deposition
CL-PVP	Cross-linked poly(4-vinylphenol)
DAE	Diarylethene
DAE_c	DAE in the closed form
DAE_o	DAE in the open form
DHA	Dihydroazulene
e^-	Electron
E	Electric field
E_c	Coercive field
ε_0	Vacuum permittivity
εr	Relative permittivity
eV	Electronvolt
FeFET	Ferroelectric field-effect transistor
FET	Field-effect transistor

h^+	Hole
High-temperature	HT
HOMO	Highest occupied molecular orbital
I_{ds}	Drain-source current
I_{off}	Lowest I_{ds} value
I_{on}	Highest I_{ds} value
I_{on}/I_{off}	I_{on}-to-I_{off} ratio
IPA	Isopropanol
ITO	Indium tin oxide
LUMO	Lowest unoccupied molecular orbital
MC	Merocyanine
PET	Polyethylene terephthalate
PMMA	Poly(methylmethacrylate)
P	Polerization
P_r	Remnant polarization
P_{sat}	Saturation polarization
PSS	Photostationary state
P(VDF-TrFE)	Poly(vinylidene fluoride-trifluoroethylene)
$R_{channel}$	Channel resistance
$R_{contact}$	Contact resistance
R_{total}	Total resistance
SP	Spiropyran
T_C	Curie temperature
T_M	Melting temperature
TGTG'	Trans-gauche-trans-gauche
TMD	Transition metal dichalcogenide
TLM	Transmission line method
TrFE	Trifluoroethylene

VB	Valence band
VBM	Valance band maximum
VDF	Vinylidene fluoride
V_{ds}	Drain-source voltage
VHF	Vinylheptafulvene
V_g	Gate voltage
V_{th}	Threshold voltage
W	Channel width
W/L	Width-to-length ratio
μ	Field effect mobility
μ_{e-}	Electron field effect mobility
$\mu_{\hbar+}$	Hole field effect mobility

Chapter 1 Introduction

Moore's law, stating that the number of transistors per silicon chip doubles every two years, predicted by Gordon Moore in 1965, has been the golden rule for electronic industry over 50 years. The main driver of Moore's law has been the miniaturization of integrated circuit. However, such projection cannot be sustained indefinitely, and transistors would eventually reach the limits of miniaturization at atomic levels.[1] In view of this, the International Technology Roadmap for Semiconductors defined three distinct paths to keep the semiconductor industry continually growing: More Moore, focusing on the continued scale down of CMOS technology; More than Moore, calling for a disruptive change in the architecture and integration strategies; and Beyond Moore, exploiting innovative technologies as complimentary to CMOS and to overcome its limit.[2]

Silicon has historically been used in most electronic devices because of its wide availability and ideal semiconductor properties. However, achieving its physical dimensions near the deeper nanoscale regime of 10 nm or beyond is challenging for existing technologies. At the nanoscale, the silicon circuits tend to possess high leakage current with increased static power consumption that generating more heat in a unit area. As silicon is reaching its limit, it is necessary to find a replacement in electronic circuits. Graphene and other two-dimensional semiconductors (2DSs) have emerged as plausible candidates, due to their breakthrough in scaling limits and preserved device performance.[3] These 2DSs combine several unique physico–chemical properties including atomic thickness, sizable bandgap, and high charge carrier mobility, opening up a variety of opportunities for the construction of high-performance devices with ultrathin body.

Albeit being outstanding, the tuning of the properties of these 2DSs in a controllable manner has been a challenge, which is of paramount importance in terms of production of practical complementary-logic devices and circuits. The combination of 2DSs with molecular system represents a promising approach to not only control the charge carrier doping, but also confer new properties to the former components.

Thus, the aim of this thesis work is to contribute to the reversible control over the charge carrier

transport via integrating of molecular system into the 2DS-based electronic devices. In particular, stimuli-responsive molecules including photochromic molecules diarylethene (DAE), spiropyrans (SPs) and ferroelectric poly(vinylidene fluoride–trifluoroethylene) (P(VDF-TrFE)) have been employed to confer their intrinsic capacities to the interfacial 2DS and fabricate multifunctional devices. Such molecular tailored strategy promotes the development of “More than Moore” technologies in terms of enriching diversification in electronic systems.

The thesis is divided into 8 chapters in the following order:

Chapter 1 places the work carried out in thesis in scientific context.

Chapter 2 provides a brief theoretical background of this work, including principles of semiconductor physics and charge transport mechanism in electronic devices, doping engineering of 2DSs, in particular focus on the molecular chemistry approaches that have been developed so far to control the charge-carrier doping along with other properties.

Chapter 3 introduces the materials employed in the work, 2DSs and stimuli-responsive materials, including their properties and characteristics.

Chapter 4 presents the experimental techniques used to characterize materials and electronic devices, as well as the device fabrication procedures.

Chapter 5 focuses on the fabrication of 2DS-based light-responsive field-effect transistors (FETs) via energy-level phototuning. In particular, the physisorbed photochromic DAEs with well-defined energy levels act as optical switching elements, thereby allowing for the fine-tuning and remote control over the charge transport of the host 2DM, either in terms of electrons in n-type dominated few-layer WSe_2 or holes in p-type dominated few-layer BP.

Chapter 6 is centered on the fabrication of ambipolar WSe_2-based optically switchable FET by interfacing the channel flake with a blend of two photochromic DAE molecules acting as light-sensitive components. The device capacity to work as memory is evaluated by the basic parameters like data

storage, retention time, and capability to work on flexible substrates.

Chapter 7 presents the operation of a ternary-responsive WSe_2 FET device by harnessing reversible isomerization of photochromic DAE molecules and the polarization of P(VDF-TrFE) polymer. Its potential application as high-density nonvolatile memory is demonstrated by data storage, retention and endurance test.

Chapter 8 is dedicated to the development of a quaternary-responsive WSe_2 FET by integrating a silane-terminated SP molecule and P(VDF-TrFE), whose output current can be modulated by light, temperature as well as external electric field.

Chapter 9 summarizes the presented work and discusses some outlooks for future developments.

References

[1] T. N. Theis, H.-S. P. Wong, *Comput. Sci. Eng.* **2017**, *19*, 41.

[2] M. M. Waldrop, *Nature* **2016**, *530*, 144.

[3] S. B. Desai, S. R. Madhvapathy, A. B. Sachid, J. P. Llinas, Q. Wang, G. H. Ahn, G. Pitner, M. J. Kim, J. Bokor, C. Hu, *Science* **2016**, *354*, 99.

Chapter 2 Theoretical background

2.1. Basic concept of semiconductor physics

2.1.1. Band theory

In solid-state physics, the band theory is a useful way to distinct between the conductors, insulators and semiconductors (Figure 2-1).[1] Electrons in an atom are present in different energy levels. The valence band (VB) involves energy levels that consist of valence electrons present in the outermost shell of an atomic structure, and the conduction band (CB) involves energy levels that consist of free electrons that are responsible for conduction. Since the CB possesses higher energy level, they are generally empty. The CB in semiconductors can accept the electrons from the VB on receiving sufficient external energy, and the conducting electrons in the CB results in the flow of current.

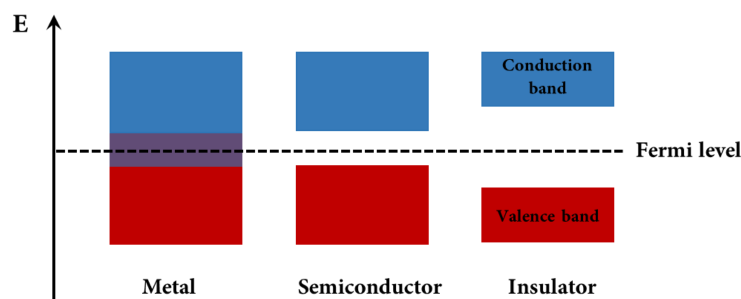

Figure 2-1. Band theory representation of different materials.

The energy difference between the highest occupied state of the VB and the lowest unoccupied state of the CB is known as the band gap, an indicator of the electrical conductivity. The greater the band gap, the higher is the energy needed to excite valence electrons to the CB. The insulators are characterized by a large band gap, so a prohibitively large energy is required to promote electrons into the CB. Conductors exhibit an overlap between the CB and VB, hence electrons can jump freely between the two bands, meaning the material is profoundly conductive. Semiconductors are characterized by a small band gap allowing a meaningful fraction of the valence electrons to get promoted into the CB when a certain amount of energy is provided to the system. Their conductivities are therefore in-between those of conductors and insulators, which is the main reason for their application in electrical circuits.

2.1.2. Types of semiconductors

Semiconductors can be classified as intrinsic semiconductors and extrinsic semiconductors. An intrinsic semiconductor is chemically pure and is made up of only a single type of atoms, such as silicon (Si), germanium (Ge), tin (Sn) in column IV, and selenium (Se), tellurium (Te) in column VI of the periodic table. There are also numerous compound semiconductors, which are composed of two or more elements, such as gallium arsenide (GaAs), a combination of gallium (Ga) in column III and arsenic (As) in column V.[2] At sufficiently high temperatures, some of the valence electrons in the semiconductor can break their bonds in the lattice structure and become available as conduction electrons, resulting in the current flow in the semiconductor.

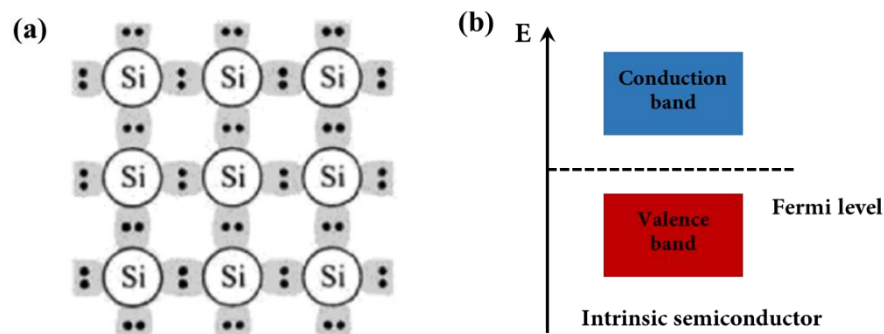

Figure 2-2. (a) Bond structure, reproduced from Ref.[3] and (b) its energy-band diagram of intrinsic semiconductor.

Fermi level is an important concept used to describe the thermodynamical equilibrium of charges in the semiconductor. It is defined as the energy level where the probability of occupation by an electron is 0.5. In the intrinsic semiconductor, the number of electrons in the CB is equal to the number of holes in VB. The probability of occupation of energy levels in CB and VB is therefore equal. Hence, the Fermi level lies in the middle of forbidden band (Figure 2-2).

Apart from heating, the conductivity of semiconductors can be greatly improved by introducing different types of atoms called impurities. These impurities modify the electrical properties of the semiconductor, making it more suitable for electronic applications. Impurities that are added to control charge carrier concentrations are called dopants. The process of adding impurity atoms is called doping, and the doped semiconductor is called extrinsic semiconductor. The extrinsic semiconductor can further

be classified into n-type semiconductor and p-type semiconductor, as shown in Figure 2-3 and 2-4.[3]

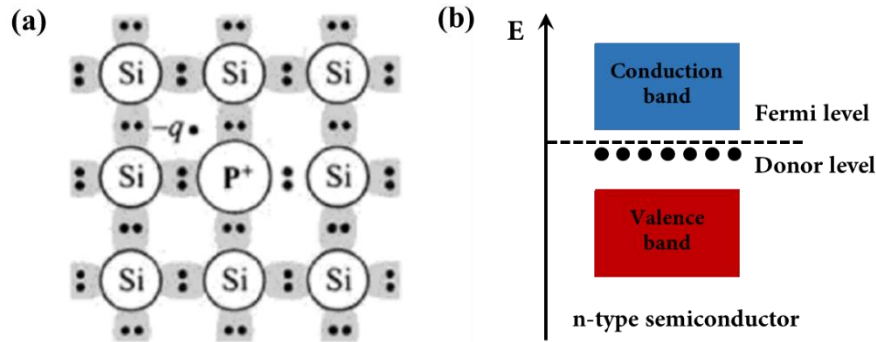

Figure 2-3. (a) Bond structure, reproduced from Ref.[3] and (b) its energy-band diagram of n-type semiconductor.

The intrinsic semiconductor silicon is pure and contains negligible impurities, with each silicon atom sharing its four valence electrons with the four neighboring atoms. When a silicon atom is replaced by a dopant that has the same electronic structure, the bonding behavior is substantially unchanged, resulting in only minor changes in bonding. While when the dopant has more or fewer electrons than the atom it replaces, it creates an extra electron or hole. This extra electron or hole can escape from the dopant and move freely in the semiconductor, causing a change in the conductivity. For example, when a silicon atom is replaced by a substitutional phosphorous (P) atom which has five valence electrons, four electrons out of five of phosphorous bond with the four electrons of silicon, leaving the fifth negative-charged electron free and donated to the CB. The phosphorous atom is thereof called donor. The energy level of the donor lies slightly lower than that of the CB. Hence, electrons can move into the CB with minimal energy. Since the number of free electrons is increased by the additional dopants, they exceed the number of holes and become the majority carriers, eventually leading to a n-type semiconductor.

In the energy band structure, the probability of occupation of energy levels by the electrons in the CB is greater than the probability of occupation of energy levels by the holes in the VB. The Fermi level is therefore shifted up near the CB.

Conversely, when a boron atom which has three valence electrons replaces a silicon atom, its three valence electrons bond with three electrons of the semiconductor, leaving a hole between the fourth

atom of the silicon atom and the boron atom. The hole accepts an electron from the neighborhood, creating a conductive hole. The boron atom is thereof referred to as an acceptor. The energy level of the acceptor is just above the VB. Electrons from the VB can thus move to the acceptor level with minimal energy. This process provides excess holes to the intrinsic semiconductor, making them the majority carriers, creating a p-type semiconductor.

In the p-type semiconductor, the probability of occupation of energy levels by the holes in the VB is greater than the probability of occupation of energy levels by the electrons in the CB. The Fermi level is therefore shifted down near the VB.

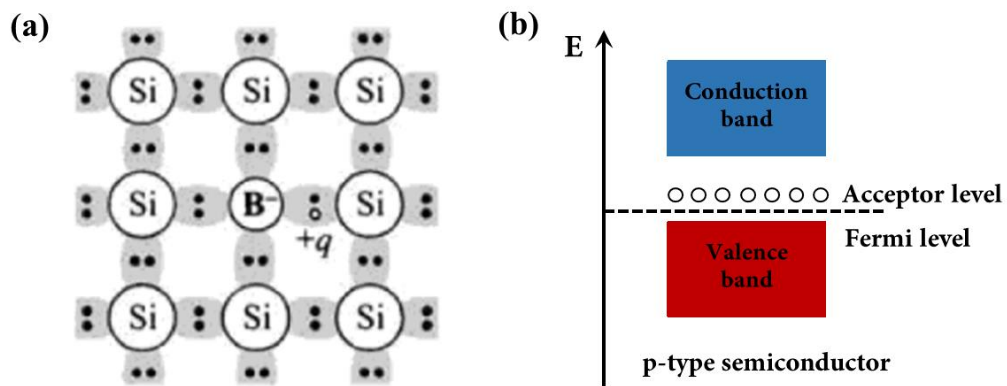

Figure 2-4. (a) Bond structure, reproduced from Ref.[3] and (b) its energy-band diagram of p-type semiconductor.

2.2. Semiconductor applications

Application of semiconductors are ubiquitous in our daily life, including mobile devices, data centers, industrial equipment, and the Internet of Things. Without semiconductors, our life would be much different – they are as critical to modern life as air or water.

The semiconductor industry started from 1947, when the first point-contact transistor based on germanium (Ge) was invented by Bardeen, Brattain, and Shockley at Bell Laboratories in the US. They were later awarded the Nobel Prize in Physics in 1956 for their contributions to the semiconductor research. Since then, the semiconductor industry grew rapidly.

Until the early 1950s, germanium was the main material used in semiconductor industry and was considered the most effective semiconductor material due to its high mobility. However, it turns out that such material was found not suitable for many applications, mainly due to two reasons: one is devices made of germanium have worse leakage currents in the OFF state, the other is they are restricted to 0 to 70 °C operation, which limits their use in rugged applications.[4] Since the middle 1960s, silicon has replaced germanium and has become the dominant semiconductor material for the device manufacturing since it is more abundant and less expensive. Moreover, devices made of silicon are found to have much lower leakage current compared with those made of germanium due to the larger bandgap of silicon, and they are able to operate at a larger temperature range, from -55 to 125°C. In addition, silicon dioxide (SiO_2), a high-quality insulator, can be easily employed in the Si-based devices.[5] Therefore, silicon technology has become widespread since then and silicon devices has accounted for more than 95% of all semiconductor products nowadays.[6]

Owing to their reliability, compactness, power efficiency and low cost, semiconductors have been employed in the manufacture of various electronic devices, including diodes, transistors and integrated circuits.[7] These devices are manufactured for both discrete devices and integrated circuits, which consist of from a few to billions of devices manufactured on a single semiconductor substrate.

2.2.1. Diode

It is one of the simplest semiconductor devices, which is typically made up of a single p-n junction.[8] It consists of a single piece of silicon, half of which is doped with impurities of n-type, and the other half doped with impurities of p-type. Both regions are coated with metal contacts so that wires can be attached. To obtain a maximum current in the low resistance, a positive voltage must be applied to the anode with respect to the cathode. The main advantage of the device is to allow the electric current to pass in one direction and prevent it in other direction, the diode is therefore a unidirectional device. Diodes have many applications in electric and digital circuits, such as half-wave rectifier, full-wave rectifier, photodiode, and light-emitting diode (LED). [9]

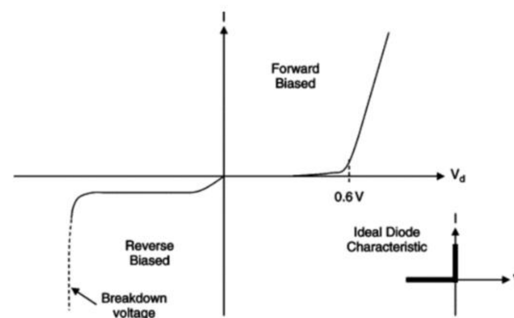

Figure 2-5. Semiconductor diode characteristic. Reproduced from Ref.[10]

The device performance of a diode is usually characterized by a current-voltage curve (Figure 2-5). Even without application of an external bias, the electrons in the n-type region can move freely to the p-type region and recombine with the holes due to the concentration differences, creating uncovered negative ions in the p-type region. In the same way, the holes diffuse into the n-type region and create uncovered positive ions. Such uncovered immobile ions form a layer that is set up across the junction line, forming a region in the middle of the diode. The region is called depletion region since all the charge carriers get combined here. The electric field across the region, which is known as the junction potential, will further prevent the migration of charge carriers from one side to the other (Figure 2-6).

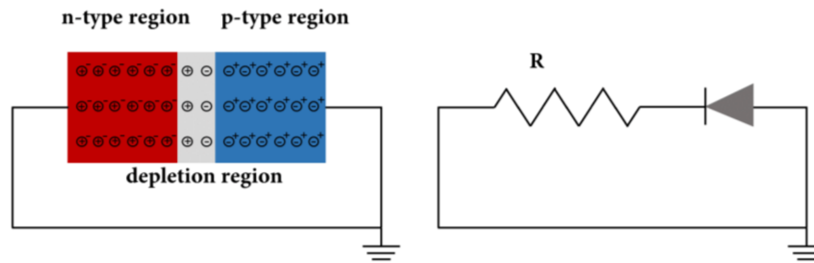

Figure 2-6. Zero biased PN junction diode.

In a forward bias condition, a positive bias is applied on the p-type region and a negative bias is applied on the n-type region. When the applied voltage is larger than the junction potential, the charge carriers start cross the barrier, which means the electrons flow through the junction to the p-type region and the holes flow to the n-type region. The sum of their current flow contributes to the total forward current (Figure 2-7).

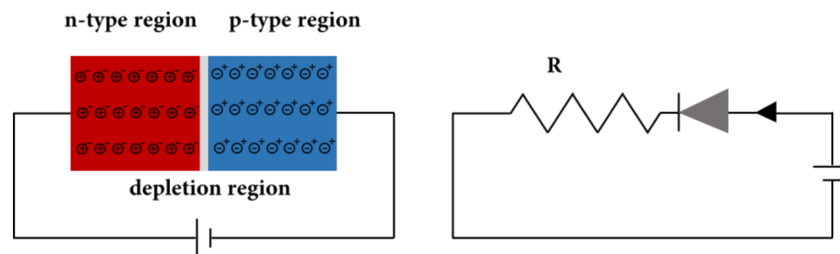

Figure 2-7. PN junction diode with forward bias.

Conversely, in the reversed bias condition, a negative bias is applied on the p-type region and a positive bias is applied on the n-type region. In such condition, the holes in the p-type region would be repelled away from the junction region, leaving more uncovered negative ions at the junction. Similarly, the electrons would also be repelled and leave uncovered positive ions. Therefore, the depletion region becomes wider, no majority carriers cross the junction. In this way, flow of current is blocked (Figure 2-8).

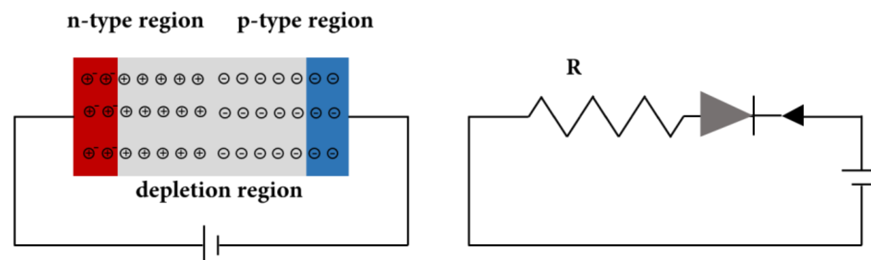

Figure 2-8. PN junction diode with reversed bias.

2.2.2. Transistor

It is a three-terminal device based on doped semiconducting material which is used in most electronic circuits. It can perform two basic functions: amplification and switching. Amplification consists of magnifying an input signal into a greater output signal, whereas switching means to control the input current through a pair of terminals while applying a voltage or current at another pair of terminals. [11]

There are a variety of transistors available in the market, including bipolar junction transistors (BJTs) and field-effect transistors (FETs). A BJT is a type of transistor that contains both electrons and holes as charge carriers and join three sections of semiconductor material with different doping concentrations. It is built up of three terminals, named as the emitter, the collector and the base. A small current injected at the base terminal will pass to the emitter and be modified or switched into a much larger current flowing between the collector and emitter terminals.[12] While different from the BJTs, the FETs controls the output current by the input voltage.

As the diagram given below, the BJTs come into two types: the NPN type and the PNP type, based on the doping types of the three main terminal regions. In an NPN transistor, a lightly p-type doped base is sandwiched between a heavily n-type doped emitter and another n-type doped collector, where the electrons are the dominant charge carriers. The emitter possesses a high concentration of electrons, so it emits electrons into the base, these electrons are then collected by the collector and sent to the following part of a circuit. Whereas for a PNP transistor, a lightly n-type doped base is sandwiched between a heavily p-type doped emitter and another p-type doped collector. It shares the analog behavior with the NPN transistor but with holes as the dominant charge carriers.

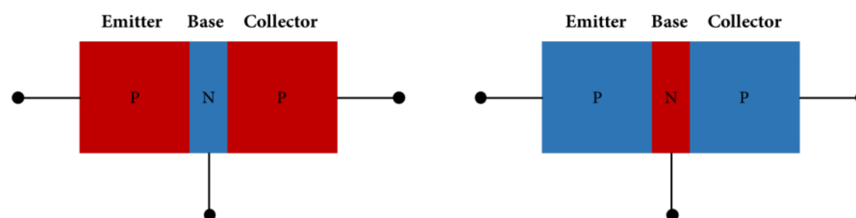

Figure 2-9. Layout of BJT transistors. Left: PNP type; Right: NPN type.

The introduction of FET devices will be further discussed in Chapter 4.4.5.

2.3. Tuning properties of two-dimensional materials

Over the past decades, the evolution of silicon technology is based on Moore's law which predicts that the number of transistors in integrated circuits would double every two years. This is achieved by steadily shrinking the size of transistors. However, this reduction in size is reaching a nanometer-scale limit in which parasitic effects such as the quantum tunnel effect have to be taken into account. To solve this problem, several solutions such as searching for a replacement material with comparable or even much higher performances than silicon have been considered.

The emergence of graphene in 2004 and later related two-dimensional semiconductors (2DSs) offer prospects of unprecedented advances in device performance at the atomic limit. Their amazing potential has proven to overcome the limitations of silicon technology, where the combination of 2DSs with silicon chips promises to surpass the current technological limitations. They have been appealing components for numerous applications including flexible/wearable electronics, sensing technologies and energy storage/conversion.

Although 2DSs have been widely used in various fields due to their extraordinary physical properties, we are still facing numerous challenges in broadening their applications. In the first market products based on 2DSs, there are two major technological challenges that required to be tackled, one is the synthesis of large-area and high-quality films of monolayer materials with low densities of defects and impurities,[13] and the other is the development of strategies to control the charge-carrier type and the doping level in 2DMs.[14] Whereas a lot of efforts has been devoted on the former,[15] relatively less work has been focused on the latter, which is nevertheless a critical hurdle for the realization of 2DSs in electronic applications. In this section, we will introduce some classic doping techniques that have been developed.

2.3.1. Conventional doping techniques

Doping refers to the process of adding impurities to a semiconductor to modify its intrinsic optical or electrical properties. The most common doping methods include thermal diffusion and ion implantation.[16]

Thermal diffusion occurs when impurity atoms or molecules migrate from an area of high concentration to an area of low concentration. Diffusion usually occurs in two steps: predeposition and drive-in. During the predeposition process, the impurity dopants, mainly in three forms, gases, liquids and solids, are introduced to the wafer substrates in a furnace at the temperature around 1000-1250 ℃. The wafers are then put into a second furnace at a higher temperature about 1300 ℃ to drive-in the dopant. The introduced dopants in this process diffuse deeper into the wafer to create the required concentration gradient. Note that the drive-in process usually occurs in an oxidizing atmosphere so that a protective layer of SiO_2 is grown over the diffused layer. The Figure 2-10 below shows the setup for the thermal diffusion.

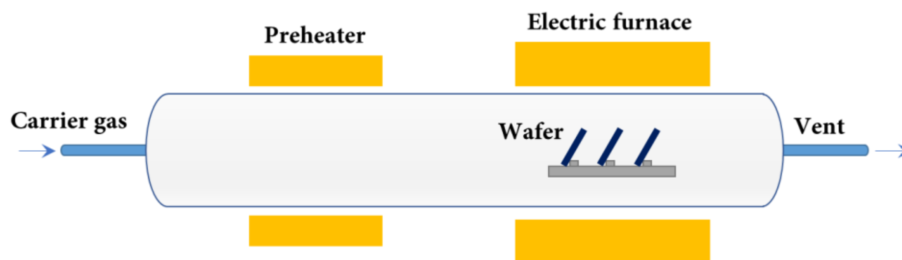

Figure 2-10. Thermal diffusion setup.

The ion implantation technique is often used to alter the physical and chemical properties of a semiconductor. During the ion implantation process, the dopants are first ionized, then these ions are accelerated by an electric field, and finally deposited in the target wafer. These dopants can penetrate into the wafer and get embedded at various depths, depending on their mass and energy. The whole process takes place at room temperature with negligible lateral diffusion. It allows precise control of dose, which is defined as the number of penetrated dopants, and the depth of the implantation. However, since the surface of the target wafer is impacted by high energy ions, it might be damaged by knocking its intrinsic atoms from their position. A high-temperature annealing treatment (800-1000 ℃) is

therefore usually performed to repair the damage and also to further incorporate the dopant atoms into the original lattice.

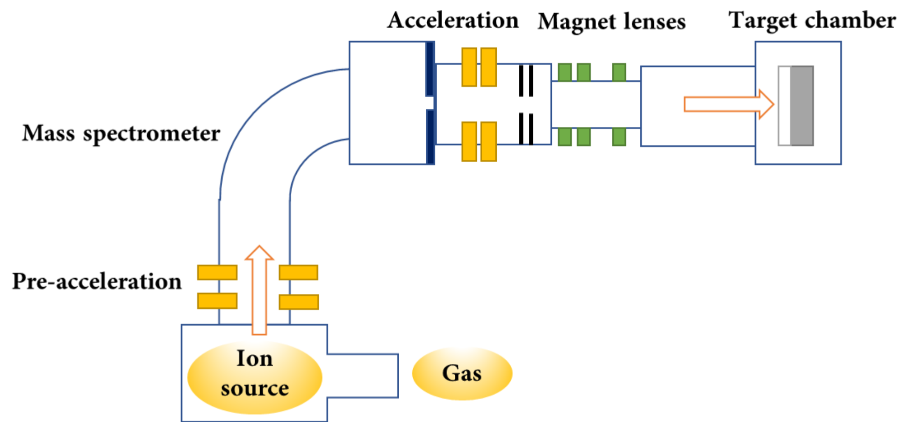

Figure 2-11. Ion implantation setup.

When comparing these two techniques, thermal diffusion usually takes place at a higher temperature, it is an isotropic process and involves lateral diffusion. Conversely, ion implantation is a fundamental process used to make microchips which requires lower temperature. It is an anisotropic process and can form very shallow junctions. However, they are both challenging to be implemented in combination with 2DMs, since damages or defects may be induced during such processes, which can cause detrimental effects on their structural and electrical characteristics, resulting in degraded device performances.

2.3.2. Doping techniques for 2DMs

2.3.2.1. Alloying

Alloying of semiconductors tunes their intrinsic optical and electrical properties by altering the energy band structure. 2D alloy is single atomic layer of alloy that is incommensurate with underlying substrate.[17] The monolayer alloys can be fabricated by mechanically exfoliation from bulk alloys, physical vapor deposition from the powders of the end materials at a low temperature, chemical vapor deposition from sulfurization and selenization of transition metal oxides, and chalcogen exchange by hetero-chalogen atoms.[18] Figure 2-12 illustrates the synthesis of large-area 2D semiconductor alloys

comprising $MoS_{2(1-x)}Se_{2x}$ monolayer by direct vaporization of $MoSe_2$ and MoS_2 powders. As from the electrical characterization, a much higher mobility was obtained for the $MoS_{2(1-x)}Se_{2x}$ monolayer FET where x = 0.30, in comparison to that of the pure MoS_2 monolayer FET where x = 0.

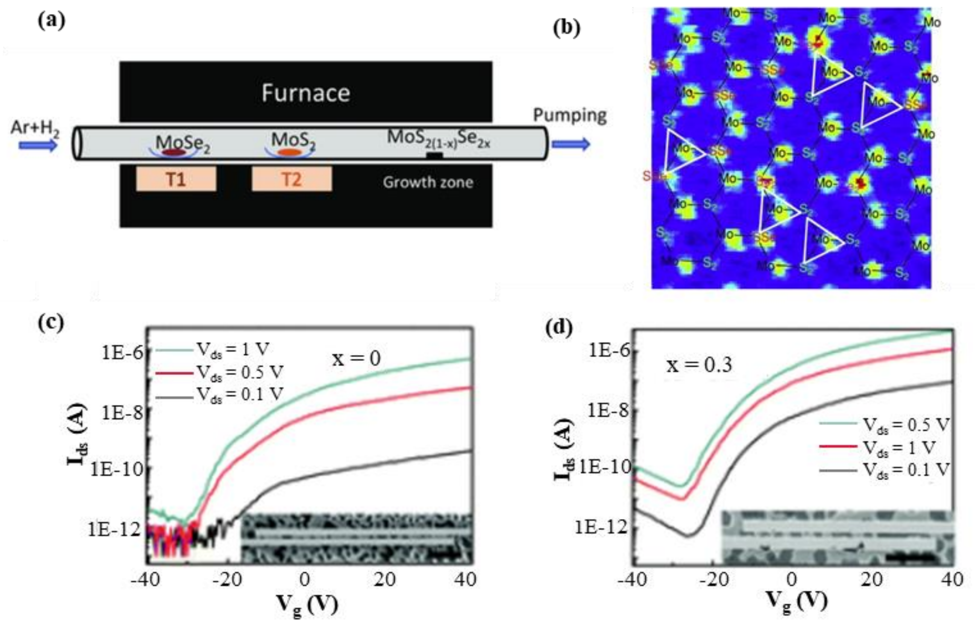

Figure 2-12. (a) Illustration of three-zone furnace for the growth of the $MoS_{2(1-x)}Se_{2x}$ monolayer. (b) HAADF-STEM image of $MoS_{1.6}Se_{0.4}$ monolayer in false color. Mo sites: yellow; S_2 sites: light blue; SSe sites: yellow, and Se_2 sites: red. (c) and (d) Transfer curves of $MoS_{2(1-x)}Se_{2x}$ monolayer. (c) for x = 0; (d) for x = 0.30. Reproduced form Ref.[19]

2.3.2.2. Transition metal substitution/incorporation

Atomic doping is a technique that can alter the structure and properties of the target material depending on the dopant atoms.[20] The intrinsic atoms in the lattice can be directly substituted if the dopant atoms are well matched in terms of size, valence, and coordination. For layered materials, dopant atoms may also intercalate between layers. Figure 2-13 shows the STEM image of the doped MoS_2 monolayers with rhenium (Re) impurities during the chemical vapor deposited growing process. By comparing the output characteristics of MoS_2 and Re-MoS_2 based FET devices, the Re doping is found to significantly improve the contacts between the metal and MoS_2, enabling ohmic behavior to be maintained over a wide range of temperatures.

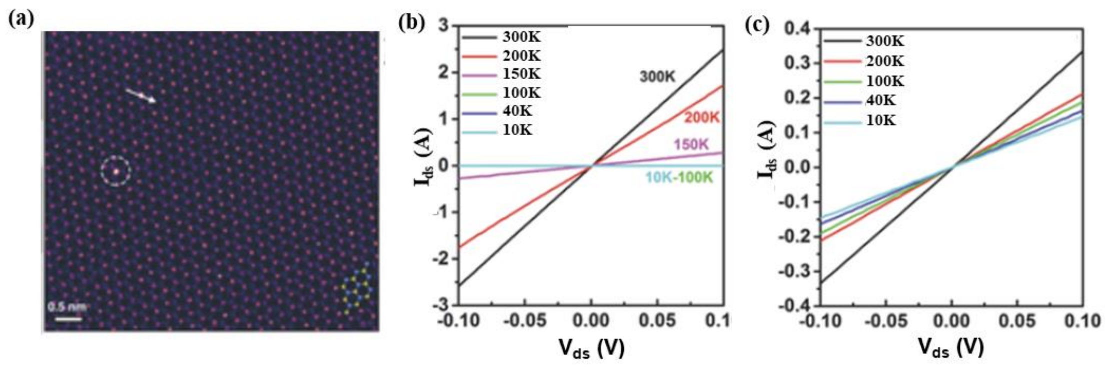

Figure 2-13. (a) Aberration-corrected Z-contrast STEM image from monolayer Re-doped MoS_2. The brown, white, and dim purple dots represent Mo, Re, and S atoms respectively. (b) and (c) Output curves of (b) pure MoS_2, (c) Re-MoS_2 for several temperatures. Reproduced from Ref.[20]

2.3.2.3. Plasma-assisted doping

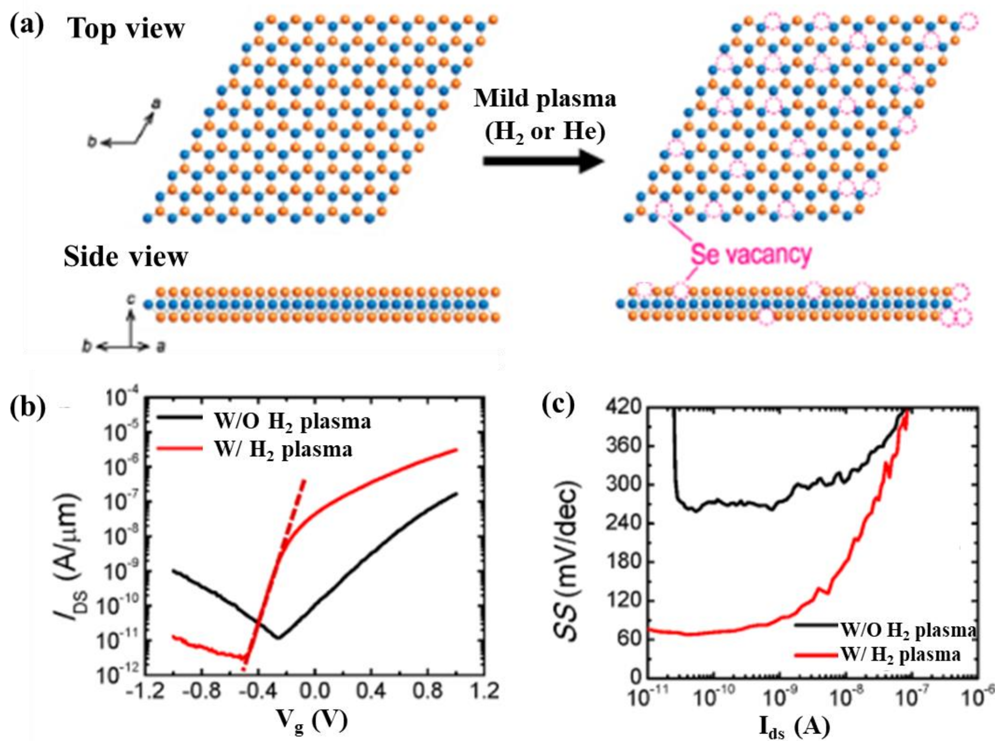

Figure 2-14. (a) Schematic of an WSe_2 flake as exfoliated (left) and after the H_2 plasma treatment. (b) Transfer characteristics of the control (no plasma treatment) and H_2-plasma-treated WSe_2 FETs. (c) Subthreshold swing of the control and H_2-plasma-treated WSe_2 FETs. Reproduced from Ref.[21]

The plasma-assisted doping method is a mature technique which uses various gas molecules including N_2, O_2 and H_2 to generate ions with high energy. With these ions bombarded on the surface of 2DM,

vacancies are prone to created.[22] Figure 2-14 shows the investigation of mild H_2 plasma treatment on the defect engineering in the WSe_2 lattice.[21] The n-type WSe_2 field-effect transistors (FETs) with plasma-treated contact regions that exhibit contact resistance significantly lower than that of devices made without plasma treatment of the contacts. Moreover, such improved contacts result in nearly ideal subthreshold swing value at room temperature, with the value of 66 mV/dec.

2.3.3. Molecular chemistry approach

As the conventional doping techniques introduced above like ion implantation and diffusion may unavoidably damage the 2D crystals and result in degraded device performances. In recent years, the use of molecular systems interfacing 2DSs has emerged as a promising versatile, not only for controlling the charge carrier doping, but also imparting them novel functionalities. 2DSs are extremely sensitive to surrounding variables due to their large surface to volume ratio. Their intrinsic properties can thereof be modified by any surface modification. Taking advantage of this character, the molecules on the surface of the 2DSs can modulate their charge-carrier density via electrical dipoles or charge-transfer process through both covalent and non-covalent interactions. Especially, molecules with functional groups possessing optical and electrical properties can activate specific interactions with 2DSs. Since an unlimited variety of molecules can be synthesized with programmed properties, such hybrid structure based on 2DS/molecule system holds great potential as the device architecture for on-demand applications.

2.3.3.1. Covalent interaction between molecules and 2DSs

Covalent functionalization of 2DSs with molecules mainly including two strategies, defect engineering and phase conversion.

The crystals of 2DSs are enriched by a variety of intrinsic defects, such as vacancies, adatoms, grain boundaries, and substitutional impurities (Figure 2-15a), which strongly influence on their optical and electronic properties, rendering it crucial to develop novel strategies of defect engineering for the realization of high-performance devices.[23] In defect engineering approach, the chemical reactivity of

the 2DS's surface is first activated by the generated defects, enabling the chemical bonds be formed between the defective sites and ad hoc molecules by S vacancy self-healing or low-temperature thiol chemistry treatment. To date, various techniques such as electron irradiation, thermal annealing, plasma treatment and physical bombardments with charged particles, have been employed to engineer chalcogen vacancies in MoS_2 nanosheets, or selenium vacancies in WSe_2, Molecules carrying thiol group like (3-mercaptopropyl)trimethoxysilane are often used to functionalize the defective MoS_2 nanosheets, which results in a significant recovery of the electrical characteristics of the related FET devices.[24] Molecules carrying selenol group are expected to repair the defective WSe_2. In Figure 2-15c, the effect of the S vacancy self-healing on the electrical properties of a MoS_2 transistor was investigated. A decrease of current can be observed in the output characteristic and the threshold voltage dramatically shifted toward zero after the S vacancy self-healing, indicating that the electrons or sulfur vacancies in the as-grown MoS_2 was removed and the healing reduced the interface trap states.[25]

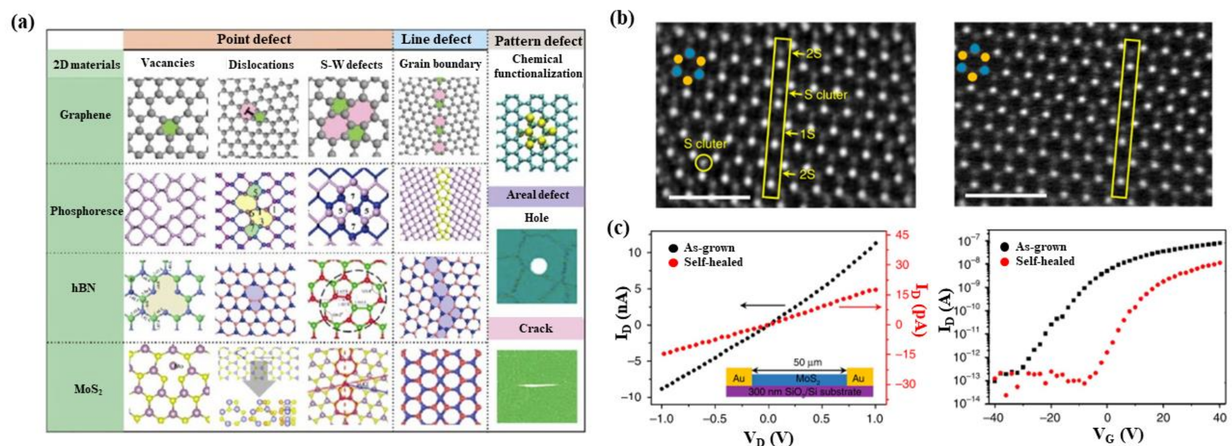

Figure 2-15. (a) Two-dimensional materials with diverse types of defects. Reproduced from Ref.[23] (b) The HAADF images of MoS_2 surface before (left) and after (right) poly(4-styrenesulfonate)-induced S vacancy self-healing. (c) Output and transfer characteristics of a monolayer MoS_2 FET before (left) and after (right) poly(4-styrenesulfonate)-induced S vacancy self-healing. Reproduced from Ref.[25]

When it comes to phase conversion approach, it relies on the reversible switch of the 2DS between the functionable metallic polytype 1T/1T' phase and the inert semiconducting polytype 1H/2H phase via chemical and thermal stimuli, like alkali metal intercalation, strain, electron beam and laser beam irradiation. For example, the exposure of substrate-supported CVD MoS_2 nanosheets to n-butyllithium can result in the phase change from 1H to 1T/1T'. The 1T/1T' phase can then be easily functionalized

by methyl iodide and iodoacetamide electrophiles via covalently bonding between the functional groups and sulfur atoms. The functionalized MoS_2 nanosheets feature a different optical property compared with the pristine material without functionalization. Therefore, by choosing ad hoc electrophile molecules, the optical and electrical properties of the target 2DSs are expected to be modified for specific applications. Moreover, mixing the two phases in a monolayer 2DS could also be interesting, which may principally modulate its property. Figure 2-16b illustrates the Ar-plasma treatment used to activate the 2H to 1T phase transition for MoS_2.[26] The kinetic energy of Ar ions was tuned well to wrench the S-Mo bond to induce the lateral sliding of top S-layer. By performing a selective-area phase transition in 2H MoS_2, we can clearly see the PL quenching in the 1T phase. Figure 2-12d shows the typical transfer characteristics of the three types devices. Large gate modulation of the 2H-channel can be seen in type I, whereas the 1T channel has much weaker gate dependence, which is expectable since the pure 1T-phase is metallic. With 1T phase on the electrode areas, the contact resistance could substantially decrease, and devices' electrical performances in turn improved.

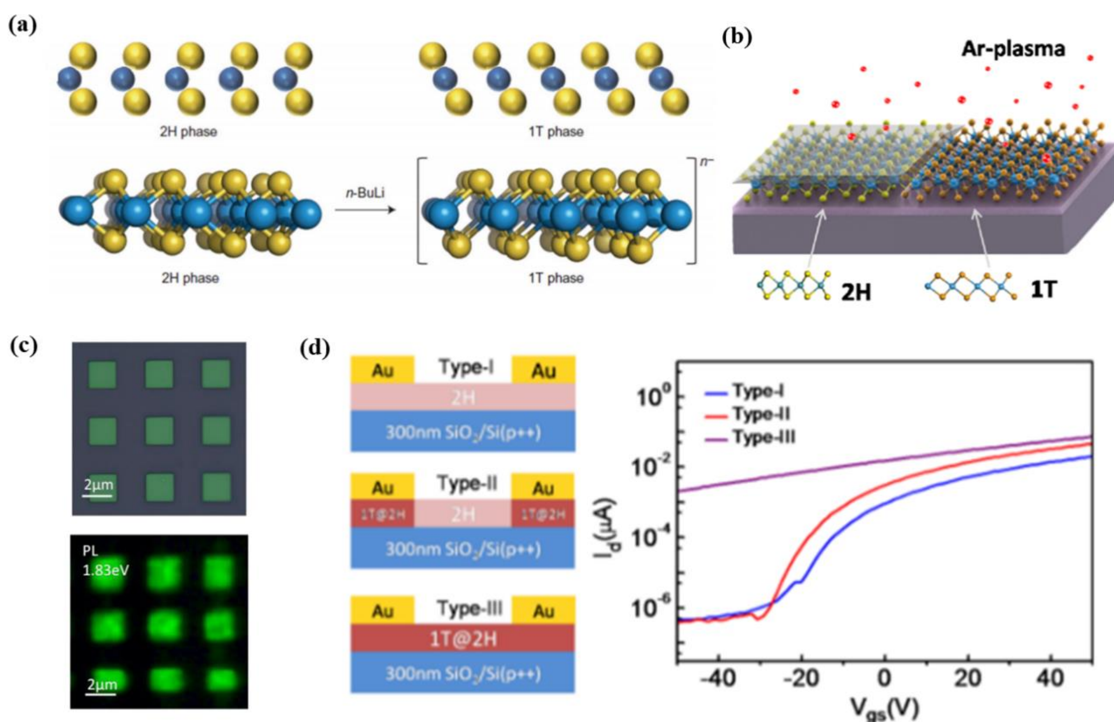

Figure 2-16. (a) Phase conversion of MoS_2 from 1H to 1T/1T'. Reproduced from Ref.[27] (b) Schematic representation of the Ar plasma-treated process. (c) PL intensity mapping on a selective-area plasma treated 2H MoS_2. (d) Performance of the FET device with a heterophase structure in MoS_2. Reproduced from Ref.[26]

2.3.3.2. Non-covalent interaction between molecules and 2DSs

Although being less robust compared with the above-mentioned covalent approach, the non-covalent approach turns out to be noninvasive. Without altering the crystal structure and formation of new chemical bonds, the approach can largely preserve the intrinsic superior properties of the 2DSs. Van der Waals interaction and π–π stacking are the most common interactions between the molecules and the target 2DS. The molecules usually comprise an anchoring group possessing a high affinity to promote the physisorption with the basal plane of the 2DS, and a functional group to impart a novel function to the system.

Charge transfer between the physisorbed molecules and 2DSs has provided the possibility to modulate the charge carrier transport in 2DMs. It relies on the match of the electrochemical redox potential of the molecules and the Fermi level of the 2DS. Electron transfer from 2DS can occur when the redox potential of the dopant molecule lies lower than the Fermi level of the 2DS, inducing p-type doping effect. Conversely, when the redox potential of the molecule lies higher than the Fermi level of the 2DS, electrons can be transferred from molecule to 2DS, or holes can be transferred from 2DS to molecule, resulting in n-type doping.

Numerous electroactive molecules have been exploited to modulate the properties of 2DSs. For example, 2,3,5,6-tetrafluoro-7,7,8,8-tetracyanoquinodimethane (F4-TCNQ) is a popular p-dopant. With its redox potential lies below the CBM of MoS_2, electron transfer can be predicted from the MoS_2 to the molecule, resulting in p type doping effect (Figure 2-17a). Such effect is evident from the evolution of the photoluminescence (PL) spectra. In the F4-TCNQ-doped MoS_2, the weight ratio of the negative trion X^- is reduced while the contribution of the neutral exciton X becomes dominant due to the electron depletion. When the F4-TCNQ-doped WS_2 is integrated as the channel material in the back-gated FET, as shown in Figure 2-17c, with increasing concentration F4-TCNQ, the threshold voltage is found to shift towards more positive gate voltage values indicating an enhanced p-type doping, in good agreement with the optical modulation. Different from F4-TCNQ, nicotinamide adenine dinucleotide (NADH) possesses a redox potential higher than the CBM of monolayer MoS_2, which can therefore

induce n-type doping. After physisorption of NADH molecules, the corresponding PL spectra of monolayer MoS_2 show opposite behavior and is characterized by a higher weight ratio of trion X^- due to electron accumulation. This example demonstrates that the molecular physisorption approach can induce charge-carrier doping and effectively modulate the optical as well as electrical properties of the target 2DS.

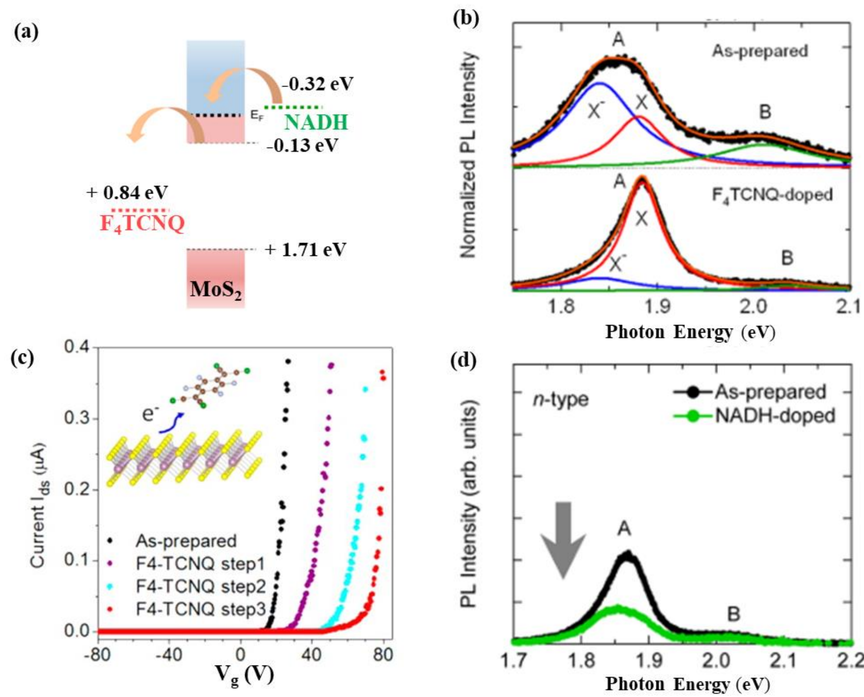

Figure 2-17. (a) Band energy alignment between MoS_2 and n- and p-type dopants. Reproduced from Ref.[28] (b) PL spectra of MoS_2 before and after being doped with F4-TCNQ. (c) Transfer evolution of WS2 FET as-prepared and after various F4-TCNQ doping steps. Reproduced from Ref.[29] (d) PL spectra of MoS_2 before and after being doped with NADH.

Dipolar interaction is another mechanism to tune the doping level in 2DSs. A molecule with an intrinsic dipole moment can generate an electric field at the interfaced 2DS. When a large quantity of the same molecules possessing the same dipole orientation lies on the 2DS surface, each single electric field sums up and results in a significant electric field. The target 2DS thus experiences an additional non-zero gate voltage, leading a shift of its Fermi level. In this way, the molecular layer leads to a doping effect depending on the dipole direction.

The molecule induced dipolar interaction can be realized by interfacing with either the bottom or the top surface of the 2DS. By using functional self-assembled monolayers (SAMs) to decorate the substrate surface, the bottom surface of the later transferred 2DS can thus be modified. The molecules possessing head groups like thiols, silane, phosphonates have been widely studied to form SAM on the Au or Si/SiO_2 substrate. For example, by inserting a 3-aminopropyltriethoxysilane (APTES) passivation layer at the MoS_2/SiO_2 interface, the threshold voltage hysteresis of MoS_2 FET is significantly reduced.[30] The top surface of the 2DS can also be decorated with molecules via physisorption. Interestingly, the molecule with same functional groups is investigated to modify the top surface of MoS_2 and is found to induce n-type doping. The results are in agreement with those obtained at the bottom surface modified 2DS FET.[31]

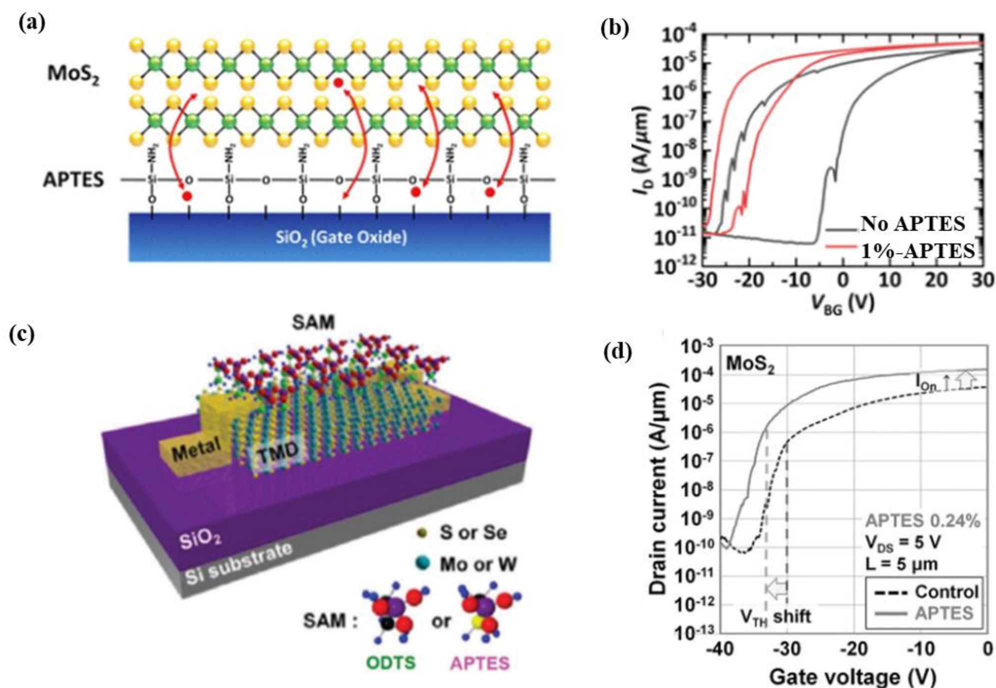

Figure 2-18. (a) Schematic illustration of MoS_2/APTES/SiO_2 structure. (b) Transfer curves of the MoS_2 FETs with and without APTES beneath. Reproduced from Ref.[30] (c) Schematic illustration of APTES/MoS_2/SiO_2 structure. (d) Transfer curves of the MoS_2 FETs with and without APTES on top. Reproduced from Ref.[31]

As mentioned above, molecules with functional groups interfacing with 2DS may enable technologically relevant applications. For example, device based on organic dye molecules/2DS can work as an ultrasensitive photodetector, due to the enhancement of its electrical response to light.[32] As

in Figure 2-19a, rhodamine 6G (R-6G) treated MoS_2 photodetectors showed an enhanced performance with a broad spectral photoresponse and a high photoresponsivity compared with the properties of the pristine MoS_2 photodetectors, due to the charge transfer of the photoexcited electrons from the R-6G molecules to the MoS_2 layer. Among all the functional molecules, one interesting group is the stimuli-responsive molecules. They possess two different states with each state exhibiting well-defined characteristics; these two states can reversibly switch between each other in response to the according stimuli, like light irradiation, electric field, magnetic field, change in pH, etc. With different states inducing different doping levels in the target 2DS, devices based on such hybrid structure are thereof endowed with the novel stimuli-responsive function. For example, switchable 2D FET with a chemically programmed electrochemical signal as a remote control can be fabricated by functionalize the MoS_2 channel with a suitably designed ferrocene-substituted alkanethiol (Fc-SH) molecule.[33] The molecule not only improves the FET performance by healing the sulfur vacancies with thiol functional groups, but also show reversible electrochemical switching on the surface of MoS_2. As illustrated in Figure 2-19d, after the adsorption of Fc-SH molecules, a small droplet of ionic liquid was applied onto the devices. A Pt wire, serving as the top gate electrode was immersed in the ionic liquid. two redox peaks can be attributed to the chemically reversible oxidation−reduction between Fc-SH and Fc^+-SH. The two states can induce different doping effects, which effectively tune the charge transport in the underlying MoS_2 layer. Our research work is based on the combination of stimuli-responsive photochromic and ferroelectric molecules with 2DS and towards the fabrication of multi-stimuli-responsive FETs, which will be discussed in the following chapter.

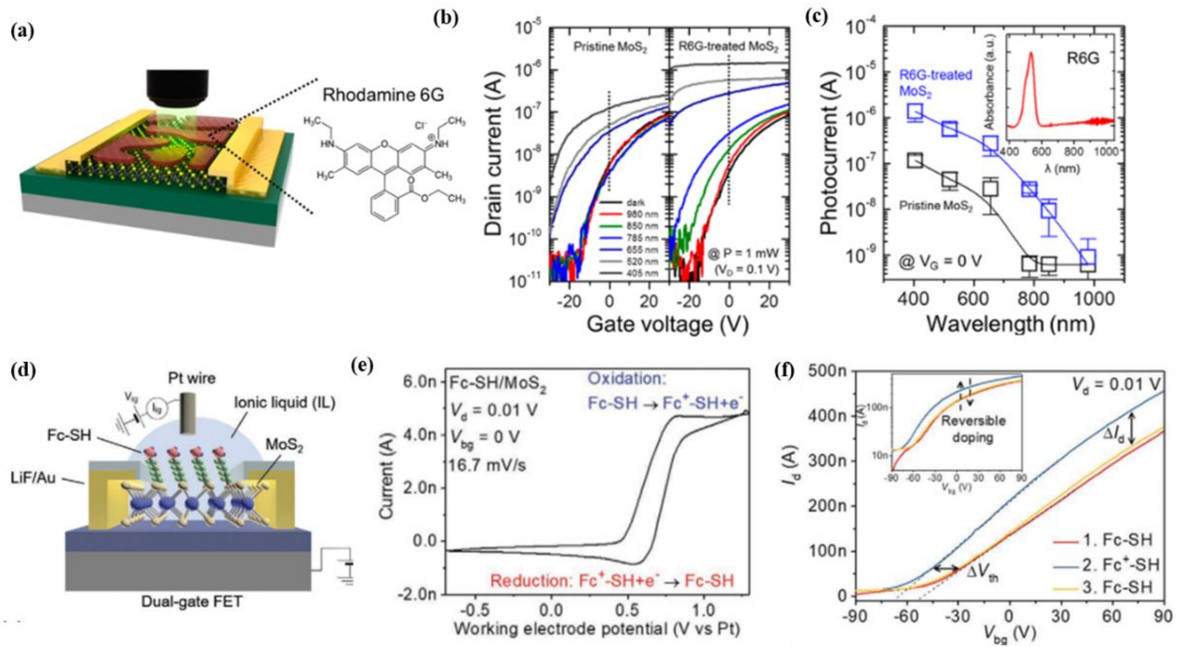

Figure 2-19. (a) Schematic illustration of MoS_2 photodetectors treated with R-6G. (b) Photoinduced transfer characteristics of the pristine and R6G-sensitized MoS_2 photodetectors under different illumination wavelengths. (c) Photocurrent at V_g = 0 V. Reproduced from Ref.[32] (d) Schematic illustration of monolayer MoS_2 FET functionalized with Fc-SH molecules. (e) The cyclic voltammogram of Fc-SH at the MoS_2−IL interface. (f) Transfer characteristics of monolayer MoS_2 FET with different Fc-SH electrochemical states. Reproduced from Ref.[33]

2.4. References

[1] D. A. Neamen, *Semiconductor physics and devices: basic principles*, New York, NY: McGraw-Hill, **2012**.

[2] K. Seeger, *Semiconductor physics*, Springer Science & Business Media, **2013**.

[3] S. M. Sze, K. K. Ng, *Physics of semiconductor devices*, John wiley & sons, **2006**.

[4] M. Tooley, *Electronic circuits: fundamentals and applications*, Routledge, **2019**.

[5] D. Crecraft, S. Gergely, *Analog Electronics: circuits, systems and signal processing*, Elsevier, **2002**.

[6] P. Siffert, E. Krimmel, *Silicon: Evolution and future of a technology*, Springer Science & Business Media, **2013**.

[7] M. Balkanski, R. F. Wallis, R. F. Wallis, *Semiconductor physics and applications*, Vol. 8, Oxford University Press, **2000**.

[8] D. L. Pulfrey, *Understanding modern transistors and diodes*, Cambridge University Press, **2010**.

[9] R. G. Roddick, Argonne National Lab., Ill., **1962**.

[10] I. Grout, *Digital systems design with FPGAs and CPLDs*, Elsevier, **2011**.

[11] M. Riordan, *IEEE spectrum* **2004**, *41*, 44.

[12] B. G. Streetman, S. Banerjee, *Solid state electronic devices*, Vol. 4, Prentice hall Englewood Cliffs, NJ, **1995**.

[13] a) J. R. Brent, N. Savjani, P. O'Brien, *Prog. Mater Sci.* **2017**, *89*, 411; b) Y. Shi, H. Li, L.-J. Li, *Chem. Soc. Rev.* **2015**, *44*, 2744.

[14] a) N. Onofrio, D. Guzman, A. Strachan, *J. Appl. Phys.* **2017**, *122*, 185102; b) V. P. Pham, G. Y. Yeom, *Adv. Mater.* **2016**, *28*, 9024.

[15] a) Y. H. Lee, X. Q. Zhang, W. Zhang, M. T. Chang, C. T. Lin, K. D. Chang, Y. C. Yu, J. T. W. Wang, C. S. Chang, L. J. Li, *Adv. Mater.* **2012**, *24*, 2320; b) Y. Zhan, Z. Liu, S. Najmaei, P. M. Ajayan, J. Lou, *Small* **2012**, *8*, 966.

[16] R. Murray, K. Haynes, X. Zhao, S. Perry, C. Hatem, K. Jones, *ECS J. Solid State Sci. Technol* **2016**, *5*, Q3050.

[17] M. Zhang, J. Wu, Y. Zhu, D. O. Dumcenco, J. Hong, N. Mao, S. Deng, Y. Chen, Y. Yang, C. Jin, *ACS Nano* **2014**, *8*, 7130.

[18] L. Xie, *Nanoscale* **2015**, *7*, 18392.

[19] Q. Feng, Y. Zhu, J. Hong, M. Zhang, W. Duan, N. Mao, J. Wu, H. Xu, F. Dong, F. Lin, C. Jin, C. Wang, J. Zhang, L. Xie, *Adv. Mater.* **2014**, *26*, 2648.

[20] J. Gao, Y. D. Kim, L. Liang, J. C. Idrobo, P. Chow, J. Tan, B. Li, L. Li, B. G. Sumpter, T.-M. Lu, V. Meunier, J. Hone, N. Koratkar, *Adv. Mater.* **2016**, *28*, 9735.

[21] M. Tosun, L. Chan, M. Amani, T. Roy, G. H. Ahn, P. Taheri, C. Carraro, J. W. Ager, R. Maboudian, A. Javey, *ACS Nano* **2016**, *10*, 6853.

[22] H. Nan, R. Zhou, X. Gu, S. Xiao, K. Ostrikov, *Nanoscale* **2019**, *11*, 19202.

[23] H. Qin, V. Sorkin, Q.-X. Pei, Y. Liu, Y.-W. Zhang, *J. Appl. Mech.* **2020**, *87*.

[24] Z. Yu, Y. Pan, Y. Shen, Z. Wang, Z.-Y. Ong, T. Xu, R. Xin, L. Pan, B. Wang, L. Sun, J. Wang, G. Zhang, Y. W. Zhang, Y. Shi, X. Wang, *Nat. Commun.* **2014**, *5*, 5290.

[25] X. Zhang, Q. Liao, S. Liu, Z. Kang, Z. Zhang, J. Du, F. Li, S. Zhang, J. Xiao, B. Liu, Y. Ou, X. Liu, L. Gu, Y. Zhang, *Nat. Commun.* **2017**, *8*, 15881.

[26] J. Zhu, Z. Wang, H. Yu, N. Li, J. Zhang, J. Meng, M. Liao, J. Zhao, X. Lu, L. Du, R. Yang, D. Shi, Y. Jiang, G. Zhang, *J. Am. Chem. Soc.* **2017**, *139*, 10216.

[27] Y. Jiao, A. M. Hafez, D. Cao, A. Mukhopadhyay, Y. Ma, H. Zhu, *Small* **2018**, *14*, 1800640.

[28] S. Mouri, Y. Miyauchi, K. Matsuda, *Nano Lett.* **2013**, *13*, 5944.

[29] N. Peimyoo, W. Yang, J. Shang, X. Shen, Y. Wang, T. Yu, *ACS Nano* **2014**, *8*, 11320.

[30] K. H. Han, G.-S. Kim, J. Park, S.-G. Kim, J.-H. Park, H.-Y. Yu, *ACS Appl. Mater. Interfaces* **2019**, *11*, 20949.

[31] D.-H. Kang, M.-S. Kim, J. Shim, J. Jeon, H.-Y. Park, W.-S. Jung, H.-Y. Yu, C.-H. Pang, S. Lee, J.-H. Park, *Adv. Funct. Mater.* **2015**, *25*, 4219.

[32] S. H. Yu, Y. Lee, S. K. Jang, J. Kang, J. Jeon, C. Lee, J. Y. Lee, H. Kim, E. Hwang, S. Lee, *ACS Nano* **2014**, *8*, 8285.

[33] Y. Zhao, S. Bertolazzi, M. S. Maglione, C. Rovira, M. Mas-Torrent, P. Samorì, *Adv. Mater.* **2020**, *32*, 2000740.

Chapter 3 Materials and molecules

This chapter is focused on the description of the graphene and related two-dimensional semiconductors (2DSs) as well as molecules used within this thesis work. Different types of stimuli-responsive molecules such as light-responsive photochromic molecules and electric-responsive ferroelectric polymers, were employed by interfacing them with 2DMs and modulate their intrinsic properties.

3.1. Two-dimensional materials

Low-dimensional nanomaterials can be broadly classified into 3 types according to the total number of their nanoscopic dimensions:

0DM (zero-dimensional material): If all three dimensions of a material are nano-sized, it would be called 0DM. A typical example of 0DM is the nanoparticle.

1DM (one-dimensional material): If two dimensions of a material are nano-sized, with the other dimension much larger, it would be 1DM, such as nanotube or nanowire.

2DM (two-dimensional material): If only one dimension of a material is nano-sized, it would be a 2DM. It is often possible to reduce the thickness of a 2DM down to a single atom.

If none of the dimensions of a material nano-sized, then it is not a nanomaterial. Instead, it should be referred to as a bulk material.

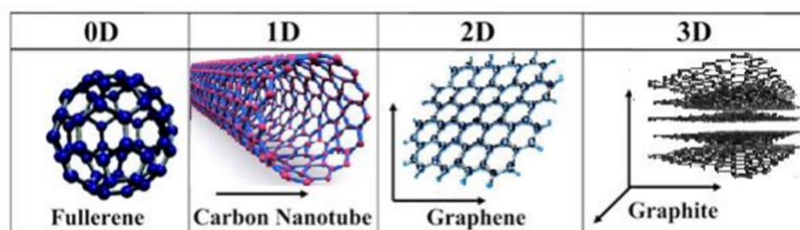

Figure 3-1. Examples for 0D, 1D, 2D, and 3D carbon nanostructures. Reproduced from Ref.[1]

Following the Moore's law, there have been much effort devoted to scaling down the dimensions of FETs. However, FETs cannot be scaled down infinitely and the scaling limitation of silicon FETs was predicted to be 5 nm, under which severe short channel effects occur.[2] As Moore's law is reaching its physical limit, 2DMs have attracted considerable attention due to their their excellent gate electrostatics and the reduced short channel effects. Especially, their inherent advantage of being capable of scaling down into atomic thickness has opened the perspective for the extension of the Moore's law into 'More than Moore'.[3]

3.1.1. Graphene

Graphene, the ancestor of the 2DMs, is an atom-thick honeycomb sheet of carbon atoms. It was first isolated from graphite by Ander Geim and Konstantin Novoselov via scotch tape method in 2004. Since then, graphene has emerged as one of the most promising nanomaterials due to its unique combination of properties.[4] For this historic contribution to graphene science, the two scientists were awarded the Nobel Prize in physics 2010. Graphene is the 2D building block for other sp2 carbon allotropes, including 0D fullerenes, 1D nanotubes, and 3D graphite.[5]

In each carbon atom, there is a total number of 6 electrons: 2 in the inner shell and 4 in the outer shell. The outer shell electrons are available for chemical bonding. While in graphene, only 3 out of the 4 electrons in the atom are covalently bonded with sp2 hybridizations, leaving 1 electron freely available for electronic conduction. These hybrid orbitals form strong in-plane σ bonds, with the interatomic distance of 0.14 nm, offering graphene with outstanding mechanical properties. While on the other hand, the left unhybridized p orbital on each carbon atom overlaps with the unhybridized orbitals from the adjacent atoms to form out of plane weak π bonds, which is responsible for graphene's excellent electronic properties.[6]

Due to such atomic arrangement, the electronic dispersion of graphene presents cones in the Brillouin zone, where its valence and conduction band meet at a single precise point, called Dirac point (Figure 3-2).[7] Because of this unique electronic structure, many fascinating properties of pristine graphene were discovered in the past few years. When it comes to the optical property, graphene has a high optical

transmittance with an optical absorption of only 2.3% over a broad wavelength range, making it almost transparent thus suitable for application as transparent electrodes that are necessary components in modern devices such as touch screens and solar cells .[8] For electrical property, it has an extremely high charge carrier mobility for both electrons and holes (up to 2×10^6 cm^2/Vs at room temperature), being much higher than the silicon based transistor (1400 cm^2/Vs).[7, 9] In addition to that, graphene also possesses high thermal conductivity (K exceeding ~3000 W mK^{-1} near room temperature),[10] the highest intrinsic strength known to exist (130 GPa), being 200 times stronger than steel,[11] the highest theoretical specific surface area (2630 m^2/g), which means a single gram of graphene can cover an entire football pitch,[12] and high Young modulus of 1 TPa[11]. These unique extraordinary properties make graphene indispensable component in applications like flexible electronics, optoelectronics, solar cells, batteries, etc. [13]

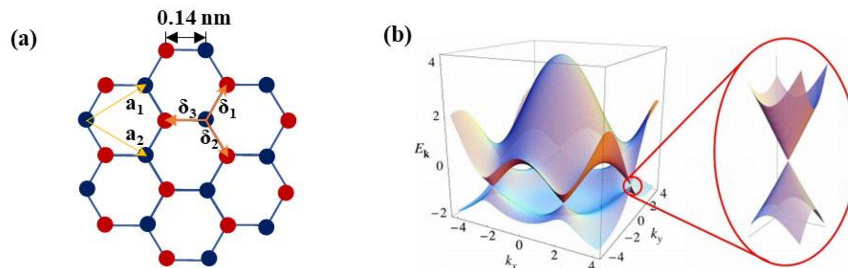

Figure 3-2. (a) Lattice arrangement of graphene, where a_1 and a_2 are the lattice unit vectors, δ_1, δ_2 and δ_3 are the nearest neighbor vectors. (b) Electronic dispersion relation of graphene lattice in first Brillouin zone. Reproduced from Ref.[7]

The market of graphene applications is essentially driven by progress in the production of graphene. To date, lots of efforts have been devoted, which can be categorized into two parts, *i.e.* the bottom up methods and the top-down methods. The former can form covalently linked 2D networks by chemical reaction of molecular building blocks, such as chemical vapor deposition (CVD) and epitaxial growth, which can yield graphene with high-quality and minor defects. The latter mostly relies on the direct exfoliation of graphite. Here are four techniques that are mainly used to produce graphene.

a. Scotch tape method

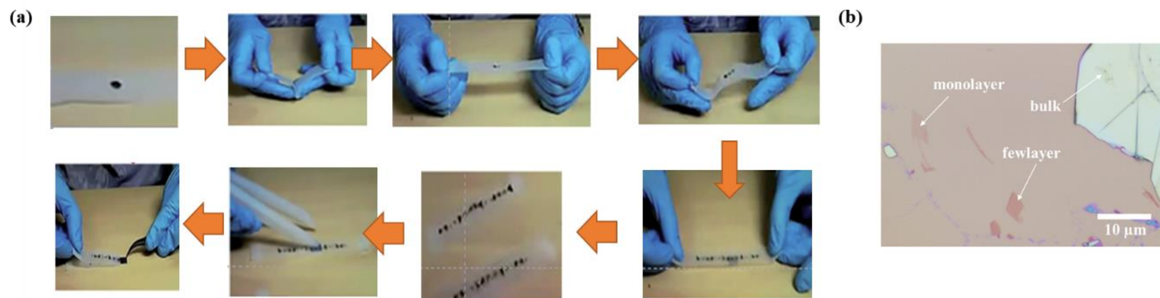

Figure 3-3. (a) Illustrative procedure of the scotch tape exfoliation. Reproduced from Ref.[14] (b) An optical microscopy image of exfoliated graphene flake with different thicknesses.

Graphite is a layered material and can be considered as a stack of individual graphene layers held together via Van der Waals interactions. In the scotch tape method, adhesive tape is used to detach the top few layers of graphite from a highly oriented pyrolytic graphite (HOPG). By repeated peeling the multilayer graphene is cleaved into various flakes of few-layer graphene. Then the tape is pressed against a substrate resulting in some materials transferring to it (Figure 3-3).[14] Since the Van der Waals force between the graphite interlayer is not as strong as the force between the graphite and the substrate, graphene flakes are possible to be obtained during such peeling process. Finally we can seek for the monolayer graphene under an optical microscope. The different colors refer to different thicknesses of flakes, from monolayer (the pale purple), few layer (the intermediate purple), and bulk (the white).

This method was demonstrated for the first time in 2004 and has been then applied to other materials.[15] The process of this method is relatively simple, and the obtained graphene is of highest quality and cleanliness with almost no defects. However, the size of the flake is limited by the crystal grains in the starting HOPG, which is generally below the order of millimeters. This drawback limits its large-scale applications, instead, the material prepared by this method is usually used for fundamental research and device fabrication. We have been employed this method during the thesis to obtain high-quality 2DMs.

b. Liquid phase exfoliation

Liquid-phase exfoliation of graphene via sonication was initiated in 2008, and it became an industrial-scale method to produce high-quality graphene in the form of liquid suspensions, inks, or dispersions.[16] It has also been extended to produce other 2DMs.[17]

This method comprises a number of different techniques: sonication, shear mixing, microfluidization, electrochemical exfoliation, etc. The most common procedure is to disperse graphite in an organic solvent, which has a similar surface energy to graphite in order to reduce the energy that needed to overcome in order to detach a graphene layer from the crystal. The solution is then sonicated and centrifuged in order to disperse the thicker flakes. By optimize the solvent and the sonication time, concentration of the graphene dispersion can be improved.[18]

Although the size of obtained flake is usually limited by the intense exfoliation process therefore not suitable for electronic devices fabrication, the liquid exfoliation method is relatively fast, low-cost, scalable, the quality of the obtained material is high, and the operating conditions are mild. The material produced by liquid phase exfoliation can be deposited on the desired substrate via drop casting, spray coating, ink-jet printing, etc. Moreover, it allows additional applications such as composites and hybrids by simple mixing of dispersion of different kinds of materials. It is reported that solution-based graphene has been integrated in high-frequency flexible electronic with a current gain cut-off frequency of 2.2 GHz.[19]

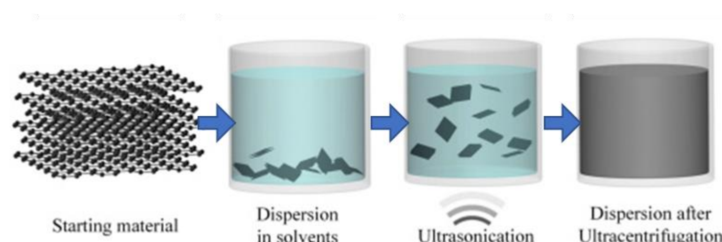

Figure 3-4. Schematic illustration of liquid phase exfoliation process. Reproduced from Ref.[20]

c. Chemical vapor deposition (CVD)

CVD has been emerged as an important method for the production of graphene since it was first reported in 2008 and 2009, using Ni and Cu substrates, which was followed by a variety of research activities to use different transition metal substrates.[21]

CVD is the process to grow graphene film on the surface of a metal substrate (which are also used as the catalysts) by exposing it to a gaseous hydrocarbon precursor such as CH_4. The reaction usually takes place in a chamber under the atmosphere of H_2 and Ar. Parameters like temperature, gas composition and deposition time should be controlled during the reaction. The CH_4 molecules first dehydrogenate on the metal surface, resulting in CH_x species. The atomic C species then diffuse and attach to the graphene domain edge, incorporated into the graphene lattice. The growth of the graphene nuclei continues until consuming all the surrounding adsorbed C species and coalesces to form a continuous film.[22]

For practical uses, the graphene film formed by CVD technique usually requires transferring to another target substrate by using wet or dry transfer technique, which remains the main drawback of CVD method since the transfer process may not preserve the quality of the as-grown graphene. Another drawback of the method is that it is relatively expensive owing to the large energy consumption.[23] While despite of these drawbacks, it is a robust and promising technique to produce continuous graphene films with uniform properties over centimeter-scale areas.

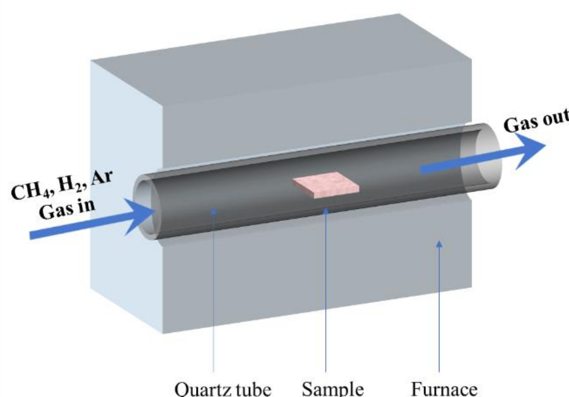

Figure 3-5. Sketch of CVD technique to grow graphene.

d. Epitaxial growth

Graphene growth by decomposition of silicon carbide (SiC) crystal is another technique that holds great potential.[24] In this technique, graphene is prepared by simply sublime the SiC in a furnace filled with Ar or in ultra-high vacuum. At high temperature more than 1400 °C, the sublimation of Si is much faster than C owing to its higher vapor pressure, therefore the remaining C can form a graphene film on the target substrate surface.[25] The quality of the graphene films derived from SiC are highly dependent on the operating temperature, heating rate and pressure. Generally, the graphene obtained contains a mixture of multilayer graphene with a high surface roughness. The main advantage of this technique is that the resulting graphene film can be directly obtained on a commercially available substrate, avoiding the transfer process.

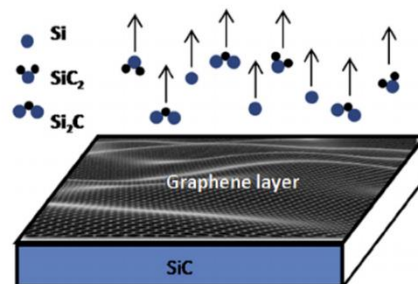

Figure 3-6. Schematic illustration of epitaxial graphene growth of on silicon carbide. Reproduced from Ref. [26]

3.1.2. Transition metal dichalcogenides (TMDs)

Although graphene was the subject of an in-depth study during the last decade because of its outstanding physico-chemical properties, its lack of bandgap induced by the Dirac cones has greatly limited its application in electronics. The transistor based on graphene cannot be properly switched off and results in a low I_{on}/I_{off} ratio. To overcome this problem, several techniques have been employed to open up a bandgap in graphene. At the same time, other semiconducting 2DMs with interesting characteristics and a sizable bandgap to support high I_{on}/I_{off} ratio have been explored. Transition metal dichalcogenides (TMDCs), a family of around 60 crystals, with the structure of MX_2, where M stands for a transition metal atom (such as Mo or W) and X represents a chalcogen atom (such as S, Se or Te), has become a promising alternative.

3.1.2.1. Molybdenum disulfide MoS_2

MoS_2 is the most well-known among all the TMDs and shares various similarities with graphite. In the single layer of MoS_2, each Mo atom is sandwiched between two S atoms, forming a S–Mo–S monolayer stacking, whereas the adjacent layers are interacted by relatively weak van der Waals forces.[27] Monolayer MoS_2, with a thickness of ~0.65 nm, was first isolated in 2005 by Novoselov and co-workers using scotch-tape method.[28] It is stable in ambient conditions, and usually consists of a mixture of two major polytopes with similar structure but different stack orders and metal atom coordination, namely 2H and 1T. 2H is an intrinsic semiconductor, where each Mo atom is covalently bonded to 6 S atoms in trigonal prismatic coordination with 3 layers per repeat unit. 1T is metallic and metastable, with Mo and S atoms arranged in octahedral coordination and 1 layer per repeat unit (Figure 3-7).[29]

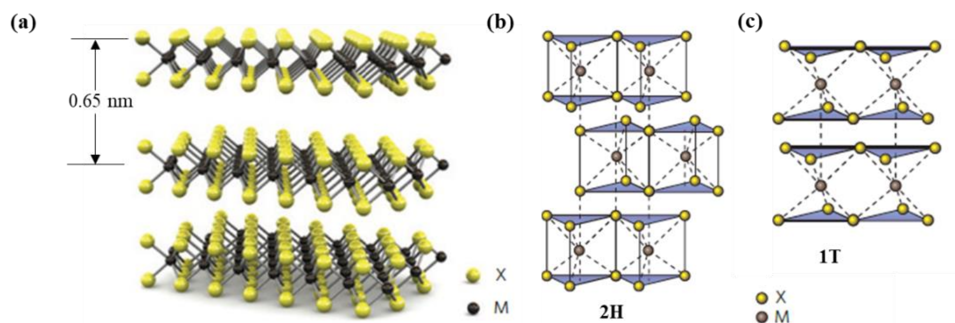

Figure 3-7. (a) 3D representation of MoS_2 structure; (b) and (c) Two polytopes of single layer MoS_2: (b) 2H trigonal prismatic; (c) 1T octahedral. Reproduced from Ref.[30]

Similarly to graphene, MoS_2 is mechanically flexible with a Young's modulus of 0.33 ± 0.07 TPa.[31] In particular, monolayer MoS_2 possesses a high absorption of of 5%–10% in the visible range,[32] making it a promising material for nanoelectronic and optoelectronic applications such as phototransistors and solar cells.[33]

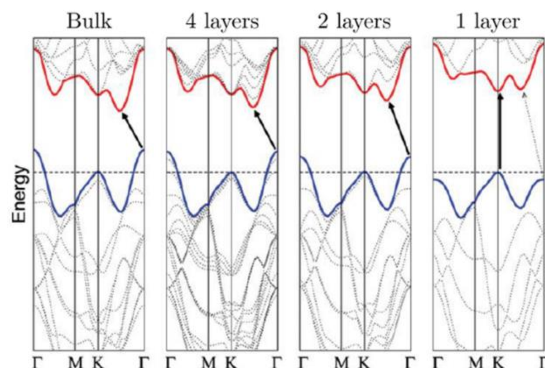

Figure 3-8. Band structure of MoS_2 with different thicknesses. Reproduced from Ref.[34]

Despite the common features, the different nature of MoS_2 has enable the material being used into wider applications. For example, graphene is a gapless semimetal, while MoS_2 possess layer dependent properties. Bulk MoS_2 is an indirect bandgap (1.3 eV) semiconductor with negligible photoluminescence. While a strong PL emerges when it is thinned to monolayer, indicating an indirect to direct bandgap transition. Calculated from first-principles density functional theory, monolayer MoS_2 has a direct bandgap of 1.9 eV, and the bandgap varies with the number of layers (Figure 3-8).[34] Such change in the band structure is due to quantum confinement and the resulting change in hybridization between p orbitals on S atoms and d orbitals on Mo atoms. The presence of this bandgap makes it interesting for applications in nanoelectronics where it allows the fabrication of transistors with low power dissipation. The mobility of a monolayer device is in the range 0.1–10 $cm^2V^{-1}s^{-1}$, which can be implemented by dielectric screening. The first implementation of a top-gate FET based on monolayer MoS_2 was reported by Kis and co-workers in 2011.[35] The top-gating with high k dielectric (HfO_2) geometry largely improves the device mobility due to the suppression of Coulomb scattering. The device showed excellent a mobility of > 200 cm^2 V^{-1} s^{-1}, ON/OFF current ratio of ~10^8, and subthreshold swing of 74 mV per decade.

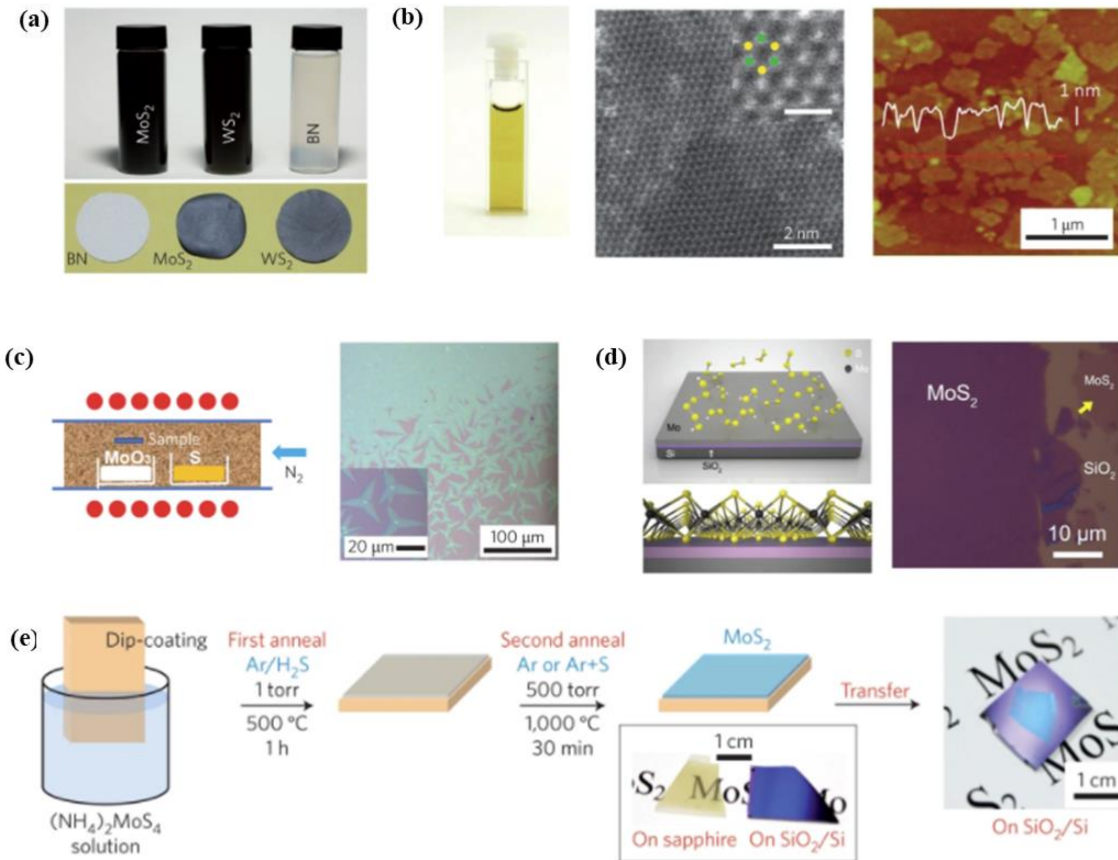

Figure 3-9. Synthesis of thin layer MoS_2 by different techniques. (a) Stable suspensions obtained by liquid-phase exfoliation (top), and thin films derived from vacuum filtration (bottom). (b) Suspension obtained by lithium-intercalated exfoliation in water. (c) CVD growth from solid S and MoO_3 precursors; (d) CVD growth from Mo exposed to S vapor on SiO_2. (e) CVD growth from a dip-coated precursor and growth in the presence of Ar + S vapor. Reproduced from Ref.[30]

Reliable production of MoS_2 is essential for translating their intrinsic properties into various applications. Therefore, substantial efforts have been devoted to preparing thin-layer MoS_2 (Figure 3-9), including top-down methods like scotch tape based mechanical cleavage as we introduced in the previous section, the same technique that were developed for graphene, liquid phase exfoliation via ultrasonication by intercalation of ionic species like N-butyllithium between the MoS_2 atomic planes to increase the distance between adjacent layer and favor the separation,[36] and bottom up synthesis like CVD method (Figure 3-9 c-e) by vaporizing and depositing S and MoO_3 powder onto the substrate;[37] depositing a thin layer of Mo onto a wafer heated with solid S; dipping substrates in a solution of $(NH_4)2MoS_4$ and heating in the S vapor atmosphere, and hydrothermal synthesis to grow single crystals from an aqueous solution in an autoclave via the reaction of molybdic acid with thiourea.[38]

3.1.2.2. Tungsten diselenide WSe_2

Another exemplary case of TMD is WSe_2, which holds great potential for complementary digital logic applications since n-type, p-type, and ambipolar transport can all be achieved by thickness modulation and electrode engineering in the corresponding transistor.[39]

WSe_2 is thermally stable in 2H phase(Figure 3-10a), with a hexagonal crystalline structure similar to MoS_2, where Se atoms locate in the lattice position of a hexagonal structure.[40] The metallic octahedral coordination 1T phase is less stable and are commonly obtained via distortion of the 2H phase as by electrical gating,[41] electron transfer during chemical treatment (i.e. lithiation during exfoliation or organolithium treatment)[42] or applied mechanical strain.[43]

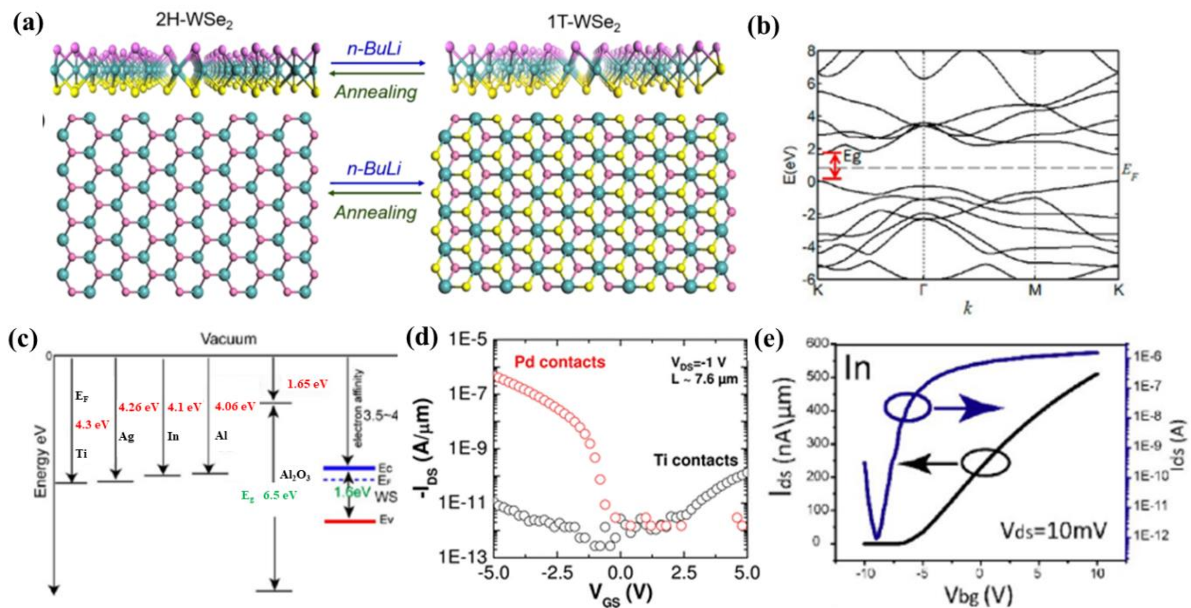

Figure 3-10: (a) side and top view of the 2H and IT structure of WSe_2. (b) band structure of monolayer WSe_2. (c) Band alignments of some potential contact metals and Al_2O_3 with respect to that of WSe_2. Reproduced from Ref.[44] (d) WSe_2 FETs with hole transport behavior. Produced from Ref.[45] (e) WSe2 FETs with electron transport behavior.

Bulk WSe_2 is an indirect bandgap (~1.2 eV) semiconductor, whereas monolayer WSe_2 exhibits a direct bandgap of ~1.65 eV,[46] offer opportunities for its potential applications in optoelectronics.[47] While in comparison with widely studied MoS_2, studies focusing on WSe_2 are still very limited. The main reason is that WSe_2 tends to form a substantial Schottky barrier with most metals that commonly used for

making electrical contacts.[48] The high contact resistance between the metal electrode and WSe_2 thereby induce poor injection, significantly influence device performance. Therefore, selecting proper metal contacts to form low contact resistance is necessary for WSe_2. Metals with high work have been selected for hole injection, and monolayer WSe_2 is the first TMD material in which p-type behavior is observed by using high work function metal Pd as the contact, with the hole mobility of ~250 $cm^2/V{\cdot}s$.[45] Metal with low work function have been selected for electron injection, and monolayer WSe_2 FET with In contact can attain an electron mobility of 142 $cm^2/V{\cdot}s$.[44]

3.1.3. Black phosphorous BP

As the most stable allotrope of phosphorus, BP is a newly discovered 2DM that has been the focus for recent research for various applications. It is a layered material similar to graphene, whose individual atomic layers are stacked together by weak van der Waals interactions, with the distance between two adjacent layers of about 5 Å. Such layered structure allows the obtaining of monolayer or few-layer thick BP from the bulk crystal by mechanical or liquid exfoliation. In a single layer, each phosphorous atom is covalently bonded with three neighboring atoms forming a puckered 2D honeycomb structure due to sp3 hybridization with zigzag configuration (Figure 3-11).[49] Different from graphene, the three bonds take up all three valence electrons of phosphorus, constructing a quadrangular pyramid structure.

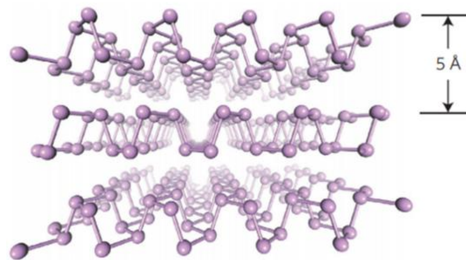

Figure 3-11. Three-dimensional representation of BP structure. Reproduced from Ref.[49]

BP has attracted tremendous attention since it bridges the energy gap between graphene and TMDs. Monolayer BP is a semiconductor with a direct bandgap of 2 eV. For few-layer BP, each added layer reduces the bandgap due to interlayer interactions, and eventually reaches 0.3 eV for bulk.[50] Figure 3-12 shows the band structures for monolayer to 5 layers.[51] Such thickness-dependent direct bandgap feature leads to remarkable applications in optoelectronics covering from visible to mid-infrared range, where TMD are limited because of their relatively large bandgap.[52]

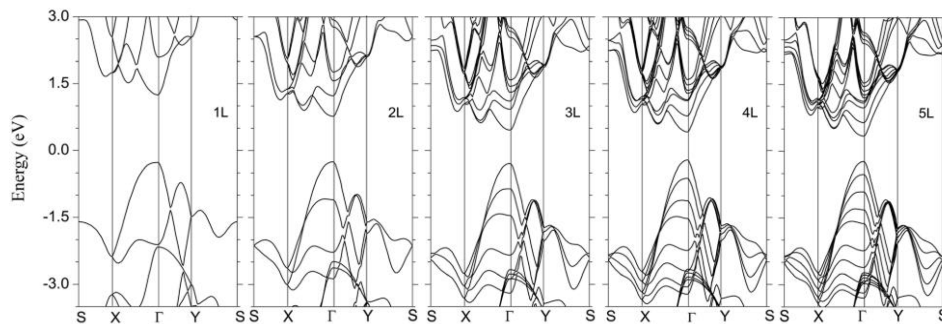

Figure 3-12. Band structures for BP from for monolayer to 5 layers obtained from HSE06 hybrid functional calculations. Reproduced from Ref.[51]

BP possesses many fascinating physical properties. FETs based on bulk BP shows the mobilities on the order of 10,000 $cm^2V^{-1}s^-1$. While the exfoliated BP flakes have presents a clear ambipolar transport behavior with a high carrier mobility over 1,000 $cm^2V^{-1}s^{-1}$, together with a high ON/OFF ratio of 10^5.[53] Such distinguished virtue are hard to achieve simultaneously by either graphene or monolayer transition metal dichalcogenides. Moreover, It has strong photon absorption and in-plane anisotropic properties, which is beneficial for applications in high performance optoelectronics, such as broadband photodetectors.[52a]

Albeit exhibiting outstanding properties, BP shows environmental instability in ambient conditions especially in its single and few-layer forms. The flake surface roughens rapidly within few hours in air, resulting in deteriorated electrical transport properties. By employing ab initio electronic structure calculations and molecular dynamics simulations, the understanding on the ambient degradation of few-layer BP are illustrated by a 3-step picture: generation of superoxide under light, dissociation of the superoxide, and eventual breakdown under the action of water (Figure 3-13.[54]

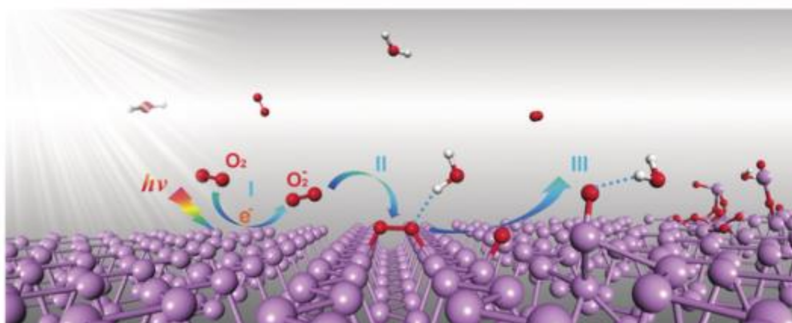

Figure 3-13. The light-induced ambient degradation process of BP. Reproduced from Ref.[54]

a. Generation of O^{2-} through a charge transfer reaction under ambient light on the surface of BP.

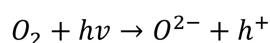

$$O_2 + hv \rightarrow O^{2-} + h^+$$

b. Dissociation of O^{2-} at the BP surface and formation of dangling P–O bonds.

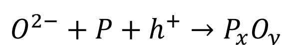

$$O^{2-} + P + h^+ \rightarrow P_xO_y$$

c. Removal of O and P from the surface by water molecules and dissolution of the top layer.

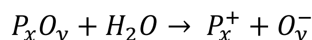

$$P_xO_y + H_2O \rightarrow P_x^+ + O_y^-$$

Various protection strategies have been proposed to protect BP against moist air. As physical protection, capping layers have been implemented to isolate BP from moist air,[55] such as Al_2O_3 layers,[56] PMMA layer, and other 2D materials like graphene and h-BN. Chemical routes rely on the surface treatment of BP with chemical species like metoxybenzene, nitrobenzene,[57] and poly(phenylenevinylene),[58] in an effort to transform it from environmentally active to being inert.

3.2. Stimuli-responsive molecules

3.2.1. Photochromic molecules

Photochromic molecules are compounds that can undergo a reversible photo-induced isomerization between two or more states upon absorption of photons with well-defined energy.[59] The two isomers feature different physical properties, which means during such reversible photoisomerization, their physical properties such as absorption spectra, fluorescence emission, conjugation, electron conductivity, electrochemical properties, magnetic properties, coordination properties, dipole moment, refractive index, dielectric constant and geometrical structure, can be modulated by light.[60] In view of such unique characteristics, scientists have used this kind of molecules as active components in optoelectronic devices that can be addressed by light. Possible applications include processing of information in the molecular-scale, biological engineering, and high-density data storage. Currently, the most popular photochromic molecules are azobenzenes, spiropyrans (SPs), diarylethenes (DAEs), and dihydroazulenes (DHAs).

3.2.1.1. Azobenzenes

The photochromic properties of azobenzenes were first investigated by Hartley and co-workers in 1937.[61] Azobenzene is a diazene (HN=NH) derivative where both hydrogens are replaced by phenyl groups. The N=N double bond have two geometric isomers and the azobenzene molecules can thereby exist in either the cis or trans configurations. The trans isomer is s 10–12 kcal mol^{-1} more stable than the cis, and therefore is predominant in the dark.[62] The trans isomer can switch to the cis by irradiation with UV light at 340 nm, and the cis isomer can reverse to trans by vis light at 450 nm or spontaneously in the dark owing to the thermodynamic stability of the latter (Figure 3-14a).

Apart from thermal stability, the two isomers possess many other distinct properties. In the unsubstituted azobenzene, the trans isomer is planar with a quasi-zero dipole moment, while the cis isomer has a bent conformation and a dipole moment of 3 Debye.[63] Moreover, for the UV-vis absorption spectra, at 440 nm, the trans isomer shows a weak n-π* peak while cis isomer has a much

stronger peak. The trans isomer has another strong π-π* peak near 320 nm, while the cis has peaks at shorter wavelength between 280 nm and 250 nm (Figure 3-14b).[64]

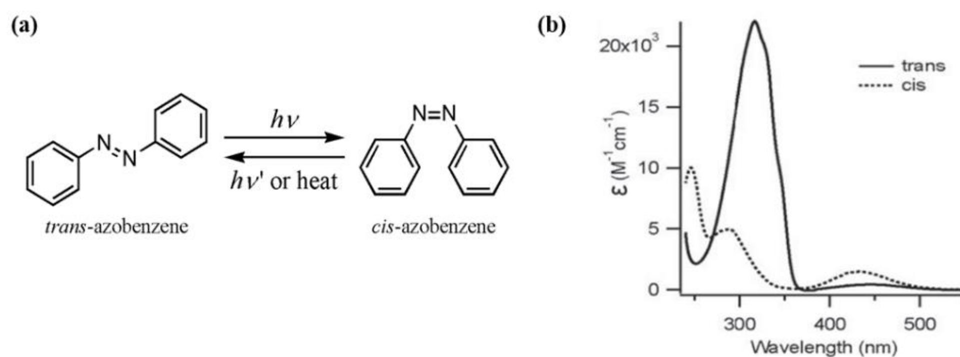

Figure 3-14. (a) Photoisomerization of azobenzene between trans and cis isomer. (b) A typical example of UV/vis absorption spectra of trans and cis isomers of azobenzene. Reproduced from Ref.[64]

The azobenzene molecules has been applied to electronic devices to impart their photo-responsivity capacity to the initially non light-switchable devices. Our group exploited a thiol-terminated biphenyl azobenzene to form SAM on the electrode of an OFET to act as active layer interface (Figure 3-15a-c).[65] The P_3HT based device presented reversible photoresponsitivity, with output current increased when the device was exposed to the UV light and restored to initial state after relaxation in the dark. The modulation behavior was attributed to three possible factors, the decreased carrier injection barrier by cis-isomer, and the change of interface film morphology and also the variation of the work function of the contacts with the electrodes. The large conformational change of azobenzene molecules during photoisomerization also enable its use for multifunctional applications.[66] As shown in Figure 3-15d-f, with graphene working as the bottom and top electrode, and azobenzene molecules grafting onto the bottom electrode surface. The corresponding devices showed light-controlled electrical transport. After UV light irradiation, the output current increased by one order of magnitude and later decreased back to the previous value upon exposure to visible light. Such modulation behavior was explained by the variation of the molecular length by switching, thus altering the vertical distance of the bottom and top electrodes. Azobenzene molecules have also been employed to decorate the 2DM surface to impart a hybrid with light responsive capacity.[67] The azobenzene/MoS_2 hybrid system possesses light-tunable PL spectra behavior, whose PL peak blue shifts and the intensity increases after UV irradiation, and

convert back to the initial state after irradiation with visible light. The corresponding FET device also showed light-controlled charge transport (Figure 3-15g-i). These phenomena were induced by isomerization of azobenzene molecules between different states exhibiting diverse dipole moment. The carrier concentration and even carrier polarity of the interfaced 2DM can therefore be directly modulated via dipolar interactions.

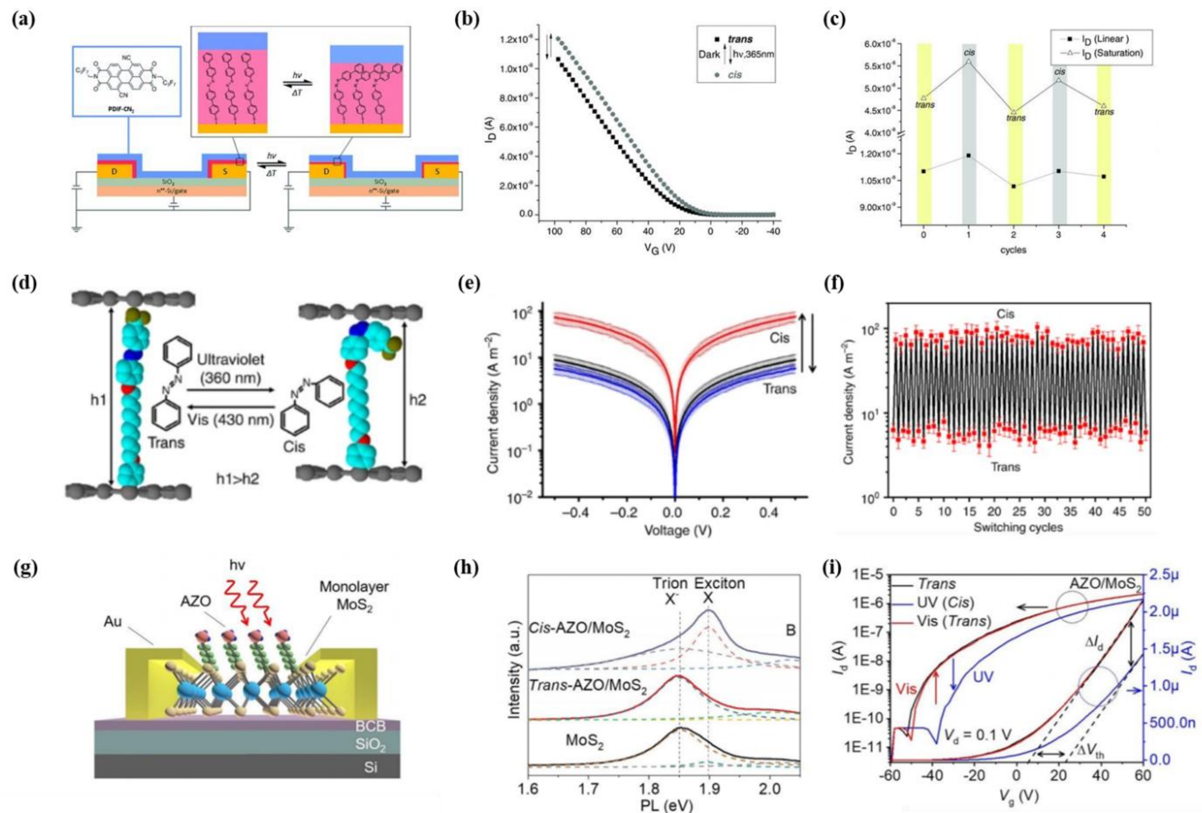

Figure 3-15. (a) Schematic illustration of the OFET with azobenzene-functionalized electrodes. (b) Transfer evolution of the OFET for one switching cycle of trans/cis azobenzene. (c) Variation of output current for consecutive switching cycles of azobenzene. Reproduced from Ref.[65] (d) Schematic illustration of graphene-aryl azobenzene-graphene device. (e) Current density evolution of the devices during one switching cycle of trans/cis azobenzene. (f) The photoinduced current switching for over 50 cycles. Reproduced form Ref.[66] (g) Schematic illustration of the FET with azobenzene on the MoS_2 surface. (h) PL spectra and (i) Transfer evolution of the FET for one switching cycle of trans/cis azobenzene. Reproduced from Ref.[67]

3.2.1.2. Spiropyrans

During the past few years, SPs has emerged as the molecule-of-choice for the construction of novel dynamic materials, due to their capacity of being able to undergo isomerization in response to a variety of orthogonal stimuli, which ranges from light, temperature, solvents, acids and bases, metal ions, redox potential, to mechanical stress.[68]

The structure of SP molecule is depicted in Figure 3-16a, which comprises an indoline and a chromene moiety bound through a spiro junction and oriented perpendicular with respect to one another. UV irradiation of the neutral closed-ring SP molecules gives rise to the zwitterionic open-ring isomer merocyanine (MC). The transformation begins with the cleavage of the C–O bond in the pyran ring, resulting in cis-MC. Then the rotation of the central C=C double bond in cis-MC ultimately yields thermally stable trans-MC (Figure 3-16a).[68] Therefore, the MC form may exist in both cis and trans isomers, while only the trans form is observed at room temperature due to the low thermal stability of the cis form. The MC isomer can return to SP spontaneously in the dark or can be accelerated by vis light illumination and heating.[69]

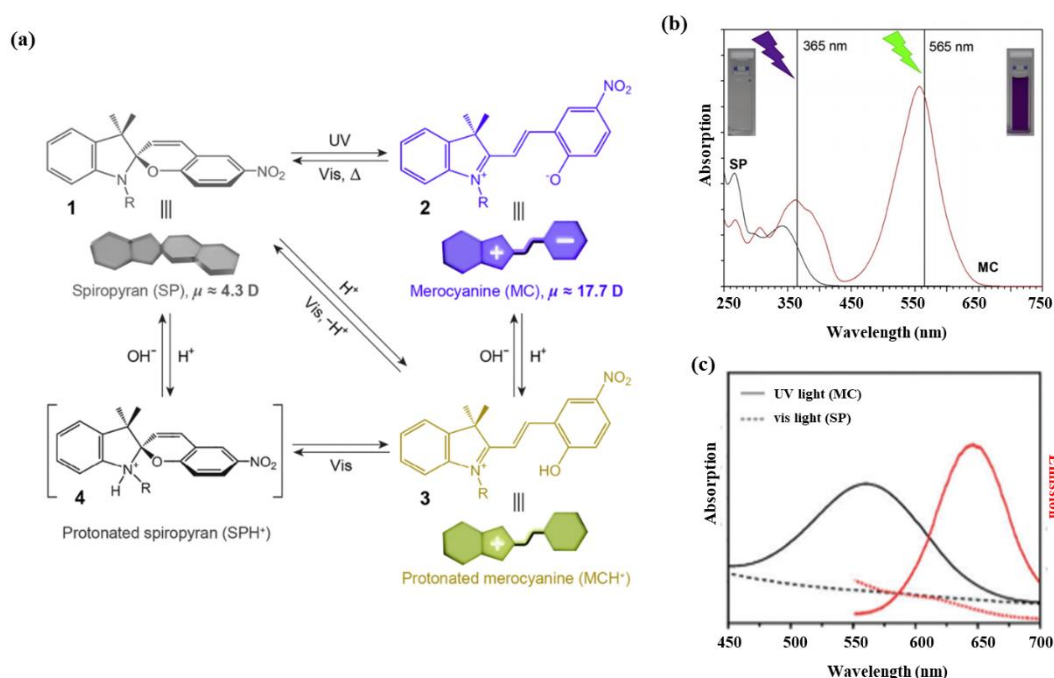

Figure 3-16. (a) Photoisomerization of SP between the four states: SP, MC, protonated merocyanine (MCH^+), and protonated spiropyran (SPH^+). Reproduced from Ref.[68] (b) UV/vis absorption spectra, (c) Emission spectra of SP and MC isomers. Reproduced from Ref.[70]

The structure difference between SP and MC isomers induces a markedly difference in their optical and electrical properties, which allows their widespread utility. First of all, density functional theory calculations have shown that the dipole moment of SP normally lies in the range of 4-6 Debye, while the value for MC is largely increased to 14-18 Debye due to the formation of charge-separated species.[71] Secondly, the SP isomer is optically colorless in the vis range and shows two localized bands at the UV range (Figure 3-16b). One band located at ∼272-296 nm is attributed to the π–π* electronic transition in the indoline moiety, and the other band at ∼323-351 nm originates from the chromene moiety. While the MC isomer appears deep blue and has strong absorption band at ~550-600 nm. Thirdly, the two isomers shows different emission behavior (Figure 3-16c): the SP isomer has no emission, while MC has an intense emission band centered at ~650 nm.[70] Fourthly, the structure difference between the two isomers makes the SP occupy less volume than MC, which may give a mechanical response when they are functionalized on the planar surface, beneficial for biophysical systems.[72] Based on these characteristics, various investigations on the study of SP-based dynamic materials have been reported, such as SP-functional polymers, photo-control inorganic nanoparticles and so on.

Optically controllable transistors based on SP molecules have also been proposed. Guo et co-workers reported the fabrication of OFET by blending P_3HT with SP to form a hybrid active layer, whose output current increased when UV light turned on and restored under the irradiation of visible light (Figure 3-17a-c).[73] Such modulation behavior may be explained by two possible mechanisms. One is that the charge-separated MC form possess larger dipole moment, which can form an electrostatic environment that act as a local negative gate-voltage. Another possible reason is that the HOMO level of MC is lower than that of SP. As a result, the increased energy gap between the HOMO levels of P_3HT and MC enhance the driving force for hole transport. Later on, a similar work was proposed by replacing P_3HT with poly(triarylamine) (PTAA), while obtaining the opposite switching behavior: the output current reduced by UV irradiation and reversed under vis irradiation (Figure 3-17d-f).[74] The possible mechanism for this phenomenon is that the ionic polarized SP-open works as a carrier scattering site and trap the carriers in blend film thus leading to the decrease of current. When combining SP with

2DMs, optically switchable FETs can be realized. Figure 3-17g-i presents the switching behavior of FET based on graphene and MoS_2 with a spin-coated SP layer on top, both showing significant n-type doping effect induced by MC molecules after UV irradiation.[75] Such doping effect was induced by the presence of positive vertical dipoles in MC molecules. With positively charged side is lifted up in each single molecule, the MC assembly resulted in a significant electrical dipole oriented perpendicular to the 2D surface.

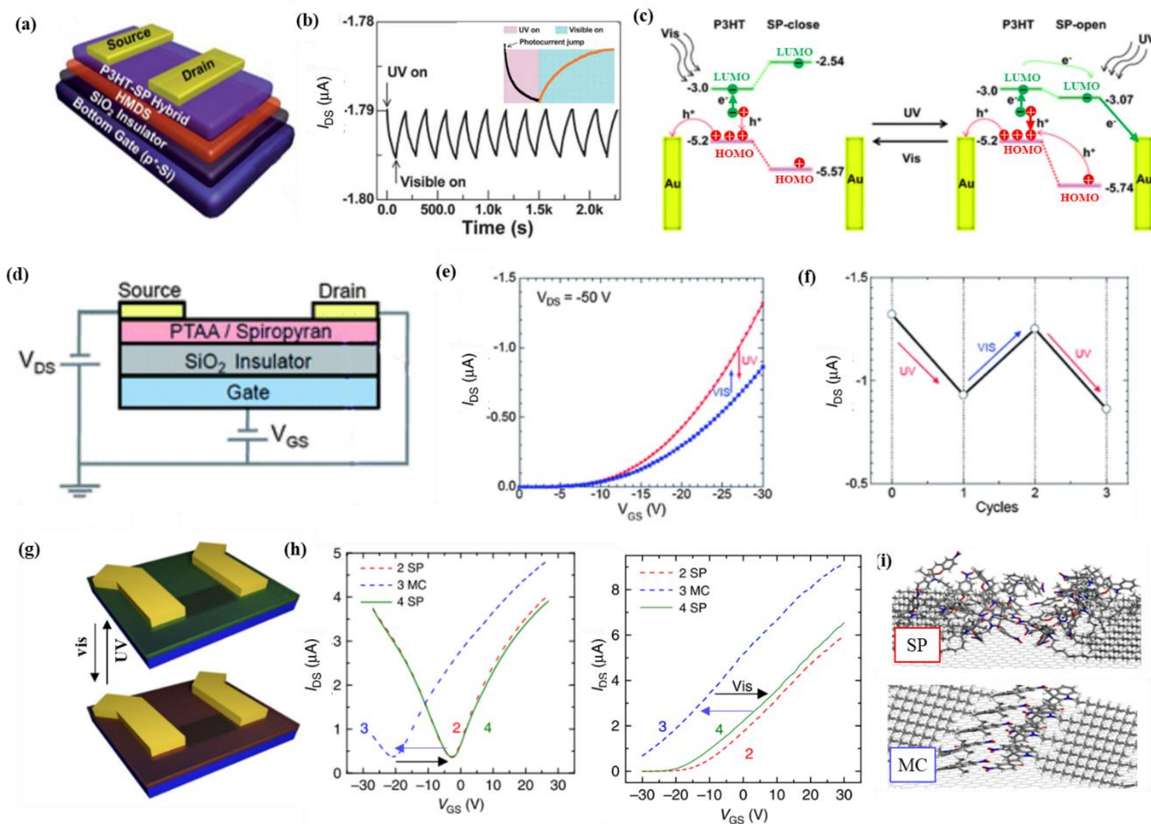

Figure 3-17. (a) Schematic illustration of the optically switchable OTFT based on P_3HT and SP. (b) Dynamic current behavior under UV/vis irradiation cycles. (c) Energy level diagram and working model of P_3HT-SP hybrid systems (d). Reproduced from Ref.[73] (d) Schematic illustrations of the transistor involving PTAA and SP. (e) Transfer evolution by alternating UV and vis irradiation. (f) Drain current modulation during 2 switching cycles. Reproduced from Ref.[74] (g) Schematic illustrations of FET based on 2DM with SP. (h) Transfer evolution by alternating UV and vis irradiation for graphene/SP FET (left) and MoS_2/SP FET (right). (i) Representative snapshot of the calculated dynamic evolution of the SP and MC assembly. Reproduced from Ref.[75]

3.2.1.3. Diarylethenes

DAEs, being another typical example of photochromic molecules, was pioneered by Irie and co-workers in 1980s.[76] Since then, they have received growing attention since they are particularly suitable as switching units and fulfil the requirements to be applied in various practical applications due to their excellent properties: high fatigue resistance, high quantum yield, short response time, thermal bistabiliy and photo-tunable energetic levels.

a. Quantum yield

The DAE molecules can undergo reversible photocyclization between their ring-open isomer and ring-closed isomer under UV/vis light. The ring-open isomers exist two conformations, which can interconvert between each other at room temperature. One conformation has two aromatic rings in parallel orientation and the other in antiparallel orientation (Figure 3-17a). Since the photocyclization can only occur from the antiparallel conformation, the quantum yield of the cyclization is dependent on the population ratio of the antiparallel conformation, which is usually 50%.[59] As increasing the antiparallel ratio can result in an increase in quantum yield, therefore various strategies have been proposed, for example, introduction of bulky isopropyl groups at 2 and 2' positions of bisbenzothienylethene to increase the relative stability of the antiparallel conformation (Figure 3-18b),[77] or, bridge the 2 and 4 positions of thiophene rings by a considerably long –CH_2SCH_2– linkage to fix the antiparallel conformation (Figure 3-17c).

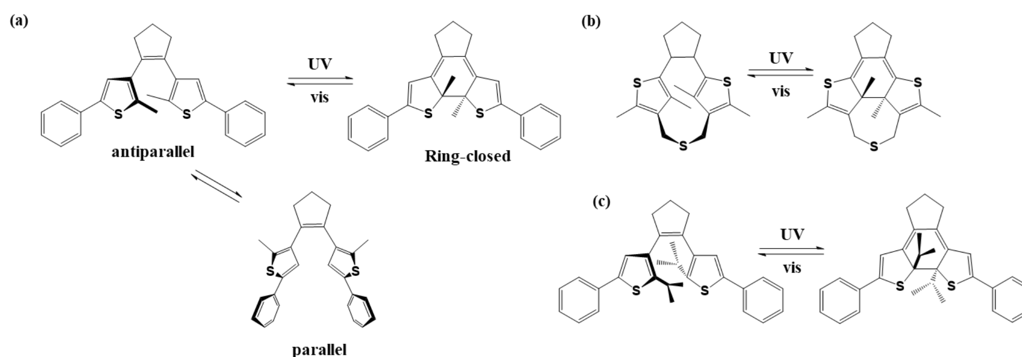

Figure 3-18. (a) Photoisomerization of DAE between ring-open isomer with antiparallel conformation and ring-closed isomers. Reproduced from Ref.[78]

b. Thermal stability

Thermal stability of the ring-closed isomers is one of the most promising advantages for DAE molecules serving as active elements in memory applications, which is controlled by the enthalpy difference between the ring-open and ring-closed isomers in the ground state.[60a] It was demonstrated that such stability is dependent on the aryl groups: (a) aromatic stabilization energy: molecules with thiophene, benzothiophene, or furan heterocycles serving as aryl groups are much stale than those with phenyl, pyrrolyl, or indolyl rings; (b) electron-withdrawing substituents: introduction of electron-withdrawing substituents can weaken the central carbon–carbon bonds in the closed-ring isomers thus decrease its stability; (c) steric hindrance of the substituents at the reactive carbons: bulky substituents can lead to thermal cycloreversion reactions of the closed-ring isomer.[79]

c. Fatigue resistance

Fatigue resistance is another necessary property when applying the molecular switches as functional units in various applications. It has been observed that distinct DAE derivatives have different photochemical side reactions, e.g., oxidation or elimination reactions of the ring-closed isomer. In particular, the formation of an annulated byproduct was considered as the major source of fatigue over the broad range of DAE structures.[80]

A typical example of the absorption spectra of DAE switches during the course of UV irradiation is shown in Figure 3-18. The ring-open isomer possesses a strong absorbance in the UV range. Upon UV irradiation, a new band centered at 522 nm appears that is characteristic for the ring-closed isomer. The band intensity keeps increasing until reaching the photostationary state (PSS). When the sample is further subjected to UV illumination, a slow decrease of the vis absorbance can be observed, accompanied by a small hypochromic shift of the band, indicating the formation of the annulated byproduct. The formation process is initiated by photochemical C−S bond cleavage. Radical migration and bicyclohexane formation lead to the condensed-ring byproduct. The byproduct formation process is not reversible, thus leading to a significant loss of photochromic material after repeating such illumination cycle for several times (Figure 3-19c). To improve the fatigue resistance and suppress the byproduct formation, strategies have been proposed like introduction of strong acceptor groups (CF_3

and SF_5) on the adjacent phenyl rings.[81] Figure 3-19d shows the absorbance evolution of DAE molecule with SF_5 group, which shows a high fatigue resistance. Another strategy is to introduce acetyl groups at 6- and 6′-positions, which are considered to suppress the photochemical C−S bond cleavage and the radical migration.[82]

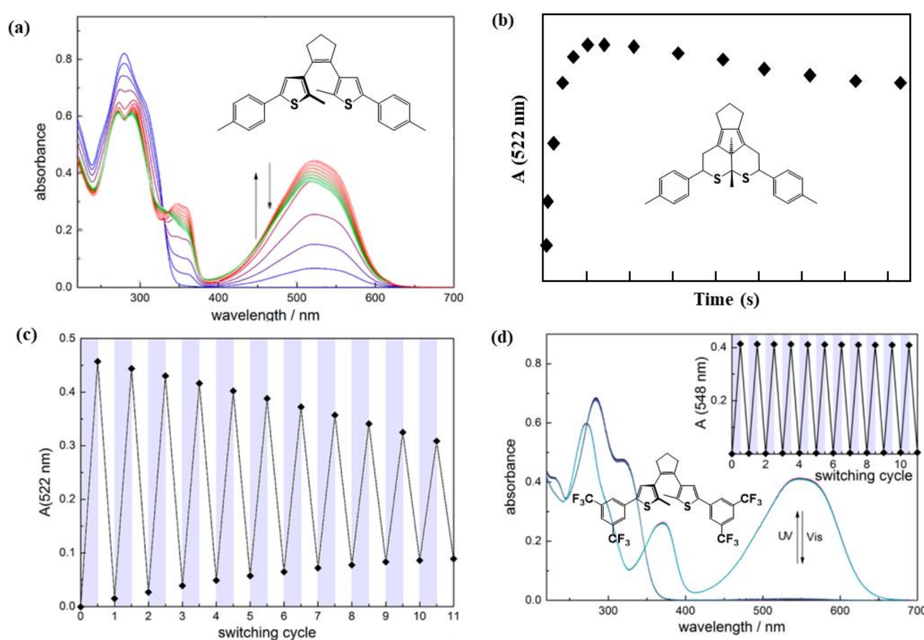

Figure 3-19. (a) Absorption spectra of DAE molecules during the course of UV irradiation, from blue to red: initial to PSS; from red to green: further irradiation after reaching PSS. (b) Evolution of absorbance at the vis range with UV irradiation time. (c) Evolution of absorbance at the vis range during repetitive UV/vis switching cycles with a low fatigue resistance. (d) Evolution of absorbance at vis range of DAE molecule with SF_5 group during repetitive UV/vis switching cycles with a high fatigue resistance. Reproduced from Ref.[81a]

d. Modulating the charge transport in semiconductors via energy-level phototuning

One of the most important and special features of DAE molecules is their phototunable energy levels, which means that when irradiated with UV/vis light, the molecules can switch between their ring-open and ring-closed isomers, accompanied with a switch of their corresponding HOMO/LUMO energy level. This phenomenon may be explained as the number of double bonds in the open form is larger than that in the closed form, thus the energy of HOMO in the open form is expected to be lower than that of the closed form. In the ring-open form, the conjugation is localized on the heteroaromatic rings. While in the ring-closed form the molecule belongs to a conjugated system, whose HOMO and LUMO orbitals

are essentially delocalized π orbitals extending over the whole backbone of the molecule, therefore the HOMO-LUMO gap is significantly smaller after the switching.[83] Such characteristic allows the molecules to induce different trapping behavior when they are combined with semiconducting materials with suitable energy levels. In particular, for p-type semiconductor, if the HOMO level of the DAE molecule in one form is higher than its VB and the other form is lower, the molecule will act as a trap for holes in one form and not the other. Conversely, for n-type semiconductor, tunable LUMO levels can make a molecule switch from scattering center to charge trap for electrons. This effect can be exploited to modulate the charge carrier transport of a semiconductor upon irradiation at the defined

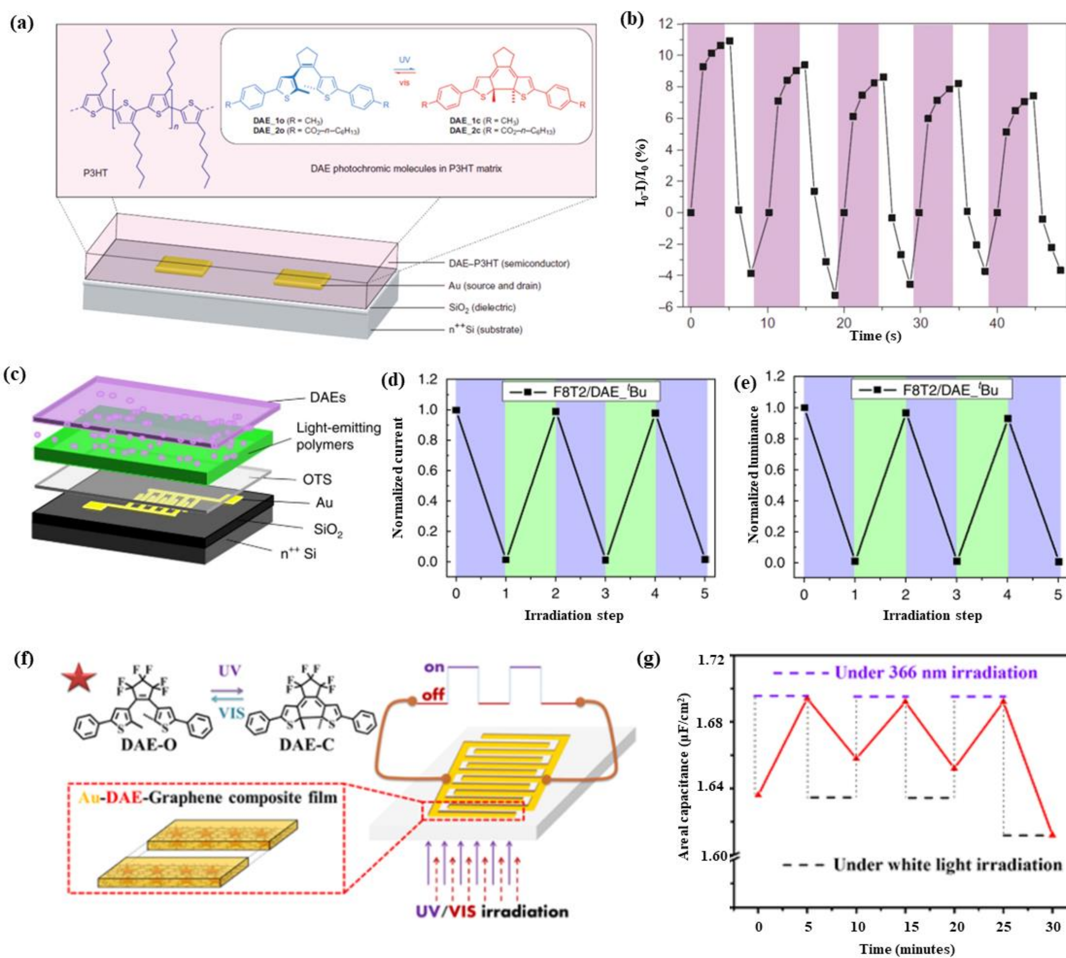

wavelengths.

Figure 3-20. (a) Schematic illustration of the optically switchable OTFT based on P_3HT and DAE. (b) Dynamic switching of an OTFT under several UV/vis irradiation cycles. Reproduced from Ref.[84] (c) Schematic illustration of the optically switchable OSOLET based on light-emitting polymers with DAE. (d) and (e) Reversible modulation of OSOLET (d) current, (e) luminance during UV/vis irradiation cycles. Reproduced from Ref.[85] (f)

Schematic illustration of optically switchable micro-supercapacitor based on DAE-graphene composite film. (g) Switching behavior of DAE−graphene micro-supercapacitor by alternating UV/vis irradiation. Reproduced from Ref.[86]

Such mechanism was first realized by using blends of DAEs with a polymeric semiconductor P_3HT acting the electroactive material to fabricate optically switchable organic thin-film transistors (OTFTs).[84] The dual functionality in these OTFTs was achieved by engineering the energy levels of the blend through the insertion of the DAE phototunable energy levels in the polymer matrix. As shown in Figure 3-20a and b, a dynamic control of the output current of the device could be achieved by UV/vis irradiation in a reversible manner without significant fatigue for several irradiation cycles. To go a step further, optically switchable organic light-emitting transistors (OSOLETs) can be fabricated by integrating DAEs into the light-emitting semiconducting layer of organic light-emitting diode (Figure 3-20c-e). Both output current and electroluminescence can be simultaneously modulated by irradiating the devices at distinct wavelengths. Another example was the fabrication of photoswitchable micro-supercapacitor based on a DAE-graphene composite film (Figure 3-20f and g).[86] The light-responsive CV curves showed that the total capacitance increased under UV irradiation, recovered to original value under white light irradiation, and could be modulated for several cycles alternating light irradiation.

3.2.1.4. Dihydroazulenes

DHA molecules were investigated for the first time by Daub and co-workers in the 1980s.[87] They can undergo a 10-electron retro-electro-cyclization to vinylheptafulvene (VHF) isomer by UV irradiation. The initial VHF isomer in its s-cis-conformation is metastable and will convert into its more stable s-trans-conformer. The VFH can in turn, back to DHA by a thermally induced cyclization.[88] The ring-opening reaction from DHA to VHF occurs with a high quantum yield and is accompanied with significant changes in the physical properties, such as dipole-moment, emission and absorption spectra. The DHA exhibits a characteristic absorption band around 350 nm while the VHF has a more intense absorption band around 470 nm. Furthermore, the DHA is usually fluorescent while VHF is generally non-fluorescent because of a radiation-less deactivation of the excited state.

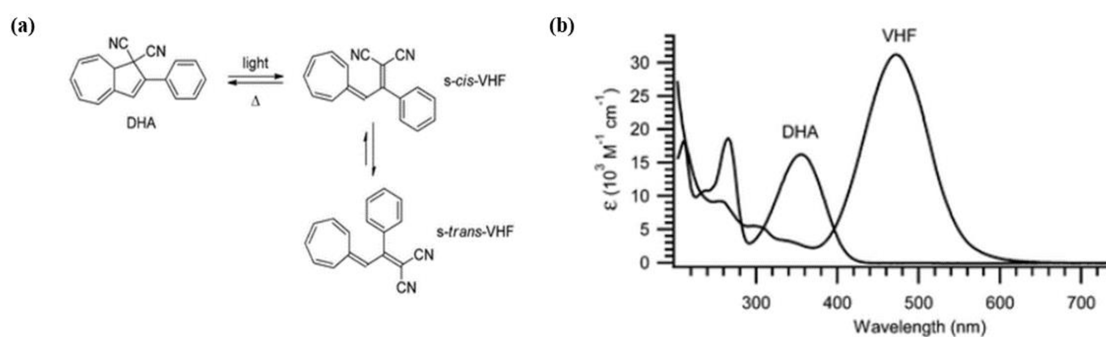

Figure 3-21. (a) Photoisomerization between ring-closed DHA and ring-open VHF forms. Reproduced from Ref.[89] (b) UV/vis absorption spectra of DHA and VHF isomers. Reproduced from Ref.[90]

3.2.2. Ferroelectric materials

Ferroelectric materials were first discovered in 1920 in the form of bulk single crystals of Rochell salt.[91] They belong to the broad family of dielectrics that have spontaneous stable polarization states switchable by application of a sufficient external electric field.

The term "ferroelectricity" stems from the "ferromagnetism", which is used to describe magnetic materials when measuring the magnetization of a ferromagnet as a function of magnetic field. Similarly, ferroelectricity is the characteristic of ferroelectric materials when measuring the electric polarization as a function of electric field.

When most materials are polarized with an electric field E, the polarization P induced is almost exactly proportional to the E, resulting in a linear function. While for ferroelectric material, its polarization does not vary with the electric field in a linear way. It has a remnant polarization P_r even when the applied electric field is zero. Such ferroelectric polarization originates from the alignment of dipoles inside the material and is bistable, i.e., when the direction of the applied electric field is reversed, orientation of the dipole moment will also inverse, giving rise to a ferroelectric hysteresis loop.

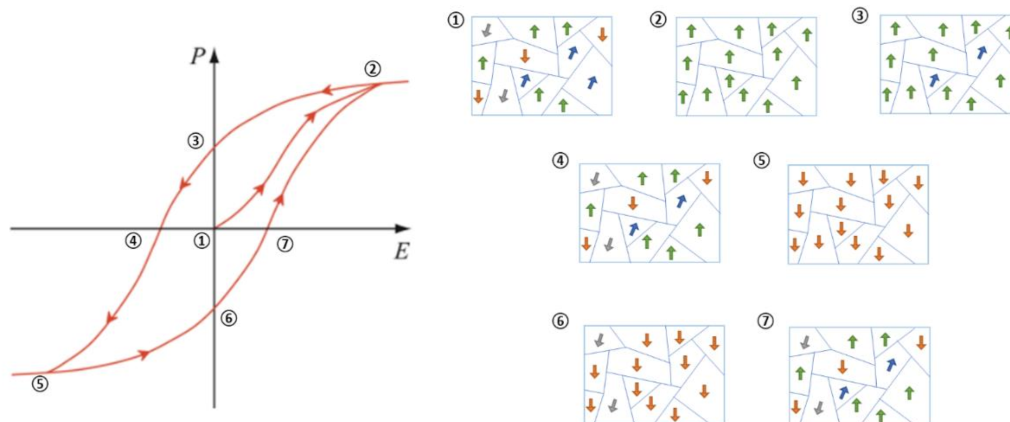

Figure 3-22. A typical example of ferroelectric hysteresis loop, right images are schematized ferroelectric material with defined orientation of the ferroelectric domains at different polarization states.

A typical example of ferroelectric hysteresis loop is shown in Figure 3-22. Starting from the original state ①, the ferroelectric material can be schematized by crystallites that form various ferroelectric

domains. The intrinsic polarization is represented by arrows oriented in random directions. When the material is poled by an increasing electric field E, the polarization P increases, and the dipoles are generally aligned. At higher E, P goes into saturation until all the dipoles are aligned into one direction, corresponding to sate ②. The extrapolation of this high-field regime to zero field yields the saturation polarization P_{sat}. Once the electric field is reduced to zero, the material shows a remnant polarization P_r at state ③, at the intersections with the P-axis. Then, under application of an opposite electric field, the polarization reduces until reaching zero at the negative coercive field $-E_c$ at state ④. E_c is determined at the intersections with the E-axis, which is the minimum value of the electric field that must be applied in order to switch the full saturated polarization. When E keeps increasing in the negative direction, the material finally gets into saturation at the opposite polarization $-P_{sat}$ at state ⑤, with the dipoles aligned to the opposite direction. Reducing the electric field from negative direction to zero, the material shows an opposite remnant polarization -Pr at state ⑥. Then under application of a positive electric field from zero to positive coercive field E_c, the polarization decreased to zero at state ⑦.

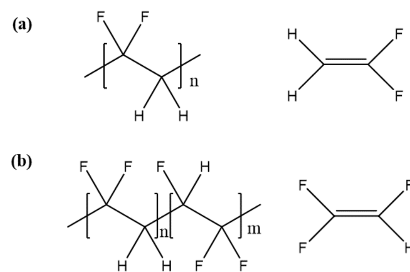

Figure 3-23. (a) Chemical structure of PVDF and its monomer. (b) Chemical structure of P(VDF-TrFE) and the monomer of TrFE.

The instability of the polar structure is a necessity for a material to be ferroelectric. Polyvinylidene fluoride (PVDF) is one of the most representative ferroelectric materials, with the monomer unit of CH_2CF_2 (Figure 3-23a). Its ferroelectricity originates from the electropositive hydrogen atoms and electronegative fluorine atoms, which forms a polar band with the main chain carbon. The monomer is semi-crystalline in nature, half-crystalline and half-amorphous. Its structure is intermediated between polyethylene $-CH_2-CH_2-$ and polytetrafluoroethylene $-CF_2-CF_2-$ and hence gives both high flexibility like polyethylene and also the stereochemical constraints of polytetrafluoroethylene. The orientation of

the dipole is controlled by the molecular conformation and can form at least four different crystalline phases (Figure 3-24): α (or form II), β (form I), γ (form III), and δ (form IV).[92] The α phase possesses a trans-gauche-trans-gauche (TGTG; T-trans, G-gauche)) conformation, in which the F and H substituents are at 180 ° and at ± 60 ° alternatively. The absence of steric strains between the F molecules makes it the lowest potential energy state among the four polymorphs. The dipole moment in this state is arranged antiparallelly within a single unit cell so that each dipole is neutralized by its neighbor that is oriented in the opposite direction. Therefore, α phase the most stable while non ferroelectric. The β phase has an all-trans planar zigzag conformation, with all the F and H molecules aligned in the same direction perpendicular to the carbon backbone. Therefore, the β phase owns the largest spontaneous polarization among all the phases.[93] Since the direction of the polarization can be switched according to the direction of the external electric field, the β phase is responsible for the ferroelectricity of the PVDF. The γ phase is in the intermediate T3GT3G' conformation, with weaker polarization compared with the β phase.[94] The δ phase is the parallel version of the α phase, which can be obtained by poling α phase under a high electric field.[95] The γ phase and δ phase are also polar, while their spontaneous polarization is only half that of the β phase.

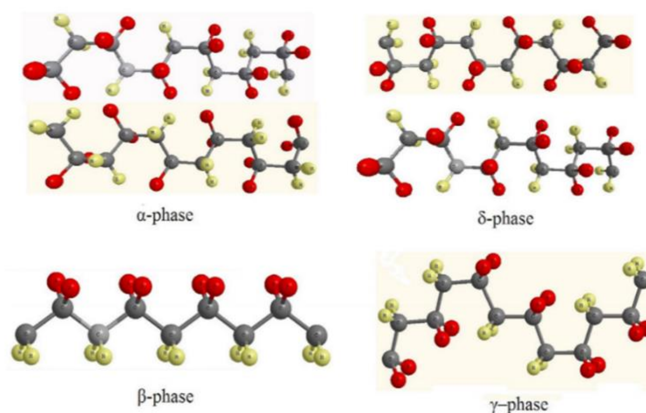

Figure 3-24. Chain conformations of the α, β, γ and δ phases of PVDF. Produced from Ref.[96]

In order to exploit the ferroelectricity of the PVDF, the polar β phase is the most desirable, while thin PVDF films processed directly from the melt or from the solution is mostly the non-polar α-phase due to its thermodynamic stability.[97] Therefore, a lot of efforts have been devoted to explore effective ways

for inducing piezoelectric β phases. One of the most common methods is to mechanically stretch the α-phase films at a suitable temperature.[98] By stretching the PVDF film, the polymer chains can be aligned into an all-trans planar zigzag conformation, the crystals with β phase is therefore induced.[99] Another method is by crystallization from polar solvents like N,N-dimethylformamide (DMF) or N,N-dimethyl acetamide (DMAc).

In 1968 Lando and Doll suggested that the introduction of a small amount of trifluoroethylene (TrFE) into PVDF to form a copolymer poly(vinylidene fluoride trifluoroethylene (P(VDF-TrFE)) can induce direct crystallization of the material into the polar β phase by melting or solvent casting.[100] The structure of the copolymer P(VDF-TrFE) with the monomer unit of $(CH_2CF_2)_n$-$(CHFCF_2)_m$ is illustrated in Figure 3-23b. Because of the similar size of the hydrogen and fluorine atoms, VDF and TrFE units are randomly distributed along the main carbon chain, allowing for the formation of the all-trans conformation in analogous with the PVDF in β phase.[101] Moreover, the interchain distance in the β phase is slightly larger than that of pure PVDF, therefore it is easier for the dipole rotation around the carbon backbone for the copolymer.

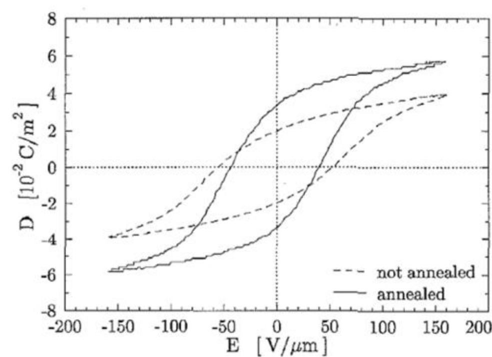

Figure 3-25. Hysteresis loops of a 56/44 mol% PVDF-TRFE copolymer film as prepared and after annealing. Reproduced from Ref.[102]

One important parameter for PVDF-based materials is the Curie temperature, T_C, that marks the transition of the material from the ferroelectric phase to the paraelectric phase and vice versa. Above T_C the material will be paraelectric and lose their permanent ferroelectricity, i.e., the dipoles are randomly oriented. Note that the Curie temperature is absent in pure PVDF because it melts before the phase transition.

Another classification of P(VDF-TrFE) copolymers was introduced to describe the crystal phase, the low-temperature (LT) phase with all-trans conformation, similar to PVDF β-phase, the high-temperature (HT) phase with TGTG conformation similar to PVDF α-phase, and the cooled (CL) phase similar to PVDF γ-phase.[103] The material can undergo phase transition between each other if it is annealed, stretched or poled. The LT phase transforms into the HT phase via the CL phase during heating above the Curie temperature, and the HT phase then transforms into the CL phase during the cooling process. The CL phase can be converted into the more regular LT phase by stretching or by applying an electric field at room temperature.[104] Therefore it is proposed that when the copolymer P(VDF-TrFE) is annealed at a temperature between the T_C and T_M (the melting temperature), there occurs an enhanced β-phase fraction and further crystallization of the material.[105] Consequently, their ferroelectric response can be enhanced after annealing. Figure 3-25 shows the comparison of the hysteresis loop of a 56/44 mol% PVDF-TRFE copolymer film as prepared by spin coating from dimethylformamide and after annealing, which clearly demonstrates that the annealing induces higher crystallinity and thus larger remnant polarization of the sample.[102] Compared with pure PVDF, the preferential formation of β-phase of the copolymer P(VDF-TrFE) give them a broader variety of applications in electroactive applications. Note that the copolymer can afford a crystallinity reaching 90% while the value for PVDF is around 50%. Therefore, larger polarization is expected in the copolymer P(VDF-TrFE).[106]

Due to its intrinsic ferroelectric and piezoelectric characteristics, robust chemical resistance and high thermal stability, P(VDF-TrFE) is appealing for applications like memories, wearable electronics, and pressure sensors. One of the simplest types of ferroelectric memories is the thin-film metal-ferroelectric-metal capacitor, in which information is stored by aligning the direction of the internal polarization either in the upward or downward direction and can be retrieved by applying a bias voltage to obtain a higher or a lower charge displacement. Figure 3-26a illustrates the external poling of a P(VDF-TrFE) based capacitor.[107] The vertical poling was achieved by the application of an external electric field on a top electrode on top of a spin-coated P(VDF-TrFE) film, while lateral poling was achieved by depositing Al strips on top. Figure 3-25c shows the C-V curves from three capacitors with the same

thickness of the P(VDF-TrFE) film but different poling conditions: vertical-poled, lateral-poled, and unpoled. The curve exhibits a hysteresis with butterfly loops due to polarization reversal, indicating the change of capacitance from an accumulation state to an inversion state. The vertical-poled device possesses the highest value of capacitance, followed by unpoled and lateral-poled films, demonstrating that the polarization orientation in the ferroelectric layer directly impacts capacitor performance.

Apart from capacitors, metal-insulator-semiconductor diodes is another type of two-terminal device, whose capacitance can be changed via accumulating, depleting, and inverting charges at the interface of semiconductor and the dielectric by sweeping the bias voltage. Figure 3-26d displays the representative C-V curves of pentacene diodes with different dielectric materials: nonferroelectric PMMA and P(VDF-TrFE).[108] No hysteresis is observed when PMMA is used as the dielectric layer, while a clockwise direction of hysteresis in the P(VDF-TrFE) based diode, indicative of the ferroelectric polarization.

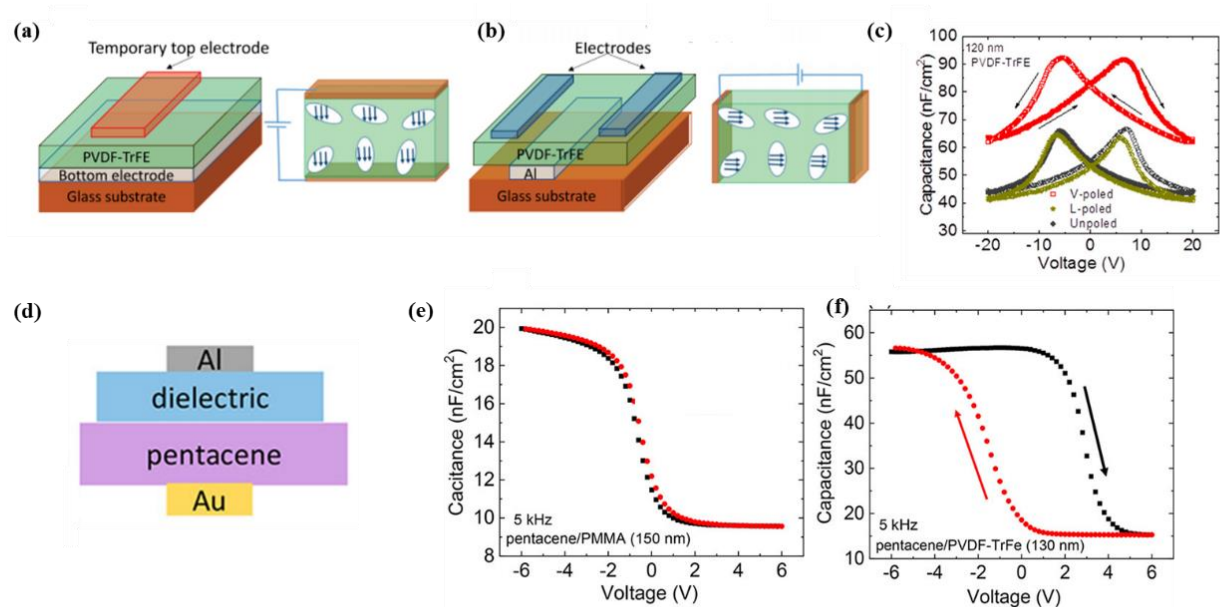

Figure 3-26: a, b) Schematic of vertical (a) and lateral (b) poling of P(VDF-TrFE), respectively. (c) C-V curves for vertical-poled, lateral-poled, and unpoled P(VDF-TrFE) films. Reproduced from Ref.[107] (d) Schematic of metal-insulator-pentacene diodes. e, f) C-V curves from pentacene diodes with PMMA (e) and P(VDF-TrFE) (f) dielectric layers. Reproduced from Ref.[108]

Great interest has been given to organic ferroelectric field-effect transistors (FeFETs) because of their nondestructive readout, rewritability and low power consumption. In a conventional FET, the

conducting channel is in contact with the gate dielectric layer, so that the surface characteristics of the gate dielectric crucially influence its charge carrier transport. When the gate dielectric is ferroelectric, the polarization field can either accumulate or deplete charge carriers in the conducting channel, resulting in resistive nonvolatile memory properties for information storage and charge sensing. In 2012, Cheolmin Park et al. reported a flexible nonvolatile FeFET device based on P_3HT (Figure 3-26a).[109] The transfer characteristic of the device shows current hysteresis arising from the ferroelectric polarization of the PVDF-TrFE layer (Figure 3-26b). To study the memory retention, the writing voltage was applied to the gate, the the source-train current was recorded as a function of time. Finally, the device shows highly reliable data retention up to approximately 10^5 s (Figure 3-25c). Moreover, multiple data write/erase endurance measurements were launched, and consistent rewritable cycles were observed over 100 cycles, as shown in Figure 3-26d.

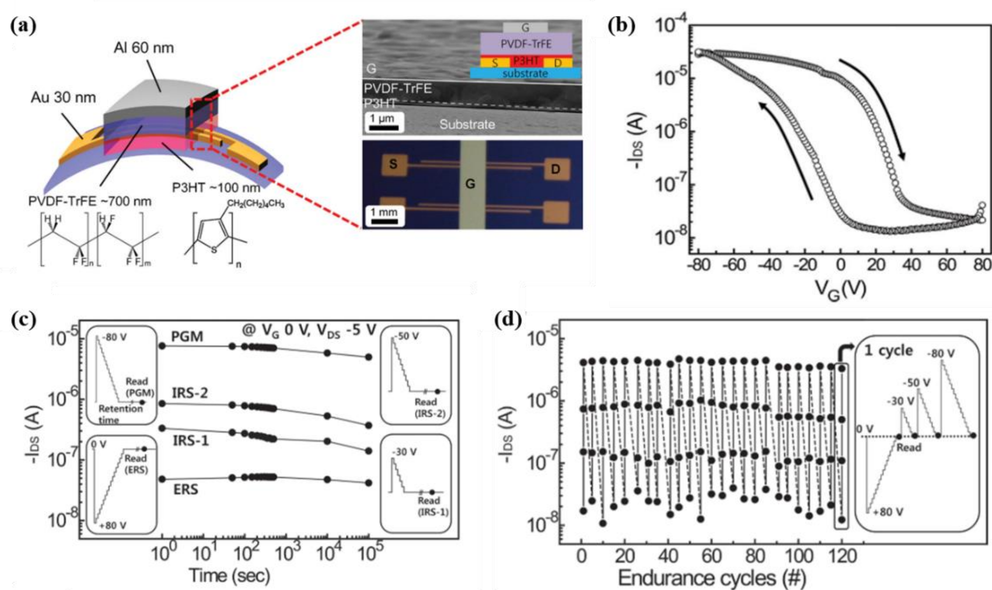

Figure 3-26: (a) Schematic illustration of the FeFET device with a P_3HT channel and P(VDF-TrFE) insulator. (b) Transfer curve of the device with hysteresis characteristic. (c) retention characteristics and (d) multiple write/erase endurance cycles in FeFET. Reproduced from Ref.[109]

The integration of 2DMs with ferroelectric materials has also been investigated. Figure 3-27a shows a typical example of FeFET using P(VDF-TrFE) as the top gate and MoS_2 as the channel material. Its transfer curve in top-gate configuration shows a large memory window which confirms the ferroelectric polarization switching process.[110] While the transfer curve in back-gate configuration with SiO_2

serving as the dielectric only shows a small hysteresis which is due to the surface adsorbates like water and oxygen molecules. The stable remnant polarization of P(VDF-TrFE) can provide an ultrahigh local electrostatic field in the MoS_2 channel. Based on the polarization direction of P(VDF-TrFE): without polarization (P_{fresh}), upward polarization (P_{up}), and downward polarization (P_{down}), the device can in turn achieve three different current levels. The P_{up} state corresponds to a depletion of the charge carriers in the channel, which shows the lowest current value compared with the other two states. On the countary, the P_{down} state corresponds to the accumulation of carriers in the MoS_2 channel, thereof possesses the highest current value. The photoresponse at 635 nm of the device is then compared for these three states. As shown in Figure 3-27d, the photoresponse is very small in both P_{fresh} and P_{down} state. While in the P_{up} state, a significant photoresponse can be observed, which can be explained as the photogenerated current dominants the channel current, resulting in a high-efficient photocurrent extraction, and ensuring their application as photodetectors with high detectivity. Apart from photodetectors, FeFET based on 2DMs can also be applied in memory applications. The memory switching current dynamics and the retention properties of a typical MoS_2 FeFET is displayed in Figure 3-27c and d.[111] When periodic positive or negative top-gate voltage bias is applied to the device, the P(VDF-TrFE) layer is efficiently switched, and very clear current dynamic responses with nearly constant ratios of more than 10^4 is observed. The retention properties of the two states are measured by recording the current after the top-gate bias. In Figure 3-27d, the two distinctive states can maintain for 10 min without serious degradation.

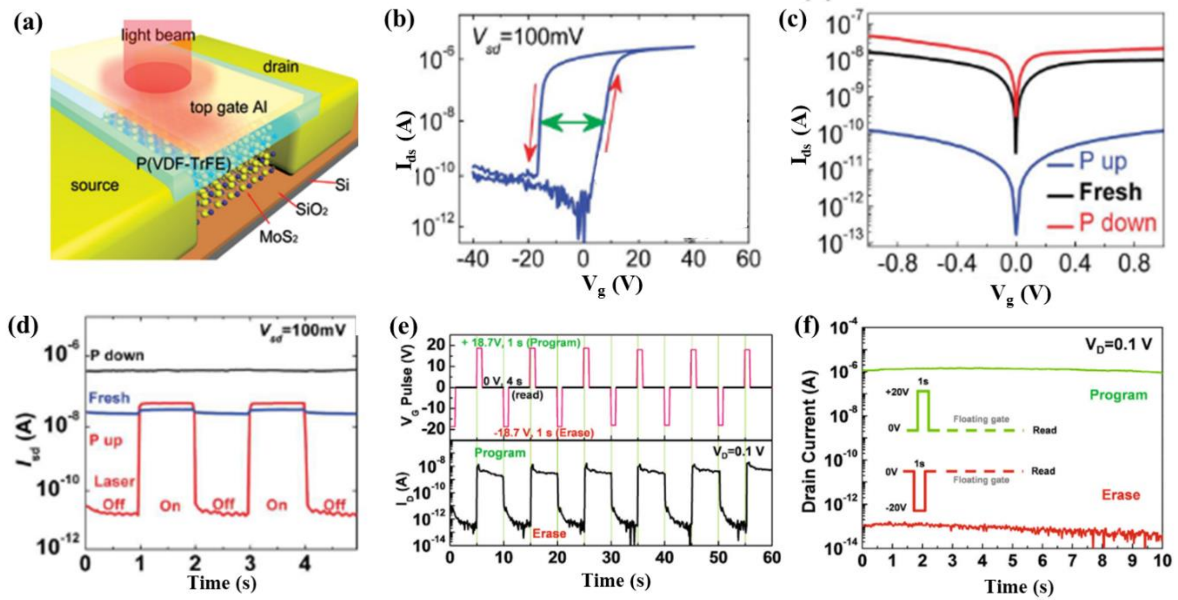

Figure 3-27. (a) Schematic illustration of the MoS_2 FeFET. (b) The transfer characteristic of MoS_2 FeFET in top-gate configuration with P(VDF-TrFE) serving as electrode. The transfer characteristic of the same device in back-gate configuration with SiO_2 serving as dielectric is shown in inset. (c) Output characteristic of the device with three states of ferroelectric layer: P_{fresh}, P_{up}, and P_{down}. (d) Photoresponse of the device with three states of ferroelectric layer. Reproduced from Ref.[110] (e) Current dynamics of the MoS_2 FeFET under periodic top-gate bias. (f) Retention properties of the MoS_2 FeFET at P_{up} and P_{down} states. Reproduced from Ref.[111]

3.3. References

[1] C. P. Bergmann, F. M. Machado, *Carbon nanomaterials as adsorbents for environmental and biological applications*, Springer, **2015**.

[2] M. Chhowalla, D. Jena, H. Zhang, *Nat. Rev. Mater.* **2016**, *1*, 1.

[3] T. N. Theis, P. M. Solomon, *Science* **2010**, *327*, 1600.

[4] a) K. S. Novoselov, A. K. Geim, S. V. Morozov, D. Jiang, Y. Zhang, S. V. Dubonos, I. V. Grigorieva, A. A. Firsov, *Science* **2004**, *306*, 666; b) E. P. Randviir, D. A. Brownson, C. E. Banks, *Mater. Today* **2014**, *17*, 426.

[5] A. K. Geim, K. S. Novoselov, in *Nanoscience and technology: a collection of reviews from nature journals*, World Scientific, **2010**, 11.

[6] L. E. F. Torres, S. Roche, J.-C. Charlier, *Introduction to graphene-based nanomaterials: from electronic structure to quantum transport*, Cambridge University Press, **2020**.

[7] A. H. Castro Neto, F. Guinea, N. M. R. Peres, K. S. Novoselov, A. K. Geim, *RvMP* **2009**, *81*, 109.

[8] R. R. Nair, P. Blake, A. N. Grigorenko, K. S. Novoselov, T. J. Booth, T. Stauber, N. M. R. Peres, A. K. Geim, *Science* **2008**, *320*, 1308.

[9] S. V. Morozov, K. S. Novoselov, M. I. Katsnelson, F. Schedin, D. C. Elias, J. A. Jaszczak, A. K. Geim, *Phys. Rev. Lett.* **2008**, *100*, 016602.

[10] A. A. Balandin, *Nat. Mater.* **2011**, *10*, 569.

[11] C. Lee, X. Wei, J. W. Kysar, J. Hone, *Science* **2008**, *321*, 385.

[12] M. D. Stoller, S. Park, Y. Zhu, J. An, R. Ruoff, *Nano Lett.* **2008**, *8*, 3498.

[13] a) G. Konstantatos, M. Badioli, L. Gaudreau, J. Osmond, M. Bernechea, F. P. G. De Arquer, F. Gatti, F. H. Koppens, *Nat. Nanotechnol.* **2012**, *7*, 363; b) F. Bonaccorso, L. Colombo, G. Yu, M. Stoller, V. Tozzini, A. C. Ferrari, R. S. Ruoff, V. Pellegrini, *Science* **2015**, *347*, 1246501; c) F. Bonaccorso, Z. Sun, T. Hasan, A. C. Ferrari, *Nat. Photonics* **2010**, *4*, 611.

[14] M. Yi, Z. Shen, *J. Mater. Chem. A* **2015**, *3*, 11700.

[15] a) S. A. Ansari, H. Fouad, S. Ansari, M. P. Sk, M. H. Cho, *J. Colloid Interface Sci.* **2017**, *504*, 276; b) E. Gao, S.-Z. Lin, Z. Qin, M. J. Buehler, X.-Q. Feng, Z. Xu, *J. Mech. Phys. Solids* **2018**, *115*, 248.

[16] Y. Hernandez, V. Nicolosi, M. Lotya, F. M. Blighe, Z. Sun, S. De, I. McGovern, B. Holland, M. Byrne, Y. K. Gun'Ko, *Nat. Nanotechnol.* **2008**, *3*, 563.

[17] a) J. Shen, Y. He, J. Wu, C. Gao, K. Keyshar, X. Zhang, Y. Yang, M. Ye, R. Vajtai, J. Lou, *Nano Lett.* **2015**, *15*, 5449; b) J. N. Coleman, M. Lotya, A. O'Neill, S. D. Bergin, P. J. King, U. Khan, K. Young, A. Gaucher, S. De, R. J. Smith, *Science* **2011**, *331*, 568.

[18] U. Khan, A. O'Neill, M. Lotya, S. De, J. N. Coleman, *Small* **2010**, *6*, 864.

[19] R. J. Smith, P. J. King, M. Lotya, C. Wirtz, U. Khan, S. De, A. O'Neill, G. S. Duesberg, J. C. Grunlan, G. Moriarty, J. Chen, J. Wang, A. I. Minett, V. Nicolosi, J. N. Coleman, *Adv. Mater.* **2011**, *23*, 3944.

[20] F. Bonaccorso, Z. Sun, *Opt. Mater, Express* **2014**, *4*, 63.

[21] a) X. Li, W. Cai, J. An, S. Kim, J. Nah, D. Yang, R. Piner, A. Velamakanni, I. Jung, E. Tutuc, S. K. Banerjee, L. Colombo, R. S. Ruoff, *Science* **2009**, *324*, 1312; b) A. Reina, X. Jia, J. Ho, D. Nezich, H. Son, V. Bulovic, M. S. Dresselhaus, J. Kong, *Nano Lett.* **2009**, *9*, 30.

[22] X. Li, C. W. Magnuson, A. Venugopal, J. An, J. W. Suk, B. Han, M. Borysiak, W. Cai, A. Velamakanni, Y. Zhu, *Nano Lett.* **2010**, *10*, 4328.

[23] a) W. Kern, G. L. Schnable, *IEEE Trans. Electron Devices* **1979**, *26*, 647; b) N. Petrone, C. R. Dean, I. Meric, A. M. Van Der Zande, P. Y. Huang, L. Wang, D. Muller, K. L. Shepard, J. Hone, *Nano Lett.* **2012**, *12*, 2751.

[24] D. Badami, *Carbon* **1965**, *3*, 53.

[25] W. A. De Heer, C. Berger, M. Ruan, M. Sprinkle, X. Li, Y. Hu, B. Zhang, J. Hankinson, E. Conrad, *Proc. Natl. Acad. Sci.* **2011**, *108*, 16900.

[26] N. Mishra, J. Boeckl, N. Motta, F. Iacopi, *Phys. Status Solidi A* **2016**, *213*, 2277.

[27] D. Jariwala, V. K. Sangwan, L. J. Lauhon, T. J. Marks, M. C. Hersam, *ACS Nano* **2014**, *8*, 1102.

[28] K. S. Novoselov, D. Jiang, F. Schedin, T. Booth, V. Khotkevich, S. Morozov, A. K. Geim, *Proc. Natl. Acad. Sci.* **2005**, *102*, 10451.

[29] G. Eda, H. Yamaguchi, D. Voiry, T. Fujita, M. Chen, M. Chhowalla, *Nano Lett.* **2011**, *11*, 5111.

[30] Q. H. Wang, K. Kalantar-Zadeh, A. Kis, J. N. Coleman, M. S. Strano, *Nat. Nanotechnol.* **2012**, *7*, 699.

[31] V. Yadav, S. Roy, P. Singh, Z. Khan, A. Jaiswal, *Small* **2019**, *15*, 1803706.

[32] M. Bernardi, M. Palummo, J. C. Grossman, *Nano Lett.* **2013**, *13*, 3664.

[33] a) J. Pak, J. Jang, K. Cho, T. Y. Kim, J. K. Kim, Y. Song, W. K. Hong, M. Min, H. Lee, T. Lee, *Nanoscale* **2015**, *7*, 18780; b) E. H. Cho, W. G. Song, C. J. Park, J. Kim, S. Kim, J. Joo, *Nano Res.* **2015**, *8*, 790.

[34] A. Splendiani, L. Sun, Y. Zhang, T. Li, J. Kim, C.-Y. Chim, G. Galli, F. Wang, *Nano Lett.* **2010**, *10*, 1271.

[35] B. Radisavljevic, A. Radenovic, J. Brivio, V. Giacometti, A. Kis, *Nat. Nanotechnol.* **2011**, *6*, 147.

[36] P. Joensen, R. Frindt, S. R. Morrison, *Mater. Res. Bull.* **1986**, *21*, 457.

[37] Y.-H. Lee, X.-Q. Zhang, W. Zhang, M.-T. Chang, C.-T. Lin, K.-D. Chang, Y.-C. Yu, J. T.-W. Wang, C.-S. Chang, L.-J. Li, T.-W. Lin, *Adv. Mater.* **2012**, *24*, 2320.

[38] H. Ramakrishna Matte, A. Gomathi, A. K. Manna, D. J. Late, R. Datta, S. K. Pati, C. Rao, *Angew. Chem. Int. Ed.* **2010**, *49*, 4059.

[39] C. Zhou, Y. Zhao, S. Raju, Y. Wang, Z. Lin, M. Chan, Y. Chai, *Adv. Funct. Mater.* **2016**, *26*, 4223.

[40] W. Schutte, J. De Boer, F. Jellinek, *J. Solid State Chem.* **1987**, *70*, 207.

[41] Y. Li, K.-A. N. Duerloo, K. Wauson, E. J. Reed, *Nat. Commun.* **2016**, *7*, 1.

[42] M. Naz, T. Hallam, N. C. Berner, N. McEvoy, R. Gatensby, J. B. McManus, Z. Akhter, G. S. Duesberg, *ACS Appl. Mater. Interfaces* **2016**, *8*, 31442.

[43] A. P. Nayak, T. Pandey, D. Voiry, J. Liu, S. T. Moran, A. Sharma, C. Tan, C.-H. Chen, L.-J. Li, M. Chhowalla, *Nano Lett.* **2015**, *15*, 346.

[44] W. Liu, J. Kang, D. Sarkar, Y. Khatami, D. Jena, K. Banerjee, *Nano Lett.* **2013**, *13*, 1983.

[45] H. Fang, S. Chuang, T. C. Chang, K. Takei, T. Takahashi, A. Javey, *Nano Lett.* **2012**, *12*, 3788.

[46] A. Kumar, P. Ahluwalia, *Eur. Phys. J. B* **2012**, *85*, 1.

[47] B. W. Baugher, H. O. Churchill, Y. Yang, P. Jarillo-Herrero, *Nat. Nanotechnol.* **2014**, *9*, 262.

[48] V. Podzorov, M. Gershenson, C. Kloc, R. Zeis, E. Bucher, *Appl. Phys. Lett.* **2004**, *84*, 3301.

[49] L. Li, Y. Yu, G. J. Ye, Q. Ge, X. Ou, H. Wu, D. Feng, X. H. Chen, Y. Zhang, *Nat. Nanotechnol.* **2014**, *9*, 372.

[50] H. Asahina, K. Shindo, A. Morita, *J. Phys. Soc. Jpn.* **1982**, *51*, 1193.

[51] Y. Cai, G. Zhang, Y.-W. Zhang, *Sci. Rep.* **2014**, *4*, 6677.

[52] a) J. Wu, G. K. W. Koon, D. Xiang, C. Han, C. T. Toh, E. S. Kulkarni, I. Verzhbitskiy, A. Carvalho, A. S. Rodin, S. P. Koenig, *ACS Nano* **2015**, *9*, 8070; b) Q. Guo, A. Pospischil, M. Bhuiyan, H. Jiang, H. Tian, D. Farmer, B. Deng, C. Li, S.-J. Han, H. Wang, *Nano Lett.* **2016**, *16*, 4648.

[53] L. Li, Y. Yu, G. J. Ye, Q. Ge, X. Ou, H. Wu, D. Feng, X. H. Chen, Y. Zhang, *Nat. Nanotechnol.* **2014**, *9*, 372.

[54] Q. Zhou, Q. Chen, Y. Tong, J. Wang, *Angew. Chem. Int. Ed.* **2016**, *55*, 11437.

[55] A. Avsar, I. J. Vera-Marun, J. Y. Tan, K. Watanabe, T. Taniguchi, A. H. Castro Neto, B. Ozyilmaz, *ACS Nano* **2015**, *9*, 4138.

[56] J. Pei, X. Gai, J. Yang, X. Wang, Z. Yu, D.-Y. Choi, B. Luther-Davies, Y. Lu, *Nat. Commun.* **2016**, *7*, 10450.

[57] C. R. Ryder, J. D. Wood, S. A. Wells, Y. Yang, D. Jariwala, T. J. Marks, G. C. Schatz, M. C. Hersam, *Nat. Chem.* **2016**, *8*, 597.

[58] T. M. Cardozo, A. l. J. Aquino, M. Barbatti, I. Borges Jr, H. Lischka, *J. Phys. Chem. A* **2015**, *119*, 1787.

[59] H. Tian, S. Yang, *Chem. Soc. Rev.* **2004**, *33*, 85.

[60] a) M. Irie, *Chem. Rev.* **2000**, *100*, 1685; b) F. M. Raymo, M. Tomasulo, *Chem. Soc. Rev.* **2005**, *34*, 327.

[61] G. S. Hartley, *Nature* **1937**, *140*, 281.

[62] H. M. D. Bandara, S. C. Burdette, *Chem. Soc. Rev.* **2012**, *41*, 1809.

[63] H. Fliegl, A. Köhn, C. Hättig, R. Ahlrichs, *J. Am. Chem. Soc.* **2003**, *125*, 9821.
[64] A. A. Beharry, G. A. Woolley, *Chem. Soc. Rev.* **2011**, *40*, 4422.
[65] N. Crivillers, E. Orgiu, F. Reinders, M. Mayor, P. Samorì, *Adv. Mater.* **2011**, *23*, 1447.
[66] S. Seo, M. Min, S. M. Lee, H. Lee, *Nat. Commun.* **2013**, *4*, 1920.
[67] Y. Zhao, S. Bertolazzi, P. Samorì, *ACS Nano* **2019**, *13*, 4814.
[68] R. Klajn, *Chem. Soc. Rev.* **2014**, *43*, 148.
[69] L. Kortekaas, J. Chen, D. Jacquemin, W. Browne, *J. Phys. Chem. B* **2018**, *122*, 6423.
[70] M. Schulz-Senft, P. J. Gates, F. D. Sönnichsen, A. Staubitz, *Dyes Pigm.* **2017**, *136*, 292.
[71] M. Levitus, G. Glasser, D. Neher, P. F. Aramendía, *Chem. Phys. Lett.* **1997**, *277*, 118.
[72] H. Gruler, R. Vilanove, F. Rondelez, *Phys. Rev. Lett.* **1980**, *44*, 590.
[73] Y. Li, H. Zhang, C. Qi, X. Guo, *J. Mater. Chem.* **2012**, *22*, 4261.
[74] Y. Ishiguro, R. Hayakawa, T. Chikyow, Y. Wakayama, *J. Mater. Chem. C* **2013**, *1*, 3012.
[75] M. Gobbi, S. Bonacchi, J. X. Lian, A. Vercouter, S. Bertolazzi, B. Zyska, M. Timpel, R. Tatti, Y. Olivier, S. Hecht, M. V. Nardi, D. Beljonne, E. Orgiu, P. Samorì, *Nat. Commun.* **2018**, *9*, 2661.
[76] M. Irie, M. Mohri, *J. Org. Chem.* **1988**, *53*, 803.
[77] K. Uchida, E. Tsuchida, Y. Aoi, S. Nakamura, M. Irie, *Chem. Lett.* **1999**, *28*, 63.
[78] M. Takeshita, M. Nagai, T. Yamato, *Chem. Commun.* **2003**, 1496.
[79] D. Kitagawa, K. Sasaki, S. Kobatake, *Bull. Chem. Soc. Jpn.* **2011**, *84*, 141.
[80] M. Irie, T. Lifka, K. Uchida, S. Kobatake, Y. Shindo, *Chem. Commun.* **1999**, 747.
[81] a) M. Herder, B. M. Schmidt, L. Grubert, M. Pätzel, J. Schwarz, S. Hecht, *J. Am. Chem. Soc.* **2015**, *137*, 2738; b) W. A. Sheppard, *J. Am. Chem. Soc.* **1962**, *84*, 3072.
[82] M. Irie, T. Fukaminato, K. Matsuda, S. Kobatake, *Chem. Rev.* **2014**, *114*, 12174.
[83] G. l. Reecht, C. Lotze, D. Sysoiev, T. Huhn, K. J. Franke, *ACS Nano* **2016**, *10*, 10555.
[84] E. Orgiu, N. Crivillers, M. Herder, L. Grubert, M. Pätzel, J. Frisch, E. Pavlica, D. T. Duong, G. Bratina, A. Salleo, N. Koch, S. Hecht, P. Samorì, *Nat. Chem.* **2012**, *4*, 675.
[85] L. Hou, X. Zhang, G. F. Cotella, G. Carnicella, M. Herder, B. M. Schmidt, M. Pätzel, S. Hecht, F. Cacialli, P. Samorì, *Nat. Nanotechnol.* **2019**.
[86] Z. Liu, H. I. Wang, A. Narita, Q. Chen, Z. Mics, D. Turchinovich, M. Kläui, M. Bonn, K. Müllen, *J. Am. Chem. Soc.* **2017**, *139*, 9443.
[87] J. Daub, T. Knöchel, A. Mannschreck, *Angew. Chem. Int. Ed.* **1984**, *23*, 960.
[88] M. Abedi, M. Pápai, K. V. Mikkelsen, N. E. Henriksen, K. B. Møller, *J. Phys. Chem. Lett.* **2019**, *10*, 3944.
[89] S. L. Broman, M. B. Nielsen, *Phys. Chem. Chem. Phys.* **2014**, *16*, 21172.
[90] S. Broman, S. Brand, C. Parker, *Arkivoc* **2011**, *9*, 51.
[91] J. Valasek, *Phys. Rev.* **1921**, *17*, 475.

[92] E. Kabir, M. Khatun, L. Nasrin, M. J. Raihan, M. Rahman, *J. Phys. D: Appl. Phys* **2017**, *50*, 163002.

[93] a) S. Chen, K. Yao, F. E. H. Tay, C. L. Liow, *J. Appl. Phys.* **2007**, *102*, 104108; b) P. Martins, C. M. Costa, M. Benelmekki, G. Botelho, S. Lanceros-Mendez, *CrystEngComm* **2012**, *14*, 2807.

[94] A. J. Lovinger, *Macromolecules* **1981**, *14*, 322.

[95] M. Li, I. Katsouras, K. Asadi, P. W. M. Blom, D. M. d. Leeuw, *Appl. Phys. Lett.* **2013**, *103*, 072903.

[96] E. Kabir, M. Khatun, L. Nasrin, M. J. Raihan, M. Rahman, *Journal of Physics D: Applied Physics* **2017**, *50*, 163002.

[97] R. G. Kepler, R. Anderson, *Adv. Phys.* **1992**, *41*, 1.

[98] P. Sajkiewicz, A. Wasiak, Z. Gocłowski, *Eur. Polym. J.* **1999**, *35*, 423.

[99] V. Sencadas, M. V. Moreira, S. Lanceros-Méndez, A. S. Pouzada, R. Gregório Filho, "α-to β Transformation on PVDF Films Obtained by Uniaxial Stretch" *Mater. Sci. Forum* **2006**.

[100] J. Lando, W. Doll, *J. Macromol. Sci., B2* **1968**, *2*, 205.

[101] a) B. Ameduri, *Chem. Rev.* **2009**, *109*, 6632; b) A. J. Lovinger, G. Davis, T. Furukawa, M. Broadhurst, *Macromolecules* **1982**, *15*, 323.

[102] B. Ploss, *IEEE Transactions on. IEEE Trans.* **1998**, *5*, 91.

[103] a) K. Tashiro, K. Takano, M. Kobayashi, Y. Chatani, H. Tadokoro, *Ferroelectrics* **1984**, *57*, 297; b) K. Tashiro, Y. Abe, M. Kobayashi, *Ferroelectrics* **1995**, *171*, 281.

[104] a) D. E. S. Arifin, J.-J. Ruan, "Study on the curie transition of P(VDF-TrFE) copolymer" *Mater. Sci. Eng.* **2018**; b) T. Soulestin, V. Ladmiral, F. D. Dos Santos, B. Ameduri, *Prog. Polym. Sci.* **2017**, *72*, 16.

[105] K. Koga, H. Ohigashi, *J. Appl. Phys.* **1986**, *59*, 2142.

[106] T. Furukawa, *Phase Transitions* **1989**, *18*, 143.

[107] A. Laudari, A. Mazza, A. Daykin, S. Khanra, K. Ghosh, F. Cummings, T. Muller, P. Miceli, S. Guha, *Phys. Rev. Appl.* **2018**, *10*, 014011.

[108] A. Laudari, J. Barron, A. Pickett, S. Guha, *ACS Appl. Mater. Interfaces* **2020**, *12*, 26757.

[109] S. K. Hwang, I. Bae, R. H. Kim, C. Park, *Adv. Mater.* **2012**, *24*, 5910.

[110] X. Wang, P. Wang, J. Wang, W. Hu, X. Zhou, N. Guo, H. Huang, S. Sun, H. Shen, T. Lin, M. Tang, L. Liao, A. Jiang, J. Sun, X. Meng, X. Chen, W. Lu, J. Chu, *Adv. Mater.* **2015**, *27*, 6575.

[111] Y. T. Lee, D. K. Hwang, S. Im, *J. Korean Phys. Soc.* **2015**, *67*, 1499.

Chapter 4 Experimental techniques

4.1. Device fabrication

4.1.1. Substrate preparation

4.1.1.1. Si/SiO_2 substrates

Si/SiO_2 substrates used for the fabrication of field-effect transistors were purchased from IPMS Fraunhofer Institute. These n doped Si were covered by a thermally grown SiO_2 as gate dielectric. Note that the substrates were treated with hexamethyldisilazane and covered with a layer of photoresist to provide protection during the wafer dicing process. The as-received substrates were first rinsed with acetone to roughly remove the photoresist, followed by acetone and isopropanol (IPA) bath respectively for 20 min in an ultrasonic cleaner. Finally, they were dried with a flow of nitrogen. The HDMS can be removed by UV-ozone before using the substrate when it is essential.

The basic principle for removal of surface contaminants by UV-ozone cleaning involves 3 steps.[1]

a. The oxygen in the atmosphere absorbs the UV radiation at 184.9 nm, creating free oxygen radicals and ozone.

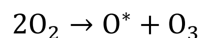

$$2O_2 \rightarrow O^* + O_3$$

b. The generated ozone then absorbs the UV radiation at 253.7 nm, forming free oxygen radicals. Simultaneously, the contaminant molecules on the surface also absorb the UV radiation and are dissociated into excited molecules or free radicals.

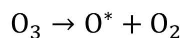

$$O_3 \rightarrow O^* + O_2$$

$$\text{Contaminant molecules} \rightarrow \text{Excited molecules} + \text{Free radicals}$$

c. The dissociated molecules react with free oxygen radicals, forming gaseous molecules like H_2O and CO_2 and removing from the surface.

4.1.1.2. Polyethylene terephtalate substrates

Polyethylene terephtalate (PET) substrates used for flexible applications were purchased from Thorlabs. They were coated with a layer of indium tin oxide (ITO) serving as gate material. They follow the same cleaning procedure with the rigid Si/SiO_2 substrate.

4.1.2. Mechanical exfoliation

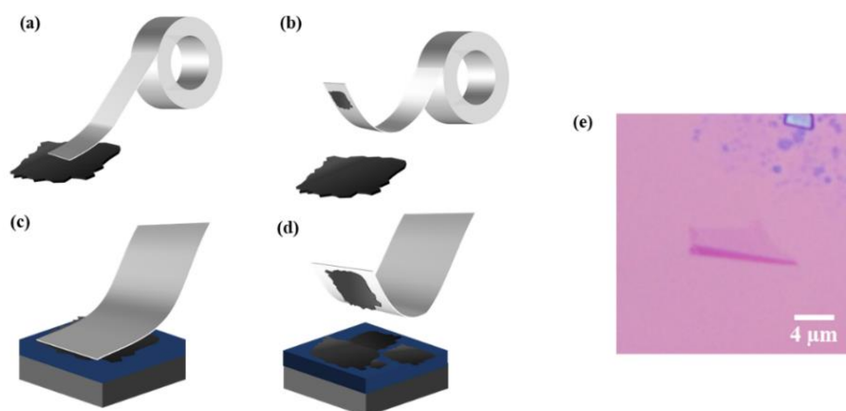

Figure 4-1. (a) to (d) Conventional scotch tape exfoliation process. (e) Optical microscopy image of a monolayer graphene flake.

The monolayer or few-layer thick 2D flakes were obtained by mechanical exfoliation via the conventional scotch tape method as described in the previous chapter.[2] A small piece of bulk crystal of the target 2D material was first transferred onto a clean glass wafer, and then an adhesive tape was carefully placed to detach the top multilayers. By repeated peeling the multilayers on the tape, the material would be cleaved into various few-layer flakes and fully cover the tape. Finally, the tape was pasted to a pre-cleaned Si/SiO_2 substrate and slowly detached, leaving the substrate covered with exfoliated materials. The high-quality monolayer or few-layer 2D flakes can be identified in assistance of an optical microscope. Figure 4-1e shows an example of a monolater graphene flake.

4.1.3. Laser writer photolithography

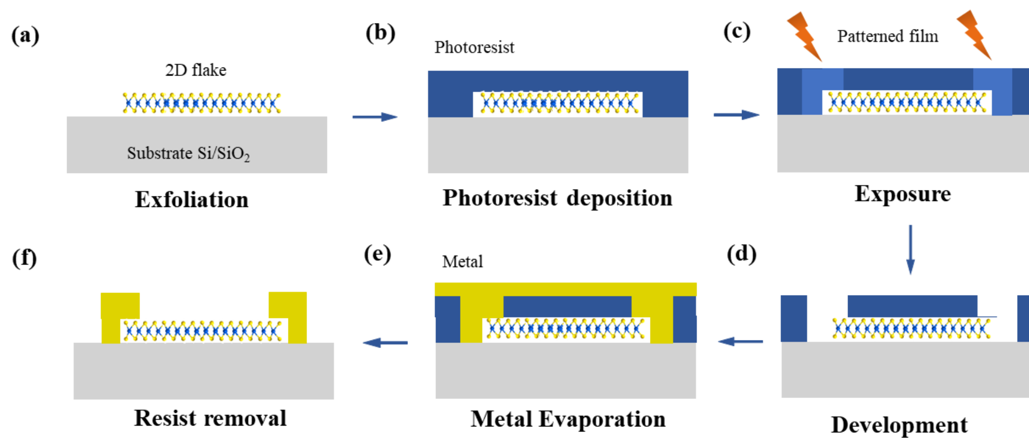

Figure 4-2. The fabrication process of a FET device by photolithography: (a) The target 2D flake is positioned on the substrate. (b) The substrate is covered with a player of photoresist. (c) The photoresist film is irradiated with a laser writer in the pattern we designed. (d) the substrate is immersed in a develop solution to remove the irradiated photoresist. (e) The needed metal is evaporated on the substrate. (f) Metal in unwanted area is removed by washing away the rest photoresist.

For fabrication of field-effect transistor (FET) devices based on a 2D flake, the electrical contacts were patterned in assistance of laser writer photolithography, a writing technique used for high resolution lithography. The sample substrate was first baked on a hotplate at 120 °C for 1 min to remove moisture. Then a uniform thin layer of positive photoresist (AZ1505) was coated on the substrate (3000 rpm, 45s), followed by baking the substrate on a hotplate at 120 °C for 1 min to drive off excess photoresist solvent. After baking, the CleWin5 software was used to design the shape of future electrodes on the chosen flakes. The photoresist film was irradiated very precisely in the pattern we designed by an intense laser at 405 nm within a Microtech laser writer. Note that the power of the laser beam is optimized to order to write channel length with a high resolution around 1.5 μm. If the power is not strong enough, some photoresist residue will be left on the patterned aera. While if the the power is too intense, the patterned aera will be over exposed, shortening the channel length. In the patterned area, the photoresist was isomerized, and its solubility was thus changed, enabling being etched by a special solution called ‘developer’ (726 MIF). The sample was finally immersed in the developer solution and agitated gently for 15 s and rinsed with distilled water.

4.1.4. Metal evaporation

After photolithography, metal was deposited on the substrate to construct electrodes. We placed desired metal in a crucible and fixed the substrate on a sample-holder. The chamber was then sealed and pumped the atmosphere first with a rotary pump, followed by a turbo pump in order to reach an ultra-high vacuum. The metal evaporation usually starts at 10^{-7} bar to avoid contaminant absorbed on the substrate. When the vacuum was reached, an electric current was slowly applied through the crucible to heat the metal by Joule effect. When the temperature was high enough to melt the metal, the metal started to vaporize. The shutter switched from close to open so that the metal vapor would condensate on the substrate. In this way, a layer of desired metal was deposited on the whole surface of the substrate, and its thickness is accurately monitored through a resonance. Note that the evaporation rate was kept lower than 0.05 nm/s to ensure the homogeneity and intensity of the metal film. Once the metal film deposited on the substrate reached the desired thickness, the shutter would be closed. Then the current slowly deceased to 0 and the substrate could be taken out from the chamber after 20 min when it was totally cooling down.

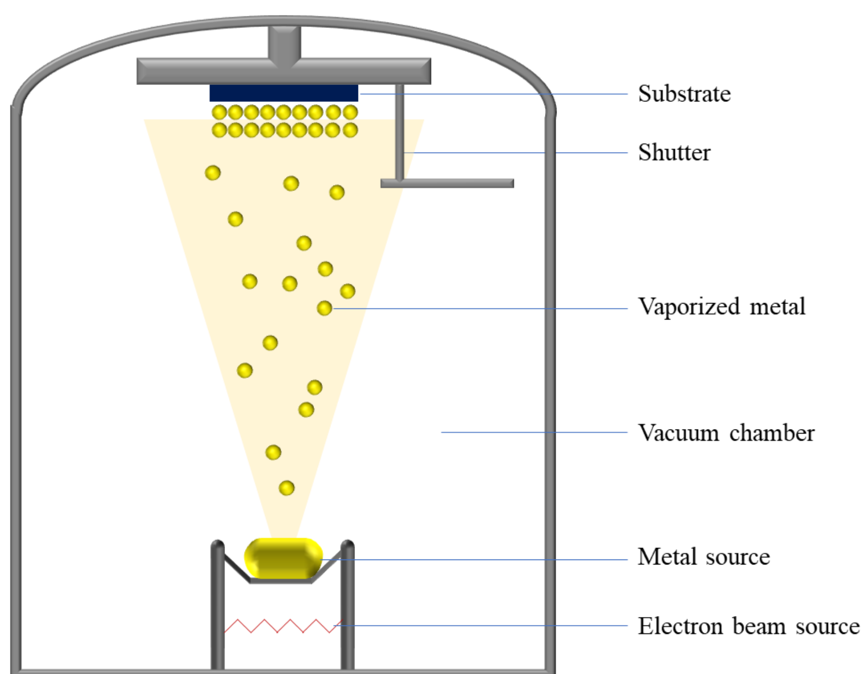

Figure 4-3. Sketch of a metal evaporation setup.

The metal film now covered the whole substrate and the area where there should be no contacts could be removed by washing the remaining photoresist. For this purpose, the lift-off method was applied in which the sample was first immersed in an acetone bath at 50 °C for one hour, followed by a gently bubbling of acetone to remove the photoresist. Finally, the substrate with desired pattern is fabricated. Figure 4-4 shows two representative images of a FET device based on a few-layer WSe_2 flake. The substrate can be annealed over 100 °C for overnight in high vacuum to remove atmospheric absorbents in its surface and photoresist residue when it is essential.

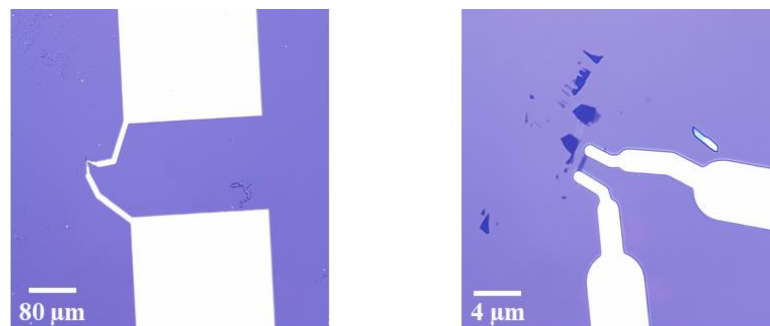

Figure4-4. Optical microscopy images of a FET device based on a few-layer WSe_2 flake.

4.2. Molecular deposition by spin-coating

Spin-coating is a widely used technique to deposit a uniform thin film with nanoscale thickness onto a substrate. The desired molecules were first dissolved in a volatile solvent. Then the substrate was fixed on a rotary plate, the solution dissolving desired molecules (~ 100 μL) was dispensed on the substrate to cover the whole surface. Parameters like speed, time, and acceleration were defined which can influence the thickness of the coated film. Note that the film thickness is also related to the concentration and viscosity of the solution. The solvent was evaporated during the spin process, resulting in a relatively planar molecular film.

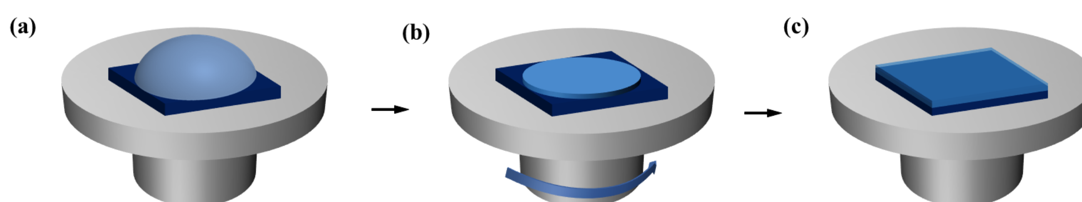

Figure 4-5. Sketch of the spin-coating process.

4.3. Wet transfer method

4.3.1. Polymer-assisted FET device transfer process

The as-fabricated FET on Si/SiO_2 substrate can be transferred onto a flexible PET substrate by using the typical poly(methyl methacrylate) (PMMA)-assisted transfer process. The flexible substrate uses indium tin oxide (ITO) serving as back-gate electrode and 80 nm cross-linked poly(4-vinylphenol) (CL-PVP) as dielectric material. To prepare the CL-PVP solution (60 mg/mL), CL-PVP is mixed with poly(melamine-co-formaldehyde) methylated (PMF) with a weight ratio of 5:1 and dissolved in propylene glycol monomethyl ether acetate solvent. The CL-PVP solution is spin coated (2000 rpm, 60 s) ITO coated PET substrate. Then the substrate is annealed at 150 °C for 90 min.

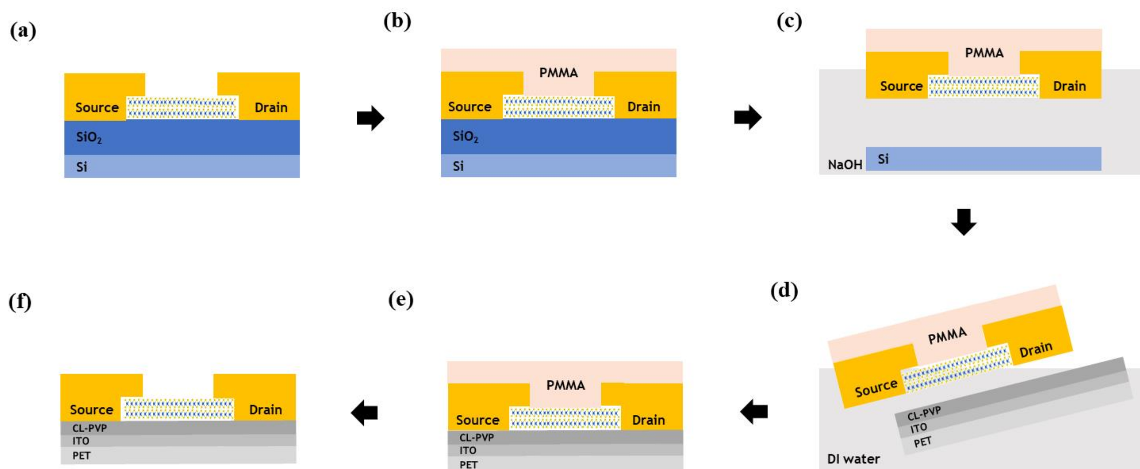

Figure 4-6. Transfer process of a FET device from Si/SiO_2 substrate to PET/ITO/CL-PVP substrate. (a) FET device is first fabricated on a Si/SiO_2 substrate. (b) The device is coated with a layer of poly(methyl methacrylate) (PMMA). (c) The PMMA-coated device is floated in a NaOH bath to etch the SiO_2 layer. (d) and (e) The PMMA supported FET layer is transferred to a deionized water bath and later transferred to a PET/ITO/CL-PVP substrate. (f) The PMMA layer is finally removed by soaking the sample in hot acetone.

A layer of PMMA was spin-coated (2000 rpm, 60 s) on the device which serves as the supporting layer during the whole process, followed by baking at 130 °C for 30 min to solidify PMMA layer. Later the PMMA coated substrate was floated on a 5 M NaOH bath to etch the SiO_2 layer, leaving the PMMA supported WSe_2 FET layer floating on the solution. The layer was subsequently transferred to deionized water bath and rinsed for three times before transferring to the PET/ITO/CL-PVP substrate. Finally, the

PMMA layer was removed by soaking the sample in hot acetone for 30 min by 3 times.

4.3.2. Polymer-assisted CVD 2D material transfer process

For UV/vis absorption measurement, the CVD 2D material on Si/SiO_2 substrate was transferred onto a quartz substrate by using the PMMA-assisted transfer technique. The detailed steps were similar as the FET device transfer process.

4.4. Synthesis of the DAE derivatives used in the thesis

Three DAE derivatives have been employed in the thesis. The synthesis was carried out at Humboldt-Universität zu Berlin. The reaction sketch and the synthesis procedure are presented as follows:

DAE_1: 1,2-Bis(2-(3,5-bis(trifluoromethyl)phenyl)-5-methylthiazol-4-yl)perfluorocyclopent-1-ene

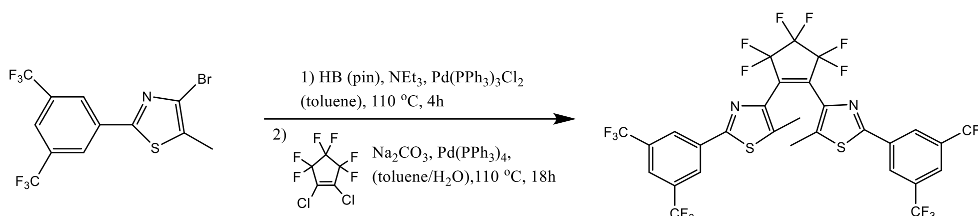

1 eq. of bromothiazole, 6 eq of triethylamine and 0.05 eq. of $Pd(PPh_3)_2Cl_2$ were dissolved in 15 mL of dry toluene and the mixture was degassed with argon. After the addition of 3 eq. of pinacolborane, the mixture was refluxed for 4 h at 120 °C. After cooling to 80 °C, an aqueous solution of Na_2CO_3 was slowly added. Then, 0.33 eq. of 1,2-dichlorohexafluorocylopent-1-ene and 0.02 eq. of $Pd(PPh_3)_4$ were added and the mixture, and stirred at 100 °C for 18 h. After cooling down to room temperature the mixture was extracted with ethyl acetate and the combined organic layers were washed with brine and dried over $MgSO_4$.

DAE_2: 1,2-Bis(5-(4-N,N-dimethylaminophenyl)-2-methylthien-3-yl)cyclopent-1-ene

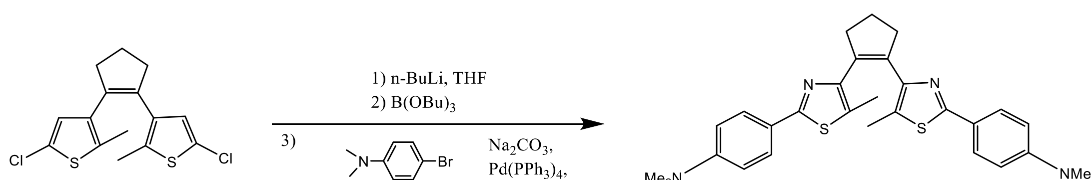

1 eq. of 1,2-bis(5-chloro-2-methylthiophen-3-yl)cyclopent-1-ene was dissolved in 15 mL of anhydrous THF, then 3 eq. n-BuLi was added dropwise at room temperature. Then, 3 eq. tri(n-butyl) borate was added in one portion and the resulting mixture was stirred at room temperature for 1h. In the meantime, 5 eq. 4-N,N-dimethylaminobromobenzene was dissolved in 15 mL of toluene, adding 0.1 eq. $Pd(PPh_3)_4$. An aqueous solution of 13 eq. Na_2CO_3 and the previously prepared borylated bisthienylcyclopentene solution were added. The mixture was stirred at 80 °C for 16 h. After cooling to room temperature, 100

mL of water were added and the mixture was extracted with 50 mL of ethyl acetate three times. The combined organic phases were washed with brine, dried over $MgSO_4$ and evaporated.

DAE_3: 1,2-Bis(5-(4-methoxyphenyl)-2methylthien-3-yl)cyclopent-1-ene

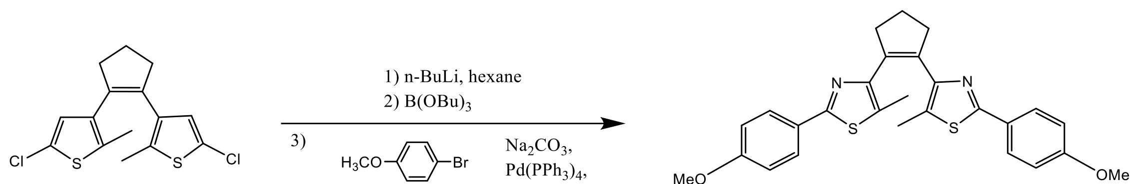

Similar with DAE_2, 1 eq. of 1,2-bis(5-chloro-2-methylthiophen-3-yl)cyclopent-1-ene was dissolved in hexane, then 3 eq. n-BuLi was added dropwise at room temperature. Then, 3 eq. tri(n-butyl) borate was added in one portion and the resulting mixture was stirred at room temperature for 1h. In the meantime, 5 eq. 4-bromo-anisole was dissolved in 15 mL of toluene, adding 0.1 eq. $Pd(PPh_3)_4$. An aqueous solution of 13 eq. Na_2CO_3 and the previously prepared solution were added. The mixture was stirred at 80 °C for 16 h.

4.5. Characterization techniques

4.5.1. Surface characterization: Atomic Force Microscopy

The Atomic Force Microscopy (AFM) is the most versatile technology to study the surface morphology of the sample at the nanometer scale by measuring the force between the probe and the sample surface. It was first invented by Gerd Binning et al. in 1986 based on the concept of scanning tunneling microscope (STM).[3] While the STM only allows to investigate conductive samples, the AFM has extended the application to imaging almost any type of samples, including polymers, ceramics, glass and composites.

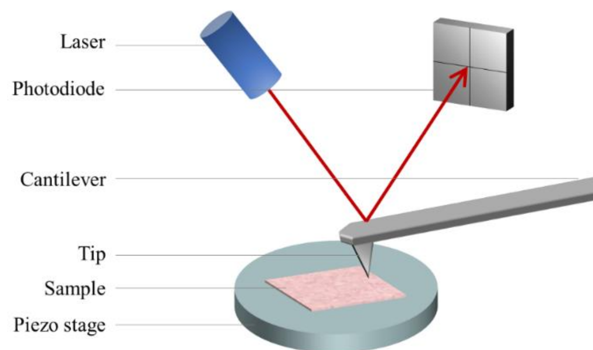

Figure 4-7. Sketch of an Atomic Force Microscopy setup.

A typical AFM consists of an oscillating cantilever with a sharp silicon nitride tip to scan the sample surface, a laser, a 4-quadrant photodiode and a scanner (Figure 4-7). The technique is based on the attractive and repulsive forces reflected by the cantilever. As the tip approaches the sample surface, the attractive force between the tip and the surface causes the cantilever to deflect towards the surface. While if the distance gets even closer by about 0.1 nm, the increasing repulsive force will cause the cantilever to deflect away from the surface. The deflection is then measured by the laser spot reflected from the top surface of the cantilever into an array of the photodiode. Regarding the cantilever as a spring, the strength of the interaction between the tip and sample surface can thus be characterized with Hooke's Law:

$$F = -k \cdot x$$

Where

F is the force,

k is the spring constant,

x is the cantilever deflection.

The AFM can be operated in two modes: contact mode and tapping mode. In the contact mode, the tip is in a soft and constant contact with the sample surface. It can provide an accurate image with high resolution but the sample may be damaged since its surface is scratched by the tip. In the tapping mode, the distance between the tip and the sample is kept intermediate in the tens-of-nanometer scale so that the cantilever is kept oscillating without touching the surface. This mode is less destructive to the surface and the tip compared with the former while the resolution is decreased. Note that in order to increase the quality of the results obtained, each spot is being recorded twice by trace and retrace.

The morphology of the sample surface induces changes in the amplitude of the cantilever oscillations, which is detected by the laser beam. Different interactions between the tip and the sample surface may generate different intensities of the reflected light. Such difference can be recorded by the photodiode. With a voltage applied to the piezoelectric scanner which moves in the Z direction at each point, the signal is sent to the controller feedback loop which keeps the distance between the cantilever and the sample maintaining a constant. Therefore, an accurate topological illustration of the sample surface is generated.

4.5.2. Raman and photoluminescence spectroscopy

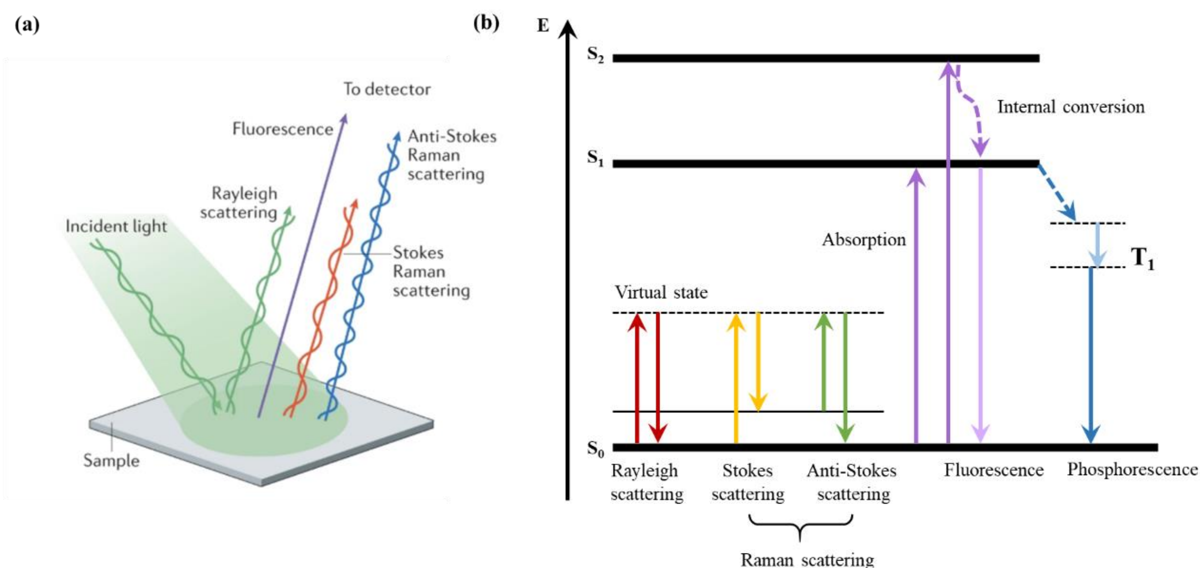

Figure 4-8. (a) Light interaction with the sample molecules, reproduced from Ref.[4] (b) Representative energy levels for Rayleigh, Stokes, Anti-stokes scattering and photoluminescence.

When an incident light is on a molecule, it can interact with the constituent molecules in numerous ways (Figure 4-8a). It can always result in two types of light scattering: elastic and inelastic. A major part of the scattered light is elastic scattering, which is also known as Rayleigh scattering, refers to the condition when the frequency of the scattered light remains the same with the incident light. While only a minor part scatters inelastically, this is the condition when the incident light interacts with the molecule, the frequency of the scattered light will thereof be changed, resulting in inelastic scattering. Depending on the energy of the molecule, the inelastic scattering can be further divided into two parts. If the molecule is initially in its ground state and gains energy from the incident light, the frequency of the scattered light will be lower, resulting in Stokes Raman scattering. Conversely, if the molecule is in higher vibrational state and the incident light gains vibrational energy from the molecule during the interaction, then the frequency of the scattered light will be higher than that of incident light, which is known anti-Stokes Raman scattering (Figure 4-8b). If the energy of the illuminating photons matches an electronic energy level of the molecule, they can excite the molecule to this state. Photoluminescence (PL) is the process when these electrons return to their equilibrium states and emit light. Depending on the duration of emission time, the process can be further divided into fluorescence and phosphorescence.

When the electrons undergo internal energy transitions before relaxing to its ground state by emitting photons, some of the absorbed energy is dissipated so that the emitted light photons are of lower energy than those absorbed, the process is called fluorescence. This is a prompt process that occurs very shortly. Phosphorescence is along-lived photoluminescence, in which the absorbed energy undergoes intersystem crossing into a state with a different spin multiplicity before relaxing to the ground state. Therefore, phosphorescence is even rarer than fluorescence, since a molecule in the triplet state has a good chance of undergoing intersystem crossing to ground state before phosphorescence can occur.

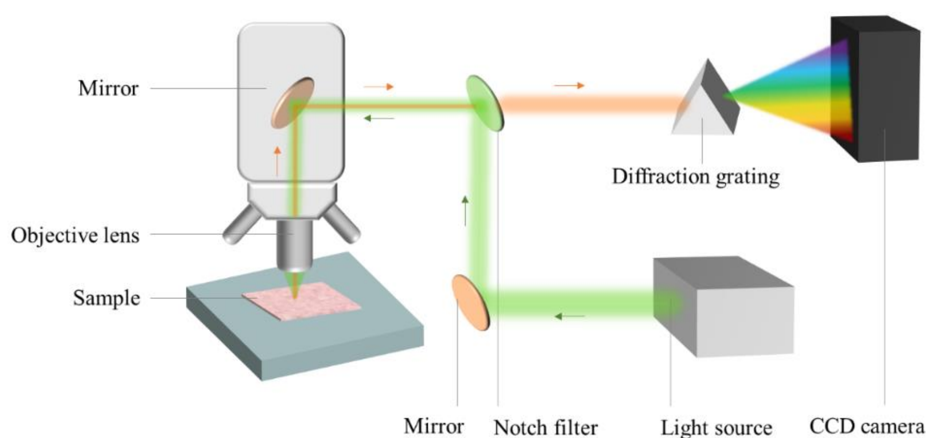

Figure 4-9. Sketch of an Atomic Force Microscopy setup.

Raman spectroscopy is a widely used spectroscopic technique to characterize a material, which is based on the inelastic scattering of light.[5] It gives the vibrational spectrum of the sample material, of which the shift in wavelength provides the chemical and structural information. It can be used to observe rotational, vibrational and other modes of low frequency within a system. PL can provide information about the composition and solid-state structure of the material. The high spectral resolution of a Raman spectrometer can be useful in performing PL spectroscopy of solid-state materials. A schematic layout of the Raman microscope is shown in Figure 4-9. The sample substrate is placed on the microscope stage. The excitation light from a laser (532 nm) is reflected by the Notch filter and focused down onto the sample through the objective lens of the microscope. The resulting Raman scattering from the sample is collected by the objective lens and transmitted back to the Notch filter. Note that the filter attenuates the incident excitation light and only passes the Raman scattering. The remaining Raman

scattering then enters the monochromator which uses a diffraction grafting to disperse the beam into a different band of wavelengths. Finally, a CCD camera is used to detect the resulting spectrum.

4.5.3. UV-vis absorption spectroscopy

UV-vis absorption spectroscopy is a quantitative technique that can measure how much a molecule is capable to absorb light, by comparing the light intensity that passes through the sample molecule with respect to the reference.

A UV-vis spectrophotometer usually consists of a light source, a diffraction grating to separate the different wavelengths of light, a holder for the sample/reference and a detector (Figure 4-11). The light source is often a Halogen filament (300–2500 nm for visible range) and a deuterium arc lamp (190–400 nm for UV range). A beam of light from the source is separated by a diffraction grating. The monochromatic beam in turn is split into two equal intensity beams by the chopper. The sample beam passes through the cuvette containing the sample solution. The reference beam passes through the cuvette containing only the solvent. The intensities of these light beams are then measured by the detectors and compared.

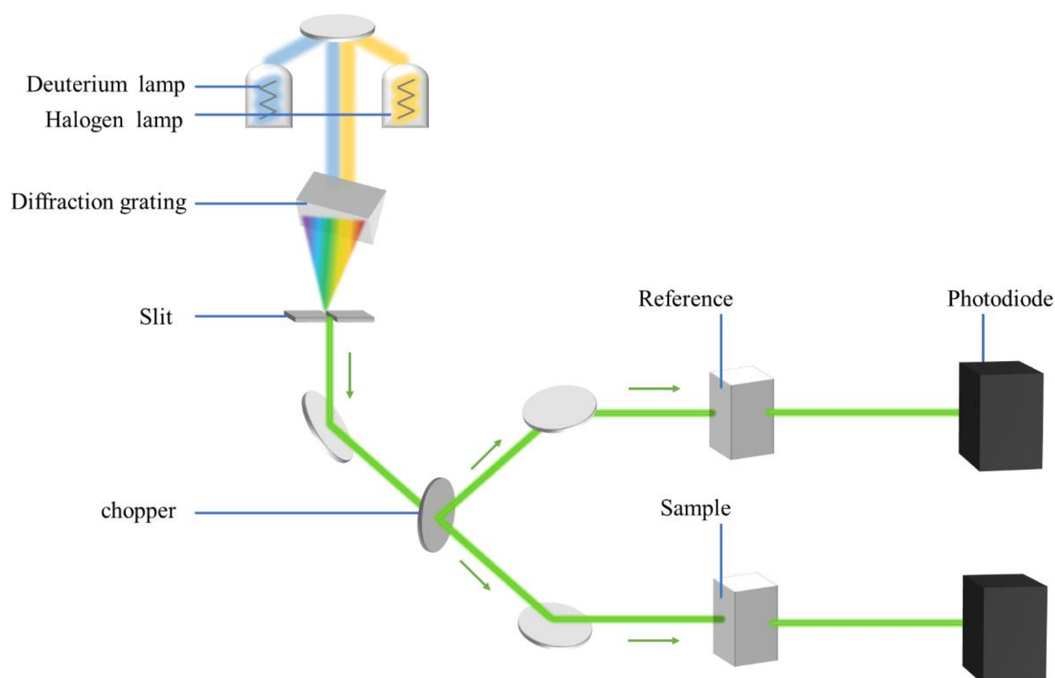

Figure 4-10. Sketch of a UV- vis spectrophotometer.

The intensity of the reference beam, which should have suffered no light absorption, is defined as I_0. The intensity of the sample beam is defined as I. The absorption of the sample may be presented as transmittance $T = I/I_0$ or absorbance $A = -logT = -\log(\frac{I}{I_0})$.

With the known absorbance, the concentration of the sample can be determined by using Beer-Lambert Law.

$$A = \varepsilon lc$$

Where

A is the measured absorbance,

ε is the absorption coefficient,

l is the path length,

c is the concentration.

4.5.4. Water contact angle

The water contact angle has been an important parameter to determine the wetting ability of a sample surface. The shape that a water drop takes on a surface depends on the surface tension of the fluid and the nature of the surface. At the boundary between droplets and the gaseous environment, the surface tension causes a curved contour. At the edge of the drop, where the contour merges into the bearing surface, the contact angle between the interface liquid/solid and the tangent to the interface liquid/ gaseous forms.

If the liquid runs evenly on the solid surface, complete wetting is present with a contact angle of 0°.

An angle between 0° and 90° corresponds to a wettable hydrophilic surface.

An angle between 90° and 180° indicates a not wettable hydrophobic surface.

If the angle clearly approaches the value of 180°, the surface is ultra-hydrophobic and is completely liquid-repellent, which is defined as lotus effect.

During the measurement, the sample is placed on a mobile sample stage. A syringe filled will water is fixed above the sample and an optical camera is aligned and focused on the sample. After a 2 μL drop of water is deposited on the sample, the camera takes a picture and the instrument software will measure the corresponding contact angle.

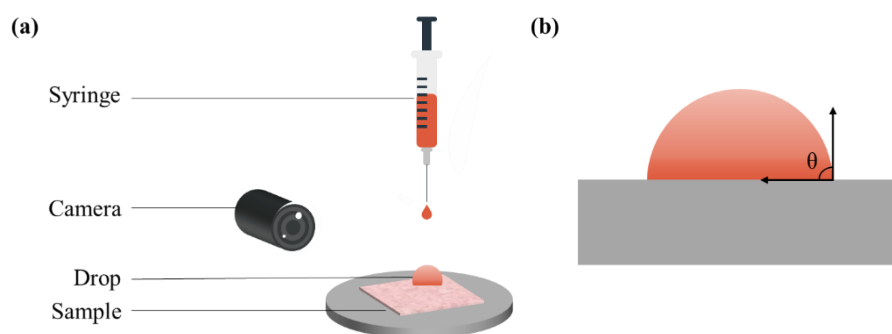

Figure 4-11. (a) Sketch of water-contact angle setup. (b) Example of contact angle.

4.5.5. Energy level determination

The CB/VB energy levels for 2DMs were taken from reported work, which were obtain by calculation using the plane wave code CASTEP (WSe_2)/VASP (BP) with the framework of DFT. Screen-exchange hybrid functional are utilized.

The energy levels for DAE molecules were determined by cyclic voltammetry (CV), in reference to the ferrocene redox couple (Fc/Fc^+), derived from the reduction/oxidation peak potentials. The measurement was performed using a PG310 USB (HEKA Elektronik) potentiostat. A three-electrode configuration contained in a non-divided cell consisting of a platinum disc (d = 1 mm) as working electrode, a platinum plate as counter-electrode, and a saturated calomel electrode with an agar-agar-plug in a Luggin capillary with a diaphragm as reference electrode was used.

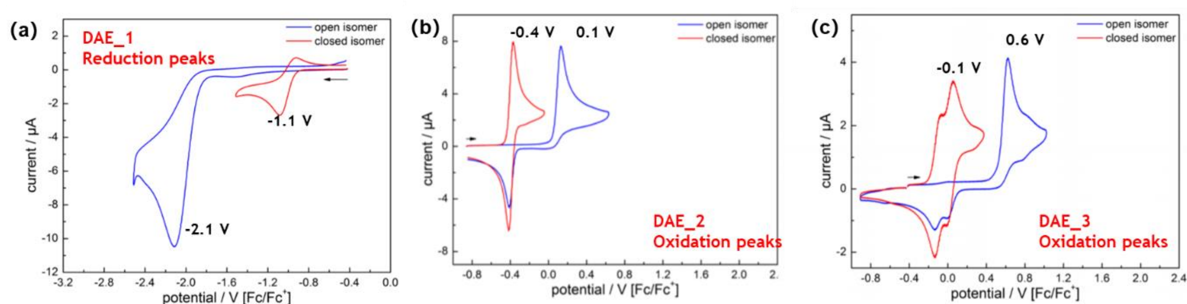

Figure 4-12. Cyclic voltammetry of (a) DAE_1, (b) DAE_2 and (c) DAE_3 in acetonitrile/0.1 M Bu4NPF6.

4.5.6. Electrical characterization

4.5.6.1. Field-effect transistors

The field-effect transistor (FET) represents the building block for modern electronics. The concept of it was first patented by Lilienfeld in 1925 and by Heil[6] in 1934.[7] The first working FET was fabricated by Bardeen and Brattain in 1947, followed by Shockley's bipolar junction transistor in 1948. In 1956 they were conferred with the Nobel prize and the FET was defined as “the most important invention of the 20th century”.

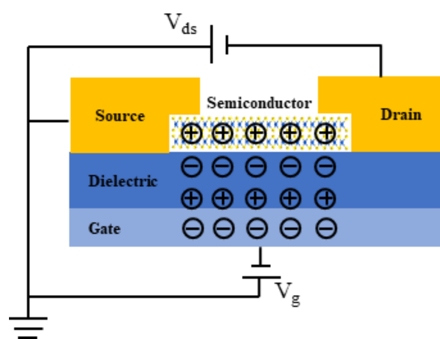

Figure 4-13. Sketch of a field-effect transistor.

A FET is a three-terminal device, which consists of three metallic conducting electrodes: source (S), drain (D) and gate (G), and an insulating layer (dielectric) and a semiconductor. The source and drain electrode are connected by the semiconductor, and they are separated with the gate electrode by the dielectric (Figure 4-13). Upon application of a positive potential on the gate electrode, the negative charges will be attracted between the dielectric/semiconductor interface, with an additional potential between the source and drain, the attracted charges can flow in the channel. The general working principle of a FET therefore is to use the voltage at gate electrode to control the flow of current from source to drain electrode.

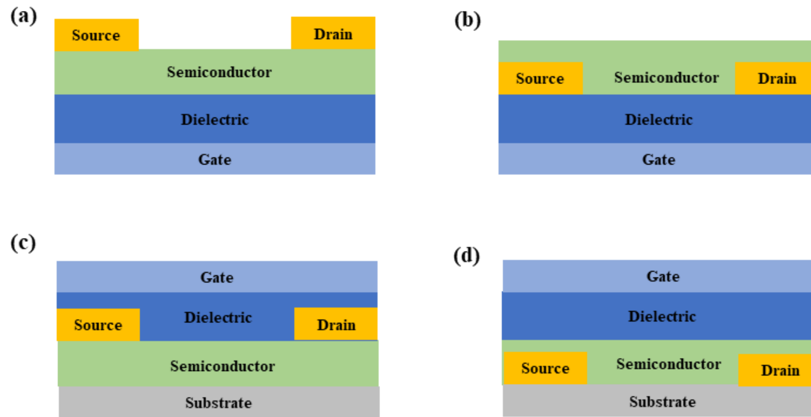

Figure 4-14. Different geometries of FET devices: (a) top contact, bottom gate; (b) bottom contact, bottom gate; (c) top contact, top gate; (d) bottom contact, top gate.

According to the stacked order, FETs can be classified into four different geometries (Figure 4-14): top/bottom gate with top/bottom contact. Since each geometry has its own merits and drawbacks, the choice of the geometry is decided by practical fabrication conditions. When the source and drain electrodes are deposited on top of the semiconductor, while the gate at the bottom, it forms top contact, bottom gate geometry. In this geometry, the contact area between the source electrode and the semiconductor is relatively large, and their interface is intimate, which allows a facilitated injection. While if the source and drain electrodes are directly deposited on the dielectric, with the semiconductor on top, it forms the second geometry: bottom contact, bottom gate. In this geometry, the substrate gate/dielectric with pre-patterned electrodes can be purchased in advance since the deposition of the semiconductor is the last step. This geometry can therefore largely facilitate the device fabrication process. The top contact, top gate geometry is used when a high *k* dielectric compared with SiO_2 is employed, which allows to improve the device mobility. The drawback is that it requires the greatest number of production steps.

4.5.6.2. Extraction of electrical parameters

The electrical properties of the semiconductor are usually determined by performing the current versus voltage measurement from the FET device, which allows to trace the transfer curve and the output curve. The transfer curve is obtained by recording the source-drain current I_{ds}, when sweeping the gate bias V_g and applying a constant source-drain bias V_{ds}. The output curve is obtained by recording I_{ds} at a constant V_g when sweeping the V_{ds}. In most cases, multiple curves for different V_g are shown in output measurement.

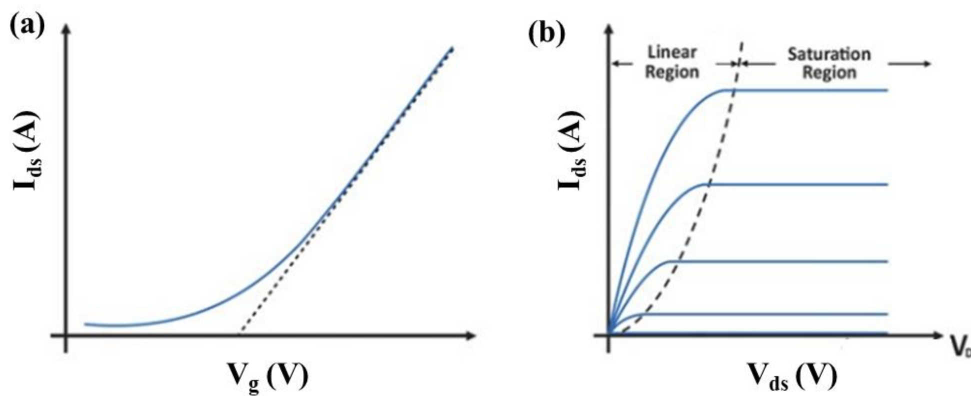

Figure 4-15. A typical example of the (a) Transfer; (b) Output curve for a n-type semiconductor.

The key parameters to define the intrinsic electrical properties of the semiconductor and the FET device performance can be extracted from these two curves. In particular, the charge carrier mobility (μ), the threshold voltage (V_{th}) and the I_{on}/I_{off} ratio.

The charge carrier mobility defines how quickly the carrier can move through the semiconductor when an electric field E is applied.[8]

$$V_d = \mu \cdot E$$

Where V_d is the carrier drift velocity caused by the electric field E.

The charge Q induced at the gate voltage V_g that higher than V_{th} at the certain position x can be expressed as:

$$Q = C_i(V_g - V_{th} - V_x)$$

The drain current I_{ds} can therefore be expressed as:

$$I_{ds} = W \cdot Q \cdot \mu \cdot E = W \cdot C_i(V_g - V_{th} - V_x) \cdot \mu \cdot E$$

Where W is the width of the channel.

Known that $E = \frac{dV}{dx}$,

$$I_{ds} = W \cdot C_i(V_g - V_{th} - V_x) \cdot \mu \cdot \frac{dV}{dx}$$

As we can see, the transfer curve has two different regimes: linear regime (when I_{ds} changes linearly with V_{ds}) and saturation regime (when I_{ds} reaches saturation).

I_{ds} in the linear regime can therefore be defined as:

$$I_{ds,lin} = \frac{W}{L} \cdot C_i \left[\left(V_g - V_{th}\right) \cdot V_{ds} - \frac{1}{2} {V_{ds}}^2) \right] \cdot \mu_{lin}$$

Since $V_{ds} \ll V_g - V_{th}$,

$$I_{ds,lin} = \frac{W}{L} \cdot C_i \cdot \left(V_g - V_{th}\right) \cdot V_{ds} \cdot \mu_{lin}$$

The mobility in the linear regime can therefore be extracted as:

$$\mu_{lin} = \frac{\partial I_{ds,lin}}{\partial V_g} \frac{L}{W} \cdot \frac{1}{C_i} \cdot \frac{1}{V_{ds}}$$

While in the saturation regime,

$$I_{ds,sat} = \frac{1}{2} \cdot \frac{W}{L} \cdot C_i \cdot \left(V_g - V_{th}\right)^2 \cdot \mu_{sat}$$

Therefore,

$$\mu_{sat} = 2 \cdot \left(\frac{\partial \sqrt{I_{ds,lin}}}{\partial V_g} \right)^2 \frac{L}{W} \cdot \frac{1}{C_i}$$

While when using the above expression to determine the charge carrier mobility in a FET device, the value might be underestimated since they consider the total resistance R_{total} including contact resistance $R_{contact}$ instead of only channel resistance $R_{channel}$.

The contact resistance is an indicator of how easily the charge carrier can be injected from the electrode to the semiconductor. Actually, when the charges are injected, the flow will first be reduced by the metal resistance R_m. Then it is injected from the metal to the channel. Due to the energy level mismatch between the HOMO/LUMO of the semiconductor and the work function of the metal electrode, there is an injection barrier which will further reduce the flow, leading to the contact resistance. Later, the flow in the semiconductor will be reduced again by the channel resistance R_{semi}, which is dependent on the channel length. To be collected on the other electrode, the flow will experience for the second time the injection barrier and the metal resistance. Note that R_m is small and can usually be neglected.

There are several techniques to measure contact resistance, one of the most prevalent the transmission line method (TLM). According to TLM, the total resistance can be plotted as a function of the channel length L:[9]

$$R_{total} = 2R_m + 2R_{contact} + R_{semi} \approx 2R_{contact} + \frac{R_{sheet}}{W} \cdot L = 2R_{contact} + \frac{1}{\mu_0 C_i (V_g - V_{th}) W} \cdot L$$

Where μ_0 is the intrinsic mobility excluding contact effect.

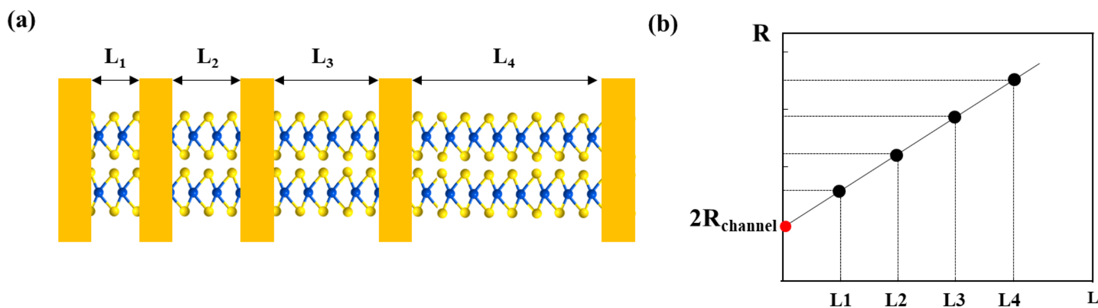

Figure 4-16. (a) Schematic illustration of TLM structure. (b) Example of total resistance versus channel length plot.

It suggests that total resistance has a linear dependence with the length of the channel. Therefore, to determine the contact resistance by TLM, a couple of devices should be fabricated with various channel lengths L, then their total resistances can be plotted as a function of the length L (Figure 4-16). The linear extrapolation at zero channel length is the value for contact resistance. The slope of the linear function can then be used to estimate the intrinsic mobility of the FET device.

Gated four-probe measurement is another alternative way to address the contact resistance.[10] As shown in Figure 4-17, the device consists of four probes arranged linearly in a straight line at equal distance from each other. During the measurement, a constant current is passed through the four probes and the potential drop across the middle two probes is measured. In the linear regime, the charge-carrier density in the channel is almost uniform, giving a linear potential profile in the channel from source to drain. Since the potentials V_1 and V_2 at the positions L_1 and L_2 are known from the measurement, they can be used to linearly extrapolate the channel potential to the source and drain contacts (Figure 4-15b). The contact resistances can thus be calculated from the potential drops at the source (ΔV_S) and at the drain (ΔV_D) using $R_S = \frac{\Delta V_S}{I_D}$ and $R_D = \frac{\Delta V_D}{I_D}$, while μ_0 can be obtained from the potential drop across the channel ΔV_{ch}.

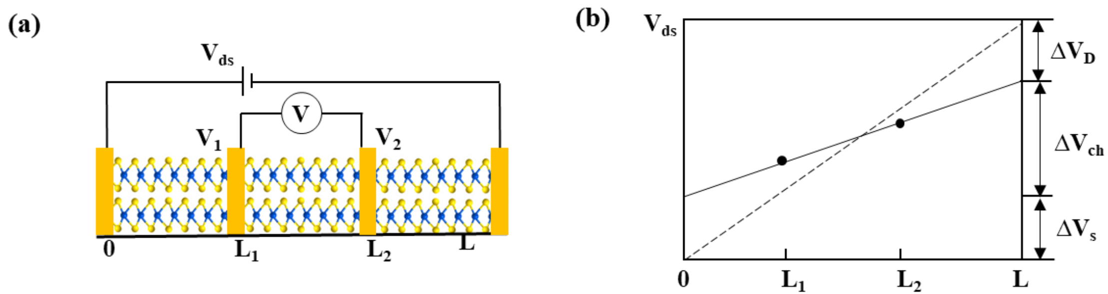

Figure 4-17. (a) Schematic of the measurement configuration for four-probe field-effect mobility. (b) Potential profile in the channel of device in the linear regime.

The threshold voltage V_{th} is another important parameter that defined as the minimum gate voltage V_g that is required to create a conducting path between the source and drain electrodes. The value can be obtained by using a linear extrapolation in the transfer curve.[11]

The I_{on}/I_{off} ratio is the ratio value of the maximum current I_{ds} to the minimum current I_{ds}. It defines the device capacity to switch from ON state to OFF state. A high I_{on}/I_{off} is usually preferred since a high ON current represents high performance of the device, and a low OFF current represents less leakage power.

The subthreshold swing is defined as the change in gate voltage which must be applied in order to create a one decade change in the output current. It describes an exponential behavior of the current as a

function of voltage. It can be calculated using the formula:

$$SS = In10\frac{kT}{q}\left(1 + \frac{C_d}{C_{ox}}\right)$$

Where $\frac{kT}{q}$ is the thermal voltage,

C_d is the depletion capacitance,

C_{ox} is dielectric capacitance.

The minimum subthreshold swing of a conventional device can be found by letting $C_d \rightarrow 0$, yielding $SS = In10\frac{kT}{q}$. Therefore, at room temperature, SS has a thermionic limit of 60 mV/dec.

In 2DM based FETs, the charge carrier transport and scattering are confined to the plane of the material. The charge carrier mobility is affected by several scattering mechanisms:

a) Acoustic and optical phonon scattering. The mobility is increasingly affected by phonon scattering with increasing temperature. At low temperatures (T < 100 K), the acoustic component dominates, but at higher temperatures the optical component dominates.

b) Coulomb scattering at charged impurities. Coulomb scattering is caused by random charged impurities located within the material. The improvement of room-temperature mobility of MoS_2 transistors from ~ 0.5–3 $cm^2\ V^{-1}s^{-1}$ to ~ 200 $cm^2V^{-1}s^{-1}$ can be realized by dielectric screening of Coulomb scattering on charged impurities by using gate dielectric materials with a high dielectric constant. The carrier concentration and bandgap can be tuned by adding ionic impurities, but the mobility is also decreased through scattering, so the choice of doping level in a particular device can strongly influence its performance. By considering the mean free path of carriers, the impurity concentration required to make impurity scattering dominant over phonon scattering is calculated to be ~$5 \times 10^{11}\ cm^{-2}$, which corresponds to heavy doping.

c) Surface interface phonon scattering and roughness scattering. Such effect can be very important in extremely thin 2DMs.

The degree to which these scattering mechanisms affect the charge carrier mobility is influenced by layer thickness, carrier density, temperature, effective carrier mass, electronic band structure and phonon band structure.

4.5.6.3. Electrical setup

The device electrical characterization was performed using a Keithley 2636A Dual-channel System Source Meter, with a Cascade Microtech M150 probe-station in a glove box filled with nitrogen. The sample was placed on a metallic holder which can be biased with a gate voltage V_g. Two micromanipulators allow to move two tungsten probes that carry the electric current connecting to the source and drain electrodes respectively, localized with the help of the optical microscope. The source electrode is connected to ground and the drain would be imposed with a voltage V_{ds}. A monochromator setup can be used to illuminate the sample.

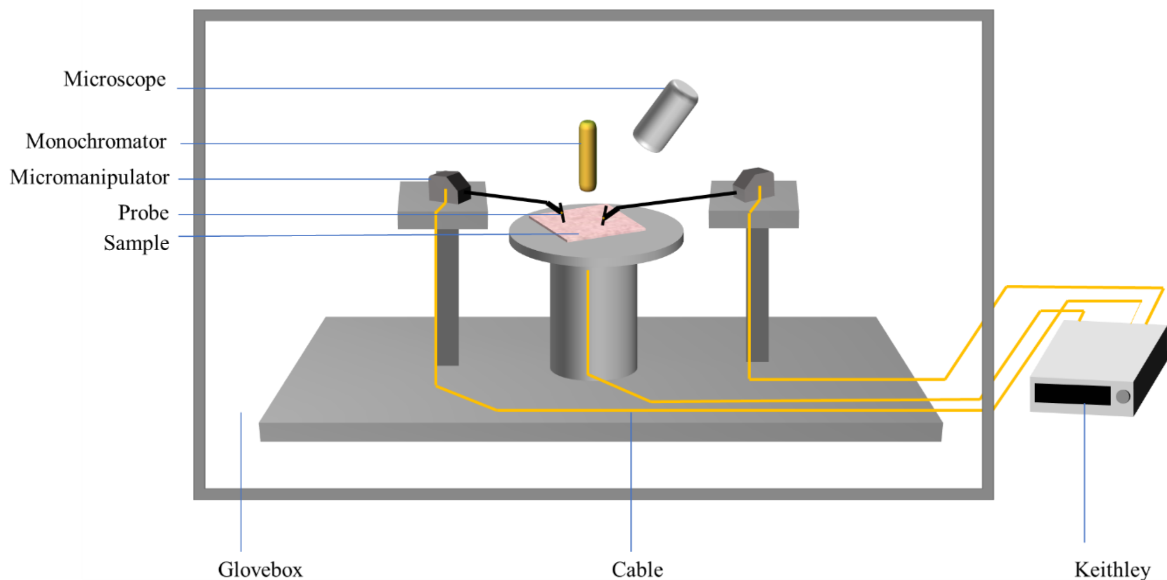

Figure 4-18. Sketch of a probe-station setup for electrical characterization.

4.6. References

[1] R. Kohli, in *Developments in Surface Contamination and Cleaning*, William Andrew Publishing, Oxford **2015**, 71.

[2] K. S. Novoselov, A. K. Geim, S. V. Morozov, D. Jiang, Y. Zhang, S. V. Dubonos, I. V. Grigorieva, A. A. Firsov, *Science* **2004**, *306*, 666.

[3] G. Binnig, C. F. Quate, C. Gerber, *Phys. Rev. Lett.* **1986**, *56*, 930.

[4] S. Mosca, C. Conti, N. Stone, P. Matousek, *Nat. Rev. Dis. Primers* **2021**, *1*, 21.

[5] R. S. Das, Y. K. Agrawal, *Vib. Spectrosc* **2011**, *57*, 163.

[6] L. J. Edgar, *U.S. Patent*, US1745175A, **1930**.

[7] O. Heil, *British Patent*, GB439457A, **1935**.

[8] G. Horowitz, *Adv. Mater.* **1998**, *10*, 365.

[9] M. Weis, J. Lin, D. Taguchi, T. Manaka, M. Iwamoto, *Appl. Phys. Lett.* **2010**, *97*, 263304.

[10] B. Radisavljevic, A. Kis, *Nat. Mater.* **2013**, *12*, 815.

[11] G. Horowitz, R. Hajlaoui, H. Bouchriha, R. Bourguiga, M. Hajlaoui, *Adv. Mater.* **1998**, *10*, 923.

Chapter 5 Modulating the charge transport in n-type WSe_2/p-type BP via energy level phototuning

The controlled functionalization of semiconducting two-dimensional materials with photo-responsive molecules enables the generation of novel hybrid structures as active components for the fabrication of high-performance multifunctional field-effect transistors (FETs) and memories. In this chapter we report on the realization of optically switchable FETs by decorating the surface of the two-dimensional semiconductors (2DSs) such as WSe_2 and black phosphorus (BP) with suitably designed diarylethene (DAE) molecules to modulate their electron and hole transport, respectively, without sacrificing their pristine electrical performance. The efficient and reversible photochemical isomerization of the DAEs between the open to the closed isomer, featuring different energy levels, made it possible to generate photo-switchable charge trapping levels, resulting in the tuning of charge transport through the 2DSs by alternating illumination with UV and visible (vis) light. The device revealed excellent data retention capacity combined with multiple and well-distinguished accessible current levels, paving the way towards its use as active element in multilevel memories.

5.1. Introduction

For application of 2DSs in opto-electronics, more and more efforts have been devoted to the investigation and device optimization based on 2DSs such as transition metal dichalcogenides (TMDs) and more recently also to BP since they combine efficient charge transport characteristics, with a finite band-gap, to enable controlled optimal transistors operation.[1] Unfortunately, the 2DS's structures define their properties, which are difficult to be tuned or modified via the conventional doping strategies.[2] In this regard, it is highly appealing to manipulate the electronic properties of 2DSs, by also conferring them new functions, towards emergence of novel applications in opto-electronics and related technologies. In view of the highest sensitivity of 2D materials to subtle changes in the local environment,[3] their functionalization with photosensitive molecules represents a powerful strategy for modifying their intrinsic properties when exposed to electromagnetic fields.[4] The modification of the properties of 2D materials when interacting with molecules can result in doping effects due to either

charge transfer processes or interfacial dipoles.[5] Recently, in order to go beyond the mere doping effect induced modification, much attention has been given to the combination of 2DMs with a molecular building blocks which could impart reversible and phototunable characteristics.[4] Among various approaches, the use of photochromic molecules as optically responsive components makes it possible to form stable hybrid structures with molecular-driven photoresponsivity.[6] Switchable electronic properties can be realized with such hybrid systems, thus enabling them to serve as active materials for transistors/memories that can be switched on and off via light irradiation at specific wavelengths. Moreover, the use of light as external stimuli offers a fast, non-invasive and easily addressable way to trigger molecular switches and modulate the property of the hybrid materials.

The most popular photochromic molecules reported so far are azobenzenes,[7] spiropyrans[8] and DAEs.[9] During the last five years the former two molecules have been combined with 2DMs to fabricate multifunctional FETs.[10] Due to a variation of the molecular dipole moment between their two photo-isomers local electrostatics are modified, leading to light-controlled reversible doping.[10a, 10c] Instead, the use of DAEs in combination with 2DMs is still rather unexplored. DAEs possess significant advantages for applications in (digital) electronics as they combine efficient photoisomerization in the solid state with high fatigue resistance, thermal bi-stability and strictly defined phototunable energetic levels.[11] Upon irradiation with UV or vis light, DAEs can be toggled between their cross-conjugated ring-open (DAE_o) and π-conjugated ring-closed (DAE_c) isomers, accompanied by a reversible change of their corresponding HOMO and LUMO energy levels. Thereby, the charge transfers between the 2DS and DAE component and thus the density of charge carriers in the 2DM can be modified. This makes DAEs suitable candidates to reversibly adjust the electrical performance of FETs based on 2DMs.

In this chapter, we present the use of charge transfer as a physical process to realize light responsive FETs based on few-layer WSe_2 and few-layer BP by combining them with suitable DAE molecules. We demonstrate that a reversible control on the electron and hole transport of the FET device could be achieved upon illumination at specific wavelengths, without exhibiting significant fatigue over at least 16 irradiation cycles. The field-effect mobility photo-modulation is around 61% for electrons in WSe_2, and 42% for holes in BP, thus outperforming the one observed for 2DMs coupled with spiropyran and

azobenzene previously. In addition, the devices exhibit an excellent data retention capacity as evidenced by negligible variation of output current upon storage for one week in the dark. Furthermore, five distinguishable output current levels with a high accuracy readout are attained, making our system highly promising for its potential applications in multilevel memories when fast light pulses with low areal power density are employed.

5.2. Experimental methods

5.2.1. Match of energy levels between DAE and 2DM

Three DAE derivatives[11-12] displaying different highest occupied molecular orbital (HOMO)/lowest unoccupied molecular orbital (LUMO) energy levels have been designed and synthesized in view of the frontier orbitals of WSe_2[13] and BP[14]. The requirement to achieve photo-modulation relies on the matching of the energy levels between the host 2DS and DAE molecules, to enable the appearance of trapping states. Likewise when blended with organic semiconductors,[15] the two isomers, DAE_o and DAE_c, feature different energy levels and can be expected to affect differently the charge transport process through the 2DSs.

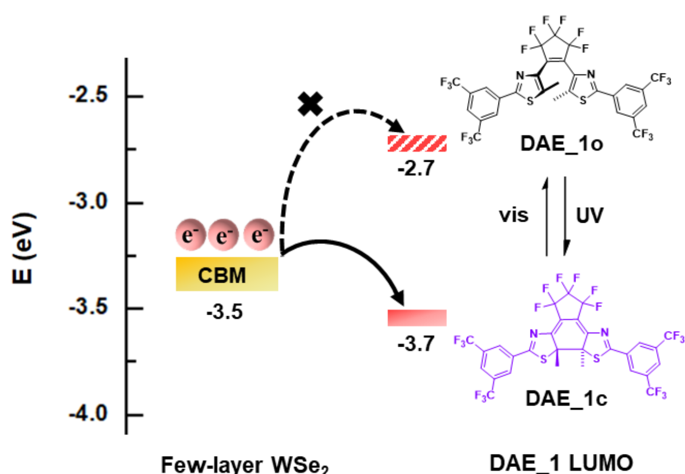

Figure 5-1. Energy level diagram of electron transport between WSe_2/DAE_1.

A schematic illustration of the energy level alignment between WSe_2/DAE_1 is depicted in Figure 5-1. For the intrinsically n-doped WSe_2, the energy of the conduction band minimum (CBM) is located

between the LUMO levels of DAE_1o and DAE_1c. In other words, the LUMO of DAE_1o features a higher energy value compared to the CBM of WSe_2, thereby impeding the electron transfer from WSe_2 to DAE_1o. Conversely, the DAE_1c isomer behaves as trapping site for WSe_2 electrons, resulting in a decrease of electron density in the FET device.

Similarly, for the BP FET with p-type dominant transport, the VBM of BP lies energetically between the HOMO levels of DAE_2o and DAE_2c. The driving force for hole trapping therefore exists only in the closed form of DAE_2, leading to a reduced hole density. To further reveal the role of energy levels of DAEs with respect to the tuning of the charge transport in 2DM, we extended our study to BP/DAE_3. With the HOMO of DAE_3c being isoenergetic to the VBM of BP, the photo-triggered hole trapping is nullified.

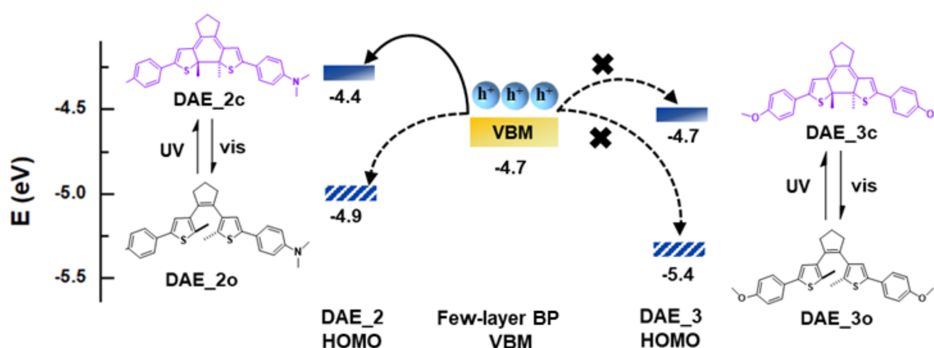

Figure 5-2. Energy level diagram of hole transport between BP/DAE_2 and BP/DAE_3.

5.2.2. Device preparation

High-quality flakes of 2D target materials (few layer WSe_2 or BP) are obtained by typical micro-mechanical exfoliation from bulk crystals (from HQ Graphene) with scotch tape and pressed onto highly n doped SiO_2 (90 nm)/Si substrates. Electrodes (Au 50 nm for WSe_2, Cr/Au 5 nm/45 nm for BP) are defined by laser writer, followed by thermally metal evaporation and lift-off process. The devices are annealed overnight (WSe_2 at 110 °C and BP at 200 °C) in ultra-high vacuum to remove the photoresist residues. The photoactive film is obtained by spin-coating DAE molecules from chloroform solutions (0.02 mg/mL) onto the substrate. (Details on the syntheses, photochemistry in solution and energy level determination of three DAE molecules have been previously reported.[12, 16] A mild baking at 55 °C for 1 hour is later performed to ensure the evaporation of chloroform. Since BP undergo degradation upon exposure to ambient air, the exfoliation and lift-off process are all performed in glovebox filled with N_2. Figure 5-3a shows an example of optical microscopy image of the WSe_2 FET device and 5-3b shows the device structure.

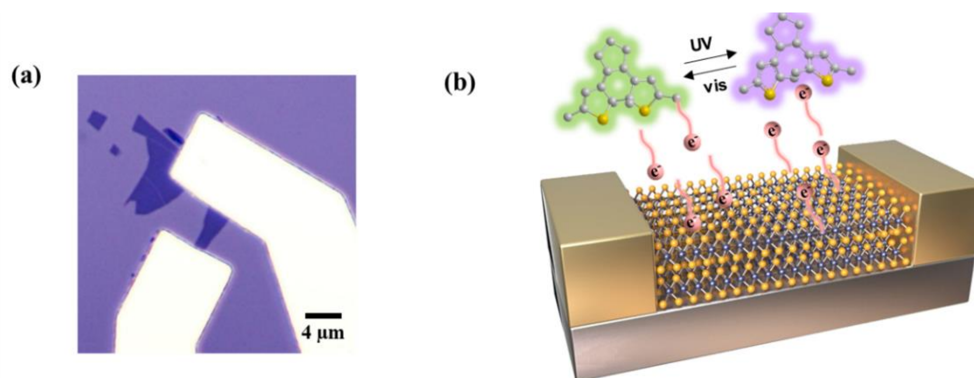

Figure 5-3. (a) An optical microscopy image of the WSe_2 FET device; (b) Schematic of the 2DM/DAE device structure.

5.2.3. Sample preparation for UV-vis absorption spectroscopy

Monolayer chemical vapor deposition (CVD) WSe_2, DAE film, and the WSe_2/DAE hybrid film is prepared on quartz substrate for UV-vis absorption spectroscopy.

CVD grown WSe_2 is purchased from SixCarbon. The poly(methyl methacrylate) (PMMA) solution is purchased from micro resist technology GmbH (MicroChem 950 PMMA C2). The as purchased CVD

grown WSe_2 (on SiO_2/Si substrate) is transferred onto a pre-cleaned quartz substrate (size: 1×1 cm^2) by using the PMMA-assisted wet transfer method, as introduced in chapter 4.3.

The DAE film is obtained by spin-coating (1000 rpm, 60 s) chloroform solutions (0.02 mg/mL) onto the quartz substrate or on WSe_2. A post baking at 55 °C for 1 hour after spin-coating is performed to ensure the complete chloroform evaporation. Note that the DAE film is prepared by using the same procedure used for fabricating FETs.

5.2.4. Characterization methods

UV/vis absorption spectra in film are recorded with a JASCO V-650 spectrophotometer. UV light irradiation is carried out by using an analysis lamp (312 nm, 6 W, Herolab), and vis light irradiation is performed using a white lamp (Dolan-Jenner MI-150 Illuminator) coupled with a long pass filter (> 520 nm).

Atomic force microscopy (AFM) images are recorded using a Nanoscope (Veeco Multimode V) in tapping mode under ambient conditions.

Raman spectra are recorded by using a Renishaw inVia spectrometer equipped with 532 nm laser.

The isomerization induced charge carrier density in the linear region of the transfer curve can be estimated by the formula below:[17]

$$\Delta n = \frac{C_i \Delta V_{th}}{e}$$

Where C_i is the gate capacitance per unit area;

V_g is the gate voltage, V_{th} is the threshold voltage.

The charge carrier mobility can be extracted in the linear regime from the transfer curve using the following equation:[18]

$$\mu = \frac{dI_{ds}}{dV_g} \cdot \frac{L}{W} \cdot \frac{1}{C_i} \cdot \frac{1}{V_{ds}}$$

Where L and W are the channel length and width of the FET respectively;

V_{ds} and I_{ds} is the source-drain voltage and current.

5.3. Results and discussion

5.3.1. Optical characterization

UV/vis absorption spectra of the three DAE molecules in film on quartz substrate were first characterized during the course of UV irradiation until reaching the photostationary state (PSS). In general, the PSS is reached under UV irradiation for 2 min and recovery within 5 min under vis light. As displayed in Figure 5-4, the three molecules show similar band evolution during UV irradiation. The initial spectrum for open isomer has a typical band at 312 nm. Following UV irradiation, the intensity of the peak around 312 nm clearly decreases, while another peak around 530 nm, originating from the closed isomers appears. The peak intensity gradually increases until reaching PSS state. The initial spectrum can be reobtained after vis illumination.

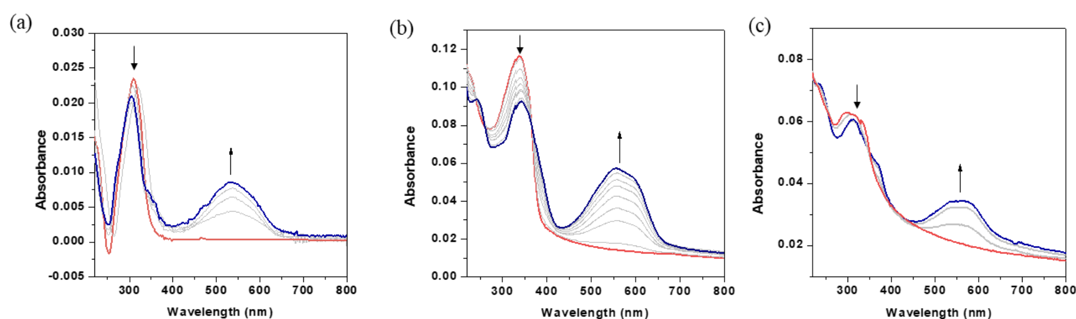

Figure 5-4. UV/vis absorption spectra of (a) DAE_1 (b) DAE_2 and (c) DAE_3 in film on quartz substrate during the course of UV irradiation until reaching the PSS.

To evaluate the tendency of DAE to undergo efficient photochemical isomerization when deposited on WSe_2, UV-vis absorption spectra of bare WSe_2, DAE film and WSe_2/DAE in the dark and after UV/vis irradiation have been recorded in Figure 5-5. The spectrum of monolayer WSe_2 possesses 4 predominant bands at ~ 420, 520, 600, and 740 nm in the range of 200-850 nm, in agreement with previous reports.[19] The absorption spectrum is unchanged upon exposure to UV or vis light. The spin-coated DAE films on WSe_2 displayed a spectrum which resembles the sum of WSe_2 and DAE, as it combines all their representative bands. Upon UV irradiation, the photochemical isomerization from DAE_1o to DAE_1c occurs, with a spectroscopic behavior being similar to the neat DAE_1 film. The band at 312 nm from DAE_1o clearly diminishes, while the band at 530 nm which originates from DAE_1c appears and superimposes with another band from WSe_2 at 520 nm, turning into a broader band. The initial spectrum can be completely re-established after sequential vis light irradiation. These observations provide clear evidence that the photoisomerization of DAE_1 is not perturbed by the underlying WSe_2 surface.

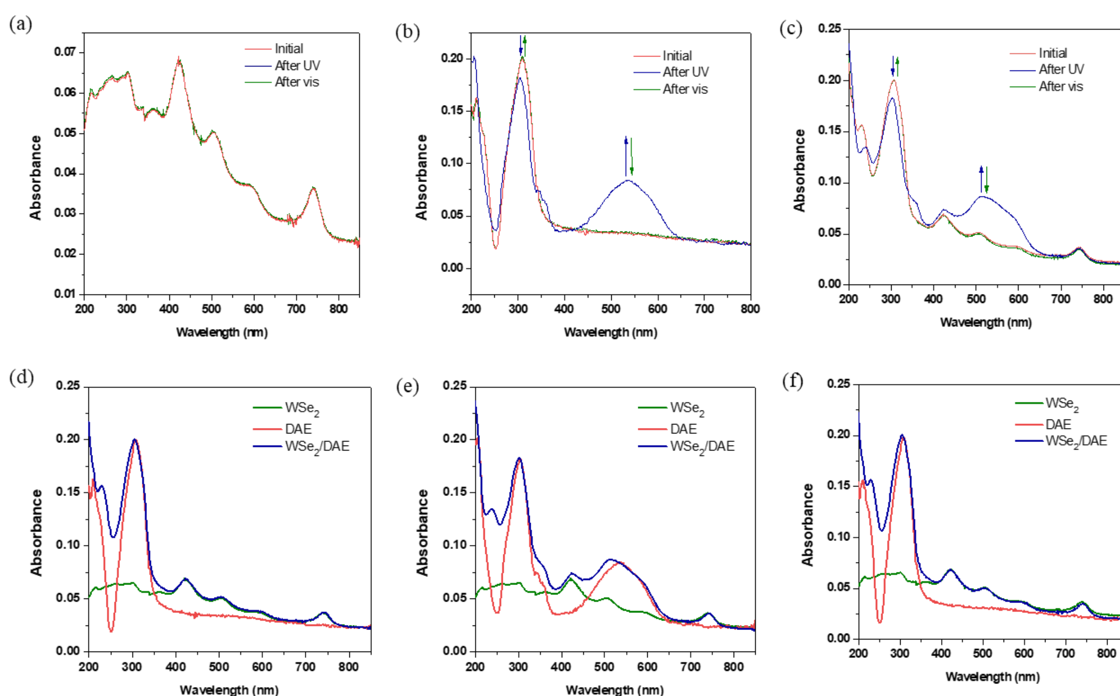

Figure 5-5. (a) to (c): UV/vis absorption spectra of (a) WSe_2, (b) DAE film and (c) WSe_2/DAE in dark and after UV/vis irradiation; (d) to (e): same dataset with (a) to (c) while plotted in another combination. UV/vis absorption spectra of WSe_2, DAE film and WSe_2/DAE (d) in the dark, (e) after UV irradiation, (f) after vis irradiation.

5.3.2. Characterization of 2DSs

The 2D flakes after exfoliation were first identified by optical microscope and Raman spectra and their thicknesses are further characterized by AFM.

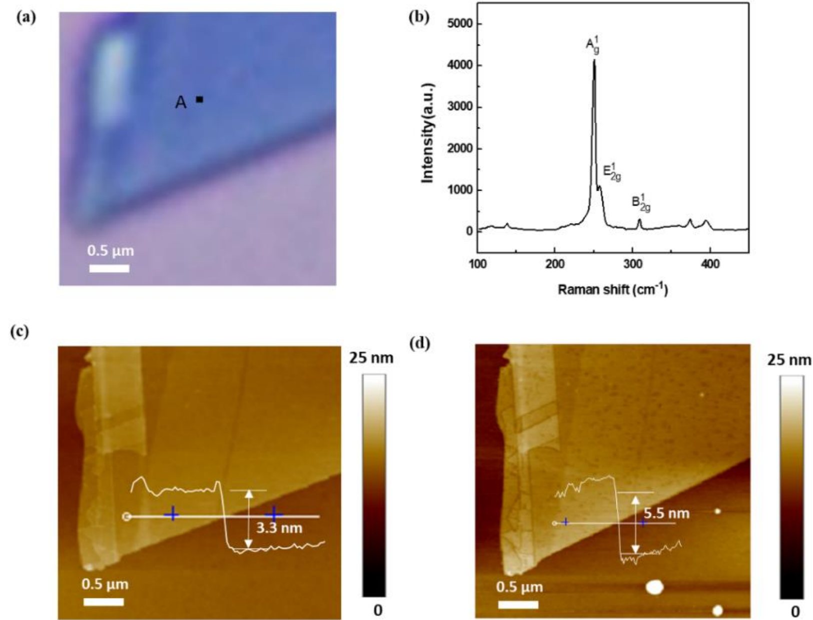

Figure 5-6. (a) Optical microscopy image, (b) Raman of few-layer WSe_2, (c) and (d) AFM image of the same flake (c) before (d) after DAE deposition.

Note that both of our chosen 2DSs show thickness-dependent physical properties and transport characteristics, especially for band structure evolution and carrier mobility. Though the electron trapping by DAE is favored by WSe_2 with higher CBM level thus thinner thickness, a high electron mobility is essential for achieving multilevel storage with a quantity of distinguishable current levels. Given that the highest electron mobility value for exfoliated WSe_2 is achieved for 12 atomic layers,[20] in order to find a good compromise between the ratio of electron transport modulation and the high device mobility, we have targeted WSe_2 flakes with an average thickness of 3.3 nm (corresponding to 6 atomic layers). Moreover, when compared to monolayer thick films, the few-layer flakes are found to have a better stability and tendency to form lower Schottky barriers with metal contacts.[21] Similarly, for BP the hole trapping is favored with lower VBM level, thus thinner flakes and 12 nm thickness exfoliated BP FET exhibits the highest hole mobility.[22] For this reason we have focused on flakes with a thickness of ca. 4.6 nm (corresponding to 8 atomic layers).

Figure 5-6a shows a typical optical microscopy image of few layer WSe_2 flake. The Raman spectra at point A is shown in Figure 5-6b, which has three active modes, E^1_{2g}, A_{1g} and B^1_{2g}. It suggests the few-layer structure and good material quality of the WSe_2 flake. Figure 5-6c and 5-6d displays the surface morphology of the same flake before and after DAE film deposition. The AFM image for bare WSe_2 flake reveals a smooth surface with thickness ~3.3 nm. After spin coating the molecular film, the surface roughness is clearly enhanced. By comparing the thickness of the same area, the thickness of DAE film is calculated to be ~2.2 nm.

Figure 5-7a shows an optical microscopy image of few layer BP flake. Its Raman spectra at point B shows three prominent peaks around ~360, 440 and 470 cm^{-1}, namely A^1_g, B_{2g} and A^2_g, respectively, which originate from the different variational modes of BP crystal lattice. The AFM image in Figure 5-7c suggests its thickness of ~4.9 nm.

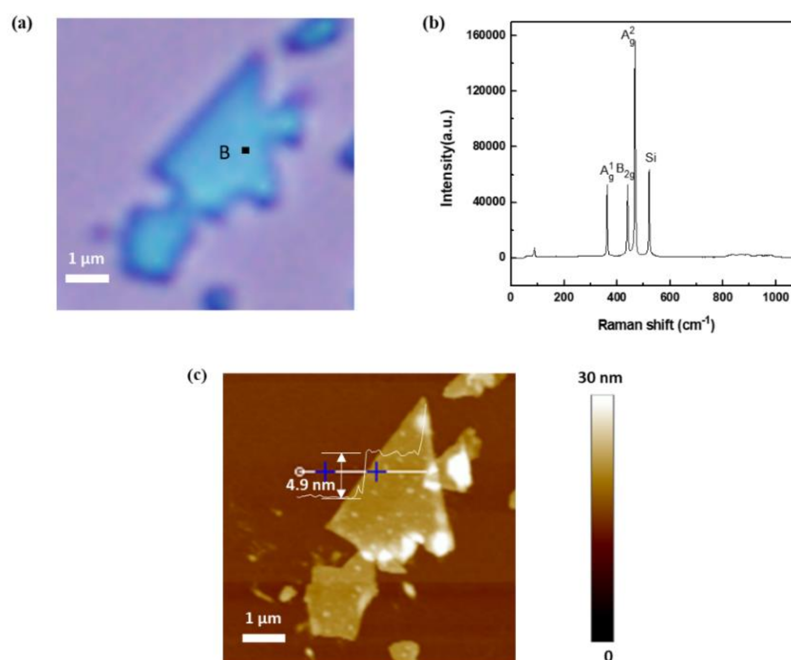

Figure 5-7. (a) Optical microscopy image, (b) Raman and (c) AFM image of few-layer BP.

5.3.3. Electrical characterization

5.3.3.1. Electrical characterization for WSe_2/DAE_1

To investigate the effect of the photo-switching of DAE_1 on the charge transport in WSe_2 based devices, FETs incorporating a few-layer of mechanically exfoliated WSe_2 flakes have been fabricated and characterized. Initially, the transfer and output characteristics of devices based on bare WSe_2 have been measured. Then, the measurement has been repeated after deposition of the DAE_1o thin film and after UV/vis irradiation. The evolution of the transfer curves is shown in Figure 5-8a. The device incorporating bare WSe_2 exhibited a typical electron-dominant transport behavior, with a threshold voltage V_{th} of 7.7 V and electron mobility μ_e (extracted from the transfer linear regime) of 16.6 $cm^2/V\cdot s$. The V_{th} shifts to 8.8 V upon physisorption of the DAE thin film, and the μ_e decreased to 14.3 $cm^2/V\cdot s$, indicating a minor p-type doping effect on WSe_2. Such an effect is attributed to the increasing charge scattering centers or trapping states by DAEs. Importantly, such a minor decrease in mobility indicates that upon physisorption of a DAE layer the WSe_2 largely preserves its pristine electrical performance. The conversion from DAE_1o to DAE_1c by UV irradiation for 30 s induced an additional p-type doping. The μ_e drops from 14.3 $cm^2/V\cdot s$ to 5.6 $cm^2/V\cdot s$ corresponding to a modulation of 60.8%. On the same time, the V_{th} is upshifted by 2.5 V, accompanied with a decreasing electron density $\triangle n_e$ of 6.25×10^{11} cm^{-2}. Such UV-induced p-doping effect can be ascribed to the fact that the DAE isomerization to the ring-closed form lowered its LUMO energy level by 1.1 eV, corresponding to a level below the CBM of WSe_2, allowing the electron donation from the WSe_2 to the DAE_1c. Moreover, upon vis light irradiation, the reverse process back to the DAE_1o occurs accompanied with a full recovery of the initial electrical characteristics. Such an evidence suggests that the modulation is related to the different photo-isomer states of DAEs and can be controlled upon alternating irradiation of UV and vis light.

Back gate sweeping (from 30 V to -30 V) is also implemented (Figure 5-8b). The obtained transfer curves present a similar evolution as forward gate sweeping, indicating that the transport modulation of WSe_2 applies to both forward and backward gate sweeping in spite of the hysteresis.

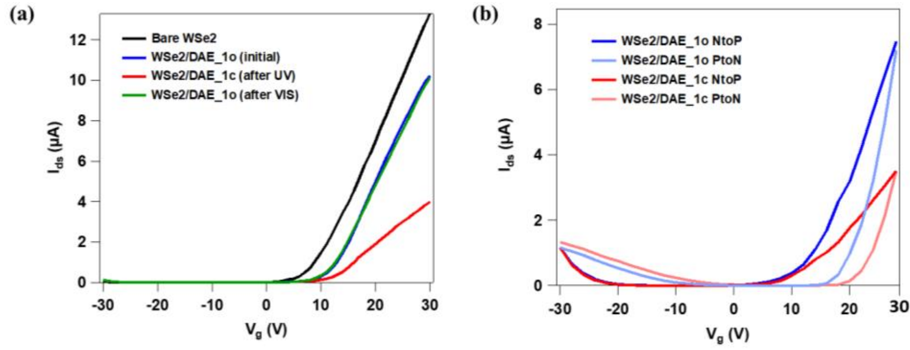

Figure 5-8. (a) Transfer evolution of bare WSe_2, WSe_2/DAE_1 as prepared and after UV/vis irradiation. (b) Transfer characteristics of WSe_2/DAE_1 via backward gate sweeping (V_g from 30 V to -30 V).

In order to rule out the possibility that the contribution to the modulation coming from WSe_2, it is mandatory to perform a blank test in which the electrical characteristics of the device based on bare WSe_2 without DAEs under the same irradiation conditions are measured. As displayed in Figure 5-9, the device exhibits no sign of photoresponsive behavior.

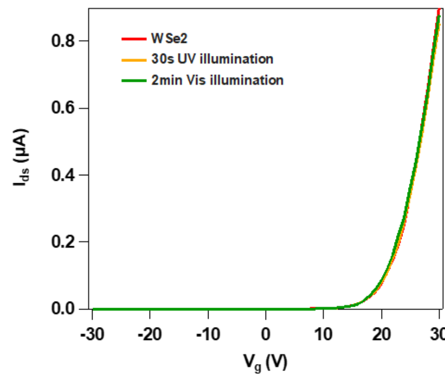

Figure 5-9. blank test on bare WSe_2 as prepared and after UV/vis irradiation.

Figure 5-10 displays the output characteristics of WSe_2/DAE_1o and WSe_2/DAE_1c respectively. The curves are linear and symmetrical, confirming the ohmic behavior of WSe_2 with respect to Au contact. With different applied source-drain voltage V_{ds}, source-drain current I_{ds} exhibits a downshift for DAE_1c modified WSe_2 compared to the case of DAE_1o, in analogy with the results of the transfer measurements.

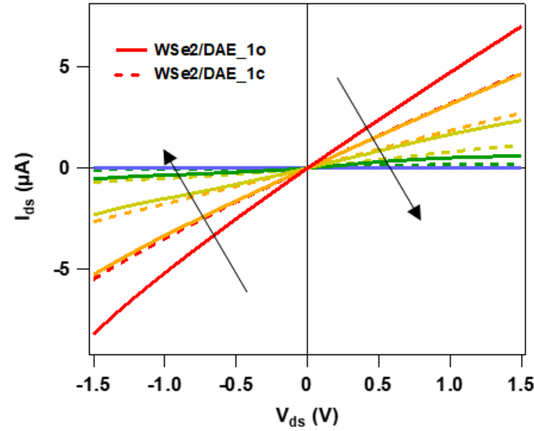

Figure 5-10. Output evolution of WSe_2/DAE_o and WSe_2/DAE_c for V_g from -30 V to 30 V in steps of 10 V.

The electrical characteristics are fully recovered upon vis light irradiation. Subsequently, UV/vis illumination cycles were carried out to investigate the stability of the DAE triggered photoswitching in the hybrid device. Figure 5-11a plots transfer curves acquired from 10 illumination cycles and 5-11b plots the normalized I_{ds} at V_g = 30 V and V_{ds} = 2 V over these cycles. The photoinduced current modulation is calculated to be ca. 61.7 %, showing an efficient electron trapping by DAE_1c. The absence of degradation demonstrates that the light driven current modulation possesses good stability, reversibility, and reproducibility.

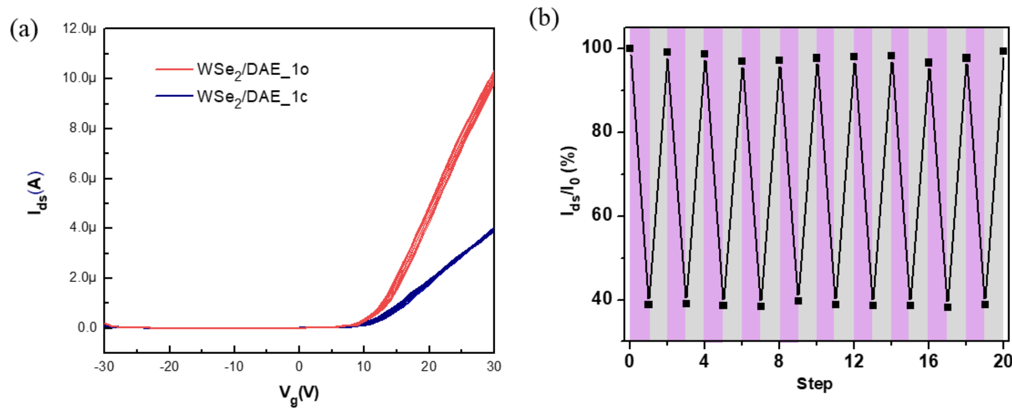

Figure 5-11. (a) WSe_2/DAE_1o-WSe_2/DAE_1c switching cycles for 10 times; (b)I_{ds} modulation over 10 illumination cycles with alternative UV (violet shaded areas) and vis (grey shaded areas) light. All current values are normalized to the initial value obtained from the as prepared WSe_2/DAE_1o. The connecting lines are used as guides to the eye.

In Figure 5-12, we present a multilevel current achieved by irradiating the device at different fixed times over 4 cycles. Level 0 is the current state when DAEs are all in their open form, corresponding to the current value obtained at $V_g = 30$ V in the transfer measurement of DAE_1o. Level 1 is reached upon 2 s of UV irradiation, and Levels 2, 3 and 4 are obtained by further UV irradiation for 4 s, 8 s and 16 s, respectively. Note that the entire UV irradiation time (30 s) is the same as we used in the former illumination cycles and Level 4 converges to the exact value of I_{ds} when DAEs are all in closed form. We performed 4 switching cycles; the standard deviation of each level is calculated and then divided by the total current difference between DAE_1o and DAE_1c (Table 5-1). The value obtained is below 1% for all these 5 levels, indicating that the device can attain a multitude of current levels with a high accuracy readout.

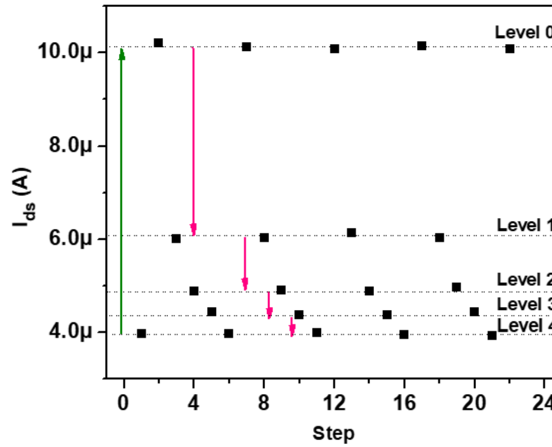

Figure 5-12. Multilevel current at fixed illumination times over 4 cycles. All single points of I_{ds} are values recorded from the transfer curve at $V_g = 30$ V and $V_{ds} = 2$ V.

Table 5-1. Calculated standard deviation for each current level presented in Figure 5-13.

	Level 0	Level 1	Level 2	Level 3	Level 4
I_{ds} cycle 1 (μA)	10.22	6.01	4.89	4.37	3.96
I_{ds} cycle 2 (μA)	10.13	6.03	4.90	4.36	3.96
I_{ds} cycle 3 (μA)	10.08	6.13	4.88	4.37	3.99
I_{ds} cycle 4 (μA)	10.15	6.02	4.97	4.43	3.94
I_{ds} cycle 5 (μA)	10.08				3.92
I_{ds} average (μA)	0.05	0.05	0.03	0.03	0.02
Standard deviation (μA)	10.13	6.05	4.91	4.38	3.96
Standard deviation/ I_{ds} gap	0.008	0.008	0.005	0.004	0.004

In view of the thermal stability of both photo-isomers, the devices incorporating DAEs are expected to exhibit good retention characteristics. Figure 5-14 displays the I_{ds} evolution upon different storage times. The standard derivation for these two levels is calculated respectively and divided by the current difference between DAE_1o and DAE_1c (I_{ds}_1o – I_{ds}_1c, Table 5-2). The negligible variation of both current levels after one week, as quantified by a standard deviation below 1.5% of the total current difference, provides unambiguous evidence for the excellent retention capacity of our devices, which renders them interesting elements for potential application as non-volatile memories.[23] Note that here the modulation of I_{ds} is up to 84.6%, and the intrinsic value of electron mobility (1.7 $cm^2/V\cdot s$) is 10 times lower than the above device (16.6 $cm^2/V\cdot s$). This is because the thickness of WSe_2 is thinner, which favors the electron transfer to DAE_1c and lowers the mobility. The result is consistent with our preliminary prediction.

The device is kept under dark except UV/vis irradiation to trigger the DAE photoswitching process. The higher current level belongs to DAE_1o and the lower belongs to DAE_1c.

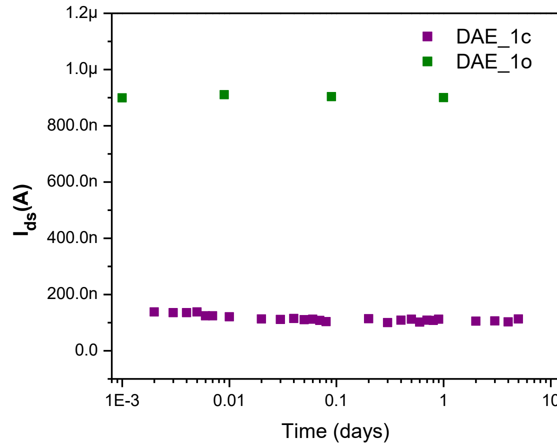

Figure 5-13: I_{ds} evolution with storage time in the dark.

Table 5-2. Calculated standard deviation for I_{ds}_1o and I_{ds}_1c in the Figure 5-13.

	Average Ids (µA)	**Standard deviation (µA)**	**Standard deviation/ I_{ds} difference**
I_{ds}_1o	0.90	0.004	0.005
I_{ds}_1c	0.11	0.011	0.013

I_{ds} difference = I_{ds}_1o – I_{ds}_1c

To further elucidate the effect of DAE photoswitching, the dynamic variation of I_{ds} with time is measured under alternating dark and illumination conditions, revealing similar trends as in previous experimental observations (Figure 5-14a). Owing to the bias stress effect when applying a constant positive gate voltage, the I_{ds} decays with time.[24] To address separately the contribution of DAE photoswitching, the bias-induced decay is fitted and subtracted from the curve (Detailed fitting curve and fitting parameters is provided in Figure 5-14c and Table 5-3). Figure 5-14b displays an example of one switching cycle (each cycle contains 15 s UV ON + 45 s light OFF + 120 s vis ON + 60 s light OFF). The violet boxed regions indicate the period when the UV light is on and the grey boxed regions indicate the period when the vis light is on. The initial current increase upon UV light is due to

photocurrent, which can be attributed to the conventional band-to-band transition that generates electron-hole pairs.[25] The I_{ds} then decreases gradually with time, as a result of the isomerization to DAE_1c, a process accompanied with electron donation from WSe_2 to DAE_1c. When UV irradiation is terminated, the decrease in photocurrent leads a rapid drop of I_{ds} owing to the exciton relaxation.[25] Similarly, for the case of vis illumination, the I_{ds} showed a sudden jump which is the photoresponse, followed by an increase because of the DAE_1c to DAE_1o back-isomerization. On the OFF state, I_{ds} resumes to the initial value before UV illumination, proving the modulation of I_{ds} by DAE photoswitching. The absence of fatigue for at least 16 static illumination cycles demonstrates that the device possesses an excellent stability and endurability.

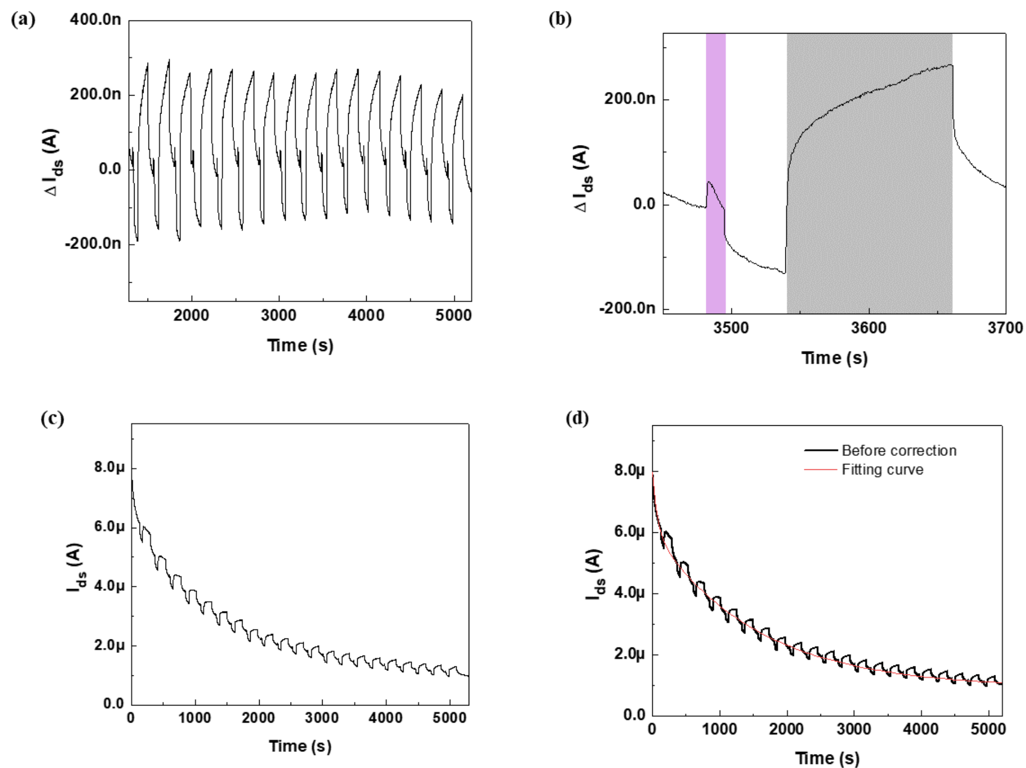

Figure 5-14. I_{ds}–time measurement under alternative dark and illumination conditions at V_g = 30 V and V_{ds} = 2 V (a) over 16 illumination cycles; (b) an example of one illumination cycle. Each cycle contains 15 s UV (violet shaded areas) and 2 min vis (grey shaded areas) light. The curve is corrected for bias stress effect; (c) Original curve without fitting; (d) fitting curve to correct the bias stress.

The curve is fitted by using the formula: $y = A_1*\exp(-x/t_1) + A_2*\exp(-x/t_2) + y_0$

Table 5-3. Parameters for the bias stress fitting curve.

	Value	**Standard deviation**
$\mathbf{y_0}$	7.34E-08	3.27E-10
$\mathbf{A_1}$	7.83E-08	5.66E-10
$\mathbf{t_1}$	29.74977	0.5013
$\mathbf{A_2}$	2.84E-07	3.15E-10
$\mathbf{t_2}$	974.05481	3.50119

For the sake of comparison, the I_{ds}-time measurement is also performed for the device based on bare WSe_2. As illustrated in Figure 5-15, the device shows only photoresponse, with I_{ds} ramps upon illumination and suddenly resumes to origin value under dark condition. The blank test unequivocally proves that WSe_2 is not responsible for the electron transport modulation under illumination.

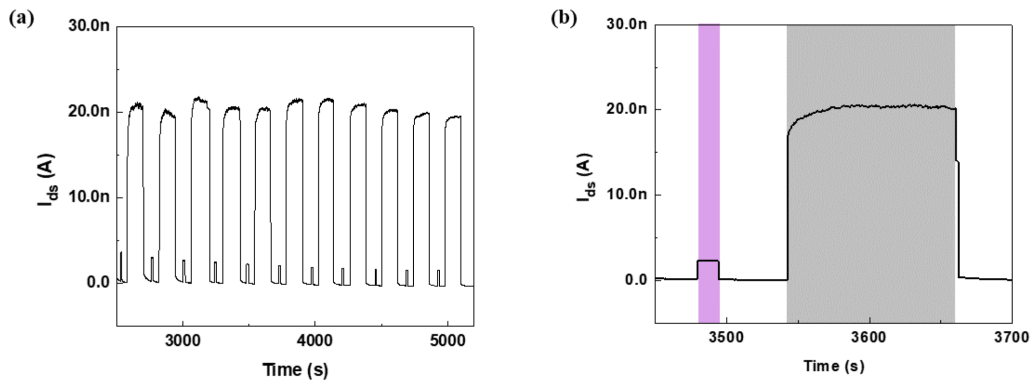

Figure 5-15. Control experiment on WSe_2. I_{ds}–time measurement under alternative dark and illumination conditions at $V_g = 30$ V and $V_{ds} = 2$ V: (a) over 11 illumination cycles, and (b) example of 1 illumination cycle.

5.3.3.2. Electrical characterization for BP/DAE_2 and BP/DAE_3

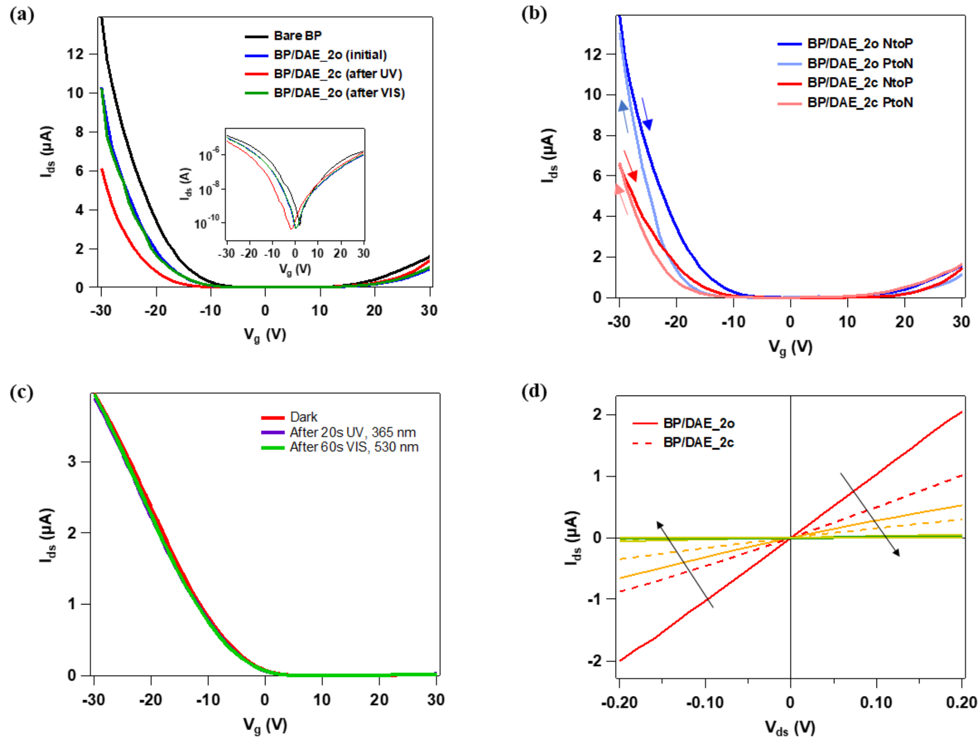

Figure 5-16. Electrical characterizations of BP/DAE_2 devices. (a) Transfer evolution of bare BP, BP/DAE_2 as prepared and after UV/vis irradiation. Inset: the same curves represented on a logarithmic scale; (b) Transfer characteristics via backward gate sweeping (V_g from 30 V to -30 V); (c) Transfer evolution of bare BP as prepared and after UV/vis irradiation; (d) Output evolution of BP/DAE_2o and BP/DAE_3c for V_g from -30 V to 30 V in steps of 10 V.

To demonstrate the general applicability of the charge transport modulation in two-dimensional semiconductors via energy level phototuning we applied same procedure to BP based FET (Figure 5-16a). The pristine BP device shows p-type-dominant electrical characteristics with a hole mobility μ_h = 87.2 $cm^2/V\cdot s$. Upon deposition of the DAE_2o film, the V_{th} downshifted and μ_h decreased to 68.7 $cm^2/V\cdot s$, suggesting that BP is potentially n-type doped by DAE_2. Subsequent UV irradiation reveals a further decrease of μ_h by a modulation of 48.9%. The variation is accompanied with a negative shift of V_{th} by 2.7 V as well as a decrease of hole density Δn_h of 6.75×10^{11} cm^{-2}, revealing a further n-type doping effect and a depletion of the hole carriers. All these variations are recovered back by vis illumination. Such reversible doping effect complies with our picture of hole trapping process: UV irradiation induces the photo-isomerization from DAE_2o to DAE_2c, leading to an increase of

corresponding HOMO energy level. The higher HOMO level of DAE_2c act as traps for holes from BP, which is reflected in the decrease of hole density. The vis irradiation converts the photochromic molecules back to ring-open form. Backward gate sweeping is likewise carried out on BP/DAE_2 devices, which shows the same evolution as forward gate sweeping. Reference device with bare BP shows no response by the same light irradiation, therefore the optically induced hole transport modulation can be ascribed to the light-response of the DAE photoswitch. The measured output characteristics show the same tendency of I_{ds} modulation.

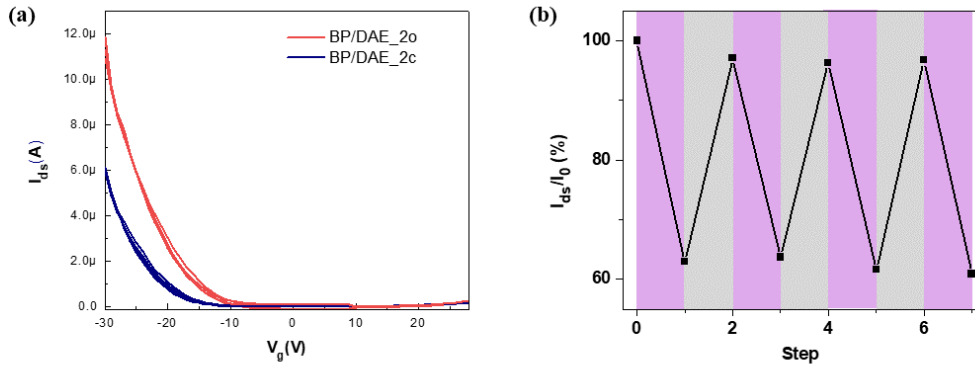

Figure 5-17. (a) Transfer evolution of BP/DAE_2 under 4 UV/vis irradiation cycles; (b)Normalized I_{ds} modulation over 4 illumination cycles with UV (violet shaded areas) and vis (grey shaded areas) light at V_g = -30 V and V_{ds} = 2V.

As shown in Figure 5-17, the modulation of I_{ds} at V_g = -30 V is around 37.4 % and is stable over the measured 4 illumination cycles.

To support above-mentioned interpretation, we have extended our study to BP/DAE_3. Clearly, the I_{ds} decreases after DAE_3 deposition, while no further variation is observed as a result of either UV or vis light irradiation. Taking into account the energy levels depicted in Figure 5-2, the result is not surprising because of the absence of driving force for hole transfer from BP to DAE_3c. This phenomenon provides clear evidence that suitably designed DAEs possessing *ad hoc* energy level alignment with the semiconducting 2DMs is required to achieve efficient optical modulation of the charge transport in the hybrid devices.

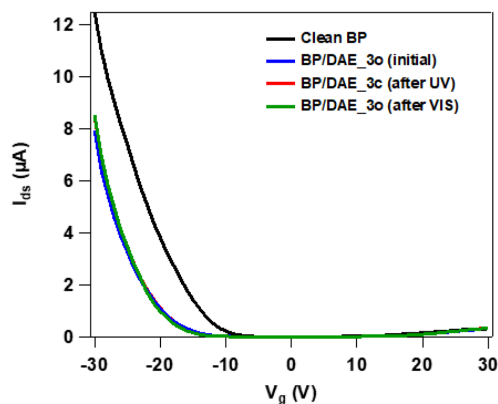

Figure 5-18. Transfer evolution of bare BP, BP/DAE_3 as prepared and after UV/vis irradiation at V_{ds} = 2 V.

5.4. Conclusion

In summary, we have fabricated two-dimensional semiconductor-based light-responsive FETs via energy level phototuning. The device's electrical performance can be reversibly modulated by light illumination with well-defined wavelengths. In particular, the physisorbed photochromic DAEs act as optical switching elements, thereby allowing for the fine-tuning and remote control over the charge transport of the host 2DM. To prove the general applicability of our approach we have challenged it by realizing n- and p-type dominated ambipolar FETs containing a few-layer WSe_2 and BP, respectively. In each pair of 2DM/DAE, the modulation is achieved when the CBM or VBM of 2DM is energetically sandwiched between the LUMO or HOMO gap of the two photo-isomers of DAEs, respectively. Our approach is thus proved feasible for both electron and hole transport modulation depending on the nature of target 2DM without sacrificing their intrinsic performance, confirming its general applicability and effectiveness. Our strategy can be extended to modulate the electrical characteristics of devices integrating other 2DMs by simply choosing suitable DAEs, thereby opening the door for multi-responsive 2DM/DAEs based FETs that can be switched ON and OFF upon irradiation with light. Noteworthy, the FET device based on such 2DM/DAE system displayed excellent data retention capacity and a high accuracy readout with several distinguishable current levels, opening perspectives towards their use as multilevel non-volatile memory. Furthermore, such controlled optical switching of the charge injection and transport in 2DM-based systems may pave the way to a new era of electronics, which incorporate novel functions in a single device based on high-performing 2D materials.

5.5. References

[1] a) F. Bonaccorso, Z. Sun, T. Hasan, A. C. Ferrari, *Nat. Photonics* **2010**, *4*, 611; b) Q. H. Wang, K. Kalantar-Zadeh, A. Kis, J. N. Coleman, M. S. Strano, *Nat. Nanotechnol.* **2012**, *7*, 699; c) F. Xia, H. Wang, D. Xiao, M. Dubey, A. Ramasubramaniam, *Nat. Photonics* **2014**, *8*, 899.

[2] S. Bertolazzi, M. Gobbi, Y. Zhao, C. Backes, P. Samorì, *Chem. Soc. Rev.* **2018**, *47*, 6845.

[3] a) C. Anichini, W. Czepa, D. Pakulski, A. Aliprandi, A. Ciesielski, P. Samorì, *Chem. Soc. Rev.* **2018**, *47*, 4860; b) Q. He, S. Wu, Z. Yin, H. Zhang, *Chemical Science* **2012**, *3*, 1764; c) S. Wu, Q. He, C. Tan, Y. Wang, H. Zhang, **2013**, *9*, 1160.

[4] Y. Zhao, S. Ippolito, P. Samorì, *Adv. Opt. Mater.* **2019**, *7*, 1900286.

[5] M. Gobbi, E. Orgiu, P. Samorì, *Adv. Mater.* **2018**, *30*, 1706103.

[6] a) E. Orgiu, P. Samorì, *Adv. Mater.* **2014**, *26*, 1827; b) X. Zhang, L. Hou, P. Samorì, *Nat. Commun.* **2016**, *7*, 11118.

[7] H. M. D. Bandara, S. C. Burdette, *Chem. Soc. Rev.* **2012**, *41*, 1809.

[8] R. Klajn, *Chem. Soc. Rev.* **2014**, *43*, 148.

[9] M. Irie, T. Fukaminato, K. Matsuda, S. Kobatake, *Chem. Rev.* **2014**, *114*, 12174.

[10] a) Y. Zhao, S. Bertolazzi, P. Samorì, *ACS Nano* **2019**, *13*, 4814; b) M. Kim, N. S. Safron, C. Huang, M. S. Arnold, P. Gopalan, *Nano Lett.* **2012**, *12*, 182; c) M. Gobbi, S. Bonacchi, J. X. Lian, A. Vercouter, S. Bertolazzi, B. Zyska, M. Timpel, R. Tatti, Y. Olivier, S. Hecht, M. V. Nardi, D. Beljonne, E. Orgiu, P. Samorì, *Nat. Commun.* **2018**, *9*, 2661; d) A. R. Jang, E. K. Jeon, D. Kang, G. Kim, B.-S. Kim, D. J. Kang, H. S. Shin, *ACS Nano* **2012**, *6*, 9207.

[11] M. Herder, F. Eisenreich, A. Bonasera, A. Grafl, L. Grubert, M. Pätzel, J. Schwarz, S. Hecht, *Chem. Eur. J.* **2017**, *23*, 3743.

[12] M. Herder, B. M. Schmidt, L. Grubert, M. Pätzel, J. Schwarz, S. Hecht, *J. Am. Chem. Soc.* **2015**, *137*, 2738.

[13] Y. Guo, J. J. Robertson, *Appl. Phys. Lett.* **2016**, *108*, 233104.

[14] Y. Cai, G. Zhang, Y.-W. Zhang, *Sci. Rep.* **2014**, *4*, 6677.

[15] E. Orgiu, N. Crivillers, M. Herder, L. Grubert, M. Pätzel, J. Frisch, E. Pavlica, D. T. Duong, G. Bratina, A. Salleo, N. Koch, S. Hecht, P. Samorì, *Nat. Chem.* **2012**, *4*, 675.

[16] J. J. D. Jong, L. N. Lucas, R. Hania, A. Pugzlys, R. M. Kellogg, B. L. Feringa, K. Duppen, J. H. V. Esch, *Eur. J. Org. Chem.* **2003**, *2003*, 1887.

[17] S. Helveg, J. V. Lauritsen, E. Lægsgaard, I. Stensgaard, J. K. Nørskov, B. S. Clausen, H. Topsøe, F. Besenbacher, *Phys. Rev. Lett.* **2000**, *84*, 951.

[18] H. Liu, A. T. Neal, P. D. Ye, *ACS Nano* **2012**, *6*, 8563.

[19] J. Lu, A. Carvalho, H. Liu, S. X. Lim, A. H. Castro Neto, C. H. Sow, *Angew. Chem.* **2016**, *128*, 12124.

[20] N. R. Pradhan, D. Rhodes, S. Memaran, J. M. Poumirol, D. Smirnov, S. Talapatra, S. Feng, N. Perea-Lopez, A. L. Elias, M. Terrones, P. M. Ajayan, L. Balicas, *Sci. Rep.* **2015**, *5*, 8979.

[21] W. Liu, J. Kang, D. Sarkar, Y. Khatami, D. Jena, K. Banerjee, *Nano Lett.* **2013**, *13*, 1983.

[22] J. Jia, S. K. Jang, S. Lai, J. Xu, Y. J. Choi, J.-H. Park, S. Lee, *ACS Nano* **2015**, *9*, 8729.

[23] S. Bertolazzi, P. Bondavalli, S. Roche, T. San, S.-Y. Choi, L. Colombo, F. Bonaccorso, P. Samorì, *Adv. Mater.* **2019**, *31*, 1806663.

[24] K. Cho, W. Park, J. Park, H. Jeong, J. Jang, T.-Y. Kim, W.-K. Hong, S. Hong, T. Lee, *ACS Nano* **2013**, *7*, 7751.

[25] Y.-C. Wu, C.-H. Liu, S.-Y. Chen, F.-Y. Shih, P.-H. Ho, C.-W. Chen, C.-T. Liang, W.-H. Wang, *Sci. Rep.* **2015**, *5*, 11472.

Chapter 6 Simultaneous optical tuning of hole and electron transport in ambipolar WSe_2 interfaced with a bicomponent photochromic layer

The interfacing of two-dimensional semiconductors (2DSs) with photochromic molecules provides an efficient solution to reversibly modulate their outstanding electronic properties and offers a versatile platform for the development of multifunctional field-effect transistors (FETs). Herein optically switchable multilevel high-mobility FETs based on few-layer ambipolar WSe_2 are realized by applying on its surface a suitably designed bicomponent diarylethene (DAE) blend, in which both, hole and electron transport can be *simultaneously* modulated for over 20 cycles. The high output current modulation efficiency (97% for holes and 52% for electrons) ensures 128 distinct current levels, corresponding to a data storage capacity of 7 bit. The device is also implemented on a flexible and transparent polyethylene terephthalate substrate, rendering the 2DSs/DAEs hybrid structures promising candidates for flexible multilevel nonvolatile memories.

6.1. Introduction

Atomically thin 2DMs combining exceptional electronic, optical, and mechanical properties, as well as chemical stability, are promising candidates as key components for various applications spanning from (opto)electronics,[1] photonics,[2] sensing,[3] to ultra-flexible and wearable electronics,[4] in the post-silicon era. In the past decade the scientific community has witnessed the booming of fundamental studies as well as technological advancements in the field of 2DSs. Alongside exploring their intrinsic properties, various physical and chemical modification strategies have been adopted in order to tune the 2DS's functions and device performances.[5] Among them, achieving a tunable control over the electronic properties of 2DSs without introducing any defects still remains a major challenge,[6] which is at the same time highly appealing for the development of practical multilevel stimuli-responsive electronics.[7] The interfacing with molecular systems possessing tunable structures and functionalities constitutes an efficient and versatile approach to provide different charge carrier doping levels and thus to reversibly modulate the opto-electronic properties of 2DSs.[8] For example, it has been demonstrated that photochromic molecules, capable of undergoing reversible isomerization between two different

states induced by light stimuli,[9] can serve as optically-responsive components when employed to functionalize unipolar 2DSs.[10] Importantly, such hybrid structures take full advantage of the ultra-high sensitivity of 2DSs to any subtle environmental change,[8b] which will emerge as an additional molecular-driven photoresponsivity. This enables the 2DSs/photochromic molecules hybrid structures to serve as active components in superior multifunctional transistors/memories that can optically be addressed and operated due to efficient and highly sensitive ON/OFF switching upon irradiation with light at defined wavelengths.[11] In the previous chapter we have demonstrated the unipolar modulation of either electron transport in few-layer WSe_2 or hole transport in few-layer black phosphorous-based optically switchable FETs by interfacing suitable photochromic molecules as optical switching elements.[12] However, the *simultaneous* photo-modulation of both electron and hole transport in the target 2D materials has not been achieved before. It would be of utmost importance for a practical multilevel transistor as well as for the development of responsive organic complementary circuits (CMOS like) and photo-tunable inverters, and as a consequence the applicability of such 2DSs/photochromic molecules hybrid systems could largely be extended.

In last chapter, we focused on WSe_2 flakes possessing an n-type dominant ambipolar behavior, with its electron current (10^{-5} A) three orders of magnitude larger than the hole current (10^{-8} A). Therefore, the modulation of hole current by operation of the photochromic molecule was not visually distinguishable. Inspired by the phenomenon that the main type of charge carrier in WSe_2 changes with its thickness, ranging from p-type, ambipolar to n-type,[13] in this work we tackle *full ambipolar* switching of charge transport in 2DM/photochromic molecule blends. For this purpose, we target few-layer WSe_2 flakes with a more balanced ambipolar behavior, with its electron and hole current on the same scale (10^{-6} A). We propose an optically switchable multilevel FET by interfacing WSe_2 with a bicomponent DAE blend consisting of two DAE molecules with specific energy levels, which are engineered in order to be capable of trapping either the electrons or the holes of WSe_2. The device is demonstrated to be able to modulate both electron and hole transport *simultaneously* by remote light stimuli. The photo-modulation is demonstrated to be efficient and reversible with negligible switching fatigue after over 20 illumination cycles. Noteworthy, the output current modulation for holes is as high as 97%, while

for electrons the modulation amounts to 52%. Moreover, such current modulation ratio can be readily tuned by controlling the light dose, which means by adjusting the irradiation duration the FET device can reach a multitude of current states. In particular, the balanced ambipolar characteristic of WSe_2 enables our device to attain 64 distinct current levels for both holes and electrons, as evidenced through a precise control and fine-tuning over the output current thereby highlighting its potential to be further developed into multilevel memories with data storage capacity of 7 bit.[14] Additionally, by taking advantage of the thermal bistability of DAE molecules at both photo-isomeric states,[15] the device is shown to possess a prolonged retention time exceeding 20 days in the dark. This result outperforms the current state-of-the-art memories based on other photochromic molecules, such as spiropyrans and azobenzenes,[16] and is highly promising for applications as non-volatile memories.[17] Remarkably, taking full advantage of the superior mechanical properties of ultra-thin 2D WSe_2, our device is also able to be operated on a flexible and transparent polyethylene terephthalate (PET) substrate, without losing its optical switching capability, which is attractive for future generation of multifunctional wearable electronics. When compared with memories based on organic semiconductors blended with DAE molecules,[18] our memories based on 2DSs show similar features while hold higher mobilities and miniaturizing size at the atomic level thickness.

6.2. Experimental methods

6.2.1. Match of energy level between ambipolar WSe_2 and DAEs.

In order to realize two charge carrier modulation, here we employed a bicomponent DAE blend, which consists of two different molecules namely DAE_1[19] and DAE_3,[20] both of which feature tunable lowest unoccupied molecular orbital (LUMO)/highest occupied molecular orbital (HOMO) energy levels above or below conduction band (CB) and valence band (VB), respectively, of WSe_2.[21] Therefore, we are able to utilize the optically responsive nature of the photochromic molecules to modulate the charge transport of both electrons and holes in the WSe_2 channel. Figure 6-1 illustrates the detailed energy-level diagram of DAE_1, DAE_3, and WSe_2. The yellow bands represent the CB/VB of few-layer WSe_2. The electron transport modulation is realized by DAE_1, since the

conduction band minimum (CBM) of WSe_2 (-3.5 eV) lies energetically between the LUMO levels of the open isomer (DAE_1o, -2.7 eV) and the closed isomer (DAE_1c, -3.7 eV). The lower LUMO of DAE_1c behaves as electron-accepting level (trapping the transferred electrons from WSe_2, thus reducing the current to gain modulation), while higher LUMO energy of DAE_1o impedes the electron transfer from WSe_2 (no modulation). Similarly, the valence band maximum (VBM) of WSe_2 (-5.1 eV) is located between the HOMO of DAE_3o (-5.4 eV) and DAE_3c (-4.7 eV), enabling the modulation of hole transport. DAE_3c behaves as a trapping site (modulation) while DAE_3o only represents a scattering center for the holes (no modulation) travelling in WSe_2. In general, upon UV irradiation at 312 nm, both DAE molecules are converted to their closed photo-isomeric states, accompanied with a simultaneous transfer of electrons and holes from WSe_2 channel to DAEs, inducing a decrease of charge carrier density in the FET device as well as the current. Conversely, upon visible (vis) light irradiation at 530 nm the DAE molecules switch back to their open isomer states, resulting in full recovery of the charge carrier density within WSe_2 also the current. Note that in order to largely preserve the intrinsic properties of WSe_2 and to minimize the perturbation of DAE molecules, the DAE blends are simply spin-coated onto the substrate and form a non-covalent bonding with WSe_2 flakes.

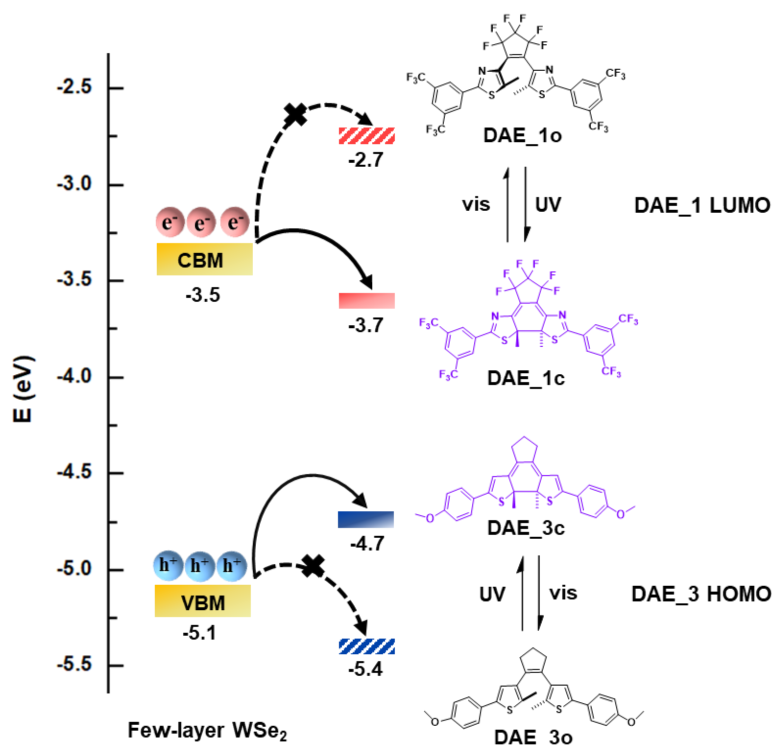

Figure 6-1. Energy level diagram of electron transport between WSe_2/DAE_1 and hole transport between WSe_2/DAE_3.

6.2.2. Device fabrication

6.2.2.1. WSe_2 FET on Si substrate

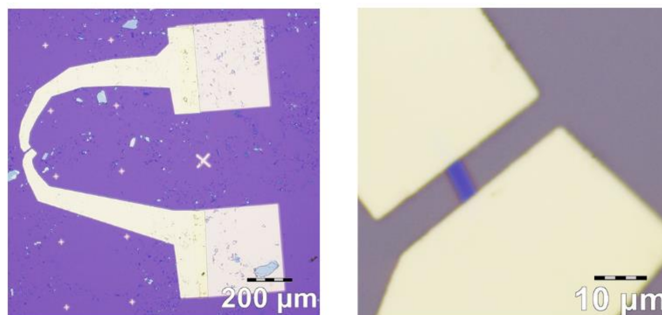

Figure 6-2. An example of optical microscopy image of the WSe_2 FET device

Few-layer WSe_2 flakes are obtained by mechanical exfoliation from bulk crystals (from HQ Graphene) with scotch tape and transferred to highly n doped Si/SiO_2 (270 nm) substrates, which enables to preserve the outstanding electronic properties with an ambipolar transport behavior, suggesting the presence of both abundant free electron and hole charge carriers in the channel. FETs devices were fabricated by using a laser writer to pattern electrodes, followed by metal evaporation (Au 60 nm) and lift-off process. The devices are annealed overnight at 110 °C in ultra-high vacuum to remove the photoresist residues. Figure 6-2 shows an example of optical microscopy image of the WSe_2 FET device and 6-3 shows the device structure.

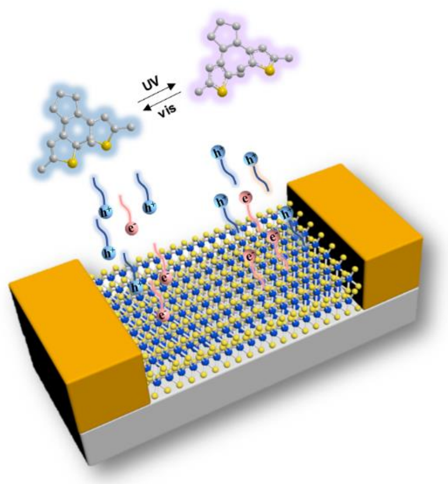

Figure 6-3. Schematic illustration of the FET device architechture based on WSe_2/DAE blend on Si/SiO_2 substrate.

6.2.2.2. WSe_2 FET on PET substrate

The as-fabricated WSe_2 FET on Si/SiO_2 substrate is transferred to PET/ITO/CL-PVP substrate by using the PMMA-assisted transfer process, as introduced the chapter 4.3.

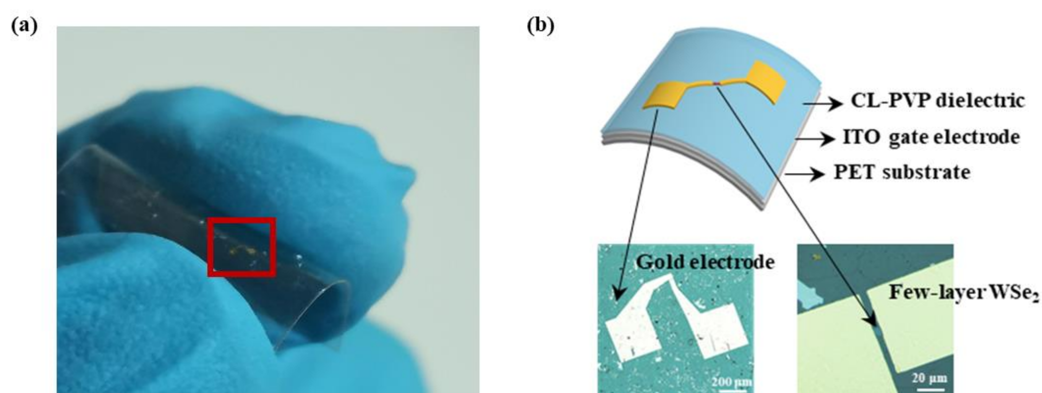

Figure 6-4. (a) Photograph of a typical WSe_2/DAE blend FET device on flexible and transparent PET substrate. (b) Schematic (top) and corresponding optical microscopy images (bottom) of FET device.

6.2.3. Sample preparation for UV-vis absorption spectroscopy

Monolayer (chemical vapor deposition) CVD WSe_2, DAE_1 film, DAE_3 film, DAE blend film, and the WSe_2/DAE blend hybrid film were respectively prepared on quartz substrate for UV-vis absorption spectroscopy.

CVD grown WSe_2 was purchased from SixCarbon. The as purchased CVD grown WSe_2 (on Si/SiO_2 substrate) was transferred onto a pre-cleaned quartz substrate (size: 1×1 cm^2) by using the poly(methyl methacrylate (PMMA) assistant wet transfer method, as introduced in chapter 4.3.

The DAE_1 film, DAE_3 film, DAE blend film was obtained by respectively spin-coating (1000 rpm, 60 s) chloroform solutions (0.02 mg/mL) onto the quartz substrate. A post baking at 55 °C for 1 hour after spin-coating was performed to ensure the complete chloroform evaporation. Note that the DAE film was prepared by using the same procedure used for fabricating FETs.

6.2.4. Characterization methods

UV/vis absorption spectra of the DAE blend film on quartz substrate is recorded with a JASCO V-650 spectrophotometer. The molecular switching is triggered either by an analysis lamp at 312 nm (1.2 mWcm^{-2}, from Herolab) for 40 s or a white lamp (from Dolan-Jenner MI-150 Illuminator) coupled with a long pass filter (> 520 nm) for 1 min.

Raman spectra were recorded by a Renishaw inVia spectrometer equipped with 532 nm laser.

Atomic force microscopy (AFM) imaging was carried out by a Nanoscope (Veeco Multimode V) in tapping mode under ambient conditions.

All electrical measurements were carried out by using a probe station connected to a Keithley 2636 in a glovebox filled with nitrogen. Device irradiation is realized by using a monochromator set-up, with either UV light (at λ = 312 nm, 0.15 mWcm^{-2}) or vis light (λ = 530 nm, 11.8 mWcm^{-2}). The PSS is reached under UV irradiation for 150 s and recovery within 20 min under vis light.

The charge carrier mobility is extracted in the linear regime from the transfer curve by the equation:[22]

$$\mu = \frac{dI_{ds}}{dV_g} \times \frac{L}{W} \times \frac{1}{V_{ds}C_i}$$

Where L is the channel length, W is the channel width, and C_i is the gate capacitance per unit area.

The molecular isomerization-induced is estimated by the equation:[23]

$$\triangle n = C_i \frac{\triangle V_{th}}{e}$$

Where $\triangle V_{th}$ is the difference of threshold voltage before and after molecular isomerization, e is the elementary charge.

6.3. Results and discussion

6.3.1. Optical characterization

The syntheses, photochemistry both in solution and in films and energy level determination of the two

DAE molecules used have been previously reported.[12, 19-20]

The absorption spectra of DAE_1 and DAE_3 show same trend after UV/vis irradiation (Figure 6-5). The initial spectrum displays a characteristic band at 312 nm, which originates from DAE_o. After UV irradiation, this band diminishes while another band centered at 530 nm appears which can be attributed to DAE_c. The initial spectrum can be recovered after subsequent vis illumination, confirming the switching ability of the DAE compounds in the solid state. Importantly, both two DAEs show similar molar absorptivities, speed of photoisomerization (quantum yields), and almost quantitative formation of the ring closed isomer under UV irradiation,[20] allowing for their fully simultaneous operation in the device.

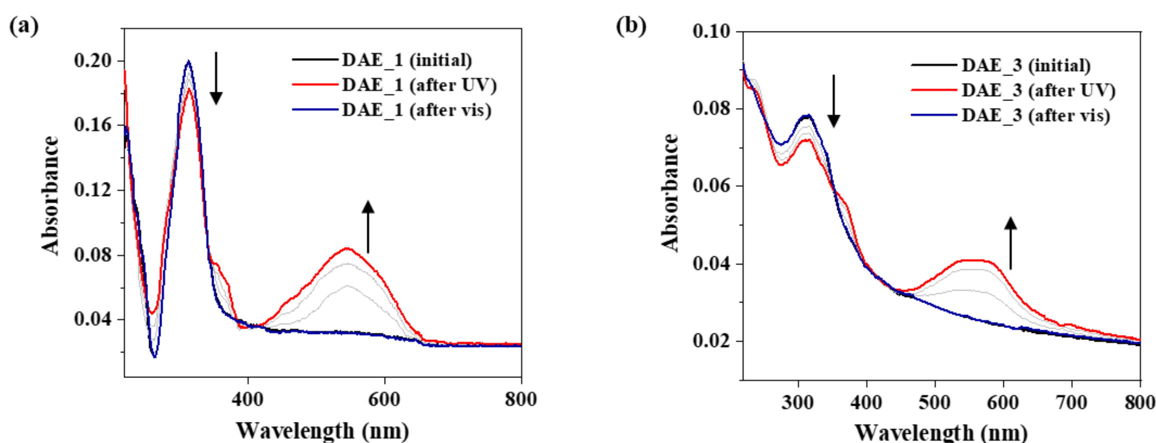

Figure 6-5. UV-vis absorption spectra for (a) DAE_1, (b)DAE_3 film during the course of UV irradiation.

To assess the photo-switching ability of DAE molecules after physisorption on WSe_2, UV-vis absorption spectra of the WSe_2/DAE blend hybrid film was initially recorded on quartz substrates. The evolution of the absorption spectra of DAE blend was similar to single molecules as DAE_1 and DAE_3 and shows same trend after UV/vis irradiation (Figure 6-6a).

The spectrum of WSe_2 possesses 4 prominent bands at ~ 420, 520, 600, and 740 nm, in accordance with previous reports[24]. It remains unchanged when subjected to either UV or vis light illumination.

For the WSe_2/DAE blend hybrid, it combines all the representative peaks of both DAE and WSe_2. following UV irradiation, the intensity of the peak around 312 nm corresponding to open isomers clearly decreases, while another peak around 530 nm originating from the closed isomers appears. The original absorption features are recovered after vis irradiation. Therefore, the DAE molecules in the solid-state blended film are still able to undergo reversible photo-isomerization when physiosorbed onto the surface of WSe_2.

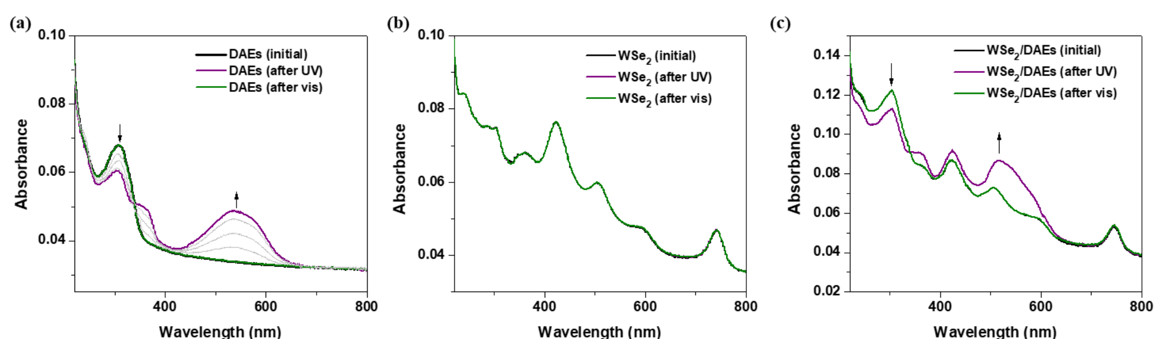

Figure 6-6. UV-vis absorption spectra for (a) DAE blend, (b) WSe_2, (c)WSe_2/DAE blend in dark and after UV/vis irradiation on quartz substrate.

6.3.2. WSe_2 characterization

The WSe_2 flakes after exfoliation were first identified by optical microscope and Raman spectra, and their thicknesses were further determined by AFM imaging.

In order to obtain a multilevel device with a quantity of distinguishable current levels, a high mobility for both electron and hole is required, therefore we target on WSe_2 flakes with an average thickness of 4.3 nm (corresponding to 7 atomic layers). Figure 6-7a shows a typical optical microscopy image of the flake, and Figure 6-7b displays its Raman spectrum at point A. The Raman spectrum possesses three active modes, E^1_{2g}, A_{1g} and B^1_{2g}, suggesting a good material quality.

AFM topographical imaging of WSe_2 flake enabled to visualize the flakes and quantify their thickness as ~4.3 nm. The surface roughness of WSe_2 flake was enhanced after molecular deposition with the average thickness increasing to ~ 6.9 nm, thereby indicating a thickness of the DAE blend film of ~2.6 nm.

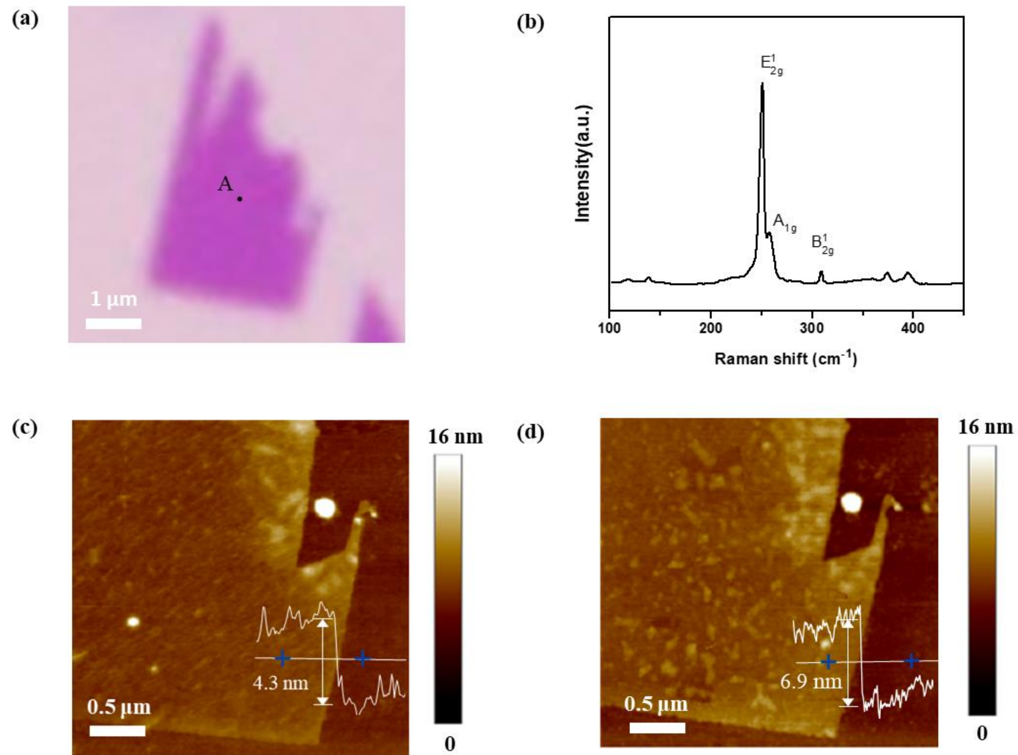

Figure 6-7. (a) Optical microscopy image and (b) Raman spectra of few-layer WSe_2; (c) and (d) Topographical AFM image of the same flake (c) before (d) after DAE blend deposition.

6.3.3. Electrical characterization

6.3.3.1. Optical switching capacity test

Back-gated FETs with patterned top-contact Au electrodes onto Si/SiO_2 substrates were fabricated based on few-layer WSe_2 flakes by means of well-established photolithography. In order to explore the photo-modulation of the electrical properties of WSe_2, a DAE blend solution with mix weight ratio of 1:1 was spin-coated on top of the fabricated device.

Figures 6-8a display the evolution of forward gate sweeping transfer characteristics of the FET devices under different light irradiation, in both linear and logarithmic scale. All the devices on Si/SiO_2 substrate are measured at drain-source voltage V_{ds} = 2 V and gate voltage V_g ranging from -90 to 90 V. The initial WSe_2 device without DAE molecules features a typical ambipolar behavior with pristine hole mobility of 71.5 $cm^2 V^{-1} s^{-1}$ and electron mobility of 21.6 $cm^2 V^{-1} s^{-1}$. Once the DAE blend is physisorbed on the WSe_2 surface, the threshold voltages for both holes and electrons move towards negative directions, whereas the hole mobility decreases to 49.2 $cm^2 V^{-1} s^{-1}$ and the electron mobility increases to 25.1 $cm^2 V^{-1} s^{-1}$. These phenomena indicate that the DAE blends, with both photochromes in their open state, induce an n-type doping effect on WSe_2. As a result of UV irradiation, a decrease of mobility can be observed for both holes (μ_{h^+} = 2.1 $cm^2 V^{-1} s^{-1}$) and electrons (μ_{e^-} = 16.9 $cm^2 V^{-1} s^{-1}$), accompanied with a downshift of threshold voltage for holes $\triangle V_{th-h^+}$= -4.8 V and a upshift for electrons $\triangle V_{th-e^-}$ = 19.1 V. Therefore, the closed-form of DAE in the blend simultaneously deplete electrons and holes from WSe_2 with $\triangle n_{h^+}$ = 3.8×10^{11} cm^{-2} and $\triangle n_{e^-}$= 1.5×10^{12} cm^{-2}, indicating a n-type doping effect on hole transport while p-type doping effect on electron transport. The modulation process was proven to be reversible by successive vis light irradiation. In this process, switching the DAE molecules back to the ring-open form fully restores the initial electrical performance. An additional backward gate sweeping measurement is illustrated in Figure 6-8c, which shows the same trend as the forward sweeping, proving that the hysteresis has no influence on the carrier transport modulation.

To eliminate the contribution from WSe_2, transfer curves of the reference device with pristine WSe_2 were also measured, which shows no variation under dark and after UV/vis illumination.

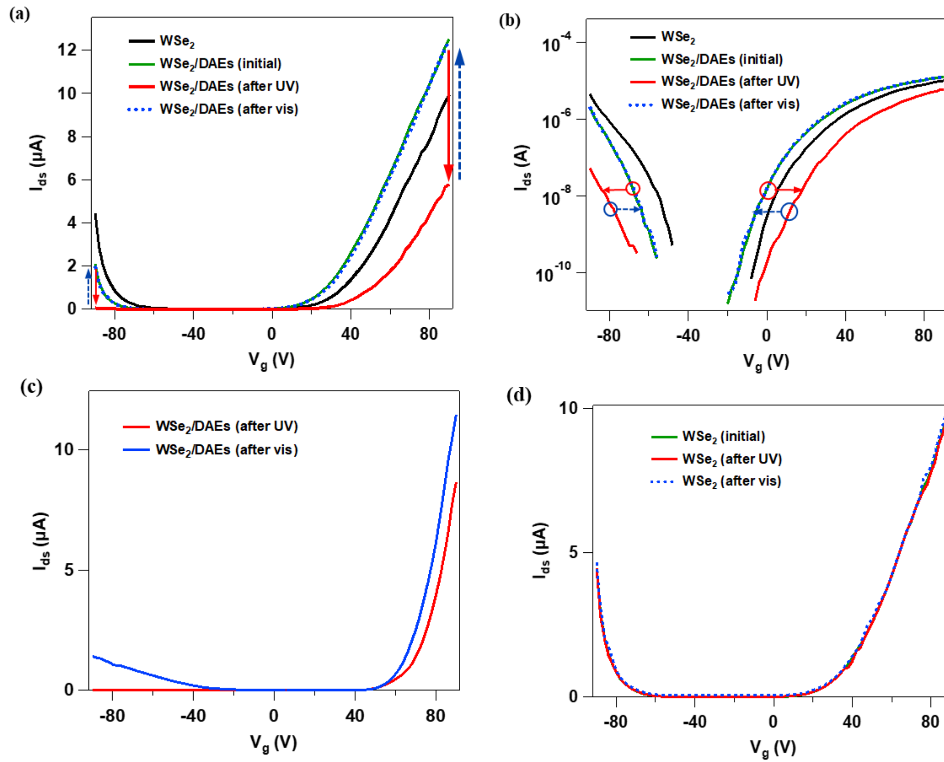

Figure 6-8. Electrical characterization of WSe_2/DAE blend FET device. (a) and (b) Transfer evolution of pristine WSe_2, WSe_2/DAE blend as prepared and after UV/vis irradiation in (a) linear and (b) logarithmic scale; (c) Transfer revolution of WSe_2/DAE blend via backward gate sweeping (V_g from 90 V to -90 V); (d) Control experiment on bare WSe_2 FET device.

In order to prove the reproducibility of such current modulation, we investigated 8 devices with each based on WSe_2 flakes with similar thicknesses. The devices show stable current modulation efficiencies under the same experimental conditions, with hole current modulation efficiencies vary from 95% to 98% and electron current modulation efficiencies vary from 48% to 53%. Such minor difference is attributed to the interface quality between WSe_2 and DAE blends.

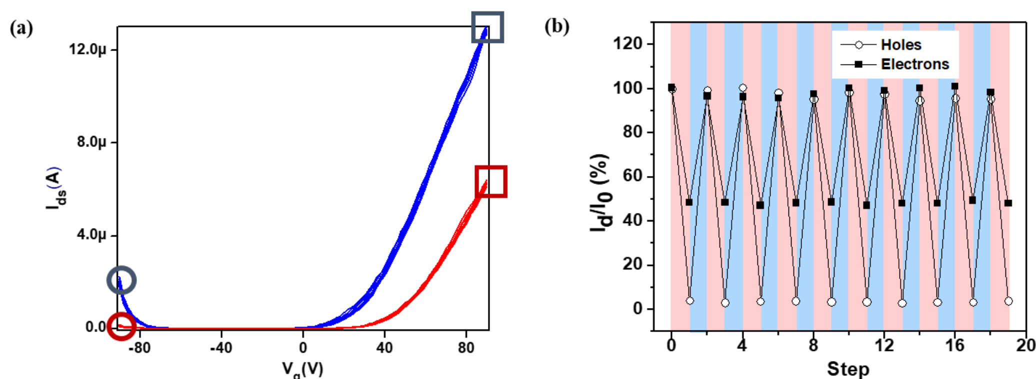

Figure 6-9. (a) WSe_2/DAE_o - WSe_2/DAE_c switching cycles for 10 times; (b) Drain current I_{ds} modulation as both open and closed isomers over 10 illumination cycles with alternative UV (red shaded areas) and vis (blue shaded areas) light. All current values are normalized to the initial value obtained from the as prepared WSe_2/DAE blend. The connecting lines are used as guides to the eye.

Due to the full recovery of all the electrical characteristics of the FET device after subsequent vis light irradiation, more illumination cycles can be launched to test the stability of such photo-modulation of the current. In Figure 6-9a we plot the normalized drain current I_{ds} for both holes and electrons taken from the transfer curves obtained during the 10 measured cycles (I_0 is the current value measured in step 0, which corresponds to the current initially after molecular deposition. Figure 6-9b plots the detailed transfer curves. The hole current is collected at V_g = -90 V and the electron current is collected at V_g = 90 V. The current modulation is as high as 97% for holes and 52% for electrons, showing a more efficient trapping for holes than for electrons. Note that different mix weight ratios of the two DAE molecules are tested (from 1:10 to 10:1), but the current modulation efficiency remains unchanged. Therefore we attribute the observed difference of modulation efficiency to the fact that the energy difference between the VBM of WSe_2 and the HOMO of DAE_3c (0.4 eV) is larger than that between the CBM of WSe_2 and the LUMO of DAE_1c (0.2 eV), thus triggering the a more efficient trapping of holes when compared to electrons. This result is also in accordance with our previous established models when DAE molecules are blended with different organic semiconductors.[25] The absence of degradation after 10 illumination cycles shows that our devices possess reasonable stability and robustness.

Figure 6-10 displays the output measurement of the FET based on DAE blend decorated WSe_2. The curves exhibit a linear and symmetric correlation between the drain current I_{ds} under different drain biases V_{ds}, demonstrating a low contact resistance of WSe_2 with Au electrodes regardless of the photo-isomeric state adopted by the DAE molecules. The current also shows similar modulation tendency as the results obtained from transfer curves, *i.e.,* under the same applied gate voltage: the current for DAE_c modified WSe_2 exhibits a downshift when compared with DAE_o modified WSe_2.

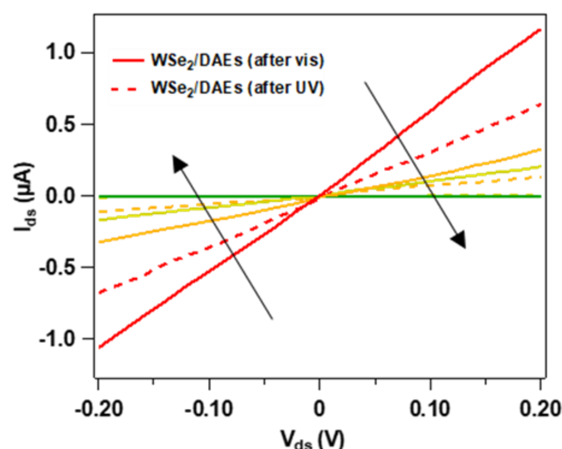

Figure 6-10. Output evolution of WSe_2/DAE blend after UV (dashed lines) and vis (solid lines) illumination for V_g from -90 V to 90 V in steps of 30 V.

To better illustrate the photo-modulation of the DAE blend-WSe_2 FET device, Figure 6-11a portrays the dynamic behavior of drain current for holes at -90 V gate voltage during 20 illumination cycles and Figure 6-11b shows one single cycle (each cycle includes four steps, *i.e.,* 5 s UV, 30 s dark, 40 s vis, 30 s dark). The red boxed region is the period when UV is on and the blue boxed region indicates when vis is on. The same measurement performed for electron current at 90 V gate voltage is shown in Figure 6-11c.

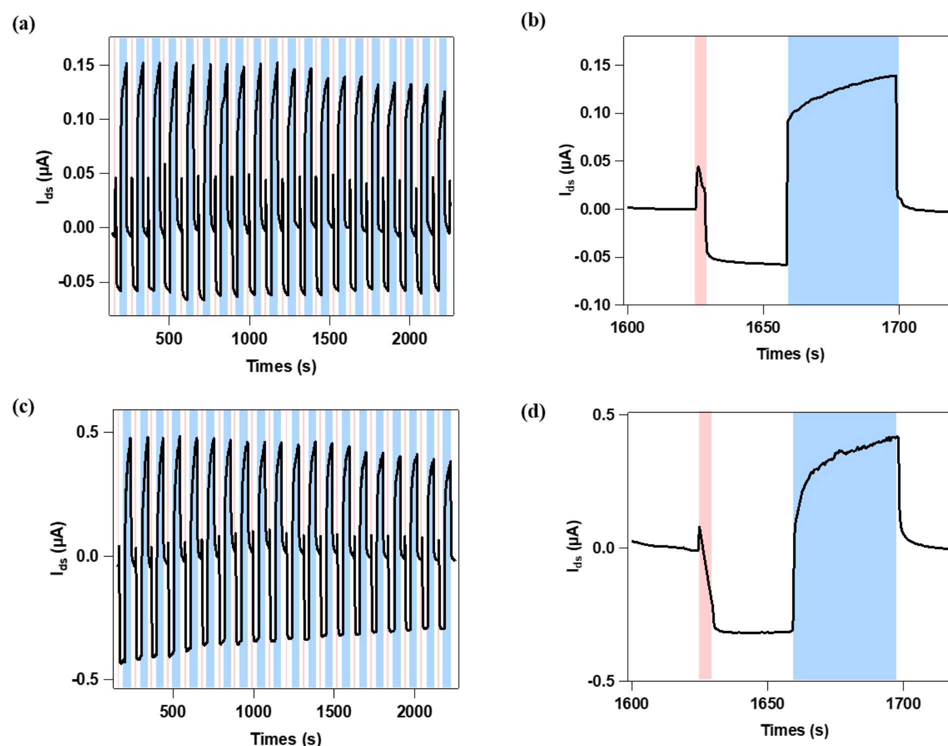

Figure 6-11. Dynamic I_{ds}-time measurement (corrected for bias stress effect) under alternative dark and UV/vis illumination conditions at V_g = -90 V and V_{ds} = 2 V for WSe_2/DAE blend during (a) 20 cycles; (b) 1 singe cycle; (c) and (d) Same measurement at V_g = 90 V and V_{ds} = 2 V.

Note that the curves are corrected for gate bias stress effect to single out the sole contribution of molecular switching (original curves and gate bias curves are provided in Figure 6-12).[26] By comparing the curves obtained, we find that the electron and hole current show the same modulation tendency under light irradiation. When the light is switched ON and OFF, the current displays a sudden increase or drop behavior, which is described as the photocurrent triggered by the generation and relaxation of electron-hole pairs.[27] During the illumination of UV light, the conversion of open to closed isomers is a time-resolved process, which leads to a gradual depletion of electrons and holes from the WSe_2 channel, resulting in a gradual decrease of the current. Conversely, under subsequent vis light illumination the current increases gradually owing to the relaxation of molecules from closed to open isomers. At the end of each cycle, the current recovers to the original value confirming that all the charge carriers are transferred back to WSe_2. In Figure 6-11a and 6-11c, we observe that after over 20 illumination cycles the modulation shows no noticeable fatigue, indicating the excellent endurability of our device.

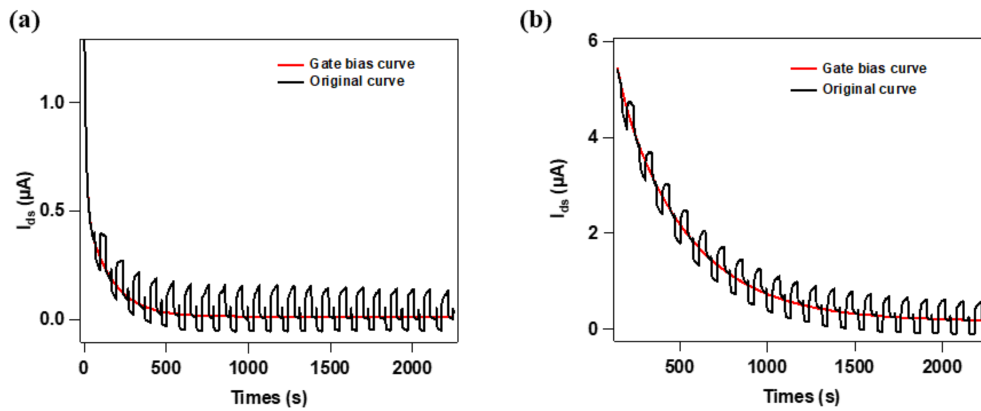

Figure 6-12. Dynamic I_{ds}–time measurement under alternative dark and illumination conditions without correcting the bias stress effect (black) and the corresponding gate bias curve (red) V for WSe_2/DAE blend for (a) holes at V_g = -90 V and V_{ds} = 2 V, (b) electrons at V_g = 90 V and V_{ds} = 2 V.

The control experiment on pristine WSe_2 device is also performed under the same UV/vis illumination conditions. As displayed in Figure 6-13, the device exhibits only photoresponse upon light exposure whereas no significant modulation is observed. Moreover, the photocurrent in pristine WSe_2 is one order of magnitude smaller than that decorated by the DAEs. Therefore, the photo-modulation of charge transport in WSe_2 can be ascribed to the molecular photoswitching behavior.

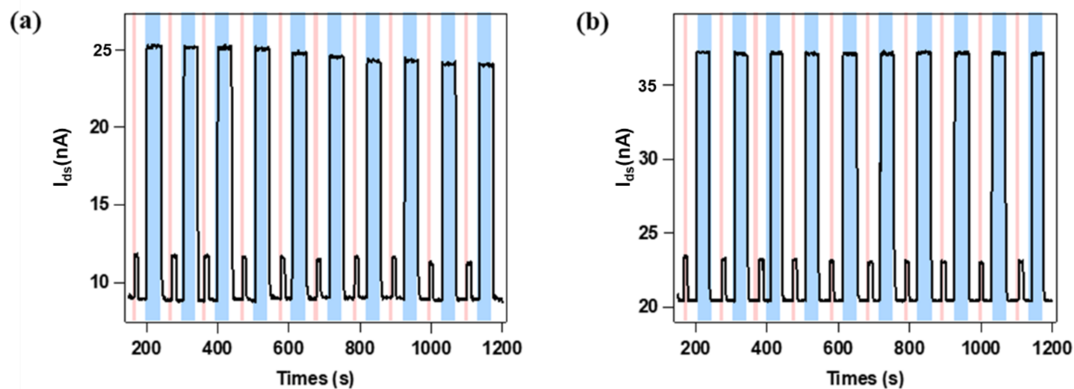

Figure 6-13. I_{ds}-time measurement under alternative dark and UV/vis illumination conditions at (b) V_g = -90 V and (c) V_g = 90 V, V_{ds} = 2 V for WSe_2 FET device.

To further elucidate the contribution of two DAE molecules individually, we perform the electrical measurement on WSe_2 device with only DAE_1 or DAE_3. As displayed in Figure 6-14, device with DAE_1 presents only electron transport modulation under illumination conditions and hole current has no obvious variation. Comparatively, device with DAE_3 can only modulate hole transport. Their current modulation efficiencies quantitatively match the results obtained in DAE blend decorated device (~52% for DAE_1 and ~97% for DAE_3). These phenomena clarify that the two molecules work separately and have no disturbance between each other.

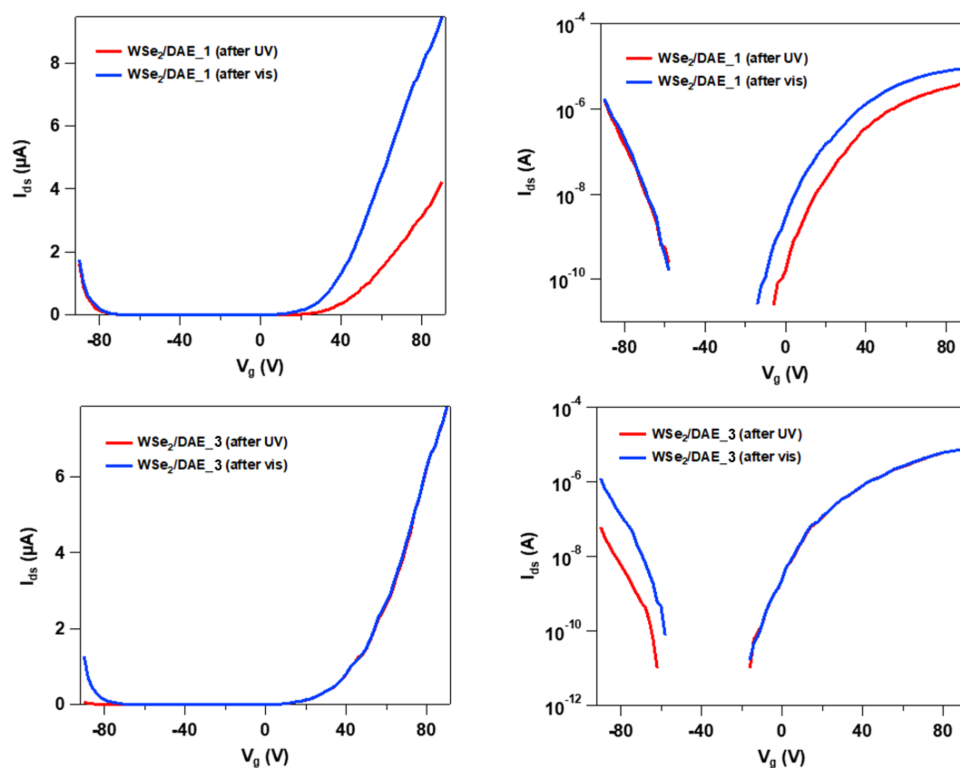

Figure 6-14. Transfer evolution of (a) and (b) WSe_2/DAE_1, (c) and (d) WSe_2/DAE_3 after UV/vis irradiation in (a) and (c) linear, (b) and (d) logarithmic scale.

6.3.3.2. Multilevel test

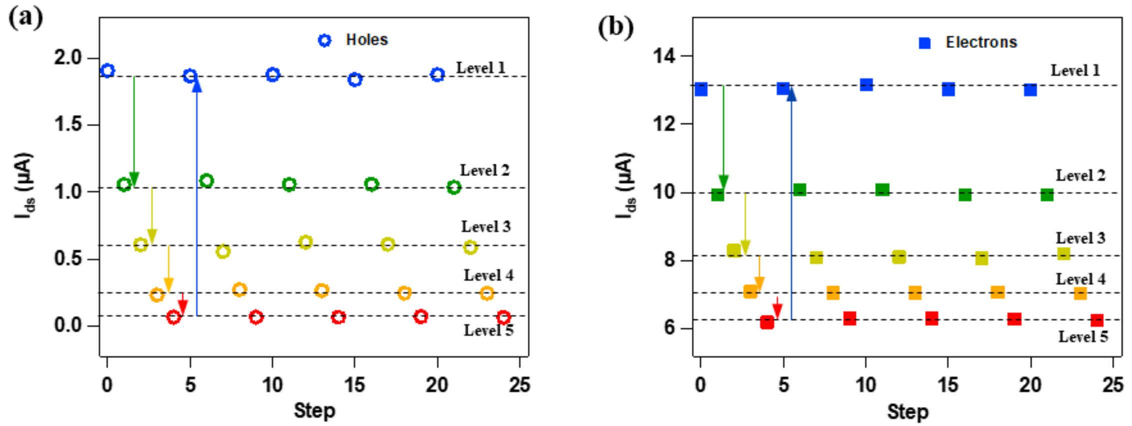

Figure 6-15. Multilevel characterization of WSe_2/DAE blend FET device. (a) 5 distinct current levels over 5 illumination cycles for holes recorded at V_g = -90 V. The levels are obtained by illuminating the device for different fixed times; (b) Same measurement recorded at V_g = 90 V for electrons.

Table 6-1. Calculated standard deviation for each current level presented in Figure 6-15a.

Holes	Level 0	Level 1	Level 2	Level 3	Level 4
I_{ds} cycle 1 (μA)	1.91	1.06	0.61	0.23	0.07
I_{ds} cycle 2 (μA)	1.87	1.08	0.56	0.27	0.07
I_{ds} cycle 3 (μA)	1.88	1.06	0.63	0.27	0.06
I_{ds} cycle 4 (μA)	1.84	1.06	0.61	0.24	0.07
I_{ds} cycle 5 (μA)	1.88	1.04	0.59	0.24	0.06
Standard deviation (μA)	0.02	0.02	0.03	0.02	0.01
Standard deviation/ I_{ds} gap	1.3%	0.9%	1.4%	0.9%	0.3%

Table 6-2. Calculated standard deviation for each current level presented in Figure 6-15b.

Electrons	Level 0	Level 1	Level 2	Level 3	Level 4
I_{ds} cycle 1 (μA)	13.03	9.92	8.29	7.09	6.19
I_{ds} cycle 2 (μA)	13.06	10.07	8.07	7.06	6.30
I_{ds} cycle 3 (μA)	13.15	10.07	8.11	7.05	6.30
I_{ds} cycle 4 (μA)	13.03	9.93	8.07	7.07	6.29
I_{ds} cycle 5 (μA)	13.01	9.93	8.21	7.03	6.25
Standard deviation (μA)	0.05	0.08	0.09	0.02	0.05
Standard deviation/ I_{ds} gap	0.8%	1.2%	1.4%	0.3%	0.7%

The drain current level for both holes and electrons are proportional to the population ratio between DAE_o and DAE_c molecules, which can be controlled by the light illumination dose. In Figure 6-15a and 6-15b we portray the multilevel current for holes and electrons respectively, which are obtained by illuminating the device at different fixed times at a well-defined areal power density. We start from Level 1, at which the current state is the result of both two DAE molecules in open forms. Later, Level 2 to Level 5 are reached after UV irradiation for 10 s, 20 s, 40 s, and 80 s, and Level 5 is the current state when all the molecules are in closed forms. By subsequent vis illumination, the current value can be restored to Level 1. Such illumination cycle is repeated for 5 times and the values obtained for each level are quite stable. Their standard deviations are calculated to be below 1.5% of the total current difference (I_{ds}_o – I_{ds}_c), thus demonstrating that the device can attain multiple current levels precisely by remote light control (detailed values for each level are provided in Table 6-1 and 6-2). To further investigate the number of levels our device can reach, we perform the I_{ds}-time test by exposing the device to a periodic UV light irradiation at intervals of 20 s (60 s – 540 s: 0.5 s per 20 s; 540 s – 860 s, 1 s per 20 s; 860 s – 1020 s: 2 s per 20 s, 1020 s – 1180 s: 4 s per 20 s; 1180 s – 1340 s: 8 s per 20 s). Figure 6-16a and 6-17a display the results: the current follows a progressive decrease after each light dose and the value holds stable at that level, representing a continuous depletion of charge carriers in

WSe_2. It was possible to attain 64 current levels for both holes and electrons with clear current changes between adjacent levels. Figure 6-16b-g and Figure 6-17b-g provide the detailed plots, justifying the validity of each current level. Therefore, a 128-level-device with a data storage capacity of 7 bit and a high accuracy readout was successfully built.

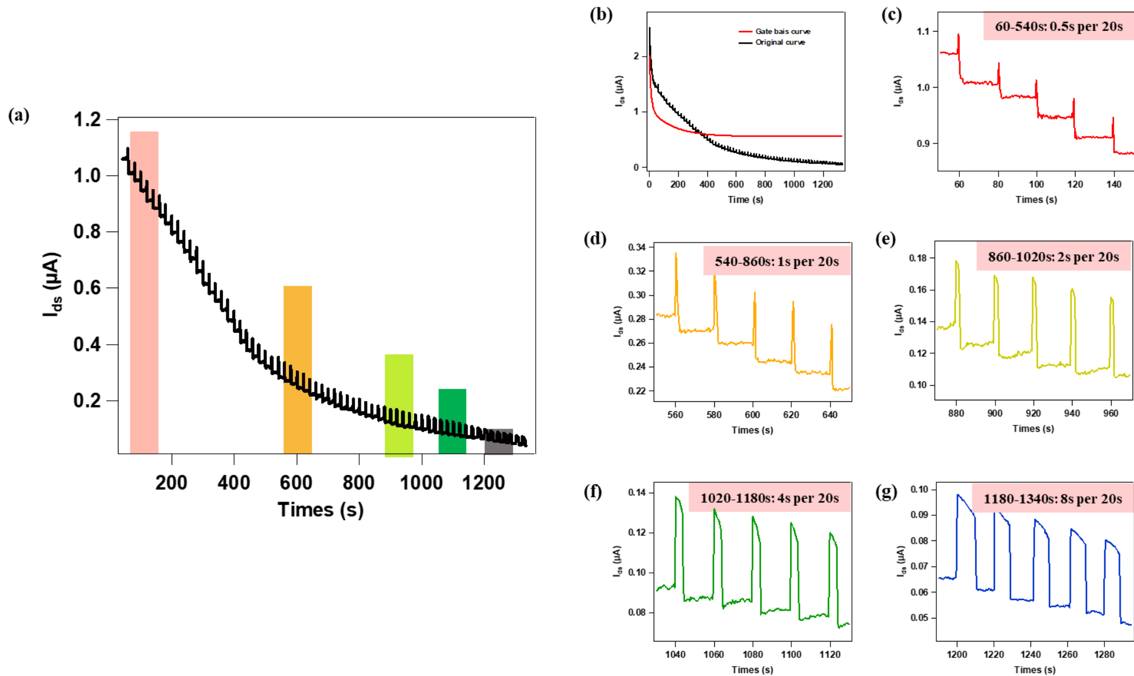

Figure 6-16. Dynamic hole current I_{ds}-time curves under periodic UV irradiation per 20 s recorded at V_g = -90 V and V_{ds} = 2 V, (a) 64 levels are achieved in total (corrected for bias stress); (b) Original curve without correcting the bias stress effect (black) and the corresponding fitting curve (red); (c-g) an enlargement of 5 levels.

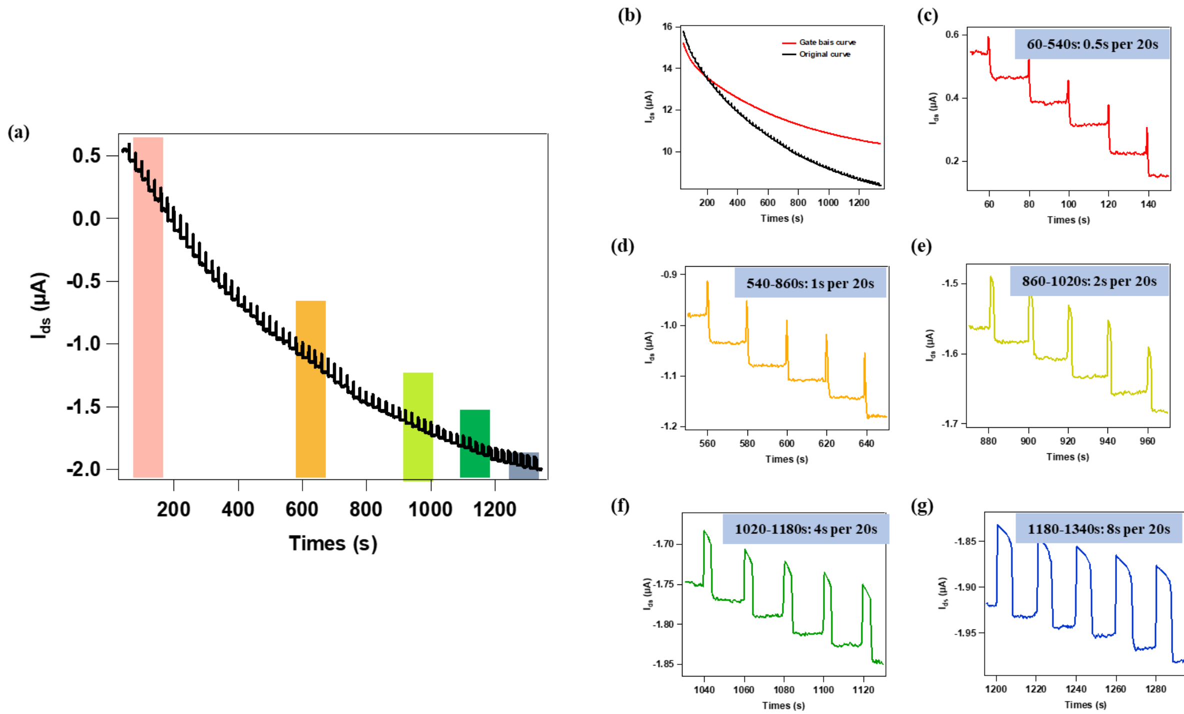

Figure 6-17. Dynamic hole current I_{ds}-time curves under periodic UV irradiation per 20 s recorded at $V_g = 90$ V and $V_{ds} = 2$ V, (a) 64 levels are achieved in total (corrected for bias stress); (b) Original curve without correcting the bias stress effect (black) and the corresponding fitting curve (red); (c-g) an enlargement of 5 levels.

6.3.3.3. Retention capacity test

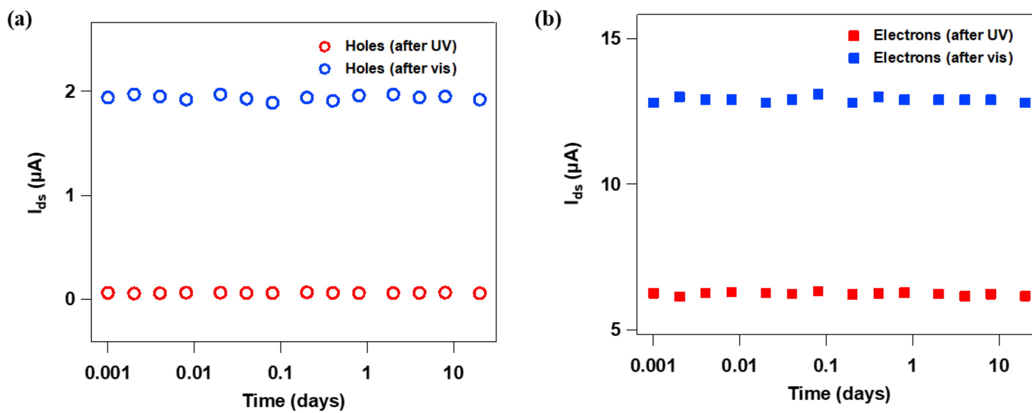

Figure 6-18. I_{ds} evolution with different storage time in the dark (a) for holes at $V_g = -90$V and $V_{ds} = 2$ V, (b) for electrons at $V_g = 90$V and $V_{ds} = 2$ V.

The unique thermal bistability of the DAE molecules can be expected to endow to the devices a good retention capacity. By keeping the device in the dark, we independently measure its hole and electron current after different storage times. The results are plotted in Figure 6-18. They reveal a highly reliable retention characteristic with the current maintains stable for both isomer states over 20 days. For each current level, the standard deviation is below 1.5% of the total current difference (Table 6-3), demonstrating a remarkable retention capacity, which is essential for a commercial non-volatile memory.

Table 6-3. Calculated standard deviation for I_{ds}_1o and I_{ds}_1c in the Figure 6-18.

	Average I_{ds} (μA)	Standard deviation (μA)	Standard deviation/ I_{ds} difference
I_{ds}_1o (holes)	1.93	0.024	1.3%
I_{ds}_1c (holes)	0.06	0.004	0.2%
I_{ds}_1o (electrons)	12.92	0.100	1.5%
I_{ds}_1c (electrons)	6.24	0.065	1.0%

6.3.3.4. Adaptability on flexible substrate

In order to demonstrate the general adaptability of our multilevel device into future flexible/wearable memories, the as-fabricated WSe_2 FET on Si/SiO_2 substrate is transferred onto a flexible PET substrate with ITO serving as back-gate electrode and 80 nm CL-PVP as dielectric material.

The device exhibits a hole mobility of 35.5 $cm^2\ V^{-1}s^{-1}$ and electron mobility of 43.3 $cm^2V^{-1}s^{-1}$, which is comparable to values obtained on rigid Si/SiO_2 substrates, suggesting that the transfer process does not significantly diminish the device's electrical performance. The transfer characteristics evolution after molecular deposition and light irradiation is displayed in Figure 6-19a. The device retains its photo-modulation ability with a hole current modulation of 96% and electron current modulation of 49%, being slightly lower than the obtained values on Si/SiO_2 substrate. We attribute this to the difference of interface quality between the substrates. The dynamic electron current variation at 90 V gate voltage during 6 illumination cycles is also investigated, revealing similar trend as on Si/SiO_2 substrate: UV

light yields a sizable drop of the current while vis light resumes the current to original value. Furthermore, a series of bending tests are performed to investigate the influence of bending cycles on the current modulation efficiency. Each cycle consists of 5 s of bending at a bending radius of 8 mm, followed by 20 s of resting time. After specific bending cycles, the device is exposed to one illumination cycle with alternate UV/vis irradiation and the corresponding transfer curves are collected. As displayed in Figure 6-19c, the effect of bending cycles on the current modulation efficiency is found to be negligible. Over 100 bending cycles are monitored, both hole and electron current can virtually preserve their modulation efficiency, suggesting a good mechanical stability of our device to work on the flexible substrate.

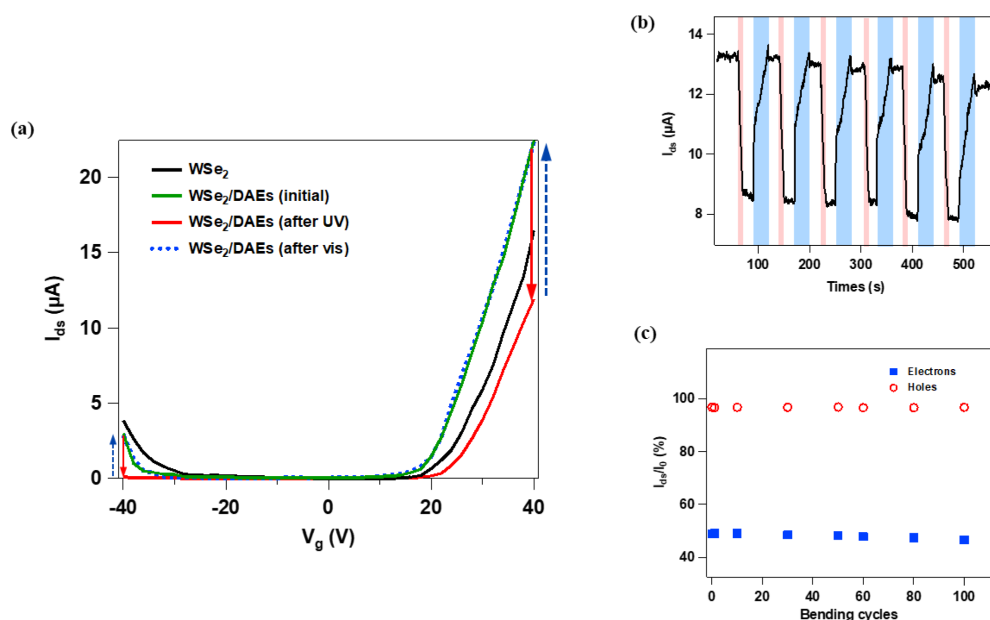

Figure 6-19. Electrical characterization of WSe_2/DAE blend FET device on flexible substrate. (a) Transfer evolution of pristine WSe_2, WSe_2/DAE blend FET as prepared and after UV/vis irradiation; (b) Dynamic I_{ds}-time measurement under alternative dark and UV/vis illumination conditions during 6 cycles at $V_g = 90$ V, $V_{ds} = 2$ V for WSe_2/DAE blend FET; (c) Drain current modulation efficiency as a function of bending cycles.

6.4. Conclusions

In conclusion, we have successfully fabricated WSe_2-based optically switchable FET by interfacing such 2DM with a blend of two photochromic DAE molecules acting as light-sensitive components. Upon light illumination, the device can modulate hole and electron transport simultaneously for at least

20 cycles with a good endurance. The electrical characterizations provide unambiguous evidence that suitably designed DAE molecules with phototunable frontier molecular orbital energy levels can systematically tune the charge transport of the target 2DM. We clearly demonstrate the feasibility and generality of our approach to optically control the transport of electrons, or holes, or both charge carriers, depending on the nature of the target 2DM, thus it offers intriguing perspectives for optically switchable ambipolar FETs based on photochromic molecules/2DMs hybrid systems. Noteworthy, our device exhibits a combination of 128 distinct current levels with a high accuracy readout and over 20 days of retention time, which is of paramount importance for future applications as multilevel non-volatile memories. Our devices are also compatible to work on flexible PET substrates as their light responsive properties are successfully preserved, and thus offer a versatile platform for applications in flexible and transparent electronics.

6.5. References

[1] a) F. Bonaccorso, Z. Sun, T. Hasan, A. C. Ferrari, *Nat. Photonics* **2010**, *4*, 611; b) Q. H. Wang, K. Kalantar-Zadeh, A. Kis, J. N. Coleman, M. S. Strano, *Nat. Nanotechnol.* **2012**, *7*, 699; c) G. Fiori, F. Bonaccorso, G. Iannaccone, T. Palacios, D. Neumaier, A. Seabaugh, S. K. Banerjee, L. Colombo, *Nat. Nanotechnol.* **2014**, *9*, 768.

[2] F. Xia, H. Wang, D. Xiao, M. Dubey, A. Ramasubramaniam, *Nat. Photonics* **2014**, *8*, 899.

[3] a) S. Mao, J. Chang, H. Pu, G. Lu, Q. He, H. Zhang, J. Chen, *Chem. Soc. Rev.* **2017**, *46*, 6872; b) C. Anichini, W. Czepa, D. Pakulski, A. Aliprandi, A. Ciesielski, P. Samorì, *Chem. Soc. Rev.* **2018**, *47*, 4860.

[4] a) S. Das, R. Gulotty, A. V. Sumant, A. Roelofs, *Nano Lett.* **2014**, *14*, 2861; b) N. Petrone, T. Chari, I. Meric, L. Wang, K. L. Shepard, J. Hone, *ACS Nano* **2015**, *9*, 8953; c) D. Akinwande, N. Petrone, J. Hone, *Nat. Commun.* **2014**, *5*, 5678.

[5] a) P. Samorì, V. Palermo, X. Feng, *Adv. Mater.* **2016**, *28*, 6027; b) V. P. Pham, G. Y. Yeom, *Adv. Mater.* **2016**, *28*, 9024.

[6] a) K. Haynes, R. Murray, Z. Weinrich, X. Zhao, D. Chiappe, S. Sutar, I. Radu, C. Hatem, S. S. Perry, K. S. Jones, *Appl. Phys. Lett.* **2017**, *110*, 262102; b) S. Bae, N. Sugiyama, T. Matsuo, H. Raebiger, K.-i. Shudo, K. Ohno, *Phys. Rev. Appl.* **2017**, *7*, 024001.

[7] a) M. E. Itkis, X. Chi, A. W. Cordes, R. C. Haddon, *Science* **2002**, *296*, 1443; b) C. Simão, M. Mas-Torrent, N. Crivillers, V. Lloveras, J. M. Artés, P. Gorostiza, J. Veciana, C. Rovira, *Nat. Chem.* **2011**, *3*, 359; c) Z. Liu, H. I. Wang, A. Narita, Q. Chen, Z. Mics, D. Turchinovich, M. Kläui, M. Bonn, K. Müllen, *J. Am. Chem. Soc.* **2017**, *139*, 9443.

[8] a) S. Bertolazzi, M. Gobbi, Y. Zhao, C. Backes, P. Samorì, *Chem. Soc. Rev.* **2018**, *47*, 6845; b) M. Gobbi, E. Orgiu, P. Samorì, *Adv. Mater.* **2018**, *30*, 1706103.

[9] L. Wang, Q. Li, *Chem. Soc. Rev.* **2018**, *47*, 1044.

[10] a) Y. Zhao, S. Ippolito, P. Samorì, *Adv. Opt. Mater.* **2019**, *7*, 1900286; b) X. Zhang, L. Hou, P. Samorì, *Nat. Commun.* **2016**, *7*, 11118.

[11] a) M. Gobbi, S. Bonacchi, J. X. Lian, A. Vercouter, S. Bertolazzi, B. Zyska, M. Timpel, R. Tatti, Y. Olivier, S. Hecht, M. V. Nardi, D. Beljonne, E. Orgiu, P. Samorì, *Nat. Commun.* **2018**, *9*, 2661; b) A.-R. Jang, E. K. Jeon, D. Kang, G. Kim, B.-S. Kim, D. J. Kang, H. S. Shin, *ACS Nano* **2012**, *6*, 9207; c) Y. Zhao, S. Bertolazzi, P. Samorì, *ACS Nano* **2019**, *13*, 4814; d) M. Kim, N. S. Safron, C. Huang, M. S. Arnold, P. Gopalan, *Nano Lett.* **2012**, *12*, 182.

[12] H. Qiu, Y. Zhao, Z. Liu, M. Herder, S. Hecht, P. Samorì, *Adv. Mater.* **2019**, *31*, 1903402.

[13] P. R. Pudasaini, A. Oyedele, C. Zhang, M. G. Stanford, N. Cross, A. T. Wong, A. N. Hoffman, K. Xiao, G. Duscher, D. G. Mandrus, T. Z. Ward, P. D. Rack, *Nano Res.* **2018**, *11*, 722.

[14] M. Irie, T. Fukaminato, K. Matsuda, S. Kobatake, *Chem. Rev.* **2014**, *114*, 12174.

[15] T. Tsujioka, H. Kondo, *Appl. Phys. Lett.* **2003**, *83*, 937.

[16] a) M. Min, S. Seo, S. M. Lee, H. Lee, *Adv. Mater.* **2013**, *25*, 7045; b) L. A. Frolova, A. A. Rezvanova, B. S. Lukyanov, N. A. Sanina, P. A. Troshin, S. M. Aldoshin, *J. Mater. Chem. C* **2015**, *3*, 11675.

[17] S. Bertolazzi, P. Bondavalli, S. Roche, T. San, S.-Y. Choi, L. Colombo, F. Bonaccorso, P. Samorì, *Adv. Mater.* **2019**, *31*, 1806663.

[18] T. Leydecker, M. Herder, E. Pavlica, G. Bratina, S. Hecht, E. Orgiu, P. Samorì, *Nat. Nanotechnol.* **2016**, *11*, 769.

[19] K. Börjesson, M. Herder, L. Grubert, D. Duong, A. Salleo, S. Hecht, E. Orgiu, P. Samorì, *J. Mater. Chem. C* **2015**, *3*, 4156.

[20] M. Herder, B. M. Schmidt, L. Grubert, M. Pätzel, J. Schwarz, S. Hecht, *J. Am. Chem. Soc.* **2015**, *137*, 2738.

[21] Y. Guo, J. Robertson, *Appl. Phys. Lett.* **2016**, *108*, 233104.

[22] H. Liu, A. T. Neal, P. D. Ye, *ACS Nano* **2012**, *6*, 8563.

[23] S. Helveg, J. V. Lauritsen, E. Lægsgaard, I. Stensgaard, J. K. Nørskov, B. S. Clausen, H. Topsøe, F. Besenbacher, *Phys. Rev. Lett.* **2000**, *84*, 951.

[24] J. Lu, A. Carvalho, H. Liu, S. X. Lim, A. H. Castro Neto, C. H. Sow, *Angew. Chem.* **2016**, *128*, 12124.

[25] E. Orgiu, N. Crivillers, M. Herder, L. Grubert, M. Pätzel, J. Frisch, E. Pavlica, D. T. Duong, G. Bratina, A. Salleo, N. Koch, S. Hecht, P. Samorì, *Nat. Chem.* **2012**, *4*, 675.

[26] K. Cho, W. Park, J. Park, H. Jeong, J. Jang, T.-Y. Kim, W.-K. Hong, S. Hong, T. Lee, *ACS Nano* **2013**, *7*, 7751.

[27] Y.-C. Wu, C.-H. Liu, S.-Y. Chen, F.-Y. Shih, P.-H. Ho, C.-W. Chen, C.-T. Liang, W.-H. Wang, *Sci. Rep.* **2015**, *5*, 11472.

Chapter 7: Ternary-Responsive Field-Effect Transistors Based on Asymmetrically Functionalized Janus Few-Layer WSe_2

Hybrids composed of two-dimensional (2D) transition metal dichalcogenides (TMDs) with stimuli-responsive molecules are prototypical components for the development of multifunctional field-effect transistors (FETs), whose output currents can be remotely controlled by external inputs. In this chapter, ternary-responsive FETs based on few-layer WSe_2 are realized by decorating its two opposite surfaces with different stimuli-responsive molecules in an asymmetric fashion: the bottom surface is interfaced with a photochromic diarylethene film and the top surface with a ferroelectric poly(vinylidene fluoride–trifluoroethylene) (P(VDF-TrFE)) layer. Such novel Janus ternary device architecture shows superior functional complexity compared with normal mono-stimuli-responsive FETs. The synergy between the two molecularly induced effects enables the devices to respond orthogonally to electric field and light irradiation, with an enhanced output current modulation efficiency of 87%. The 9 ferroelectric and 84 photo-generated states ensure 756 current levels in a single device. The over 10 cycles of cyclic endurance and more than 1000 hours of retention time confirm the reliability of each state, implementing the demand for high-density non-volatile memories, as well as enriching the diversification in "More than Moore" technologies.

7.1. Introduction

The emerging "More than Moore" technologies, which are characterized by integrating novel analog functionalities within semiconductor-based devices, bring vast diversification rather than pure miniaturization to CMOS digital circuitry.[1] The integration of molecular components into digital circuits has been demonstrated to be a powerful strategy to endow functional diversification, taking advantage of the almost infinite variety of molecules that can be synthesized.[2] Towards this end, stimuli-responsive molecules are particularly interesting because of their capacity to be interconverted between two or more states, having markedly distinct properties when subjected to external stimuli such as electromagnetic, electric or magnetic fields or changes in the environment (pH, temperature, etc.).[3]

By incorporating such molecules in a conventional FET, novel stimuli-responsive capacity can be imparted to the device thereby enabling to manipulate their electrical output by means of various external inputs. Such approach is instrumental for various applications in advanced electronic devices such as memories,[4] sensors[5] and smart logic gates.[6]

Recent efforts have been dedicated to the fabrication of stimuli-responsive devices based on 2D TMDs, which are atomically thin semiconductors possessing extraordinary electronic properties compared to their organic counterparts.[7]

Their unique physico-chemical characteristics have endorsed TMDs as promising channel material in low-power and high-performance digital electronic switches.[8] Moreover, due to their high surface-to-volume ratio, monolayer and few-layer TMDs have an exquisite surface sensitivity to any subtle surrounding environmental change, which opens up the opportunity to modify their intrinsic properties.[9] Recent studies involving stimuli-responsive molecules to decorate the surface of TMDs demonstrated this approach as a promising strategy to non-destructively modulate the charge carrier density by translating the stimuli-triggered changes at the molecular level to the modification of TMD's properties without introducing any defect.[10]

Among the possible external stimuli, light and electrical inputs are particularly interesting since they are efficient, non-invasive, and spatiotemporally precise. Photochromic molecules are optically responsive systems able to undergo reversible photoisomerization when irradiated with light at specific wavelengths.[11] Hitherto they have been utilized as optical switching elements to translate photonic information into electrical output in TMD-based FETs.[12] We recently reported a proof of this concept by exploiting tailor-designed photochromic DAE molecules to reversibly tune the charge carrier transport in few-layer WSe_2 and demonstrated a potential application of the corresponding FET as optically switchable multilevel non-volatile memory.[12a, 12b]

On the other hand, ferroelectric materials have been employed to precisely control the doping level of 2D materials.[13] According to the direction of the external electric field, their intrinsic bistable polarization can be reoriented, leading to an accumulation or depletion of the charge carriers in the

interfaced semiconducting material.[14] Interestingly, these ferroelectric field-effect transistors (FeFETs) take advantage of the binary remnant polarization states of the ferroelectric to store information and therefore have successfully been utilized in practical non-volatile memories.[15]

To date, multifarious molecularly functionalized 2D-mono-stimuli-responsive FETs have been reported, in which direct deposition of functional molecules on top of the upper channel surface served as effective and easily addressable approach to fabricate the device.[16] The inversed device structure could also be obtained by first depositing the molecules on a suitable substrate, followed by transfer of the 2D materials.[17] In all the previous studies only one face of the 2D materials was functionalized by molecules and thus a potential asymmetry arising from unequal exposure of the two surfaces to two different local environments was not exploited. Such a scenario can be achieved by the independent functionalization of each surface with a different functional molecule,[18] providing intriguing perspectives for the realization of multi-stimuli-responsive FETs.

Along these lines, here we report an unprecedented approach based on the decoration of few-layer WSe_2 flakes with two different stimuli-responsive (macro)molecules thereby generating a Janus 2D material. In particular, the bottom surface was sitting on a light-responsive DAE layer and the top surface was coated with an electrically responsive copolymer layer of P(VDF-TrFE). In this way, a multi-stimuli-responsive FET has been fabricated in which the output current could be reversibly and precisely modulated by means of either light irradiation or an electric field. Compared with conventional mono-stimuli-responsive FETs, our novel ternary device architecture combines enhanced functional complexity with fabrication simplicity. We provide unambiguous evidence for the compatibility of the device response to both optical and electrical stimuli, thereby offering an orthogonal handle for operating the device, which is beneficial for memory applications as well. By taking advantage of the synergic effect between the two (macro)molecular switches, the device has attained an enhanced modulation of the output current with an efficiency reaching up to 87%. Furthermore, with each stimulus manifesting a large number of different outputs without mutual interferences (9 electric-induced levels and 84 light-induced levels), the device yields a total number of 756 distinct states, outperforming the current state-of-the-art mono-stimuli-responsive transistors thereby providing a

decisive step forward to address the demand for high density storage memories.[12a, 19] The reliability of each state is further reflected by the endurance and retention tests for 5 arbitrary states, exhibiting a notable endurance for over 10 cycles and an excellent data retention exceeding 1000 hours. Moreover, compared with cumbersome synthesis of single molecules incorporating different functional groups to realize the multi-addressable elements,[20] our Janus modified ternary structure relies on a simple fabrication process and appears to be a universal strategy that can be extended to other 2D materials and functional molecules, offering a versatile platform for the construction of multi-stimuli-responsive devices.

7.2. Experimental methods

7.2.1. Match of energy level between WSe_2 and DAEs.

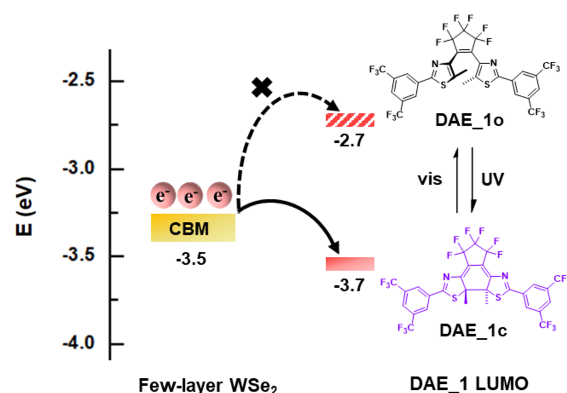

Figure 7-1. Energy level diagram of electron transport between WSe_2/DAE_1.

Note that the same molecules DAE_1 as in Chapter 5 was used. The photoisomerization of DAE molecules between ring-open DAE_1_O and ring-closed DAE_1_C form is accompanied by a major change in their corresponding energy levels.[21]By taking advantage of this unique characteristic, a DAE derivative has been designed and synthesized to possess well-defined lowest unoccupied molecular orbital (LUMO) energy levels in the two states (Figure 7-1) with respect to the conduction band of WSe_2 thereby exhibiting two different and reversible regimes of charge transfer upon light irradiation. In particular, the LUMO level of DAE_$_O$ lies higher than the conduction band minimum of WSe_2 which blocks electron transfer from the latter. On the contrary, the LUMO level of DAE_1_C lies comfortably

below the conduction band minimum of WSe_2 and thus significant electron trapping is expected.[22] In other words, in view of such reciprocal energy levels, electron transfer from WSe_2 to DAE_1_C is foreseeable by UV irradiation, and trapped electrons can get restored in WSe_2 by subsequent vis irradiation.

7.2.2. Device fabrication

7.2.2.1. P(VDF-TrFE) capacitor

The bottom electrode (60 nm Au) was first evaporated onto a Si/SiO_2 substrate through a shadow-mask. The P(VDF-TrFE) (molar ratio of 70%/30%, from Solvay) layer was created by spin-coating a 8 wt% solution in methylethylketone on another Si/SiO_2 substrate and cured at 140 °C for 2 h to increase its crystallinity.[23] The SiO_2 layer is then etched in a NaOH bath to release the layer from the substrate. After washing with distilled water, the ferroelectric layer was transferred to the pre-electrode-evaporated substrate (or to the substrate with pre-fabricated DAE/WSe_2 FET, Figure 7-2). In the final step top gate electrode (60 nm Au) was deposited on top of the ferroelectric layer. Note that the P(VDF-TrFE) layer preparation and transfer method remain the same for both capacitors and FET devices.

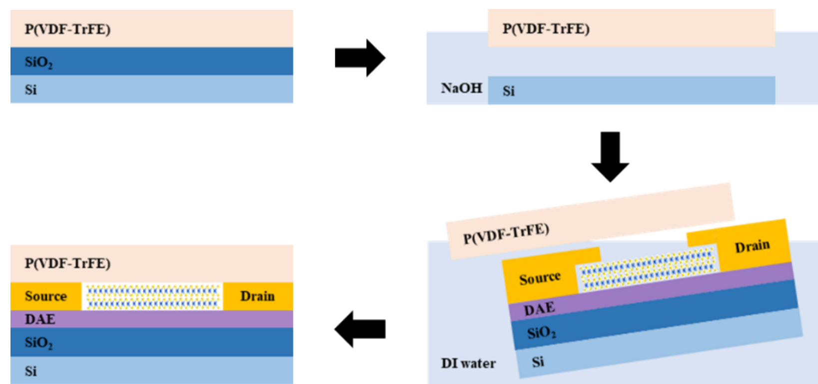

Figure 7-2. Transfer process of the P(VDF-TrFE) layer from Si/SiO_2 substrate.

7.2.2.2. DAE/WSe_2/FeFET

A layer of DAE molecule (0.2 mg/mL) was first spin-coated (1000 rpm, 60 s) to the pre-cleaned Si/SiO_2 substrate. Then mechanically exfoliated few-layer WSe_2 flakes from bulk crystal (from HQ Graphene)

were transferred onto the pre-DAE-decorated SiO_2 substrates. The source and drain electrodes were deposited using a lithography-free technique, via metal evaporation (60 nm Au) through a shadow mask, which not only protects the DAE layer from being removed during the lift-off process but also avoids contamination by photoresist residues**.** With the underlying physisorbed DAE layer guaranteeing the light responsive capacity, the top surface of WSe_2 is ready for being interfaced with the ferroelectric P(VDF-TrFE) layer to impart the ferroelectric responsive nature**.** The P(VDF-TrFE) layer was transferred on top of the DAE/WSe2 device via a wet transfer approach as described in Figure 7-2. Note that direct spin-coating of P(VDF-TrFE) solution onto the DAE/WSe_2 chip is avoided since the solvent (methylethylketone) would remove DAE molecules, and moreover, the formation of P(VDF-TrFE) film requires curing at 140 °C for 2 hours to increase its crystallinity, which may deteriorate the switching capacity of the DAE molecules.[24] Finally, a semi-transparent top gate electrode (20 nm Au) was evaporated on top of the P(VDF-TrFE) layer.

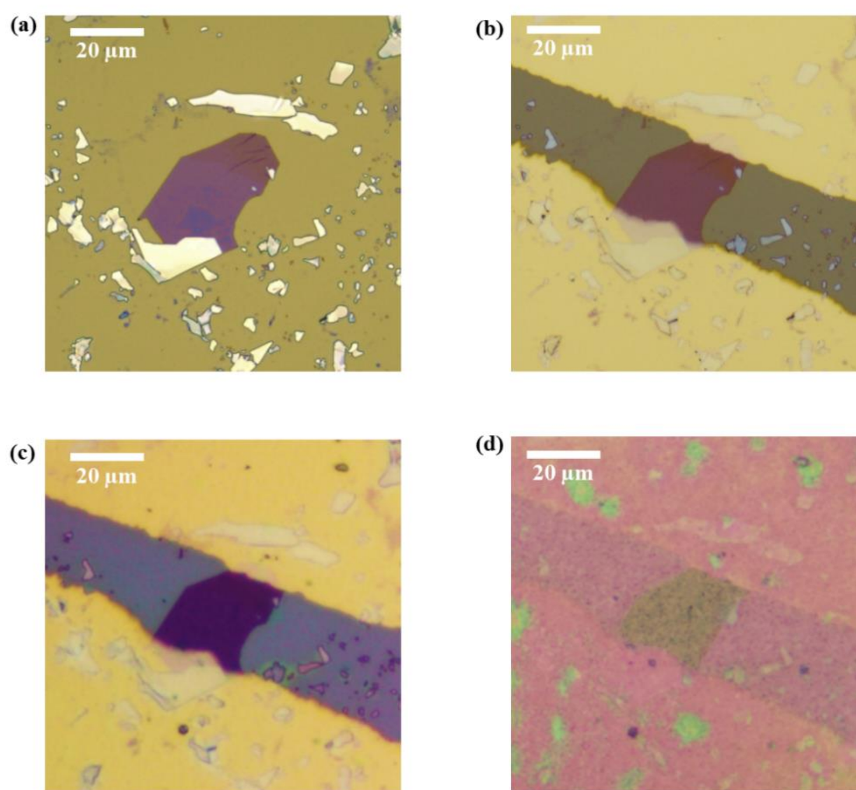

Figure 7-3. Optical microscopy images captured at four stages during the fabrication process. (a) Target WSe_2 flake with the underneath DAE_1 layer. (b) DAE_1/WSe_2 FET with evaporated source-drain electrodes. (c) DAE_1/WSe_2/FeFET with transferred P(VDF-TrFE) film. (d) DAE_1/WSe_2/FeFET with evaporated top gate electrode.

Figure 7-3 shows the optical microscopy images captured at four stages during the fabrication process: target WSe_2 flake with underneath DAE_1 layer, DAE_1/WSe_2 FET with evaporated 60 nm source-drain Au electrodes, DAE_1/WSe_2/FeFET with transferred P(VDF-TrFE) film, and DAE_1/WSe_2/FeFET with evaporated 20 nm semi-transparent top gate Au electrode. Figure 7-4 portrays the architecture of the DAE_1/WSe_2/FeFET device.

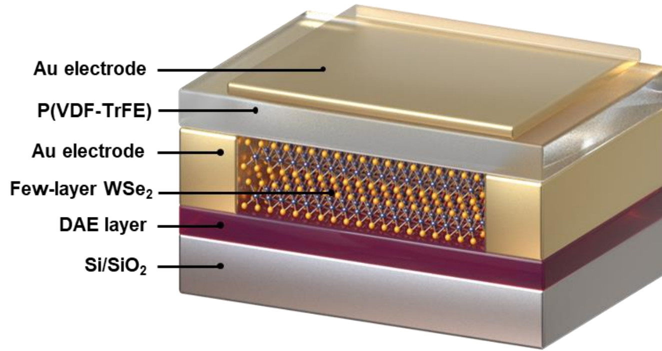

Figure 7-4. Schematic diagram of the DAE_1/WSe_2/FeFET device with double-sided decoration: the bottom surface with DAE film and the top surface with P(VDF-TrFE) layer.

7.2.3. Characterization methods

Raman spectra were recorded by a Renishaw inVia spectrometer equipped with 532 nm laser.

Atomic force microscopy (AFM) imaging was carried out by a Nanoscope (Veeco Multimode V) in tapping mode under ambient conditions.

All electrical measurements were carried out by using a probe station connected to a Keithley 2636 in a glovebox filled with nitrogen. Device irradiation is realized by using a monochromator set-up, with either UV light (at λ = 312 nm, 0.15 $mWcm^{-2}$) or vis light (λ = 530 nm, 11.8 $mWcm^{-2}$). The PSS is reached under UV irradiation for 150 s and recovery within 20 min under vis light.

The charge carrier mobility is calculated in the linear regime from the transfer curve by using the expression:[25]

$$\mu = \frac{dI_{ds}}{dV_g} \times \frac{L}{W} \times \frac{1}{V_{ds}} \times \frac{d}{\varepsilon_0 \varepsilon_r} \quad (1)$$

Where L is the channel length, W is the channel width, and ε_r is the dielectric constant, ε_r = 3.9 for SiO_2 and ε_r = 10 for P(VDF-TrFE).

7.3. Results and discussion

7.3.1. Characterization of DAE molecules, WSe_2 flake and P(VDF-TrFE) film

The surface morphology of the DAE-coated Si substrate was studied by AFM, which reveals a rather flat film without huge aggregates, only some small dots scattered onto the surface. The room-mean squared roughness R_q as determined on a 5 x 5 μm^2 area is of 0.39 nm. The value is enhanced compared with bare Si substrate, which is around 0.2 nm. (Figure 7-5a).[26]

The thickness of the target WSe_2 flake was also determined by AFM, which was found to be 5.3 nm thick, corresponding to 8 atomic layers (Figure 7-5b). Figure 7-6 displays its Raman spectrum, which possesses three active modes, in-plane vibration E^1_{2g}, out-of-plane A^1_g, and interlayer interaction B^1_{2g}, suggesting a good quality of the material.[27]

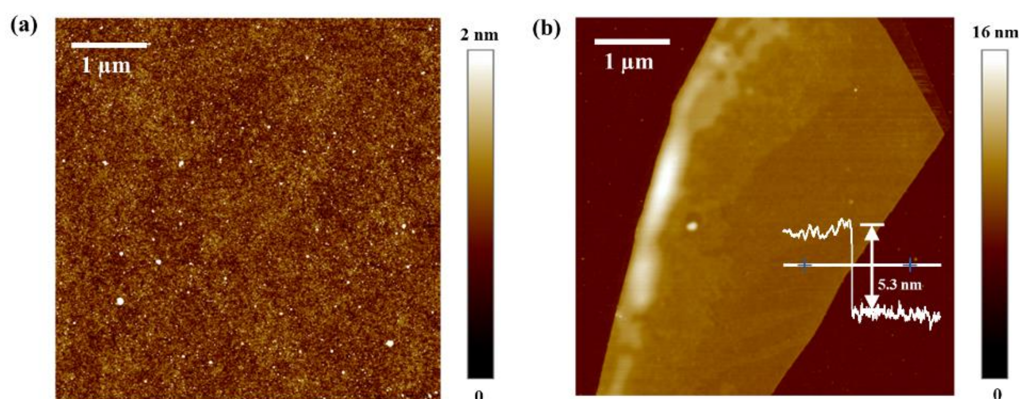

Figure 7-5. Topographical AFM image of (a) DAE film on Si/SiO_2 substrate, (b) WSe_2 flake with underneath DAE film.

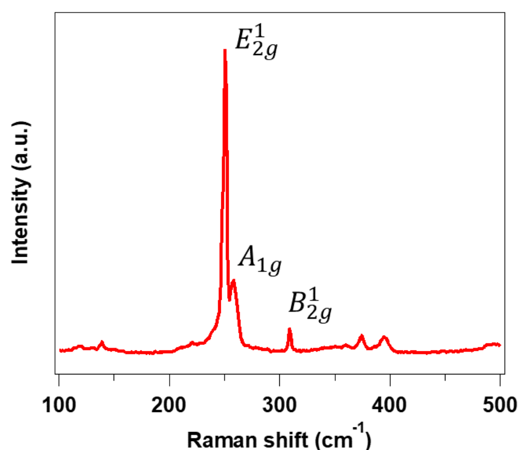

Figure 7-6. Raman spectra of few-layer WSe_2 flake.

The thickness of the P(VDF-TrFE) film was measured by a profilometer. The prepared film was first transferred to a clean Si substrate. Then a step was created by scratching the film penetrating down to the substrate. The thickness was finally determined by measuring the depth between the film and the clean substrate, which was ~ 500 nm (Figure 7-7).

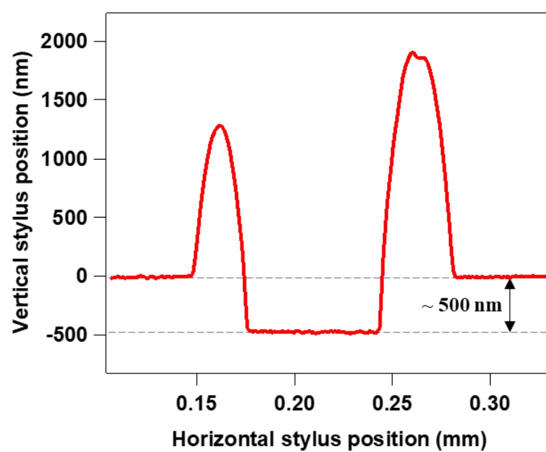

Figure 7-7. The thickness measurement of the P(VDF-TrFE) film by a profilometer.

7.3.2. Optical switching capacity of the DAE/WSe_2 FET

The photomodulation effect induced by DAE molecules was first examined in a DAE_1/WSe_2 FET. As displayed in Figure 7-8, the initial device reveals a typical n-type dominant behavior with electron mobility of 13.8 $cm^2V^{-1}s^{-1}$. Upon subsequent exposure to UV or vis light, the electron current could be reversibly modulated with an efficiency of 74%. Such value is even higher than the one obtained for the inverse heterostructure, i.e. WSe_2 coated with a top DAE layer.[12b] The improved efficiency is attributed to a better interface contact between the DAE and WSe_2 layers.

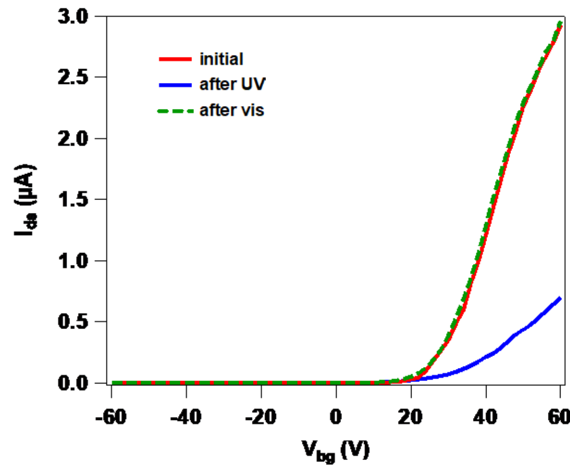

Figure 7-8. Optical switching capacity of DAE/WSe_2 FET by UV/vis illumination.

7.3.3. Electrical characterization of P(VDF-TrFE) capacitor

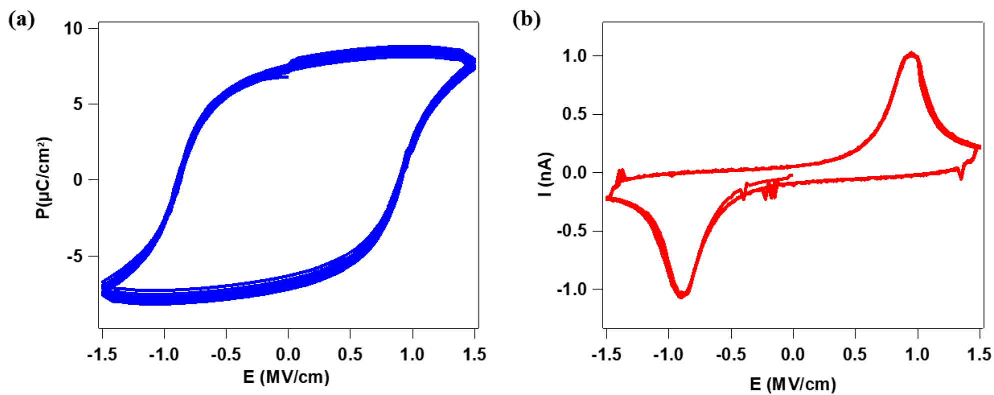

Figure 7-9. (a) The ferroelectric hysteresis loop and (b) corresponding current of a 500 nm P(VDF-TrFE) capacitor during 10 cycles.

To cast light onto the ferroelectric properties of P(VDF-TrFE) polymer, it was integrated as the dielectric material into a capacitor. Figure 7-9 shows the typical hysteresis loops for a P(VDF-TrFE) capacitor with the thickness of 500 nm. The coercive electric field appears at ≈ 0.9 $MVcm^{-1}$ (corresponding to a coercive voltage of 38 V) and the remnant polarization value is ≈ 7.3 μCcm^{-2}, indicating a good quality of the P(VDF-TrFE) film.[28] The measurement cycle was repeated 10 times to gain insight into the ferroelectric stability and no fatigue was observed.

7.3.4. Electrical characterization of DAE/WSe_2/FeFET

7.3.4.1. In top gate configuration

Regarding the DAE/WSe_2/FeFET device, its transfer characteristics were first investigated in back gate configuration, which showed a typical n-type dominant behavior with an electron mobility of 18.2 $cm^2V^{-1}s^{-1}$ (Figure 7-11, black curve). The enhanced mobility compared with DAE/WSe_2 device by adding P(VDF-TrFE) as top gate is correlated to its high dielectric constant (ε_r = 10), which suppresses the Coulomb scattering in the WSe_2 channel.[29] Next, the electrical performance of the same device was characterized in top gate configuration with P(VDF-TrFE) serving as the dielectric. As the top gate voltage (V_{tg}) sweeps between –60 V and +60 V (Figure 7-10a), the transfer curve shows a large memory hysteresis window (≈ 45 V). The generation of such memory window is entirely related to the polarization switching process of the P(VDF-TrFE). The state of the P(VDF-TrFE) can be programmed by the top gate bias: The positive voltage exceeding its coercive voltage can polarize the ferroelectric into the downward direction P_{down}. With C-H bond facing the WSe_2 channel, electrons in the WSe_2 will be engaged to compensate for the polarization charges. Conversely, the application of a negative voltage exceeding the coercive voltage will induce a polarization of the P(VDF-TrFE) into the upward direction P_{up}. In this case, with C-F bond facing the channel, the compensation charge converts from electrons to holes, leading to a depletion of electrons in the channel. Moreover, the corresponding gate leakage current I_{tg} exhibits two apparent peaks near the coercive voltage, which further proves the polarization behavior of the P(VDF-TrFE) (Figure 7-10b). The polarization remains stable during the measured 10 cycles, proving the retained dielectric and ferroelectric properties of the P(VDF-TrFE). The electron

mobility derived from the top gate configuration is 32.3 $cm^2V^{-1}s^{-1}$. Due to the better dielectric shielding effect of P(VDF-TrFE) compared to SiO_2,[30] the value is much higher than that obtained from the back gate configuration.

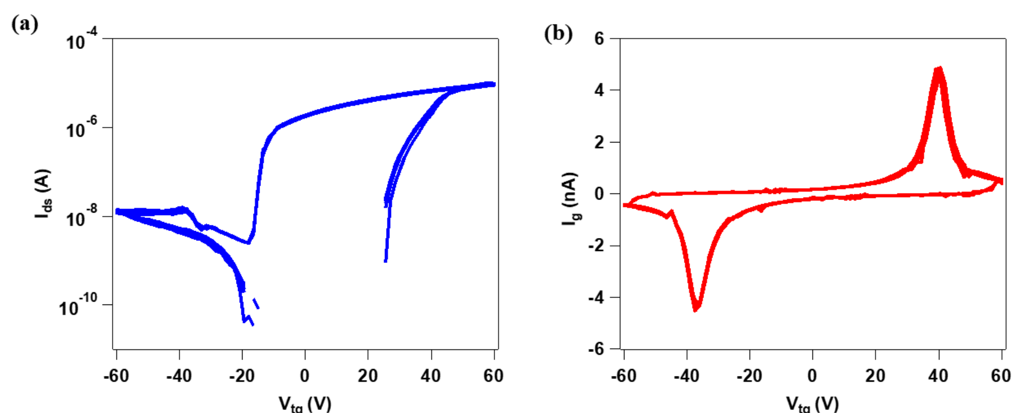

Figure 7-10. Transfer curve of a DAE/WSe_2/FeFET in top gate configuration in logarithm scale during 10 cycles (blue curve) and corresponding leakage current (red curve).

7.3.4.2. The electrical and optical switching capacity of DAE/WSe_2/FeFET

The electrical and optical switching capacity of the device was examined. For electrical switching, the electrical characteristics of WSe_2 were detected from the back gate configuration after programming the P(VDF-TrFE) into different states by applying a top gate bias exceeding its coercive voltage (±60 V). Figure 7-11a shows a representative transfer evolution cycle. In the P_{down} state, an increase of the electron current can be observed accompanied with a negative shift of the threshold voltage. In contrast, in the P_{up} state, the electron current decreased when compared to the initial state, with a modulation efficiency of 68% at a back gate voltage $V_{bg} = 60$ V (as compared with the P_{down} state). The corresponding threshold voltage moved in the positive direction. At the same time, an increase of the hole current was observed and the device showed an electron-dominant ambipolar behavior. Such effective current modulation triggered by P(VDF-TrFE) proves the electrical switching capacity of the device. We next explored the optical switching capacity rooted by DAE molecules. As presented in Figure 7-11c, the current photomodulation efficiency is largely preserved compared with DAE/WSe_2 FET, which slightly decreases from 74% to 59%, suggesting that the wet transfer process does not significantly diminish the light responsive property of DAE molecules.

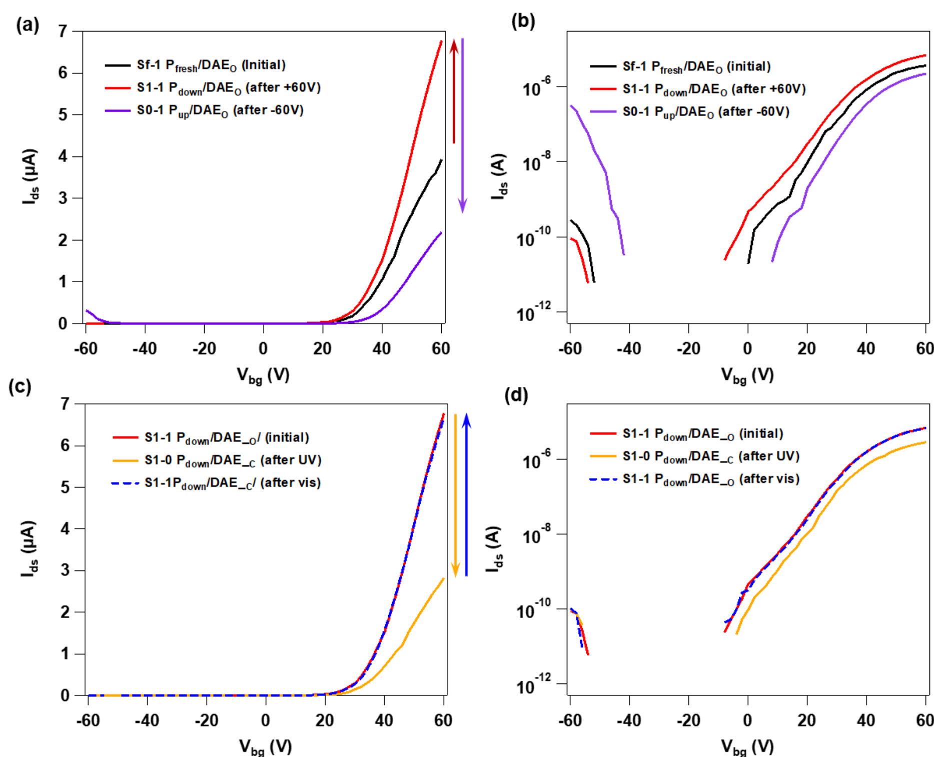

Figure 7-11. Electrical and optical switching capacity of DAE_1/WSe_2/FeFET. (a) and (b) Transfer evolution by ±60 V top gate bias in linear (a) and logarithm (b) scales. (c) and (d) Transfer evolution by UV/vis irradiation in linear (c) and logarithm (d) scales.

In an effort to demonstrate that the device can respond synergistically to light irradiation and an electric field, the two stimuli were incorporated to switch the device. In Figure 7-12a, the starting point was the state possessing the highest current level: **S1-1** P_{down}/DAE_O. The device was first exposed to UV light to switch the DAE molecules from their ring-open to their ring-closed form. With some electrons trapped by the ring-closed isomer, a decrease of the current was observed, and the device reached a second state **S1-0**: P_{down}/DAE_C. Next, the polarization direction of the polymer was switched from downward to upward by applying a negative top gate bias (–60 V). This process further depleted the electrons in the channel and the device thereof reached its lowest current level, corresponding to a third state **S0-0**: P_{up}/ DAE_C. Subsequently, vis light was used to switch the DAE molecules back to their ring-open form. In the channel, the trapped electrons were released, and the current was partially recovered, reaching a fourth state **S0-1**: P_{up}/DAE_O. Ultimately, by applying a positive gate bias (+60 V), the P(VDF-TrFE) was switched to downward direction, electrons would again be accumulated,

promoting the full recovery of the current and the device returned back to the original state **S1-1**. This reversible current modulation behavior provides unambiguous evidence that the optical switching can be incorporated in an orthogonal manner with the electrical switching.

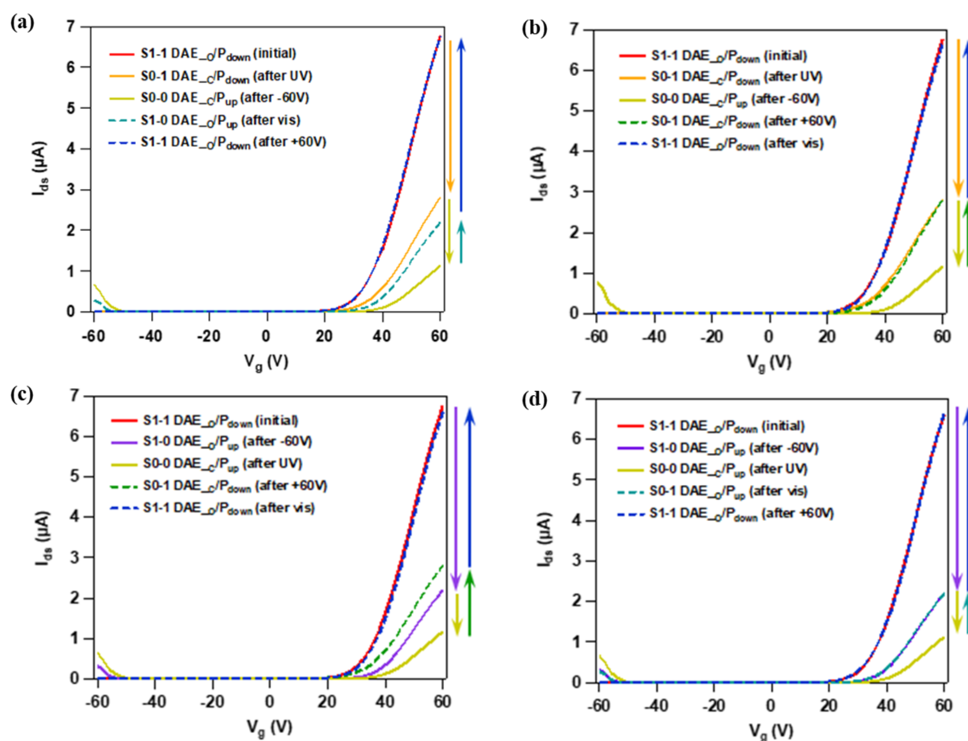

Figure 7-12. Transfer evolution by alternative UV/vis irradiation and ±60 V bias under different stimuli order.

Aiming at verifying the compatibility between the two stimuli, we further recorded the transfer evolution by reversing the stimuli sequences. Figure 7-13 shows that the 4 distinct states generated above can be freely addressed independently of the stimuli order, i.e., **S0-0** P_{up}/DAE_C can be acquired from **S1-1** P_{down}/DAE_O by 2 routes: UV irradiation + negative bias and negative bias + UV irradiation. This phenomenon demonstrated the absence of mutual interference between the light irradiation and electric field, providing evidence for the full compatibility of the electric-responsive P(VDF-TrFE) polymer with the photo-responsive DAE molecules. Figure 7-13 plots the normalized current modulation efficiency during the 4 switching cycles. In view of the synergic effect between these two molecular building blocks, the total electron current modulation efficiency reaches up to 87%. The 4 states were found to be stable during the measured cycles with different order of applied stimuli, confirming a good stability and reversibility of both electrical and optical modulation.

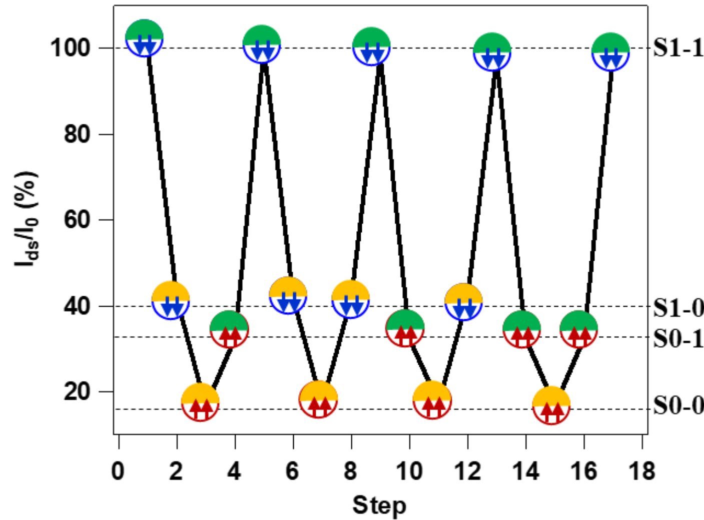

Figure 7-13. Current modulation efficiency at V_{bg} = 60 V during the 4 switching cycles with different stimuli orders.

The switching behavior was furthermore elucidated by tracking the real time current dynamics under repeated voltage and illumination operation. In Figure 7-14a, the I_{ds} current at V_{bg} = 60 V in back gate configuration was collected under cyclic ±60 V pulses applied to the top gate (each cycle contains 2 s +60 V, red boxed region; 28 s 0 V; 2 s -60 V, violet boxed region; 28 s 0 V). The measurement started from the current state with the ferroelectric polymer in the upward direction. The device was first triggered by a +60 V pulse, leading to a current spike. When the bias was reset to 0 V, the current ramps promptly to a higher level and stays constant at that value, indicating the switch of the ferroelectric polymer into downward direction. Conversely, in response to a symmetric negative pulse –60 V, the current declines back to the lower level and holds stable at that value. Under such successive cycles of ±60 V pulses, the device switched steadily between the generated two states. The current behavior at V_{bg} = 0 V modulated by periodic UV/vis illumination is shown in Figure 7-14c (each cycle contains 5 s UV, orange boxed region; 15 s dark; 15 s vis, green boxed region; 15 s dark). When the illumination was switched on, there was a surge of the current, which is attributed to the photogenerated electron-hole pairs. As the DAE isomerization progressed, the current presented a gradual decrease during UV illumination, due to the continuous trapping of electrons by photogenerated DAE_C. After the UV illumination was terminated, the current exhibited a lower value, and such reduced current could recover progressively by subsequent vis illumination. At the end of the illumination cycle, the current level

resumed to the pre-irradiation value, in good accordance with the results obtained from the transfer measurements.

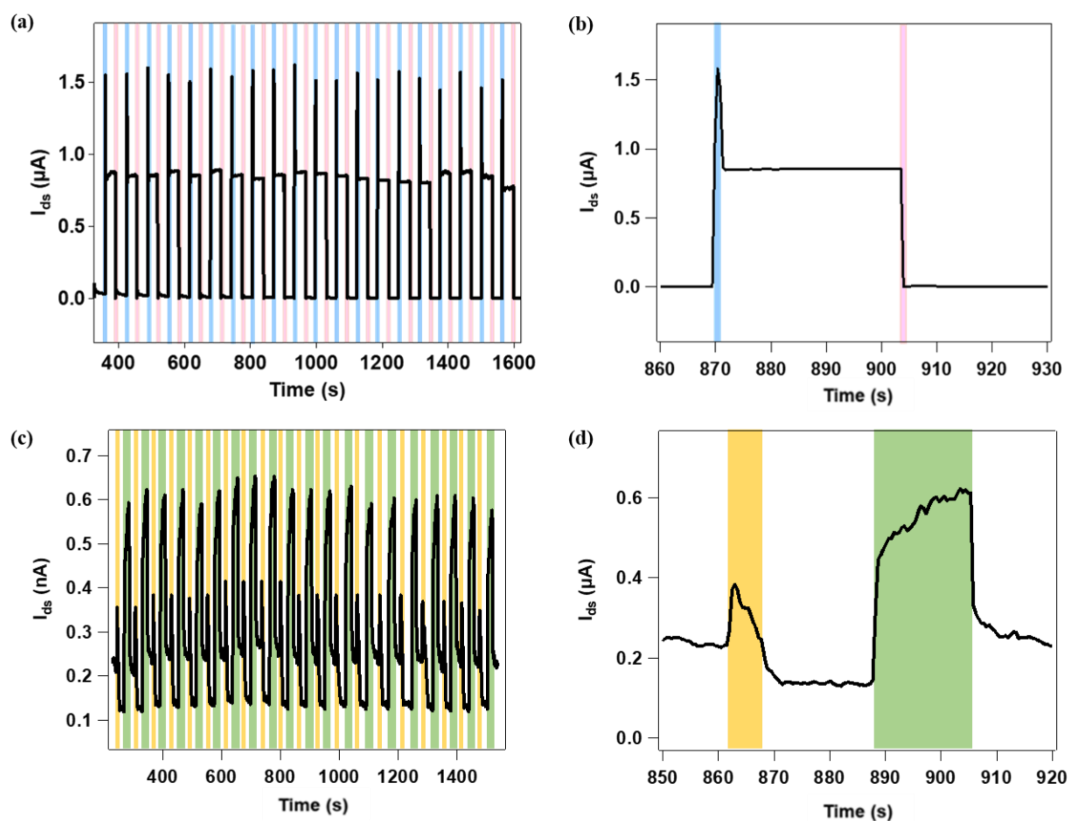

Figure 7-14. (a) and (b) Dynamic I_{ds} current switching behavior induced by applying alternating V_{tg} pulses of ±60 V at V_{bg} = 60 V and V_{ds} = 2 V during (a) 20 cycles and (b) one single cycle. (c) and (d) Dynamic I_{ds} current switching behavior induced by applying alternating UV and vis illumination at V_{bg} = 0V and V_{ds} = 4 V during (c) 20 cycles and (d) one single cycle.

In a control experiment, WSe_2/FeFET without DAE molecules was tested under the same illumination conditions, exhibiting only photoresponse yet no modulation behavior (Figure 7-15). Moreover, for both electrical and optical switching, the absence of degradation over 20 consecutive cycles confirms the durability and robustness of the device, which are crucial prerequisites for memory applications.

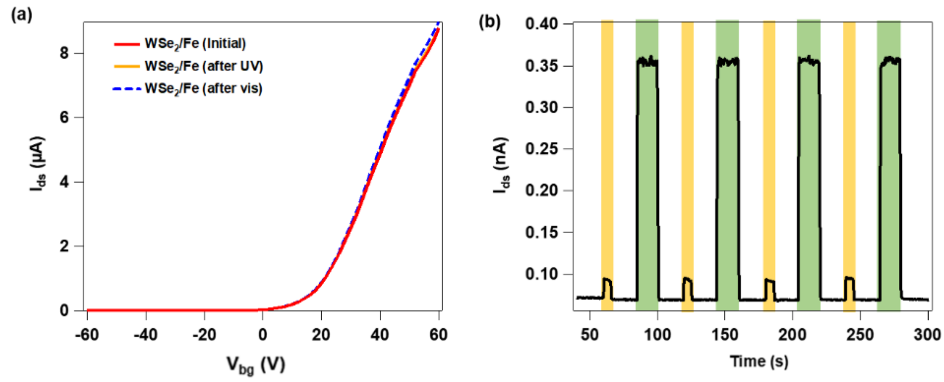

Figure 7-15. Blank experiment on WSe_2/FeFET without DAE molecules. a) Transfer evolution after UV/vis illumination. b) Dynamic current switching behavior under UV/vis illumination during 4 cycles.

7.3.4.3. Multilevel test

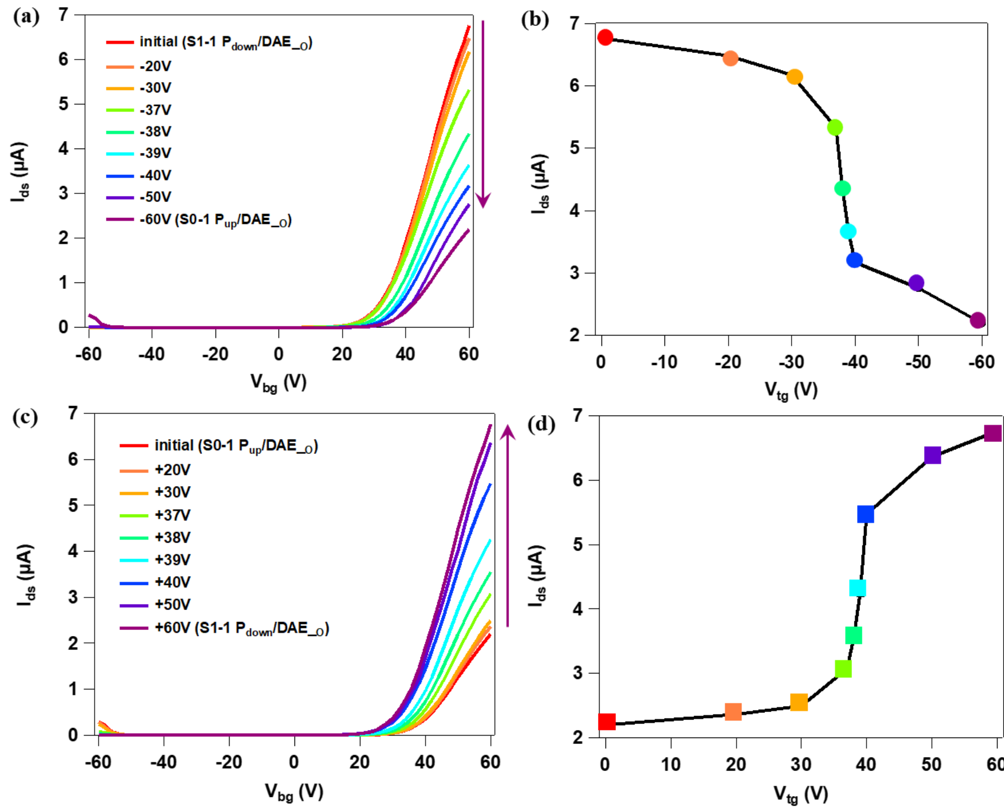

Figure 7-16. Multilevel storage between **S1-1** and **S0-1**. a, c) Transfer evolution when partially polarizing the P(VDF-TrFE) from upward to downward direction (a), and downward to upward direction (c) by sweeping top gate at various ranges, with DAE in ring-closed form; b, d) I_{ds} current at $V_g = 60$ V in (a) and (c) as a function of programmed sweep.

Since both electrical and optical modulation display a high efficiency, the suitability of our FET device as a multibit memory can be envisaged. Upon adjusting the population ratio between P_{up} and P_{down}, which can be controlled by the applied top gate voltage, intermediate ferroelectric current levels can be obtained between these two saturated states during the P(VDF-TrFE) polarization process.[31] Similarly, by tuning the population ratio between $DAE__O$ and $DAE__C$, which can be controlled by the light exposure, multiple photogenerated current levels can be achieved accordingly.[12a] In order to fulfill the demand of high density storage in practical memory applications, the maximum number of levels that can be achieved by each stimulus have been investigated.

Figure 7-16 depicts the transfer evolution from **S1-1** to **S0-1** programmed by various top gate sweeps from positive to negative direction. Note that the device was kept isolated from UV/vis illumination to ensure DAE molecules would not be disturbed. The dependence of I_{ds} at $V_{bg} = 60$ V in back gate configuration on the programmed top gate voltage was summarized in Figure 7-16b which shows a continuous decrease after each step-decreasing sweep and generates in a total number of 9 clear storage states. At the sweeping range near the coercive voltage, the current varies significantly due to the efficient switch of the ferroelectric. While the range exceeds the coercive voltage, the current decreases slowly due to the saturation of the channel. Likewise, starting from **S0-1** and applying the sweep in the opposite direction from negative to positive, the current level can increase stepwise and restore to **S1-1**. In order to demonstrate that such multilevel behavior is independent of the DAE state, another two pairs were chosen: **S1-0**/**S0-0** when DAE molecules are in their closed form, and **S1-0.55**/**S0-0.55** when DAE molecules are at an arbitrary state. As presented in Figure 7-17 and 7-18, the current exhibited the similar evolution trend and 9 distinct levels were obtained for each pair. The results imply that multilevel data storage can be achieved by precisely controlling the programming top gate voltage.

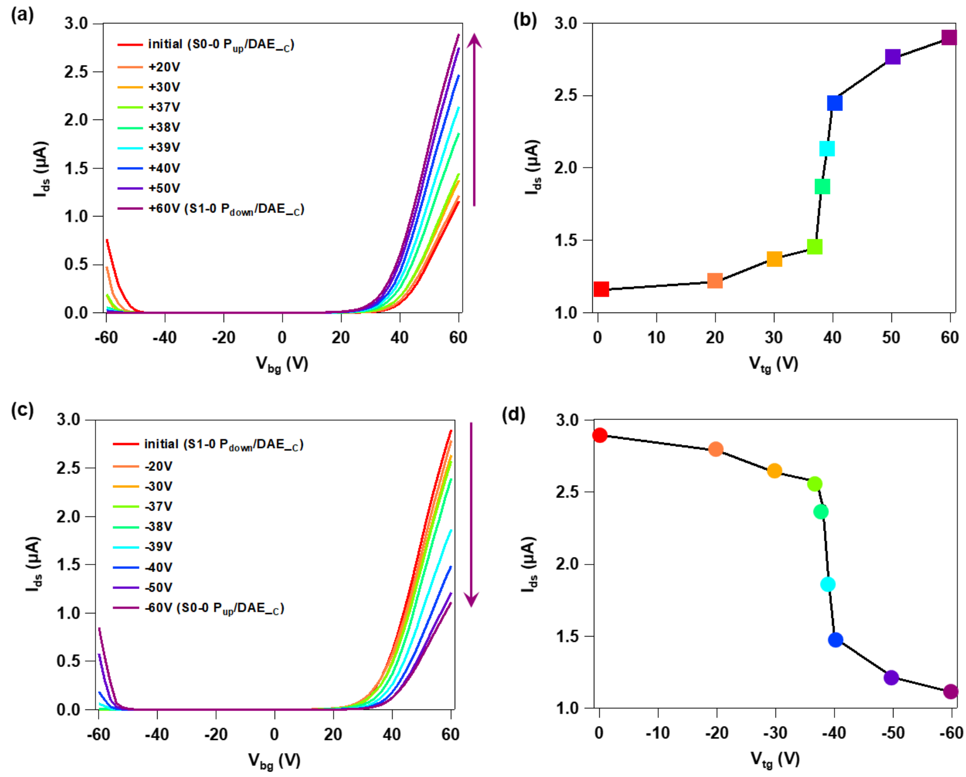

Figure 7-17. Multilevel storage between **S0-0** and **S1-0**. a, c) Transfer evolution when partially polarizing the P(VDF-TrFE) from upward to downward direction (a), and downward to upward direction (c) by sweeping top gate at various ranges, with DAE in ring-closed form; b, d) I_{ds} current at V_g = 60 V in (a) and (c) as a function of programmed sweep.

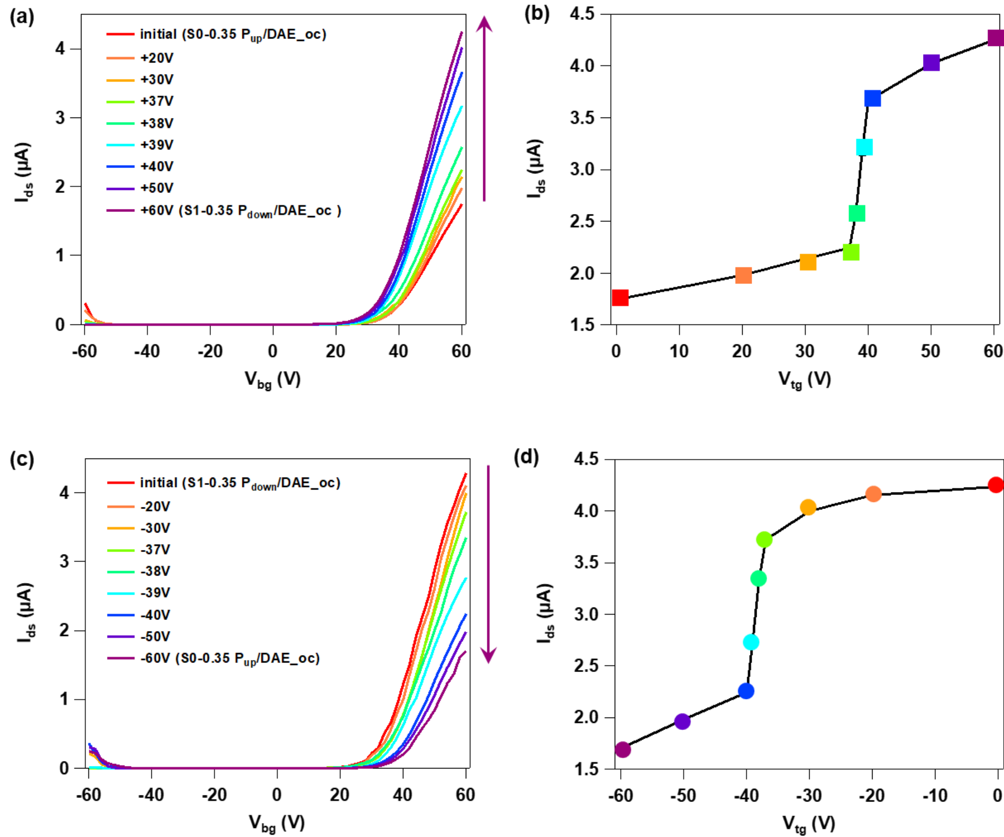

Figure 7-18. Multilevel storage between **S0-0.35** and **S1-0.35**. a, c) Transfer evolution when partially polarizing the P(VDF-TrFE) from upward to downward direction (a), and downward to upward direction (c) by sweeping top gate at various ranges, with DAE in interstate with both ring-open and ring-closed forms; b, d) I_{ds} current at V_g = 60 V in (a) and (c) as a function of programmed sweep.

When it comes to optical switching, starting from **S1-1**, the device was exposed to a periodic short time UV pulses. The corresponding dynamic current behavior was displayed in Figure 7-19, with enlarged regions in Figure 7-19d. The current decreased progressively after each light dose, proving a continual electron depletion from the WSe_2 channel. Totally 84 UV doses were employed, enabling to reach 84 current states with the final saturation state corresponding to **S1-0**. The clear current difference between each two neighbouring levels proves the validity of each state. As previously demonstrated, 9 ferroelectric states can be generated at each fixed DAE state. Therefore, with 84 photogenerated levels, the device can ideally yield a maximum number of 756 current levels, corresponding to a memory with a data storage capacity exceeding 9 bit.

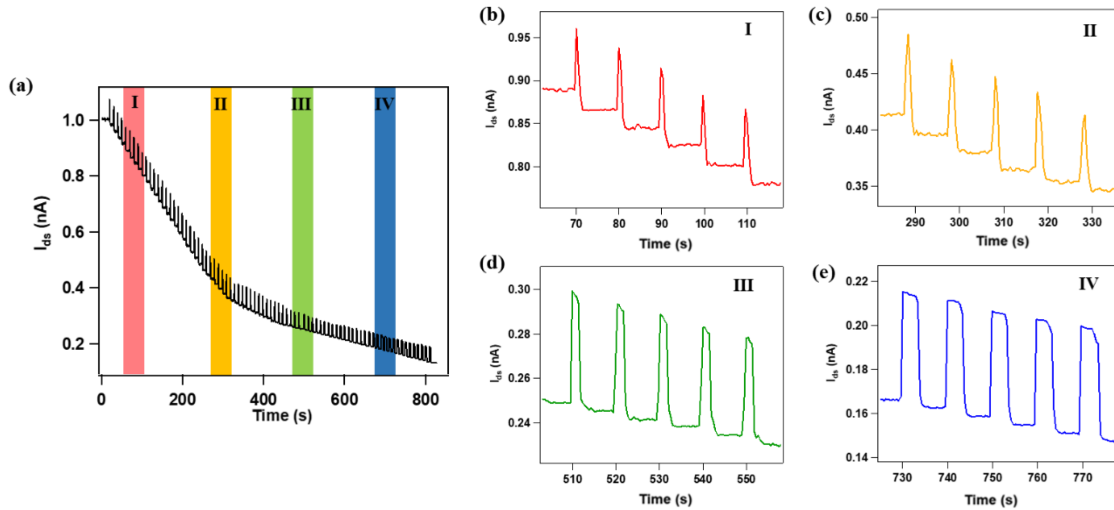

Figure 7-19. Dynamic I_{ds} current evolution behavior under exposure of short UV pulses at V_{bg} = 0 V and V_{ds} = 4 V: (a) totally obtained 84 levels and (b-d) enlarged 5 levels in region I-IV.

In order to prove such prediction, Figure 7-20 illustrates the multilevel current achieved by controlling both electric field and light illumination during 5 cycles between **S1-1** and **S0-0**. In the first cycle, in the absence of a contribution from P(VDF-TrFE), the current between **S1-1** and **S1-0** was divided into 5 well-defined levels by illumination with different time of UV dose:10 s **S1-0.55**, 20 s **S1-0.35**, 40 s **S1-0.15** and 80 s **S1-0**. Then at **S1-0**, the device went a step further by switching the P(VDF-TrFE) into P_{up} direction, arriving at the final state **S0-0**. The stored optical and electrical information can be erased by vis irradiation and positive bias, restoring to **S1-1**. In the following cycles, the P(VDF-TrFE) switching step was inserted during DAE switching process. Notably, we found that the polymer switching is accessible from any photo generated interstate and yields 4 new states: **S0-0.15**, **S0-0.35**, **S0-0.55** and **S0-1**, confirming our preliminary prediction that the device possesses the unequivocal data storage exceeding 9 bit. Moreover, the interstate obtained by different routes held stable values with negligible standard deviation, proving an accurate readout (Table 7-1).

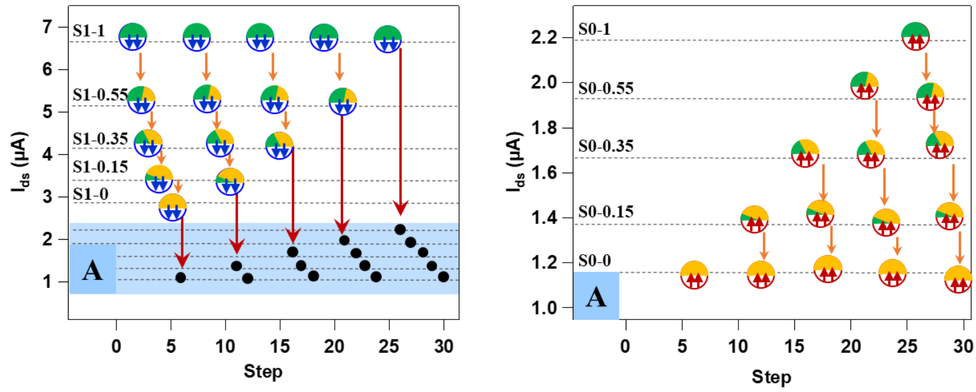

Figure 7-20. (a) Multilevel current over five cycles by different stimuli orders. (b) Enlarged levels in region A.

Table 7-1. Calculated standard deviation for each current level presented in Figure 7-19 in the main text.

Level \ I_{ds} (μA)	Cycle1	Cycle2	Cycle3	Cycle4	Cycle5	Standard deviation
S1-1	6.77	6.78	6.77	6.77	6.71	0.03
S1-0.55	5.20	5.27	5.27	5.21		0.04
S1-0.35	4.24	4.24	4.25			0.01
S1-0.15	3.49	3.49				0.00
S1-0	2.90					
S0-1					2.20	
S0-0.55				2.02	1.98	0.03
S0-0.35			1.70	1.70	1.75	0.03
S0-0.15		1.40	1.44	1.39	1.14	0.03
S0-0	1.11	1.16	1.21	1.17	1.13	0.04

7.3.4.4. Retention and endurance test

The reliability of the multilevel memory was demonstrated by both cyclic endurance and retention time tests. Apart from the full ON **S1-1** and OFF **S0-0** state, 3 arbitrary states were chosen: **S1-0.35**, **S0.5-0.35** and **S0-0.35**. The endurance test was performed under cyclic voltage/illumination operations: Starting from **S1-1**, the following states were obtained by applying 30 s UV → ±39 V sweep → –60 V pulse → 120 s UV in sequence, and **S1-1** could be reobtained by 10 min vis + +60 V pulse. Figure 7-21a profiles the drain current at V_{bg} = 60 V for these 5 states during 10 cycles. Interestingly, we observed only a minor fluctuation for each state and no deterioration, indicating that each programmed current level is highly reproducible. The retention property for each state was evaluated by independently monitoring the current as a function of storage time. It is worth noting that the device is kept without perturbation of electric field and illumination. As illustrated in Figure 7-21b, P(VDF-TrFE) fully polarized states (**S1-1**, **S1-0.35**, **S0-0.35**, **S0-0**) were steadily maintained for over 1000 h with negligible degradation, whereas **S0.5-0.35** shows a weak deterioration. This phenomenon can be explained as the partial polarization states of the ferroelectric are not thermodynamically stable and suffer from depolarization.[32] In general, the device shows reliable non-volatile characteristics. The observed robust cyclic endurance and excellent retention time is promising for application of our DAE/WSe_2/FeFET as a high density non-volatile memory.

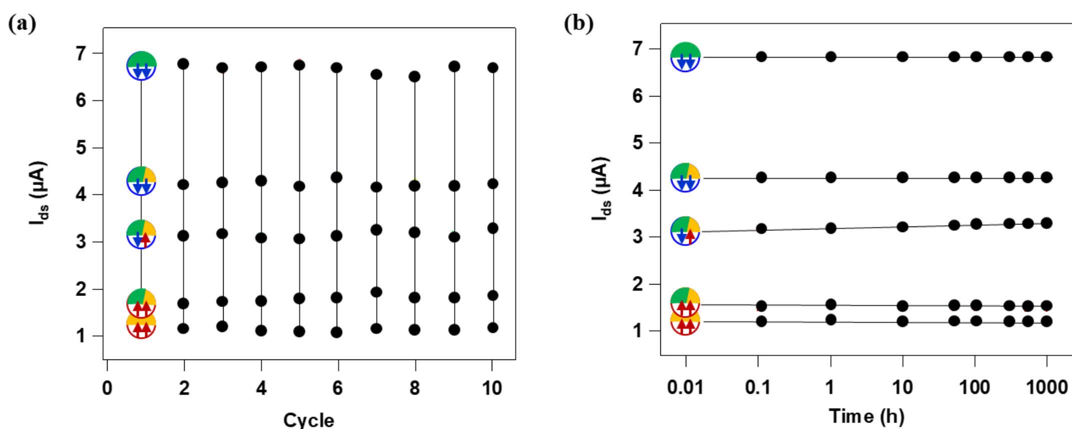

Figure 7-21. Memory characteristics of DAE_1/WSe_2/FeFET. a) Endurance performance of 5 chosen states during 10 voltage/illumination cycles. b) Time dependent retention characteristics of the 5 states.

7.4 Conclusion

In summary, by unprecedentedly interfacing 2D semiconductors with both light and ferroelectric-responsive components, we have demonstrated the operation of a multi-stimuli-responsive WSe_2 FET device. By harnessing reversible isomerization of DAE molecules and the polarization of P(VDF-TrFE) polymer, the device could respond orthogonally to light irradiation and an electric field. We observed a synergetic effect between the two stimuli, with total absence of mutual interference, yielding to an overall modulation of the output current up to 87%. Such current modulation was found being robust for over 20 cycles without perceptible attenuation. Significantly, we could achieve 9 distinguishable ferroelectric states and 84 photogenerated states, yielding to as many as 756 current levels storage in a single device. In addition, by taking full advantage of the bistability of both DAE molecules and P(VDF-TrFE) polymer, the devices demonstrated an excellent performance in cyclic endurance (10 cycles) and data retention (over 1000 h), paving the way for their application as high-density non-volatile memories. This novel ternary Janus device architecture is generally applicable to other 2D materials and stimuli-responsive molecules, thereby opening new opportunities for next-generation multi-stimuli-responsive electronics and promoting the development of "More than Moore" technologies by enriching diversification.

7.5 References

[1] a) M. M. Waldrop, *Nature News* **2016**, *530*, 144; b) T. N. Theis, H.-S. P. Wong, *Comput. Sci. Eng.* **2017**, *19*, 41; c) M. M. Waldrop, *Nature* **2016**, *530*, 144.

[2] a) M. Gobbi, E. Orgiu, P. Samorì, *Adv. Mater.* **2018**, *30*, 1706103; b) S. Bertolazzi, M. Gobbi, Y. Zhao, C. Backes, P. Samorì, *Chem. Soc. Rev.* **2018**, *47*, 6845.

[3] a) C. Simão, M. Mas-Torrent, N. Crivillers, V. Lloveras, J. M. Artés, P. Gorostiza, J. Veciana, C. Rovira, *Nat. Chem.* **2011**, *3*, 359; b) M. E. Itkis, X. Chi, A. W. Cordes, R. C. Haddon, *Science* **2002**, *296*, 1443.

[4] a) Y. Liu, Y. Yang, D. Shi, M. Xiao, L. Jiang, J. Tian, G. Zhang, Z. Liu, X. Zhang, D. Zhang, *Adv. Mater.* **2019**, *31*, 1902576; b) T. Leydecker, M. Herder, E. Pavlica, G. Bratina, S. Hecht, E. Orgiu, P. Samorì, *Nat. Nanotechnol.* **2016**, *11*, 769.

[5] a) A. Shadman, E. Rahman, Q. D. M. Khosru, *Sens Bio-sensing Res.* **2016**, *11*, 45; b) J. Liu, Y. Lu, *J. Am. Chem. Soc.* **2005**, *127*, 12677.

[6] a) P. Zhang, D. Gao, K. An, Q. Shen, C. Wang, Y. Zhang, X. Pan, X. Chen, Y. Lyv, C. Cui, *Nat. Chem.* **2020**, *12*, 381; b) X. Zhang, S. Soh, *Adv. Mater.* **2017**, *29*, 1606483.

[7] a) Q. Zhang, J. Zhang, S. Wan, W. Wang, L. Fu, *Adv. Funct. Mater.* **2018**, *28*, 1802500; b) R. Zhou, S. Zhu, L. Gong, Y. Fu, Z. Gu, Y. Zhao, *J. Mater. Chem. B* **2019**, *7*, 2588.

[8] a) M. Chhowalla, H. S. Shin, G. Eda, L.-J. Li, K. P. Loh, H. Zhang, *Nat. Chem.* **2013**, *5*, 263; b) S. Manzeli, D. Ovchinnikov, D. Pasquier, O. V. Yazyev, A. Kis, *Nat. Rev. Mater.* **2017**, *2*, 17033; c) X. Duan, C. Wang, A. Pan, R. Yu, X. Duan, *Chem. Soc. Rev.* **2015**, *44*, 8859.

[9] a) L. Yang, K. Majumdar, H. Liu, Y. Du, H. Wu, M. Hatzistergos, P. Hung, R. Tieckelmann, W. Tsai, C. Hobbs, *Nano Lett.* **2014**, *14*, 6275; b) D. M. Sim, M. Kim, S. Yim, M.-J. Choi, J. Choi, S. Yoo, Y. S. Jung, *ACS Nano* **2015**, *9*, 12115; c) S. Bertolazzi, S. Bonacchi, G. Nan, A. Pershin, D. Beljonne, P. Samorì, *Adv. Mater.* **2017**, *29*, 1606760.

[10] a) Y. Zhao, S. Bertolazzi, M. S. Maglione, C. Rovira, M. Mas-Torrent, P. Samorì, *Adv. Mater.* **2020**, *32*, 2000740; b) S. Wang, L. Tan, P. Liang, T. Liu, J. Wang, C. Fu, J. Yu, J. Dou, H. Li, X. Meng, *J. Mater. Chem. B* **2016**, *4*, 2133; c) L. Chen, X. Zhou, W. Nie, W. Feng, Q. Zhang, W. Wang, Y. Zhang, Z. Chen, P. Huang, C. He, *ACS Appl. Mater. Interfaces* **2017**, *9*, 17786.

[11] L. Wang, Q. Li, *Chem. Soc. Rev.* **2018**, *47*, 1044.

[12] a) H. Qiu, Z. Liu, Y. Yao, M. Herder, S. Hecht, P. Samorì, *Adv. Mater.* **2020**, *32*, 1907903; b) H. Qiu, Y. Zhao, Z. Liu, M. Herder, S. Hecht, P. Samorì, *Adv. Mater.* **2019**, *31*, 1903402; c) M. Gobbi, S. Bonacchi, J. X. Lian, A. Vercouter, S. Bertolazzi, B. Zyska, M. Timpel, R. Tatti, Y. Olivier, S. Hecht, M. V. Nardi, D. Beljonne, E. Orgiu, P. Samorì, *Nat. Commun.* **2018**, *9*, 2661.

[13] a) C. Zhou, Y. Chai, *Adv. Electron. Mater.* **2017**, *3*, 1600400; b) X. Chen, X. Han, Q.-D. Shen, *Adv. Electron. Mater.* **2017**, *3*, 1600460.

[14] a) Y. T. Lee, D. K. Hwang, S. Im, *J. Korean Phys. Soc.* **2015**, *67*, 1499; b) X. Wang, P. Wang, J. Wang, W. Hu, X. Zhou, N. Guo, H. Huang, S. Sun, H. Shen, T. Lin, M. Tang, L. Liao, A. Jiang, J. Sun, X. Meng, X. Chen, W. Lu, J. Chu, *Adv. Mater.* **2015**, *27*, 6575; c) D. Li, X. Wang, Y. Chen, S. Zhu, F. Gong, G. Wu, C. Meng, L. Liu, L. Wang, T. Lin, S. Sun, H. Shen, X. Wang, W. Hu, J. Wang, J. Sun, X. Meng, J. Chu, *Nanotechnology* **2018**, *29*, 105202.

[15] R. C. G. Naber, K. Asadi, P. W. M. Blom, D. M. de Leeuw, B. de Boer, *Adv. Mater.* **2010**, *22*, 933.

[16] a) A. Tarasov, S. Zhang, M.-Y. Tsai, P. M. Campbell, S. Graham, S. Barlow, S. R. Marder, E. M. Vogel, *Adv. Mater.* **2015**, *27*, 1175; b) D. Kiriya, M. Tosun, P. Zhao, J. S. Kang, A. Javey, *J. Am. Chem. Soc.* **2014**, *136*, 7853.

[17] a) Y. Li, C.-Y. Xu, P. Hu, L. Zhen, *ACS Nano* **2013**, *7*, 7795; b) S. Najmaei, X. Zou, D. Er, J. Li, Z. Jin, W. Gao, Q. Zhang, S. Park, L. Ge, S. Lei, J. Kono, V. B. Shenoy, B. I. Yakobson, A. George, P. M. Ajayan, J. Lou, *Nano Lett.* **2014**, *14*, 1354.

[18] M.-A. Stoeckel, M. Gobbi, T. Leydecker, Y. Wang, M. Eredia, S. Bonacchi, R. Verucchi, M. Timpel, M. V. Nardi, E. Orgiu, P. Samorì, *ACS Nano* **2019**, *13*, 11613.

[19] H. S. Lee, S.-W. Min, M. K. Park, Y. T. Lee, P. J. Jeon, J. H. Kim, S. Ryu, S. Im, *Small* **2012**, *8*, 3111.

[20] a) F. Tian, D. Jiao, F. Biedermann, O. A. Scherman, *Nat. Commun.* **2012**, *3*, 1207; b) F. Meng, Y.-M. Hervault, Q. Shao, B. Hu, L. Norel, S. Rigaut, X. Chen, *Nat. Commun.* **2014**, *5*, 3023; c) X. Xia, H. Yu, L. Wang, Z. ul-Abdin, *RSC Advances* **2016**, *6*, 105296.

[21] M. Herder, F. Eisenreich, A. Bonasera, A. Grafl, L. Grubert, M. Pätzel, J. Schwarz, S. Hecht, *Chem. Eur. J.* **2017**, *23*, 3743.

[22] a) K. Börjesson, M. Herder, L. Grubert, D. Duong, A. Salleo, S. Hecht, E. Orgiu, P. Samorì, *J. Mater. Chem. C* **2015**, *3*, 4156; b) Y. Guo, J. Robertson, *Appl. Phys. Lett.* **2016**, *108*, 233104.

[23] K. Koga, H. Ohigashi, *J. Appl. Phys.* **1986**, *59*, 2142.

[24] M. Carroli, D. T. Duong, E. Buchaca-Domingo, A. Liscio, K. Börjesson, M. Herder, V. Palermo, S. Hecht, N. Stingelin, A. Salleo, E. Orgiu, P. Samorì, *Adv. Funct. Mater.* **2020**, *30*, 1907507.

[25] H. Liu, A. T. Neal, P. D. Ye, *ACS Nano* **2012**, *6*, 8563.

[26] M. Beinhoff, J. Frommer, K. R. Carter, *Chem. Mater.* **2006**, *18*, 3425.

[27] P. Tonndorf, R. Schmidt, P. Böttger, X. Zhang, J. Börner, A. Liebig, M. Albrecht, C. Kloc, O. Gordan, D. R. Zahn, *Opt. Express* **2013**, *21*, 4908.

[28] S. Liu, I. Grinberg, A. M. Rappe, *Nature* **2016**, *534*, 360.

[29] D. Jena, A. Konar, *Phys. Rev. Lett.* **2007**, *98*, 136805.

[30] B. Radisavljevic, A. Radenovic, J. Brivio, V. Giacometti, A. Kis, *Nat. Nanotechnol.* **2011**, *6*, 147.

[31] a) S. K. Hwang, I. Bae, R. H. Kim, C. Park, *Adv. Mater.* **2012**, *24*, 5910; b) M. Xu, X. Zhang, S. Li, T. Xu, W. Xie, W. Wang, *J. Mater. Chem. C* **2019**, *7*, 13477.

[32] J. Lee, A. J. J. M. van Breemen, V. Khikhlovskyi, M. Kemerink, R. A. J. Janssen, G. H. Gelinck, *Sci. Rep.* **2016**, *6*, 24407.

Chapter 8: Quaternary-Responsive Field-Effect Transistors Based on Asymmetrically Functionalized Janus Few-Layer WSe_2

The projected saturation of Moore's law and the expiration of Dennard scaling has led to the demand for integrating novel analog functionalities within semiconductor-based devices. Herein, photochromic silane-terminated spiropyran (SP) derivative has been designed and synthesized, which can transform to the merocyanine (MC) isomer in response to UV illumination and reverse back by either heat or vis illumination. The SP molecule was incorporated at the dielectric-semiconductor interface in a WSe2-based field-effect-transistor (FET), coated with a ferroelectric poly(vinylidene fluoride-trifluoroethylene) layer. A quaternary-responsive FET device has thereof been unprecedently fabricated, whose output current can be remotely and reversibly controlled by heat, light as well as electric field. Thanks to the efficient tuning of each of the stimuli-responsive element and their synergic effect between each other, the device can be modulated from n-type to p-type with electrons been fully exhausted. The rational mechanism for the observed switching behaviour from the SP molecules has also been investigated, with the ionic polarized MC isomer acting as a carrier scattering site to effectively suppress electron transport in the interfaced WSe_2.

8.1. Introduction

Taking advantage of their extraordinary physical properties and compatibility with silicon-based technology, two-dimensional materials (2DMs), including graphene and transition metal dichalcogenides (TMDs), have been the target of extensive fundamental studies and technological advances over past decade.[1] Within the current More-than-Moore era, the realization of multifunctional manipulations within individual 2DM-based devices is being explored. Owing to their atomic thickness and reduced screening effect, the intrinsic properties of 2DMs are extremely sensitive to the external environment and can thereof be modulated by surface modification.[2] Various functional molecules have been incorporated into transistor operations, yet the approach is still in the embryonic phase.[3] In particular, during the last five years, considerable workload has been dedicated to the

incorporation of the stimuli-responsive molecules, which are able to exploit precise nanoscale actuations in response to chemical or physical inputs, as fundamental building blocks in the conventional electronic devices.[4] When tailored with such dynamic molecular entities, the external stimuli may act as an additional processing unit to operate the target devices, endowing them with new properties for specific applications as memories,[5] UV sensors,[6] synapse simulation,[7] and so on.

Light and electric field have been emerged as attractive external stimuli, both of which are noninvasive, remotely and digitally controllable with high spatial and temporal resolution.[8] As a mild and conveniently applied stimuli, temperature also represents one of the most widely explored inputs in the design of stimuli-responsive platforms.

Triggered by light, photochromic reactions have been recently demonstrated to be a simple-but-effective strategy to integrate optical switching into the manipulation of the carrier transport in 2DM-based FETs.[9] The development of such stimulus-responsive FETs has then been boosted by synergistically cooperating between electronic physics and multiple organic chemistry reactions. We previously achieved ternary-stimuli-responsive FETs by integrating two different stimuli-responsive elements, photochromic molecule diarylethene (DAE) and ferroelectric poly(vinylidene fluoride–trifluoroethylene) (P(VDF-TrFE) into a single WSe_2-based FET, whose output current can be reversibly controlled in accordance with the photoisomerization or ferropolarization. The physisorbed DAE layer provides a promising way towards non-destructive functionalization of the channel material, however, the weak van der Waals interaction between the molecules and the Si/SiO_2 substrate results in easy remove of the molecules during a simple rinsing procedure. As a consequence, conventional photolithography cannot be used in such device architecture, and the choice of the second stimuli-responsive element is also limited. To overcome this issue, here we synthesized a silane-terminated spiropyran (SP) derivative, another representative photochromic molecule, which can densely pack on Si/SiO_2 substrate through a strong covalent silylation.[10] Such nonvolatile chemisorption thereof facilitates the device fabrication and provides a better compatibility when integrating a third element into the system. Moreover, the photochromic reaction from SP to merocyanine (MC) can be triggered by UV light illumination, and the reverse isomerization from MC to SP can be accomplished by vis

light illumination as well as heating, adding a further thermal-responsive nature to the corresponding FET device when compared with DAE system.[11]

Herein, silane-terminated SP photochromic molecule and ferroelectric polymer P(VDF-TrFE) have been incorporated into WSe_2-based FET devices. With this combination, we obtained quaternary-stimuli-responsive FET capable of perceiving heat, light and electric field stimuli inputs and modulate output current accordingly. Following the similar Janus modified structure presented in chapter 7, the bottom surface of the WSe_2 flake is attached with a SP film, and the top surface is decorated with the P(VDF-TrFE) layer. Such hierarchical architecture enables an independent control of the output current under distinct multiple stimuli. Taking advantage of the synergic effect between the stimuli, with a significant electron current modulation efficiency of 84% from SP, and 99% from P(VDF-TrFE), the electrons in the channel can be totally exhausted when combining the two switches and the device thereof can be modulated from n-type to p-type. Moreover, by collectively pool multiple stimuli as inputs, the overreliance in a single stimulus has been reduced, which moreover increases the sensitivity and compliance of the molecular-tailored stimuli-responsive platform.

8.2. Experimental method

8.2.1. SP film functionalization

The formation of SP film via silylation of hydroxyl functions on the SiO_2 surface with silylating agents is sketched in Figure 8-1. The protocols can be described as: cleaning and activation of the Si/SiO_2 substrate to maximize the number of reactive hydroxyl groups on the surface by exposing them to UV/O_3 for 20 min. Then, these freshly UV/O_3 treated substrates were immediately immersed in a SP solution with a concentration of about 1% (dissolved in toluene) in a sealed reactor. The solution was heated at 60 °C for one hour and then left at room temperature for overnight. After taking out from the SP solution, the substrates were thoroughly rinsed with toluene, and sonicated 5 s in hexane to remove any physically adsorbed reagents. Finally, the substrates were baked at 60 °C for one hour.

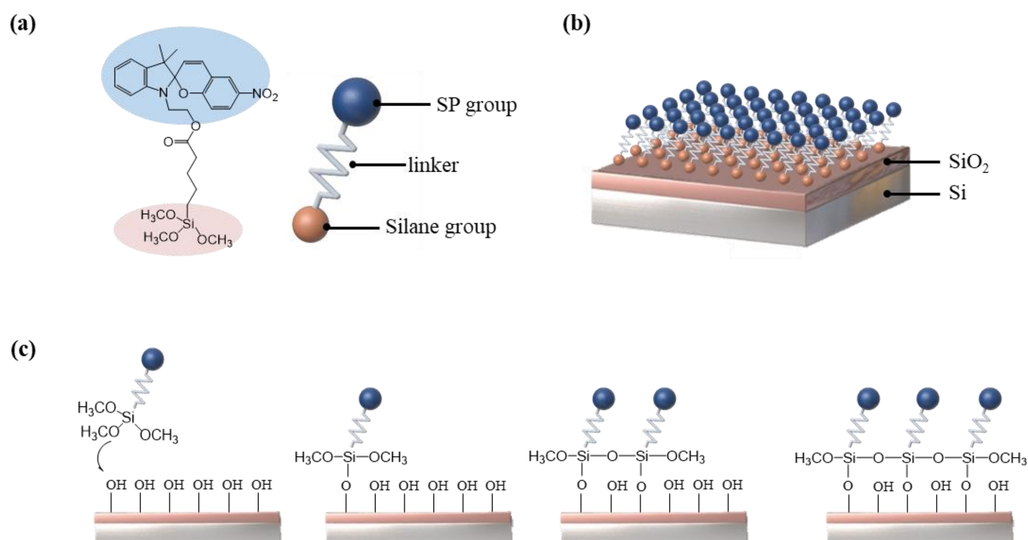

Figure 8-1. (a) chemical structure of SP derivative, (b) SP film on Si/SiO_2 substrate, (c) protocol of SP film formation of Si/SiO2 substrate.

8.2.2. Fabrication of SP/WSe_2/FeFET

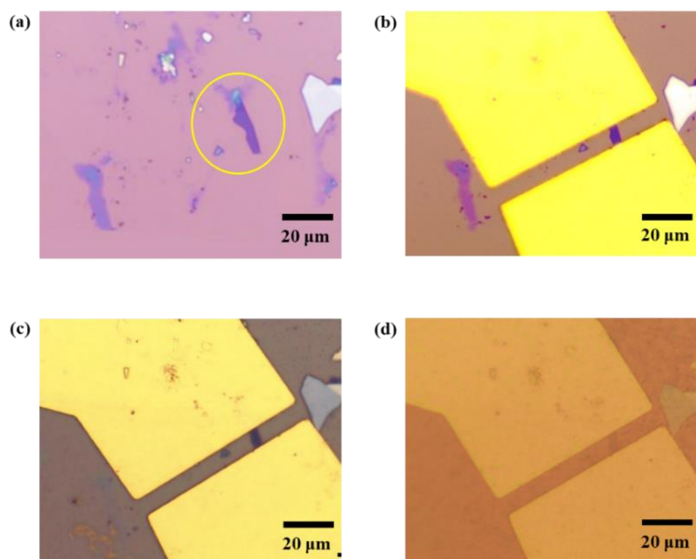

Figure 8-2. Optical microscopy images captured at four stages during the fabrication process. (a) Target WSe_2 flake with the underneath SP film, (b) SP/WSe_2 FET, (c) SP/WSe_2/FeFET with P(VDF-TrFE) film, (d) SP/WSe_2/FeFET with evaporated 20 nm semi-transparent top gate Au electrode.

The mechanically exfoliated few-layer WSe_2 flakes from bulk crystal (from HQ Graphene) were transferred onto the pre-SP functionalized SiO_2 substrates. The source and drain electrodes were patterned by using conventional photolithography method, followed by metal evaporation and liftoff

process. With the underlying physisorbed SP layer guaranteeing the light responsive capacity, the top surface of WSe_2 is ready for being interfaced with the ferroelectric P(VDF-TrFE) layer to impart the ferroelectric responsive nature. The P(VDF-TrFE) layer was spin-coated on top of the SP/WSe_2 device, followed by curing at 140 °C for 2 hours to increase its crystallinity. Finally, a semi-transparent top gate electrode (20 nm Au) was evaporated on top of the P(VDF-TrFE) layer.

Figure 8-2 shows the optical microscopy images recorded at four stages during the fabrication process: target WSe_2 flake with underneath SP layer, SP/WSe_2 FET with evaporated 60 nm source-drain Au electrodes, SP/WSe_2/FeFET with P(VDF-TrFE) film, and SP/WSe_2/FeFET with evaporated 20 nm semi-transparent top gate Au electrode. Figure 8-3 portrays the architecture of the SP/WSe_2/FeFET device.

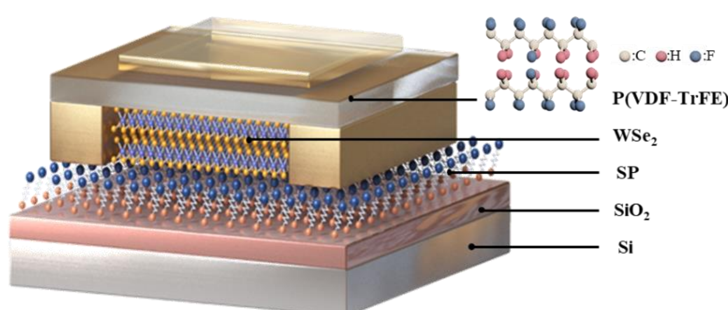

Figure 8-3. Schematic diagram of the SP/WSe_2/FeFET device with double-sided decoration: the bottom surface with SP film and the top surface with P(VDF-TrFE) layer.

8.2.3. Characterization methods

UV-vis absorption spectra and isomerization kinetics of the SP film on quartz substrate were recorded at room temperature with a Jasco V650 spectrophotometer. The molecular switching triggered by light irradiation was performed with optical fiber-coupled LEDs (from ThorLabs), with wavelength of 365 nm (1.2 mW/cm^2) or λ = 530 nm (4 mW/cm^2), by heating was performed with a hair drier. For photoisomerization kinetics, irradiation was performed in situ within the spectrophotometer chamber, by shining a beam of UV light on the front face of the quartz substrate. UV irradiation was performed for fixed intervals, and Abs_{550nm} was recorded immediately after switching off UV light.

Water contact angle was measured by a drop shape analyzer instrument Kruss DSA 100.

PL spectra were recorded by a Renishaw inVia spectrometer equipped with 532 nm laser. PL maps were acquired with 0.5 mm steps in 15 x 15 mm^2 areas. Each spectrum was taken at 0.1 s of integration time and 1 accumulation.

Atomic force microscopy (AFM) imaging was carried out by a Nanoscope (Veeco Multimode V) in tapping mode under ambient conditions.

All electrical measurements were carried out by using a probe station connected to a Keithley 2636 in a glovebox filled with nitrogen. Device irradiation is realized by using a monochromator set-up, with either UV light (at λ = 312 nm, 0.15 $mWcm^{-2}$) or vis light (λ = 530 nm, 11.8 $mWcm^{-2}$). The PSS is reached under UV irradiation for 150 s and recovery within 20 min under vis light.

The charge carrier mobility is calculated in the linear regime from the transfer curve by using the expression:[12]

$$\mu = \frac{dI_{ds}}{dV_g} \times \frac{L}{W} \times \frac{1}{V_{ds}} \times \frac{d}{\varepsilon_0 \varepsilon_r} \qquad (1)$$

Where L is the channel length, W is the channel width, and ε_r is the dielectric constant, ε_r = 3.9 for SiO_2 and ε_r= 10 for P(VDF-TrFE).

8.3. Results and discussion

8.3.1. Characterization of SP film

The reversible transformation between SP and MC is schematically illustrated in Figure 8-4a. The successful functionalization of SP film on SiO_2 surface was confirmed through UV-vis absorption spectra, water contact angle measurements, atomic force microscopy (AFM) and PL mapping.

8.3.1.1. UV-vis absorption spectra

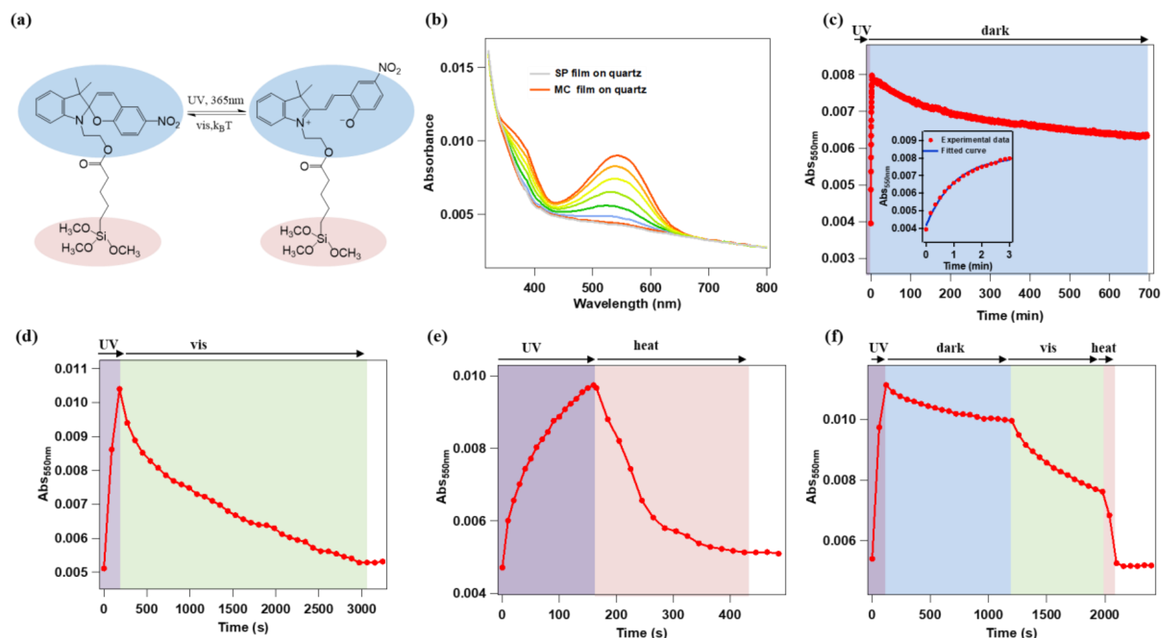

Figure 8-4. Optical characterization of the SP photoswitching. (a) Chemical structures and photoisomerization reaction between SP and MC isomer. (b) Absorption spectra of SP film on quartz substrate during the course of UV irradiation. (c) to (f) Kinetics of the SP film, as monitored by plotting the absorbance at 550 nm under UV irradiation and afterwards (c) in the dark, (d) under vis irradiation, (e) under heat, (f) in the combination of dark, vis irradiation and heat treatment.

The typical UV-vis absorption spectra of SP film on quartz substrate were initially recorded during the course of UV irradiation until reaching the photostationary state (PSS) (Figure 8-4). The typical band of MC chromophores centered at 550 nm appeared after a few seconds of UV irradiation. Therefore, the kinetics of the photoisomerization between SP and MC can be followed by monitoring the evolution of the absorbance at 550 nm (Abs_{550nm}). Abs_{550nm} kept rising by UV irradiation until all SP converted to MC after 180 s, which can be fitted by a simple exponential curve following the equation (inset in Figure 8-4c and Figure 8-5a): [13] $Abs_{550nm}(t) = Abs_{sat} - B \times \exp(-t/\tau_{hv})$, where τ_{hv} represents the time constant. After reaching PSS, MC can be restored to SP in three routes by showing a decrease of Abs_{550nm} in accordance with a first-order decay: spontaneously in the thermal condition, vis light irradiation and heating. Figure 8-4c show that ca. 37.5% of the molecules in the MC form were transformed to SP after 11 hours in the thermal condition. The switching process could be accelerated by vis light irradiation, which lasted ca. 45 min to convert all the MC into SP. Heating turned out being

the most efficient stimuli as evidenced by a kinetic which required only 4 min. When the 3 routes were combined in the same measurement, the different kinetics can be clearly singled out.

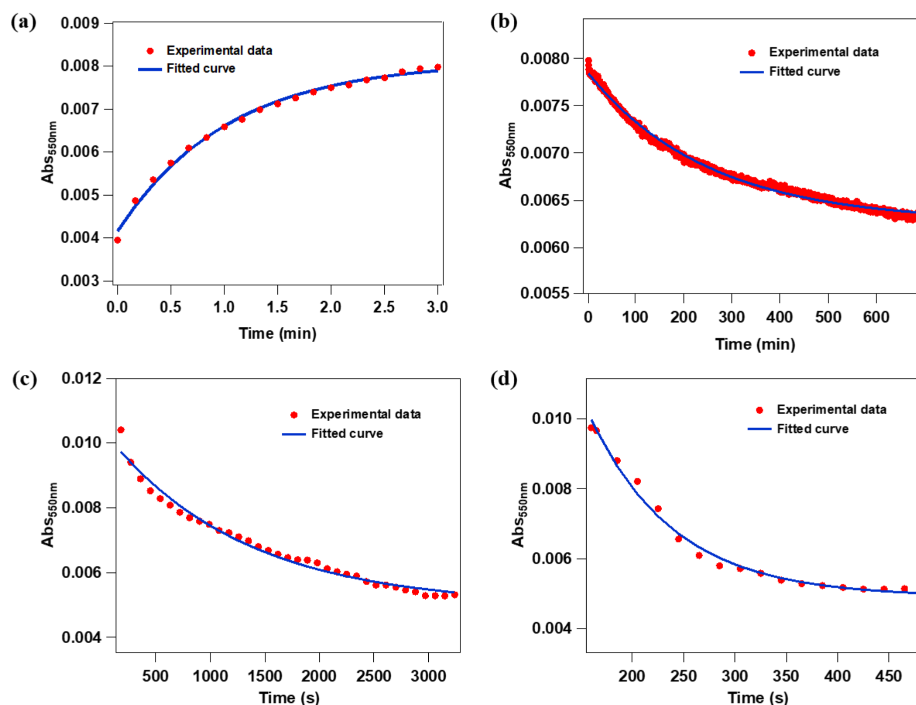

Figure 8-5. Fitting of the time evolution of absorbance at 550 nm with the equation Abs_{550nm} (t) = Abs_{sat} − B × exp $(-t/\tau_{hv})$. Red dots are experimental data and blue lines are fitted curves. The values extracted from the fit for Abs_{sat}, B and τ_{hv} are listed in Table 8-1.

Table 8-1. Parameters extracted from the fitting curves of the photoisomerization kinetics.

	Abs_{sat}	B	τ_{hv}
UV	0.00811	0.00395	1.0273
dark	0.00627	-0.00159	248.89
vis	0.00497	-0.00549	1253.97
heat	0.00491	-0.03539	85.29

8.3.1.2. Water contact angle

Water contact angle measurements of pristine, SP-treated, and after UV/heat treatment SiO_2 surfaces are displayed in Figures 8-6. The initial clean SiO_2 surface displayed hydrophilic performance, and its wettability decreased after SP functionalization. The MC, being more polar than SP,[11] is characterized by an increased hydrophilic nature when explored by contact angle measurements. More precisely, the

SP to MC isomerization exhibit a drop of the contact angle by 15.2°. The value could be recovered by further heating treatment, confirming the reversible nature of the switching from MC to SP

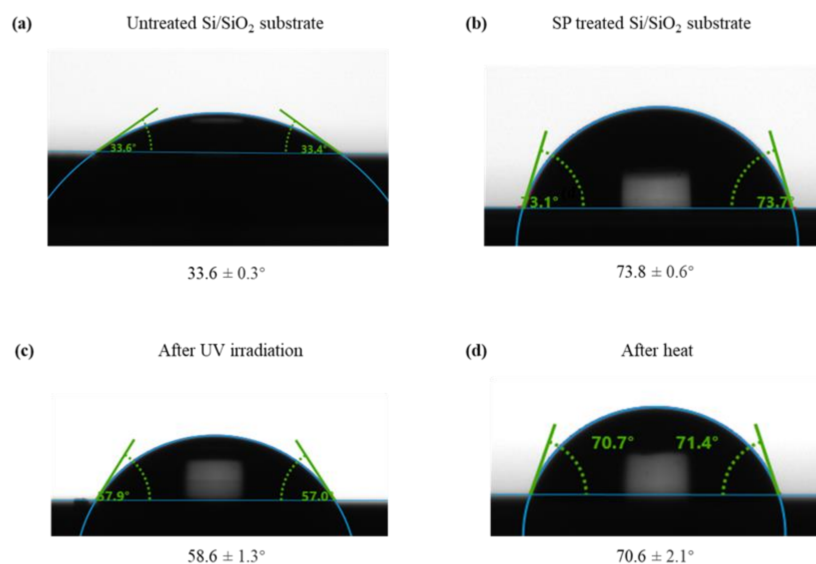

Figure 8-6. Water contact angle of (a) untreated Si/SiO_2 substrate, (b) SP treated Si/SiO_2 substrate, (c) UV treated $SP/Si/SiO_2$ substrate, (d) Heat treated $SP/Si/SiO_2$ substrate. The measurement was done by Krüss DSA 100 upon deposition of a 2 μL drop of Milli-Q water on the substrate surface.

8.3.1.3. AFM

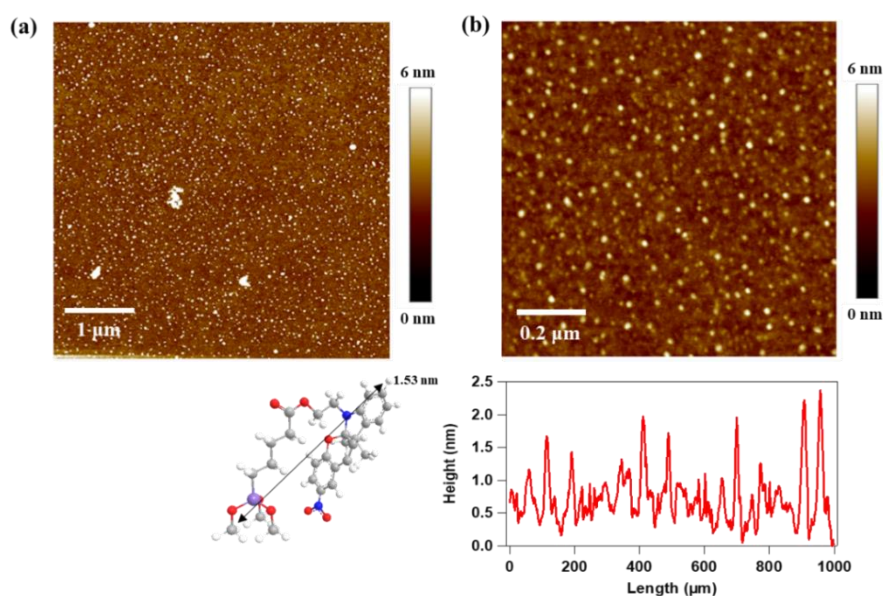

Figure 8-7. Topographical AFM image of SP treated Si/SiO_2 substrate on an area of (a) 5 x 5 μm^2, (b) 1 x 1 μm^2. The panel below shows a representative height profile. The measurement was carried out by a Nanoscope (Veeco Multimode V) in tapping mode under ambient conditions.

The morphology of the SP film was investigated by means of AFM (Figure 8-7). AFM imaging performed on SP-functionalized SiO_2 surface revealed a rather flat morphology, with the root-mean-square roughness value in an area of 1 μm x 1 μm amounting to ca. 0.17 nm. As evidenced by the topographical profile, the height of the film was 1.3 ± 0.5 nm, which correlates well with the length of a single SP molecule, which is ca. of 1.5 nanometer. The appearance of relatively larger aggregates is likely due to the self-polymerization, i.e., the silane-based SP molecules covalently bonded with neighboring molecules.[14]

8.3.1.4. PL mapping

To unveil the interaction between SP and WSe_2, 2D mapping of PL intensity over chosen WSe_2 flakes with different thicknesses was carried out. Before focusing the attention to the PL of WSe_2, the PL evolution of the SP/MC molecules were first investigated by integrating the wavelength from 560 nm to 650 nm, the range in which MC is photoluminescent while SP is not. As summarized in Figure 8-8, the as-prepared SP/WSe_2 was found to be scarcely photoluminescent. After UV illumination, the PL of the region outside the flake was strongly enhanced, indicative of an effective SP to MC isomerization. Interestingly, the region inside the flake showed a weaker PL, which can be ascribed to the quenching effect by WSe_2. Note that the applied green laser power and the obtained peak intensity were compromised, and a relatively weak laser power was utilized during the measurement in order to minimize the interaction between the laser and the MC molecules. In order to trigger the molecule back to SP form, a stronger laser power was utilized to scan the same region. As clearly indicated in Figure 8-8a, the PL after laser scanning turned back to the original state, indicative of the recovery of SP. Figure8-8b depicts the detailed PL spectra evolution in the points labeled as A and B. To investigate if the SP photoswitch is accompanied with a modulation of the optical properties of WSe_2, wavelength from 750 nm to 900 nm the range in which WSe_2 is photoluminescent were integrated. Spatial variations in the intensity across the flake were observed due to the variation of the flake thickness. The representative spectra taken from the bilayer (highlighted in C) and few-layer (highlighted in D) regions, are presented in Figure 8-8d. Point C represents a bilayer region, and its PL spectra shows a broad band

corresponding to emission from both the indirect and direct bandgaps. For the few-layer region, the emission intensity decreased strikingly compared with thinner regions, and accordingly the PL spectra contains two separate peaks, originated from the indirect and direct bandgaps emission, respectively.[15] Note that we have chosen flakes with different thicknesses for PL mapping, and similar evolution trend was obtained: An overall quenching of the PL intensity for WSe_2 was observed when molecules were in MC form compared with SP, providing evidence for the occurrence of electronic interaction between the two components. Such MC-induced PL quenching might be explained by the charge accumulation (either holes or electrons) induced Auger-like nonradiative decay.[6a] The reduced PL intensity could be completely reversed by further laser irradiation.

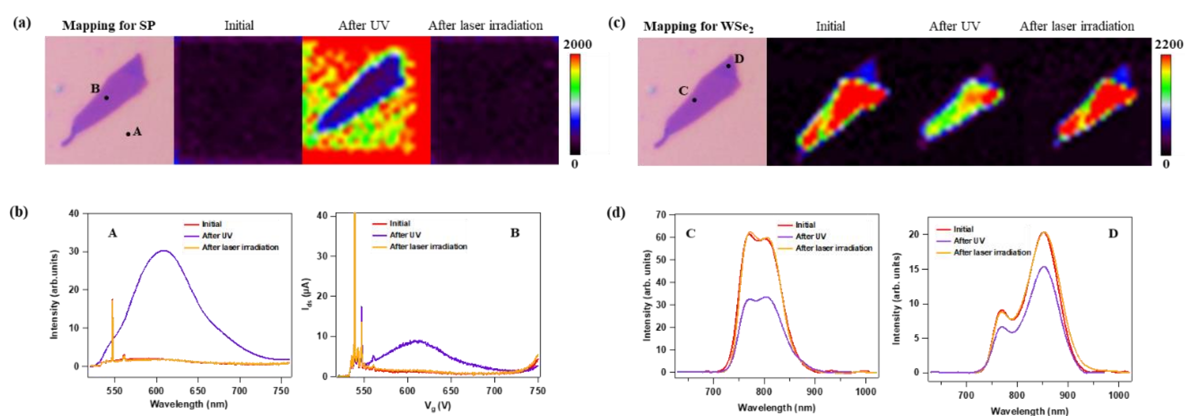

Figure 8-8. (a) Optical microscopy image of a SP/WSe_2 flake (left) and its PL intensity mapping (right) integrated from 560 nm to 650 nm as prepared, after UV irradiation, and after laser irradiation. (b) PL spectra evolution in the points labeled as A and B. (c) same flake with PL intensity mapping integrated from 750 nm to 900 nm. (d) PL spectra evolution in the points labeled as C (bilayer) and D (few-layer).

Figure 8-9 and 8-10 shows the PL evolution of SP/WSe_2 flakes with monolayer and few-layer thickness. Monolayer WSe_2 possesses direct band gap thus strong emission can be observed in its PL spectra, with a prominent peak A centered at ~760 nm. As the number of layers increases, peak I emission spectra appears, originating from indirect band gap emission, which is virtually absent in the monolayer. The emerging peak I would compete with peak A deriving from direct bandgap emission, leading to a decay of the PL quantum efficiency. It should also be noted that peak I reveals a gradual redshift and a decay of intensity with the number of layers increasing.[15] Here by comparing the PL mapping of SP/WSe_2 flakes with thickness ranging from monolayer, bilayer to few-layer, it is obvious that they all showing

the same tendency after UV and laser irradiation: the molecule luminescence increases after UV irradiation, and recovers after laser irradiation. The WSe_2 luminescence decreases after UV irradiation, also recovers after laser irradiation.

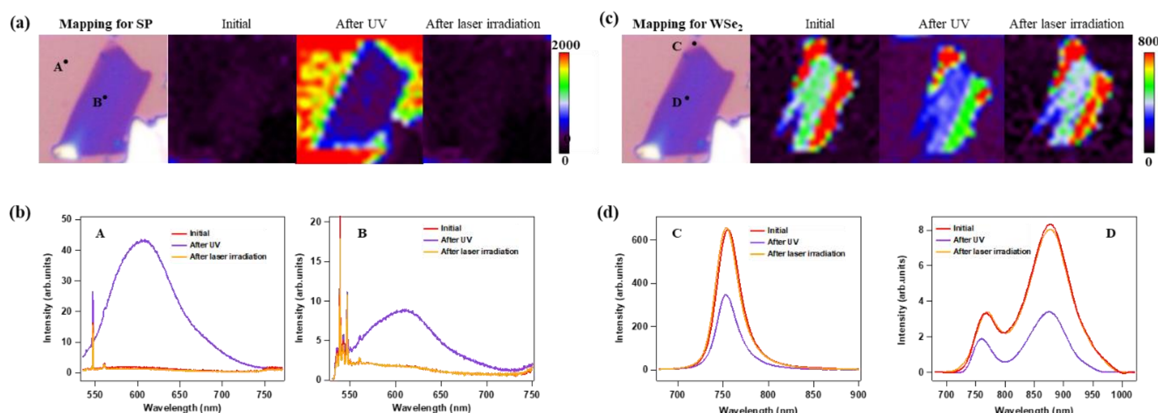

Figure 8-9. (a) Optical microscopy image of a SP/WSe_2 flake (left) and its PL intensity mapping (right) integrated from 560 nm to 650 nm as prepared, after UV irradiation, and after laser irradiation, (b) PL spectra evolution in the points labeled as A and B, (c) same flake with PL intensity mapping integrated from 750 nm to 900 nm, (d) PL spectra evolution in the points labeled as C (monolayer) and D (few-layer).

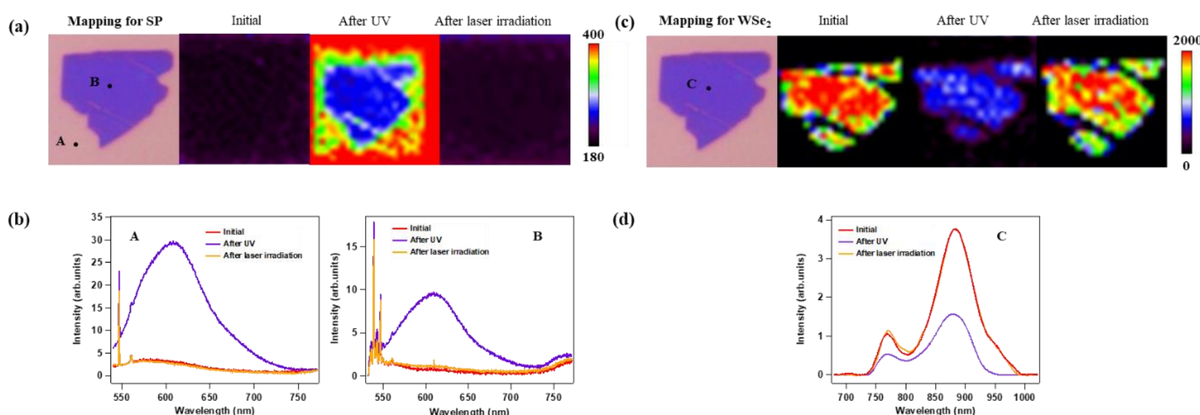

Figure 8-10. (a) Optical microscopy image of a SP/WSe_2 flake (left) and its PL intensity mapping (right) integrated from 560 nm to 650 nm as prepared, after UV irradiation, and after laser irradiation, (b) PL spectra evolution in the points labeled as A and B, (c) same flake with PL intensity mapping integrated from 750 nm to 900 nm, (d) PL spectra evolution in the points labeled as C (few-layer).

8.3.2. Electrical characterization

8.3.2.1. SP/WSe_2 FET

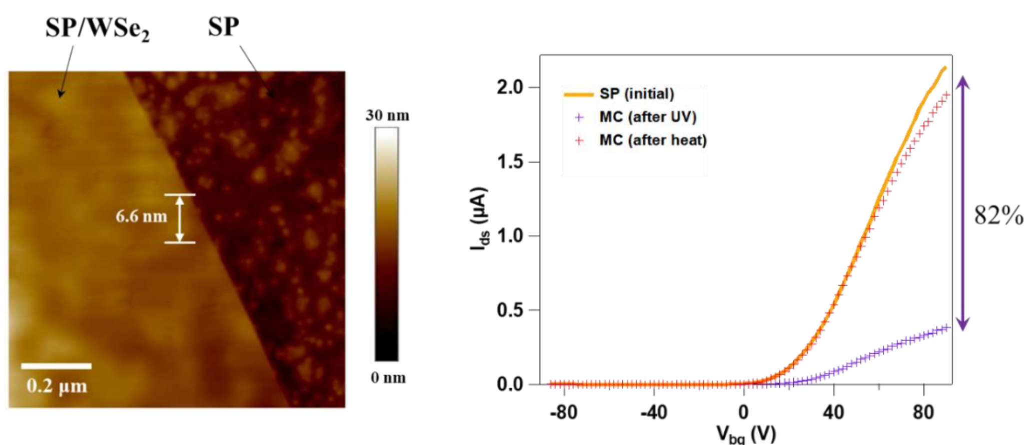

Figure 8-11. AFM image of a SP/WSe_2 flake, (b) transfer evolution of SP/WSe_2 FET as prepared and after UV, heat treatment.

To cast light onto the electronic properties of the SP/WSe_2, they have been integrated as the channel material into the FET device. The original device revealed typical n-type behavior with electron mobility of 12.4 $cm^2V^{-1}s^{-1}$ (Figure 8-11). Obviously, the electron current was altered upon UV light irradiation with a modulation efficiency of 82% and the mobility decreased to 1.1 $cm^2V^{-1}s^{-1}$, attributable to the SP conversion to MC. After heating, the current reversed almost to the initial value, which coincides well with the reversible change in the absorption spectra and PL mapping.

8.3.2.2. SP/WSe_2/FeFET

a. SP/WSe_2/FeFET in top-gate configuration

To add a further functionality for the as-fabricated optically switchable SP/WSe_2 FET, the upper surface of WSe_2 was then decorated with a ferroelectric polymer P(VDF-TrFE), followed by the deposition of a semi-transparent top-gate electrode (Au, 20 nm), to control the polarization direction of the P(VDF-TrFE) film. The transistor properties in top-gate configuration with P(VDF-TrFE) serving as dielectric material was first characterized (Figure 8-12a), which reveals obvious electron-transport-dominated ambipolar behavior. The corresponding leakage current is depicted in Figure 8-12b, with two apparent

current peaks occur near the coercive field of P(VDF-TrFE), verifying that P(VDF-TrFE) has good dielectric and ferroelectric characteristics.

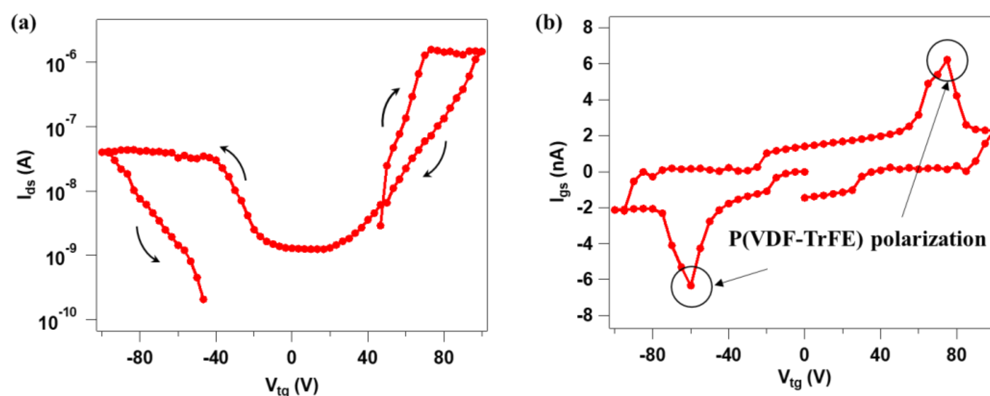

Figure 8-12. Electrical characterization of SP/WSe_2/FeFET in top gate configuration with P(VDF-TrFE) serving as dielectric (a) transfer curve, (b) corresponding leakage current.

b. Optical/thermal/electrical switching capacity of SP/WSe_2/FeFET in back-gate configuration

The optical/heating switching capacity of SP/WSe_2/FeFET was investigated in a back-gate configuration. With the dielectric constant ($\varepsilon_r = 10$) being higher than SiO_2 ($\varepsilon_r = 3.9$), the deposition of P(VDF-TrFE) is believed to suppress the Coulomb scattering in WSe_2.[1b] As a consequence, an improved electron mobility (μ_{e-} = 18.2 $cm^2V^{-1}s^{-1}$) was observed in SP/WSe_2/FeFET compared with SP/WSe_2 FET. In response to UV irradiation, the electron current decreased notably with a modulation efficiency of 84%, accompanied with the mobility decreased to 2.6 $cm^2V^{-1}s^{-1}$. Figure 8-13b depicts the reversible variation of the current during three cycles when different inputs were utilized to switch back the molecule to SP form: heating, vis irradiation and thermally at room temperature. By heating at 140 °C for 6 min and vis irradiation at 530 nm for 30 min, the effects of the previous UV irradiation were completely removed, and electrical performances resumed to original states. While by leaving device that treated with UV irradiation for overnight at room temperature, 63% of the current was restored. The kinetics in electrical measurement matched well with the UV-vis absorption spectra results.

.

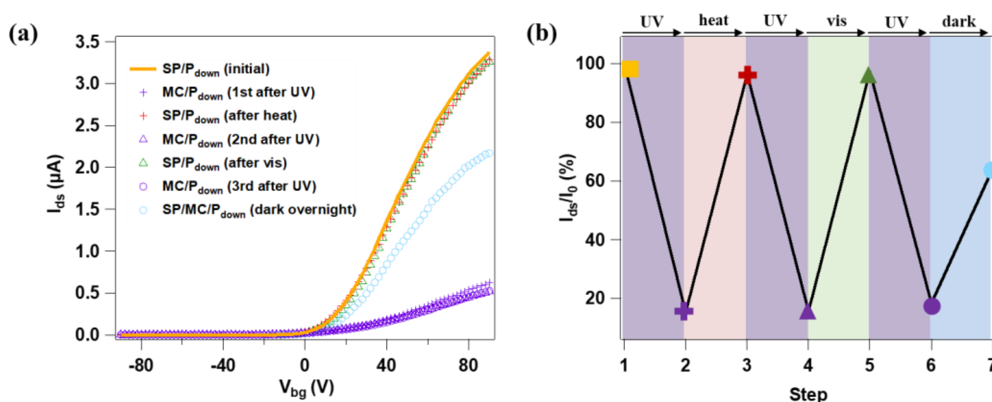

Figure 8-13. (a) Optical/thermal switching capacity of SP/WSe_2/FeFET by UV, and heat/vis/dark treatment. (b) Current modulation efficiency at V_{bg} = 90 V during the 3 switching cycles.

We also explored the reversible variations of the SP/WSe_2/FeFET device performances when P(VDF-TrFE) in upward/downward states. When a -80 V pulse was applied to the top-gate electrode, dipoles inside P(VDF-TrFE) were aligned along external electric field in the upward direction with negatively charged C-F bond facing the channel, thereby causing the pronounced depletion of electrons and accumulation of holes. The corresponding schematic representation of the polarization direction is given in the inset of Figure 8-14. Therefore, compared with that of pristine state (orange line), there is a dramatically decrease of electron current with an efficiency of 99% while an increase of hole current. The device exhibited more balanced ambipolar behavior with hole current comparable to the electron current (μ_{h+} = 0.118 $cm^2V^{-1}s^{-1}$, μ_{e-} = 0.024 $cm^2V^{-1}s^{-1}$). On the contrary, a +80 V pulse can give rise to the reversed arrangement of the dipoles in the downward direction. In this case, with positively charged C-H bond facing the channel, the current state resumed to the original state. Such reversible tuning could be repeated for at least 3 cycles without attenuation upon the successive +80 V and -80 V bias operation.

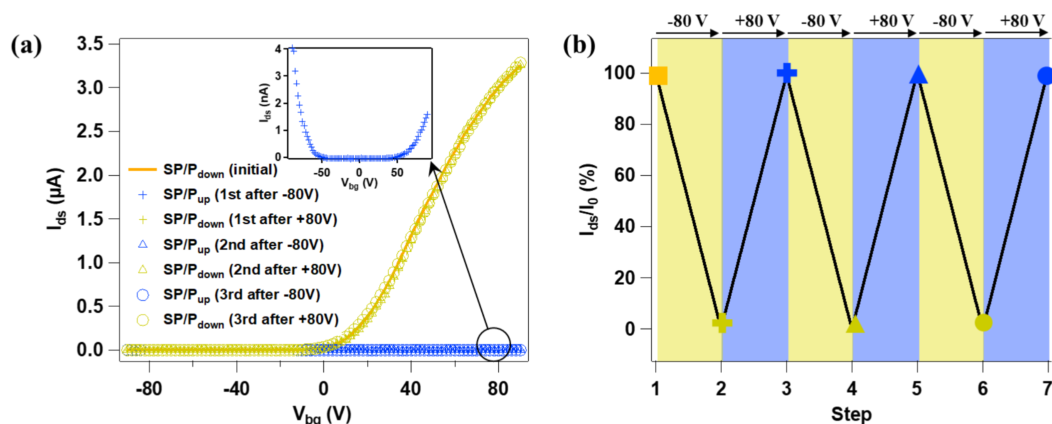

Figure 8-14. (a) Electrical switching capacity of SP/WSe_2/FeFET by ±80 V top gate bias, the inset shows the zoomed curve when P(VDF-TrFE) in upward direction. (b) Current modulation efficiency at V_{bg} = 90 V during the 3 electrical switching cycles.

In the following, to prove the compatibility between these two switching elements, we combined the light and bias stimuli in the same switching cycle. As shown in Figure 8-15a, after first stimuli of UV irradiation, the current decreased in the same ratio as the results above. More strikingly, followed by a negative bias, the electron current further decreased accompanied with an increase of hole current. The electrons in the channel were totally exhausted and the final device turned into p-type. Successive vis irradiation and positive bias led to the restoration of the original performance. Then the stimuli order was switched to first polarize the P(VDF-TrFE) into the upward direction, then switch the SP molecules into MC. The current modulation efficiency at V_{bg} = 90 V was plotted in Figure 8-15b. As expected, similar results were obtained, confirming that the two switching elements were able to work independently without any interference.

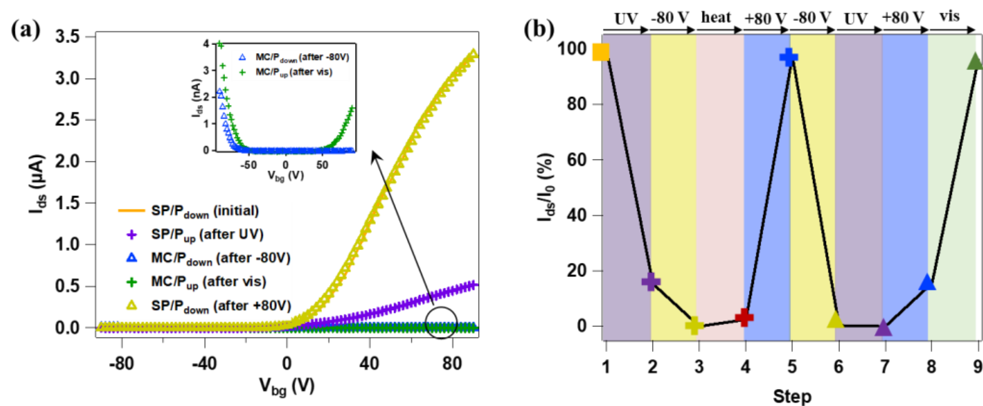

Figure 8-15. (a) Orthogonal switching of SP/WSe_2/FeFET by UV/heat/vis/±80 V top gate bias, the inset shows the zoomed curve of MC/P_{down}, and MC/P_{up} state. (b) Current modulation efficiency at V_{bg} = 90 V during the 2 switching cycles.

To better illustrate the current modulation by different stimuli, the top-gate bias and light irradiation were supplied separately as input signals, and the resulting drain current was collected as the output signal (Figure 8-16). Following the current, when a negative bias was applied, the current value greatly reduced, and stayed constant at that lower current state. Then in response to the positive bias, a current spike appeared, followed by the resume of the current. The reversible current modulation confirms the polarization of P(VDF-TrFE). Subsequently, the application of UV irradiation caused the photoisomerization of SP, lowering the current. Such current modulation cycle can be operated for at least 5 cycles, and we can clearly observe a stepwise decay of current after each cycle. These results clearly demonstrate that the SP/WSe_2/FeFET device is able to respond orthogonally to both external electric field and light irradiation.

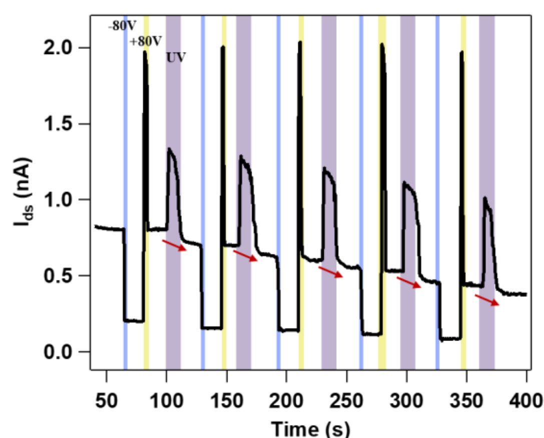

Figure 8-16. Dynamic current tracking under alternative -80V, +80V and UV illumination conditions at V_{bg} = 20 V, V_{ds} = 4 V of SP/WSe_2/FeFET during 5 cycles.

After proving the photoswitching phenomenon by SP, we then turned our attention to analyzing the switching mechanism. The isomerization between SP and MC isomer is accompanied by a variation of the dipole moment, which may alter the local electrostatic environment. Previous work has demonstrated that SP and MC isomer would assemble differently on the substrate. SP was found to be conformationally flexible, while MC can orderly assembled with the positively charged side lifted up, resulting in a n-type doping effect to the interfaced 2D material.[9a] However, this is opposite to our above electrical results, thus being excluded. Another possibility is to apply the electronic band structure to analyze the electron transfer between the SP/WSe_2 system. The highest occupied molecular orbital

(HOMO) and lowest unoccupied molecular orbital (LUMO) energy levels of SP and MC were estimated on the basis of their cyclic voltammograms. The band alignment diagram is illustrated in Figure 8-18, with conduction band (CB) and valence band (VB) values of WSe_2 calculated in the screened exchange functional.[16] Our device based on few-layer WSe_2 displayed electron-dominant transport behavior, so the CB of WSe_2 and LUMO of SP/MC were taken into account. Since the CB of WSe_2 is lower than the LUMO of both SP and MC isomer, electrons in WSe_2 can transfer to neither of these two isomers, hence the possibility of the MC molecules acting as the electron trap site can be excluded. On the other hand, when it comes to mono/bilayer flake which possesses hole-transport behavior, the VB of WSe_2 and HOMO of SP/MC should be taken into consideration. In this case, the HOMO of MC is slightly higher than the VB of WSe_2, therefore MC isomer could act as a shallow trap for holes, which might result in a drop of hole current in the corresponding device. Electrical characterization on monolayer WSe_2 was presented in Figure 8-19, which shows a reversible hole current modulation.

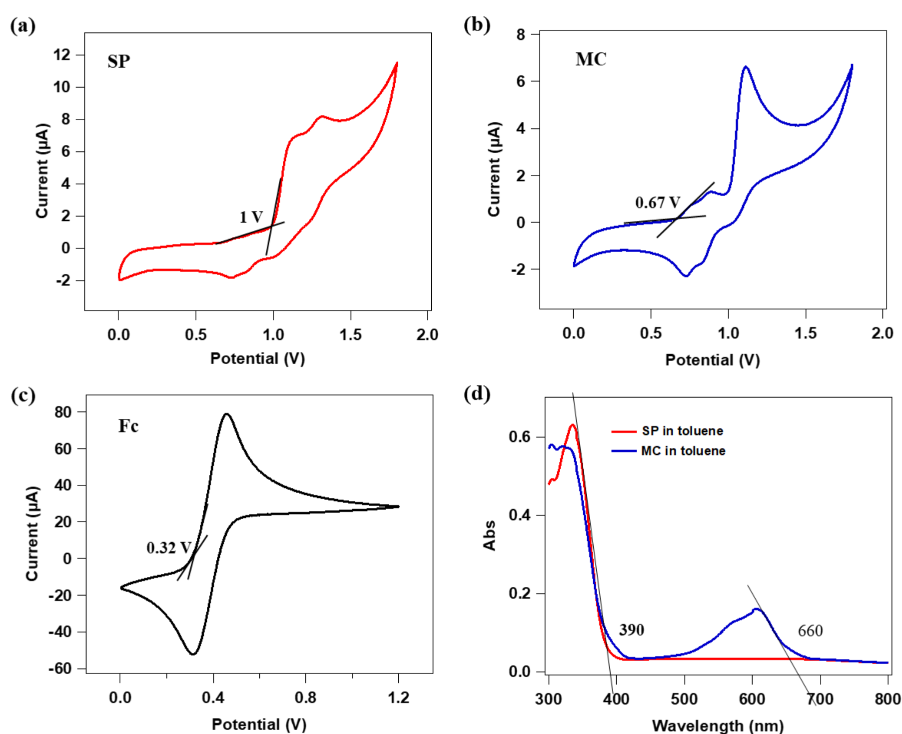

Figure 8-17. Cyclic voltammetry curves of (a) SP, (b) MC and (c) ferrocene (FC), (d) UV-vis absorption spectra of SP/MC in toluene.

	HOMO (eV)	LUMO (eV)
SP	-5.42	-2.24
MC	-5.09	-3.21
WSe_2	-4.83 - -5.17 (bulk) (mono)	-3.35 - -3.5 (mono) (bulk)

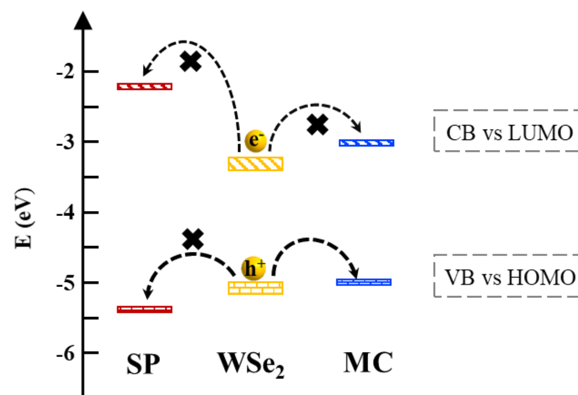

Figure 8-18. Energy level diagram of electron transport between SP/MC and WSe_2.

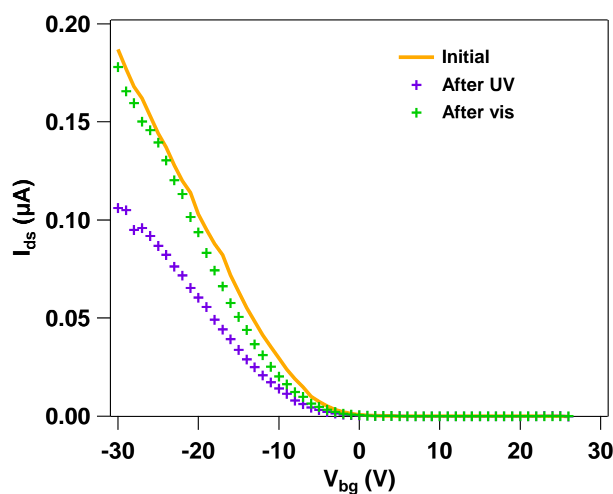

Figure 8-19. Optical switching capacity of a p-type SP/WSe_2 FET device.

Finally, we apply the ionic impurity scattering mechanism as previously reported.[17] It is generally agreed that charge carrier mobility/current of a semiconducting material is limited by the interfaced charged impurities centers, i.e., the lower current state is indicative of a higher density of scatters.[18] In our study, SP is neutral and non-polarized, while MC isomer is ionic polarized because of its opposing separated charges: the N^+ group and the O^- group. Both of these cationic and anionic parts may serve as the scattering center, inducing an attractive or repulsive force with the electrons in the channel. Due to their Coulombic interactions between each other, the trajectory of the electrons will be disturbed and follows a gradual deviation, reducing of current. The scattering manner is similar to that of Coulombic scattering by ionic impurities in semiconducting materials.[19]

To confirm such hypothesis, we performed a comprehensive analysis of the hysteresis by varying gate sweep rate and sweep range in bare WSe_2 FET, and SP/WSe_2 FET when molecules in SP and MC form. Hysteresis in the transfer characteristics of TMD-based FET devices has been attributed to several mechanisms, such as adsorption of O_2 and H_2O molecules,[20] gate-oxide[21] and oxide-TMD interface traps,[22] gate voltage stress[23] and intrinsic defects in the material.[24] It is worth noting that the only altered variable was the SP layer, as the experimental conditions and measurement environment have been kept identical. A full gate sweep consists of both forward and backward sweep, i.e., from negative gate voltage V_{bg} to positive gate voltage V_{bg} then back to negative V_{bg}. Similar trend can be found from the measured devices: a hysteresis with clockwise loop direction with its magnitude been deterministically tuned via both gate voltage sweep range and sweep rate. Figure 8-20d illustrates the comparison of the hysteresis for various sweep rates. In WSe_2 FET, the hysteresis was relatively small, which exhibited significant dependence on the sweep rate and increased from 3 V at 3.2 V/s to 22 V when the sweep rate decreased to 0.7 V/s. This is in accordance with the previous reports since the faster sweep rate inhibits electron from trapping during the measurement.[25] Larger hysteresis is observed in SP/WSe_2 and MC/WSe_2, while the variation in magnitude with the sweep rate is marginally. Therefore, the main contribution for such hysteresis can be attributed to the SP/MC layer. Ionic impurity scattering is considered the main interaction between ionic adsorbates and the charge carriers in the interfaced TMD materials, which may alter the charge distribution at the interface between SiO_2 and TMD material due to the field induced polarization effect, thus have been proposed one of the major sources of the hysteresis.[26] When comparing the hysteresis in SP/WSe_2 and MC/WSe_2, a more pronounced magnitude is clearly observed in the latter. Such phenomenon is coincident with the assumption that the ionic-polarized MC isomer serve as the scattering center.

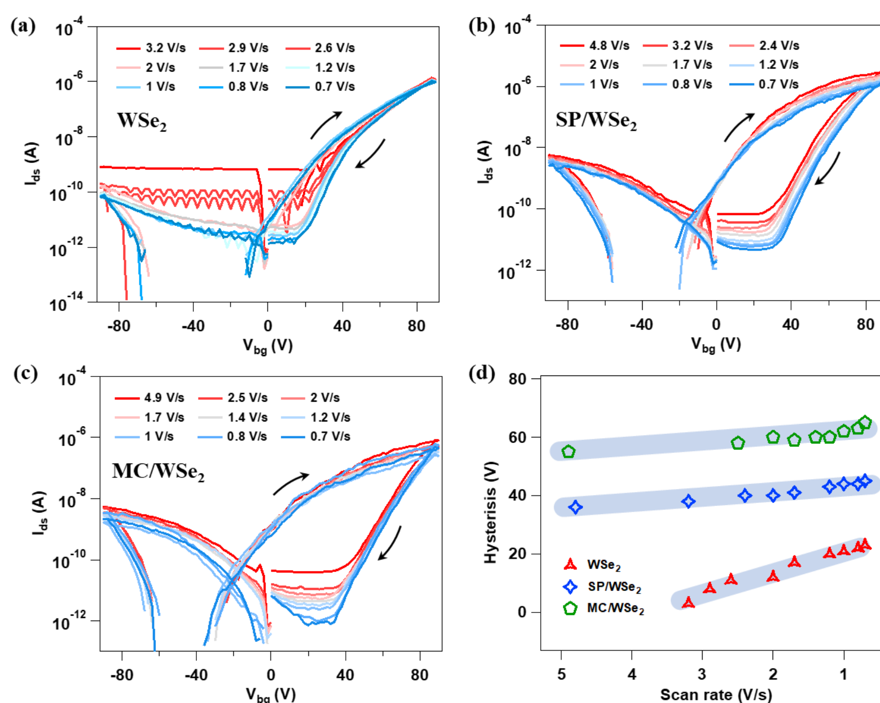

Figure 8-20. Hysteresis characterization of (a) bare WSe_2, (b) SP/WSe_2 and (c) MC/WSe_2 FET under different scan rates, (d) Hysteresis comparison between the three conditions.

Besides sweep rate, hysteresis variations have also been investigated with different sweep ranges (Figure 8-21). For WSe_2, the hysteresis is negligible in the sweep range of 30 V, whose magnitude turns larger as the range becomes wider. It indicates that hysteresis originates from charge trapping/detrapping process at higher gate bias.[24] When it comes to SP/WSe_2, the hysteresis variation turns more prominent. These variations are plotted in Figure 8-21d, where it can be clearly seen that when molecules were in MC form, the sweep range dependent hysteresis variation enhanced as compared to SP/WSe_2, which confirms that MC isomer acts as ionic scattering center that play a main role in the device performance.

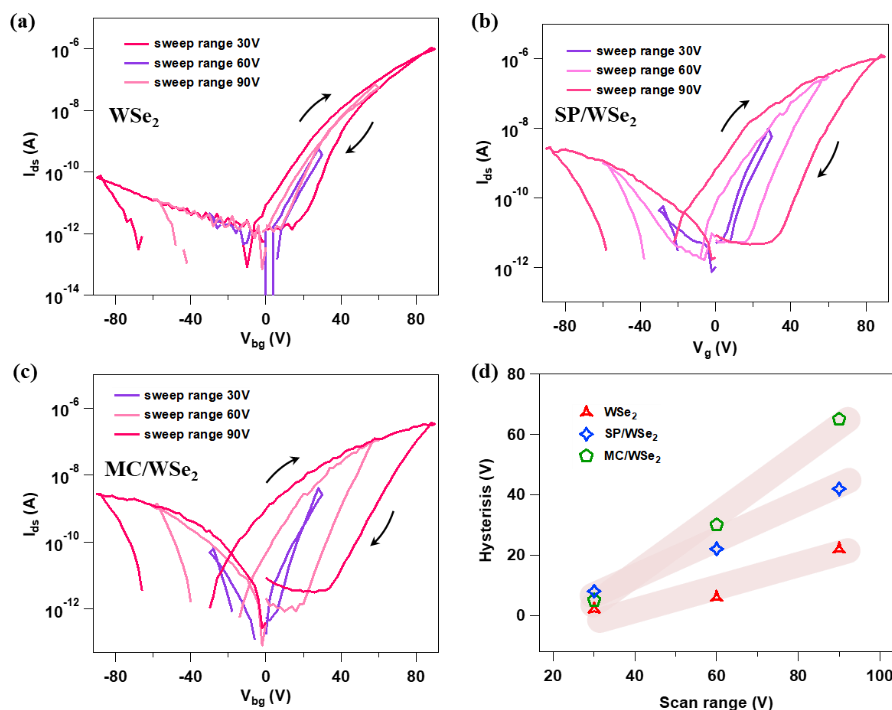

Figure 8-21. Hysteresis characterization of (a) bare WSe_2, (b) SP/WSe_2 and (c) MC/WSe_2 FET under different scan ranges, (d) Hysteresis comparison between the three conditions.

8.4. Conclusion

In conclusion, we have designed and synthesized a photochromic silane-terminated SP derivative, offering a robust molecular platform for fabrication of multifunctional FET devices. A quaternary-responsive WSe_2 FET has later been built up by combining SP and ferroelectric P(VDF-TrFE). The output current could be kindly and independently modulated by external stimuli including heating, light irradiation and electric field. Significantly, the synergic effect between the different stimuli enables a significant modulation of the charge carrier transport in the channel, which switches from n-type to p-type with electron been fully exhausted. The light induced modulation behavior from MC has been explained as the ionic polarized MC isomer plays the role of scattering center. It is anticipated that our design strategy of Janus modified structure can be extended to other TMDs, providing a general guideline to fabricate multifunctional FET devices via double-sided interfacial engineering.

8.5. References

[1] a) K. S. Novoselov, V. I. Fal′ko, L. Colombo, P. R. Gellert, M. G. Schwab, K. Kim, *Nature* **2012**, *490*, 192; b) B. Radisavljevic, A. Radenovic, J. Brivio, V. Giacometti, A. Kis, *Nat. Nanotechnol.* **2011**, *6*, 147; c) Q. H. Wang, K. Kalantar-Zadeh, A. Kis, J. N. Coleman, M. S. Strano, *Nat. Nanotechnol.* **2012**, *7*, 699.

[2] H. Wang, H. Yuan, S. S. Hong, Y. Li, Y. Cui, *Chem. Soc. Rev.* **2015**, *44*, 2664.

[3] a) M. Gobbi, E. Orgiu, P. Samorì, *Adv. Mater.* **2018**, *30*, 1706103; b) S. Bertolazzi, M. Gobbi, Y. Zhao, C. Backes, P. Samorì, *Chem. Soc. Rev.* **2018**, *47*, 6845.

[4] C. Xu, J. Zhang, W. Xu, H. Tian, *Mater. Chem. Front.* **2021**, *5*, 1060.

[5] a) T. Leydecker, M. Herder, E. Pavlica, G. Bratina, S. Hecht, E. Orgiu, P. Samorì, *Nat. Nanotechnol.* **2016**, *11*, 769; b) Y. T. Lee, H. Kwon, J. S. Kim, H.-H. Kim, Y. J. Lee, J. A. Lim, Y.-W. Song, Y. Yi, W.-K. Choi, D. K. Hwang, S. Im, *ACS Nano* **2015**, *9*, 10394.

[6] a) M. Balcı Leinen, P. Klein, F. L. Sebastian, N. F. Zorn, S. Adamczyk, S. Allard, U. Scherf, J. Zaumseil, *Adv. Electron. Mater.* **2020**, *6*, 2000717; b) H. Sun, J.-Y. Li, F.-F. Han, R. Zhang, Y. Zhao, B.-X. Miao, Z.-H. Ni, *Dyes Pigm.* **2019**, *167*, 143.

[7] a) S. Dai, X. Wu, D. Liu, Y. Chu, K. Wang, B. Yang, J. Huang, *ACS Appl. Mater. Interfaces* **2018**, *10*, 21472; b) Y. Yu, Q. Ma, H. Ling, W. Li, R. Ju, L. Bian, N. Shi, Y. Qian, M. Yi, L. Xie, W. Huang, *Adv. Funct. Mater.* **2019**, *29*, 1904602.

[8] C. Brieke, F. Rohrbach, A. Gottschalk, G. Mayer, A. Heckel, *Angew. Chem. Int. Ed.* **2012**, *51*, 8446.

[9] a) M. Gobbi, S. Bonacchi, J. X. Lian, A. Vercouter, S. Bertolazzi, B. Zyska, M. Timpel, R. Tatti, Y. Olivier, S. Hecht, M. V. Nardi, D. Beljonne, E. Orgiu, P. Samorì, *Nat. Commun.* **2018**, *9*, 2661; b) Z. Liu, H. Qiu, C. Wang, Z. Chen, B. Zyska, A. Narita, A. Ciesielski, S. Hecht, L. Chi, K. Müllen, P. Samorì, *Adv. Mater.* **2020**, *32*, 2001268; c) H. Qiu, Y. Zhao, Z. Liu, M. Herder, S. Hecht, P. Samorì, *Adv. Mater.* **2019**, *31*, 1903402; d) H. Qiu, Z. Liu, Y. Yao, M. Herder, S. Hecht, P. Samorì, *Adv. Mater.* **2020**, *32*, 1907903.

[10] M.-A. Stoeckel, M. Gobbi, T. Leydecker, Y. Wang, M. Eredia, S. Bonacchi, R. Verucchi, M. Timpel, M. V. Nardi, E. Orgiu, P. Samorì, *ACS Nano* **2019**, *13*, 11613.

[11] R. Klajn, *Chem. Soc. Rev.* **2014**, *43*, 148.

[12] H. Liu, A. T. Neal, P. D. Ye, *ACS Nano* **2012**, *6*, 8563.

[13] M. Gobbi, A. Galanti, M.-A. Stoeckel, B. Zyska, S. Bonacchi, S. Hecht, P. Samorì, *Nat. Commun.* **2020**, *11*, 4731.

[14] B. Lee, Y. Chen, F. Duerr, D. Mastrogiovanni, E. Garfunkel, E. Y. Andrei, V. Podzorov, *Nano Lett.* **2010**, *10*, 2427.

[15] K. Xu, Z. Wang, X. Du, M. Safdar, C. Jiang, J. He, *Nanotechnology* **2013**, *24*, 465705.

[16] Y. Guo, J. Robertson, *Appl. Phys. Lett.* **2016**, *108*, 233104.

[17] Y. Ishiguro, R. Hayakawa, T. Chikyow, Y. Wakayama, *J. Mater. Chem. C* **2013**, *1*, 3012.

[18] T. Ando, *J. Phys. Soc. Jpn.* **2006**, *75*, 074716.

[19] D. Chattopadhyay, H. J. Queisser, *Rev. Mod. Phys* **1981**, *53*, 745.

[20] a) D. J. Late, B. Liu, H. S. S. R. Matte, V. P. Dravid, C. N. R. Rao, *ACS Nano* **2012**, *6*, 5635; b) N. Kaushik, D. M. A. Mackenzie, K. Thakar, N. Goyal, B. Mukherjee, P. Boggild, D. H. Petersen, S. Lodha, *NPJ 2D Mater. Appl.* **2017**, *1*, 34.

[21] Y. Park, H. W. Baac, J. Heo, G. Yoo, *Appl. Phys. Lett.* **2016**, *108*, 083102.

[22] Y. Guo, X. Wei, J. Shu, B. Liu, J. Yin, C. Guan, Y. Han, S. Gao, Q. Chen, *Appl. Phys. Lett.* **2015**, *106*, 103109.

[23] K. Cho, W. Park, J. Park, H. Jeong, J. Jang, T.-Y. Kim, W.-K. Hong, S. Hong, T. Lee, *ACS Nano* **2013**, *7*, 7751.

[24] J. Shu, G. Wu, Y. Guo, B. Liu, X. Wei, Q. Chen, *Nanoscale* **2016**, *8*, 3049.

[25] J.-M. Park, D. Lee, J. Shim, T. Jeon, K. Eom, B.-G. Park, J.-H. Lee, *Semicond. Sci. Technol.* **2014**, *29*, 095006.

[26] a) S.-H. Chen, Y. Nguyen, T.-W. Chen, Z.-L. Yen, M. Hofmann, Y.-P. Hsieh, *Carbon* **2020**, *165*, 163; b) M. Egginger, M. Irimia-Vladu, R. Schwödiauer, A. Tanda, I. Frischauf, S. Bauer, N. S. Sariciftci, *Adv. Mater.* **2008**, *20*, 1018.

Chapter 9: Conclusion and perspectives

Due to their atomic thickness, large surface-to-volume ratio, free of dangling bonds, and excellent propensity to act as platform for molecular adsorption, 2D semiconductors (2DSs) are undoubtedly an ideal building block for the fabrication of high-performance stimuli-responsive systems and devices. In this thesis, we have investigated the fabrication of multifunctional field-effect transistors (FETs) by interfacing stimuli-responsive molecules with 2DSs.

In the first experimental chapter, optically switchable FETs have been realized by decorating the 2DS channel, n-type dominant WSe_2 and p-type dominant black phosphorus (BP) with suitably designed photochromic diarylethene (DAE) molecules, to modulate their electron and hole transport, respectively. The optical switching of the DAE molecules has been investigated by measuring the UV-vis absorption spectra during the course of UV/vis illumination. The FET device operation has been characterized by transfer, output measurement as well as dynamic current tracking in the dark and under/after UV/vis illumination. In each pair of 2DS/DAE, the requirement of the modulation relies on the matching of their energy levels, to enable the appearance of trapping states only in one of the DAE isomers. In the n-type WSe_2 FET device, the conversion of the molecules from DAE_1o to DAE_1c by UV irradiation induced a p-type doping with a current modulation of 61%. Similarly, for BP with p-type dominant transport, by tailoring the channel with DAE_2, UV irradiation induces a decrease of output current by a modulation of 42%. In this chapter, we provided a proof-of-concept of using ad-hoc DAE molecules to modulate the charge carrier transport of both electrons and holes depending on the nature of the host material without sacrificing their intrinsic performance, opening the door for multiresponsive 2DS/DAE-based FETs that can be switched ON and OFF upon irradiation with light.

In the second experimental chapter, based on the previous demonstrated applicability and effectiveness of 2DS/DAE approach for charge carrier modulation on unipolar 2DS, we tackle full ambipolar 2DS to realize a simultaneous remote control of two charge carriers. Here we target on few-layer WSe_2 flakes with a more balanced ambipolar behavior, with its electron and hole current on the same scale (10^{-6} A). We propose an optically switchable multilevel FET by interfacing WSe_2 with a bicomponent DAE

blend consisting of two molecules with specific energy levels, which are engineered to be capable of trapping either the electrons or the holes of WSe_2 by remote light stimuli. UV–vis absorption spectra of the DAE blend/WSe_2 film were initially recorded on quartz substrates. Note that both DAEs show similar molar absorptivities, speed of photoisomerization (quantum yields), and almost quantitative formation of the ring closed isomer under UV irradiation, allowing for their fully simultaneous operation in the device. For the electrical characterization on FET device, the output current modulation for holes is as high as 97%, while for electrons the modulation amounts to 52%. By taking advantage of the high fatigue resistance and the thermal bi-stability from DAE molecules, the devices are further employed to memory applications. The photomodulation was demonstrated to be efficient and reversible with negligible switching fatigue after over 20 illumination cycles. Moreover, the modulation ratio can be readily tuned by controlling the light dose, which means by adjusting the irradiation duration the FET device can reach a multitude of current states. In particular, the balanced ambipolar characteristic of WSe_2 enables our device to attain 64 distinct current levels for both holes and electrons, highlighting its potential to be further developed into multilevel memories with data storage capacity of 7 bit. Additionally, the device is shown to possess a prolonged retention time exceeding 20 days in the dark. Remarkably, by taking full advantage of the superior mechanical properties of ultrathin 2D WSe_2, our device is also able to be operated on a flexible and transparent poly(ethylene terephthalate) substrate with indium tin oxide serving as back-gate electrode and cross-linked poly(4-vinylphenol) as dielectric material, without losing its optical switching capability. Moreover, over 100 bending cycles are monitored on the PET device, both hole and electron currents can virtually preserve their modulation efficiency, suggesting a good mechanical stability of our device on the flexible substrate. Therefore, the new device architecture presents paramount importance for multilevel nonvolatile wearable memory applications.

In the above two chapters, optically switchable FETs have been demonstrated, by directly spin-coating the DAE molecules on top of the upper channel surface, leaving the bottom surface of the channel material undecorated. In the third experimental chapter, in order to best exploit both two surfaces of the 2D flake, we designed an unprecedented approach based on the decoration of WSe_2 flakes with two

different stimuli-responsive (macro)molecules thereby generating a Janus 2DS structure. In particular, the light-responsive DAE_1 layer was shifted on the bottom surface of WSe_2 to preserve the light-responsive capacity, and the top surface was coated with an electric-responsive copolymer poly(vinylidene fluoride-trifluoroethylene) (P(VDF-TrFE)) layer. With such architecture a multi-stimuli-responsive FET has been fabricated in which the output current could be reversibly and precisely modulated by means of either light irradiation or electric field. Compared with conventional mono-stimuli-responsive FETs, this novel ternary device architecture combines enhanced functional complexity with fabrication simplicity, offering an orthogonal handle over the device operation. Thanks to the synergic effect between the two (macro)molecular switches, the device has attained an enhanced modulation of the output current, with an efficiency reaching up to 87%. When integrating to memory application, with 9 electric-induced levels and 84 light-induced levels, the device yields a total number of 756 distinct states, outperforming the current state-to-art mono 2D stimuli-responsive transistors thereby providing a decisive step forward to address the demand for high density storage memories. The reliability of each state is further reflected by the endurance and retention tests for 5 arbitrary states, exhibiting a notable endurance for over 10 cycles and an excellent data retention exceeding 1000 hours. Moreover, compared with cumbersome synthesis of single molecules incorporating different functional groups to realize the multi-addressable elements, this Janus modified ternary structure relies on a simple fabrication process and it appears to be a more universal strategy that can be extended to other 2DSs and functional molecules, offering a versatile platform for the construction of multi-stimuli-responsive devices.

In the above chapter, the physiosorbed DAE layer provides a promising way towards non-destructive functionalization of the channel material. However, the weak van der Waals interaction between the molecules and the Si/SiO_2 substrate can result in easy removal of the molecules during a simple rinsing procedure. As a consequence, conventional photolithography cannot be exploit with such device architecture, and the choice of the second stimuli-responsive element is also limited. To overcome this issue, in the final experimental chapter, we designed and synthesized a silane-terminated SP derivative, which can densely pack on Si/SiO_2 substrate through a strong covalent silylation. Such nonvolatile

chemisorption thereof facilitates the device fabrication and provides a better compatibility when integration a third element into the system. Moreover, the photochromic isomerization from SP to merocyanine (MC) can be triggered by UV light illumination, and the reverse switch from MC to SP can be accomplished by vis light illumination as well as heating, adding a further thermal-responsive nature to the corresponding FET device compared with DAE system. The functionalization of SP film on SiO_2 surface has been confirmed through UV-vis absorption spectra, water contact angle measurements, atomic force microscopy and PL mapping. In particular, the kinetics of the photoisomerization between SP and MC has been followed by monitoring the evolution of the absorbance at 550 nm. For the electrical characterization, following the similar Janus modified structure, silane-terminated SP photochromic molecule and ferroelectric polymer P(VDF-TrFE) have been incorporated into WSe_2-based FET devices. With this combination, we obtained quaternary-stimuli-responsive FET capable of perceiving heat, light and electric field stimuli inputs and modulate output current accordingly. Such hierarchical architecture enables an independent control of the output current under distinct multiple stimuli. Taking advantage of the synergic effect between the stimuli, with a significant electron current modulation efficiency of 84% from SP, and 99% from P(VDF-TrFE), the electrons in the channel can be totally exhausted when combining the two switches and the device thereof can be modulated from n-type to p-type. The analysis of the switching mechanism of SP molecules revealed a key role played by the ionic impurity scattering mechanism. SP is neutral and non-polarized, while MC isomer is ionic polarized because of its opposing separated charges: the N^+ group and the O^- group. Both of these cationic and anionic parts may serve as the scattering center, inducing an attractive or repulsive force with the electrons in the channel. It is anticipated that our design strategy of Janus modified structure can be extended to other TMDs, providing a general guideline to fabricate multifunctional FET devices via double-sided interfacial engineering. By collectively pooling multiple stimuli as inputs, the overreliance in a single stimulus has been reduced, which moreover increases the sensitivity and compliance of the molecular-tailored stimuli-responsive platform.

In conclusion, during the four experimental chapters, we have exploited the stimuli-responsive molecular approach to fabricate multifunctional FETs whose output current can be remotely and

reversibly controlled not only by its internal electric field, but also by various external stimuli including light, heat and electric field. The projected saturation of Moore's law and the expiration of Dennard scaling has highlighted the demand for integrating novel analog functionalities within semiconductor-based devices. Stimuli-responsive molecules, which are characterized by spatial, temporal and dosage control, can be responsive to many other stimuli, like pH, redox, enzyme, magnetic field, etc, and are available commercially or through chemical synthesis. Therefore, such combination of 2DS with the virtually infinite number of stimuli-responsive molecular systems, offers countless opportunities to engineer the hybrid with characteristics on demand for device applications. In such hybrids, new functionalities can be introduced in a controlled manner, thereby opening further possibilities for developing multiresponsive devices. With more stimuli being applied into single transistor, the device turns increasingly intelligent and controllable.

In the future, the control over the nanoscale molecular ordering might be further investigated. By mastering molecular self-assembly it would be possible to interpret specific functional groups at pre-determined spatial locations with an atomic presision, enabling a direct correlation with the modulation in the electrical characteristics of the host 2DS. Moreover, our molecular chemistry approach can be extended to van der Waals heterostructures that are composed of superimposed different 2DSs with "corrected" and optimized properties. Molecules can be incorporated into these layered structures to generate novel hybrid systems in which various molecular capabilities are conferred to different 2DSs. Furthermore, to promote the industrialization, instead of mechanical exfoliation, CVD-synthesised 2DS with controlled thickness or solution-processed high-quality 2DS might be integrated into the device to ease of fabrication and allow many integrated devices over large areas. Towards the improvement of the quality of our lives, the development of the defined hybrid structure shall be focused on wearable, portable, and foldable multiresponsive electronic devices, opening a new technological era. All in all, the full exploitation of the infinite options offered by molecular science in terms of functional diversities shall yield to the emergence of new, disruptive and exotic technologies based on 2DS or related heterostructures.

Statement of work

All experiments and data analysis reported in this thesis have been carried by myself, except for the following:

Chapter 4: The synthesis of DAE molecules was carried out by Dr. Martin Herder (Berlin).

Chapter 5: The AFM study was performed by Dr. Yuda Zhao (Hangzhou).

Chapter 6: The AFM study was performed by Stefano Ippolito.

Chapter 7: The AFM study was performed by Stefano Ippolito.

Chapter 8: The synthesis of SP molecules was carried out by Dr. Agostino Garanti (Bristol). The AFM study was performed by Stefano Ippolito. The CV measurement was carried out by Dr. Zhaoyang Liu.

Prof. Paolo Samorì helped on designing various experiments and data analysis through very helpful discussion.

List of publications

Asymmetric Dressing of WSe_2 with (Macro)molecular Switches: Fabrication of Quaternary-Responsive Transistors
Haixin Qiu, Stefano Ippolito, Agostino Galanti, Zhaoyang Liu, Paolo Samorì
In press, ACS nano

Ternary-Responsive Field-Effect Transistors and Multilevel Memories based on asymmetrically functionalized Janus Few-Layer WSe_2
Haixin Qiu, Martin Herder, Stefan Hecht, Paolo Samorì
In press, Advanced Functional Materials

Photomodulation of Charge Transport in All-Semiconducting 2D-1D van der Waals Heterostructures with Suppressed Persistent Photoconductivity Effect.
Zhaoyang Liu, Haixin Qiu, Can Wang, Zongping Chen, Björn Zyska, Akimitsu Narita, Artur Ciesielski, Stefan Hecht, Lifeng Chi, Klaus Müllen, and Paolo Samorì.
Advanced Materials 32, no. 26 (2020): 2001268. (Cover page)

Simultaneous Optical Tuning of Hole and Electron Transport in Ambipolar WSe_2 Interfaced with a Bicomponent Photochromic Layer: From High-Mobility Transistors to Flexible Multilevel Memories.
Haixin Qiu, Zhaoyang Liu, Yifan Yao, Martin Herder, Stefan Hecht, and Paolo Samorì.
Advanced Materials 32, no. 11 (2020): 1907903. (Cover page)

Modulating the Charge Transport in 2D Semiconductors via Energy-Level Phototuning.
Haixin Qiu, Yuda Zhao, Zhaoyang Liu, Martin Herder, Stefan Hecht, and Paolo Samorì.
Advanced Materials 31, no. 39 (2019): 1903402

Water-Dispersed High-Quality Graphene: A Green Solution for Efficient Energy Storage Applications.
Liu, Zhaoyang, Heng Zhang, Matilde Eredia, Haixin Qiu, Walid Baaziz, Ovidiu Ersen, Artur Ciesielski, Mischa Bonn, Hai I. Wang, and Paolo Samorì.
ACS nano 13, no. 8 (2019): 9431-9441.

List of communications

Optical tuning of hole and electron transport in ambipolar WSe_2 interfaced with a bicomponent photochromic layer: from high mobility transistors to flexible multilevel memories.
Haixin Qiu, Zhaoyang Liu, Yifan Yao, Martin Herder, Stefan Hecht, and Paolo Samorì.
Graphene and 2DM (GO2020) online conference, 7 Juillet 2020, oral presentation

Optical Tuning of the charge carrier transport in 2D semiconductors via energy-level phototuning
Haixin Qiu, Zhaoyang Liu, Yifan Yao, Martin Herder, Stefan Hecht, and Paolo Samorì.
2020 online CSC-Seminar in Germany and France, 9 Septembre 2020, oral presentation

Acknowledgements

The moment has finally arrived, the end of the thesis, the end of my life in France, for nearly 8 years.

I would like to express my great gratitude to people I have met during this challenging and exciting PhD experience.

First and foremost, I want to thank my supervisor Prof. Paolo SAMORì, who accepted me as a master student as later a PhD student in his research team. I feel great fortune to work under his guidance and have received relentless assistance from him throughout these years. I am grateful for the patience, trust, and freedom he gave me in the scientific areas. Moreover, I highly appreciate his suggestion and guidance for my further work.

I am also thankful to the jury members M. David BELJONNE, M. Dominique VUILLAUME, and M. BIANCO Alberto, for accepting to be referees and dedicating time to this thesis.

I will always be grateful to Dr. Marco Gobbi, my supervisor during the master internship, who guided into the world of 2D materials. He imparted me important theoretical basis and experimental techniques, which has benefited me throughout the PhD research. And Dr. Simone Bertolazzi, my co-supervisor during the first year of the PhD. With an extreme patience and a religious altitude towards the science, he had a positive impact on my research career.

Many special thanks to my colleagues in the Nanochemistry Group, from whom I received strong support. All of them will remain in my memory, for their skills in the lab and sincere friendship. I am deeply grateful to Dr. Zhaoyang Liu, Dr. Rafael Furlan de Oliveira, Stefano Ippolito and Dr. Yuda Zhao, whom I can always go to whenever have doubt or question. Their valuable scientific suggestions had avoided many detours on my research road.

My collaborators from Berlin also played an important role, who synthesized molecules with interesting features. My work would not have been the same without their support.

It has been an enormous privilege to receive funding from Chinese Scholarship Council.

Last but not the least, I thank people in my family for their endless love, tenderness, and support, especially my parents. I owe them everything. Also, I thank my bestie Lu and her little baby Simon, who brought me great joy and energy in life outside the work.

Haixin

Université de Strasbourg

Haixin QIU

EDSC
École Doctorale des Sciences Chimiques

Interfaçage des molécules réactives avec des semi-conducteurs 2D: fabrication de dispositifs multifonctionnels

Résumé

Le travail mené dans le cadre de cette thèse s'est axé sur la fabrication de dispositifs multifonctionnels basés sur des semi-conducteurs bidimensionnels (2DS) décorés de molécules dont le courant de sortie peut être contrôlé de manière réversible non seulement par son champ électrique interne, mais aussi par divers stimuli externes, comme la lumière, la chaleur et le champ électrique. Des FET à réponse binaire ont été fabriqués en intégrant des 2DS avec des molécules photochromiques DAE. Des FET à réponse ternaire ont ensuite été réalisés en ajoutant un troisième composant, le polymère ferroélectrique P(VDF-TrFE). Les dispositifs ont démontré leur application en tant que mémoires non volatiles à haute densité. Enfin, en remplaçant DAE par SP, des FET à réponse quaternaire aux stimuli ont été fabriqués. Notre architecture de dispositif ouvre de nouvelles opportunités pour l'électronique multi-stimuli-sensible et favorise le développement de technologies «More than Moore» en enrichissant la diversification.

Mots-clés : semi-conducteurs bidimensionnels, molécules réactives, dispositifs multifonctionnels, photochromique, ferroélectrique

Résumé en anglais

The work carried out within this thesis is centered on the fabrication of multifunctional devices based on molecular tailored two-dimensional semiconductors (2DSs) whose output current can be remotely and reversibly controlled not only by its internal electric field, but also by various external stimuli including light, heat and electric field. In particular, binary-responsive FETs have been fabricated by integrating 2DSs with photochromic DAE molecules. Ternary-responsive FETs have later been realized by adding a third component, the ferroelectric P(VDF-TrFE) polymer. The devices have been demonstrated the application as high-density nonvolatile memories. Finally, by replacing DAE with SP, quaternary-stimuli-responsive FET have been fabricated. Our molecular-tailored strategy opens new opportunities for next-generation multi-stimuli-responsive electronics and promotes the development of “More than Moore” technologies by enriching diversification.

Keywords: two-dimensional semiconductors, stimuli-responsive molecules, multifunctional devices, photochromic, ferroelectric